Processing and modelling of shear-wave VSPs in anisotropic structures: case studies

by

Gareth S. Yardley

B.Sc.(Hons.) Physics 1986, University of Bristol

M.Sc. Geophysics and Planetary Physics 1988,
University of Newcastle-upon-Tyne

Thesis submitted for the degree of Doctor of Philosophy
Department of Geology and Geophysics
University of Edinburgh
1993

To

Andrew Richard Ford (1964-1990)

who saw the wild things.....
and the mountains[1]

[1]Adapted from a speech by Bilbo Baggins in "The Lord of the Rings" by J.R.R.Tolkien.

ABSTRACT

Recent work has shown that the fractures, which control productivity and fluid flow in some reservoirs, can cause the rockmass to be anisotropic to shear-wave propagation. The aim of this thesis is to extract information about fracture orientation and density from shear-waves recorded in producing formations. I examine VSP data from two areas (where productivity is fracture related): the Lost Hills field, California; and from three sites along the Austin Chalk trend, Texas. I use anisotropy estimation techniques to determine instrument polarities and the anisotropy parameters at each site. I produce anisotropic models for both areas. I am not able to resolve reservoir anisotropy using transmitted shear-waves. To determine reservoir anisotropy, I adapt reflected amplitude techniques and apply them to the Austin Chalk VSP data.

At all four sites I find that the leading split shear-wave is polarized parallel to known fracture and stress directions. The polarization direction of the rockmass changes with depth in the Lost Hills anticline leading to multiply split shear-waves. Application of estimation techniques in the presence of multiple splitting has lead to incorrect interpretations of this data set in recent publications. I modelled the multi-offset data from the BP test site, Texas, with a combination of vertical aligned cracks and horizontal thin layer anisotropy. This study demonstrates that analysis of shear-wave anisotropy can be used to determine fracture orientation for use in oil recovery projects. Reflected amplitude studies show that the Austin Chalk in the Burleson County VSP, which contains a producing reservoir, is anisotropic, whereas the Austin Chalk at the other two sites, which do not contain reservoirs, is isotropic. I conclude that analysis of reflected shear-wave amplitudes represents an important tool for identifying fractured reservoirs. Also, reflection studies can be used in cases where the reservoir is too thin for delays to build up in transmitted shear-waves.

ACKNOWLEDGEMENTS

I would like to thank my supervisor, Professor Stuart Crampin, for his continual support and enthusiasm. I would also like to thank Dr.Chris Browitt, for allowing me to work within the Seismology Group at the British Geological Survey, and Professor Creer, my supervisor within the University of Edinburgh.

I wish to thank the various members of the BGS and the Seismology Group who have helped me throughout this work, particularly: David Campden and Colin MacBeth for answering stupid questions; Gerhard Graham for writing the computer programs used in the Appendix; Xiang-Yang Li for help with programs and data analysis; Xinwu Zeng for help with estimation techniques; Phil Wild for computer support; Mike Sankey for help with processing; and also Iain Bush, Heiner Igel, Helen Rowlands and Enru Liu for many useful discussions. I appreciate the help of Peter Leary, Anton Ziolkowski, Sue Raikes, Helen Rowlands, Stuart Crampin, Mike Mueller and Colin MacBeth for their comments on this thesis.

I am grateful to the sponsors of the Edinburgh Anisotropy Project, who provided the funding for my work and for travel to conferences. Special thanks go to Sue Raikes (BP) and Mike Mueller (Amoco) for providing the Austin Chalk data.

I would also like to thank Gerhard Graham, Helen Rowlands and David Campden for the late night drinking sessions and discussions on life, the universe and anisotropy, and the *Vets on the Razz* for taking me on holidays to France and the mountains.

Finally, thanks to my family, especially my parents, Glenn and Sylvia Yardley, for putting up with me throughout this, for their support and encouragement, and the greatly appreciated financial help.

CONTENTS

CHAPTER SIX:

SHEAR-WAVE ANISOTROPY IN THE AUSTIN CHALK, TEXAS: MODELLING

CHAPTER SEVEN:

SHEAR-WAVE ANISOTROPY IN THE AUSTIN CHALK, TEXAS: NORMAL INCIDENCE REFLECTIONS

CHAPTER ONE

INTRODUCTION

1.1 INTRODUCTION

Hydrocarbon reserves will remain healthy well into the next century. Odell [1990] sees continual development in the North Sea, and large oil companies are moving into new ventures in Russia and China. However, with little chance of a decrease in demand and a finite number of hydrocarbon reserves, it is necessary to develop new ways of locating reservoirs and of increasing the yield from producing reservoirs. Nur [1989] calls for better reservoir characterization in an attempt to increase the recoverable amount of hydrocarbons trapped in the earth. The Faja field in Venezuela, for example, which is at present only a marginal producer could supply the world's current energy needs for the next 200-1000 years if a 50% recovery rate could be achieved [Nur 1989].

Hydrocarbon reservoirs often contain aligned fractures or cracks. These can provide the dominant pathway for produced oil [Mueller 1992] and can lead to permeability anisotropies as high as 1000:1 (Spraberry trend, Texas; Elkins & Skov [1960]). Knowledge of the orientation of such cracks, and fractures, can tell engineers which direction to drill horizontal wells to maximise recovery and allow enhanced oil recovery programs to be designed more effectively. This is of enormous economic importance: by 1980 40% of oil in the United States was being recovered in EOR programs [Latil *et al.* 1980]. The ability to locate regions of high fracture density is also important: productive reservoirs in the Austin Chalk, Texas, are associated with fracture swarms [Kuich 1989].

Rocks containing aligned fractures, and cracks, are elastically anisotropic. In anisotropic media shear-waves generally split into two components with different velocities. Examining shear-waves after passage through anisotropic rock may give us vital information about reservoir structure. Fracture strike, and probable direction of fluid flow, can be inferred from the polarization direction of the fast split shear-wave. The time delay between the two shear-waves can give information about fracture, and

crack, density. Analysis of split shear-waves could, therefore, be of great importance to the hydrocarbon industry [Crampin 1987a; Crampin, Lynn & Booth 1989].

It should be noted that I do not see the use of shear-wave anisotropy as a complete answer to the needs of the hydrocarbon exploration and production industries, but rather as one tool in a multidisciplinary effort.

1.2 THESIS AIMS

My aim in this thesis is to extract information about reservoir properties using shear-wave seismics. I present vertical seismic profile (VSP) case studies from two regions where productivity is known to be associated with fracturing. I process and model this data to try determine the anisotropic structure of the rockmass (particularly the reservoir layer). In doing this I examine the validity of anisotropic estimation techniques and how best they can be applied. I also examine how to extract and use the information contained in VSP reflected arrivals in cases where the reservoir is too thin to be examined by transmitted waves.

VSPs are generally associated with the latter stages of exploration (tying-in interfaces on reflection lines), and with detailed mapping of reservoir structure (location of minor faulting, etc.). With the geophones at known levels within the well, VSPs give a more controlled environment in which to study shear-waves than do surface reflection surveys. The results, once determined in this controlled setting, can then be applied to seismic reflection data in an exploration environment.

1.3 THESIS SUMMARY

In **Chapter Two**, I review relevant causes of anisotropy in rocks and describe the behaviour of shear-waves in anisotropic media. I outline the methodology used in this thesis to process, model and interpret shear-wave VSP data [Wild, MacBeth, Crampin, Li & Yardley 1993]. I also review recent successful applications of the study of shear-wave anisotropy to the hydrocarbon industry.

In **Chapter Three**, I use synthetic seismograms to show why it is easier to study VSP rather than reflection survey data, particularly when crack orientation changes with depth. This work was the first to demonstrate that anisotropic estimation

techniques may give invalid results in all but the simplest structures [Yardley & Crampin 1989, 1991]. Extensions of this work have also been published: Liu, Crampin & Yardley [1990]; and MacBeth & Yardley [1992].

Chapter Four presents a VSP case study from the Lost Hills field in California. Squires, Kim & Kim [1989] and Winterstein & Meadows [1991a] infer changes in fracture orientation with depth in the Lost Hills field from seismic data. This analysis forms a case study of the work in Chapter Three. I show that *qS1* direction, at depth, is parallel to the stress direction and that the results of the estimation techniques can be matched in models with a changing crack strike with depth. Preliminary results were presented by Yardley & Crampin [1990]. The layer stripping approach has been analyzed by MacBeth, Zeng, Yardley & Crampin [1992].

In the following three chapters I examine VSP data from three sites along the Austin Chalk trend, Texas. Reservoir productivity in the Austin Chalk is known to be associated with fracturing and I try to establish a link between shear-wave anisotropy and fracturing. This work has been published by Yardley & Crampin [1993].

In **Chapter Five**, I process the VSP data to give the anisotropy parameters: time delay; and polarization angle. I use the anisotropy estimation techniques to determine the correct source/geophone polarities and I examine how best the estimation techniques can be applied to offset data. I process shear-wave data created by a *P*-wave source to yield anisotropy parameters similar to those found using shear-wave sources.

Two of the sites have multi-offset VSPs. In **Chapter Six**, I model the anisotropic structure at these sites using a combination of vertical cracks and horizontal thin layer anisotropy. Most of the azimuthal anisotropy is in the near-surface. Modelling shows that this near-surface azimuthal anisotropy is due to vertical features which are parallel to the regional stress field.

In the previous two chapters I was not able to identify anisotropy in the Austin Chalk using transmitted shear-waves. In **Chapter Seven**, I review previous work on using vertical incidence reflected shear-waves to quantify the anisotropy in a reflector [Yardley, Graham & Crampin 1991]. I adapt this work and apply it to the Austin Chalk VSP data. The Austin Chalk at Burleson, which contains a fractured reservoir,

is anisotropic. I conclude that fractured reservoirs can be located using reflected shear-wave data.

In **Chapter Eight**, I discuss the likely causes of the anisotropy seen in the case studies. The azimuthal anisotropy appears to be stress related; however, there is little resolvable anisotropy at reservoir depths. I discuss the implications of this for the study of shear-wave anisotropy in the hydrocarbon industry. I also make suggestions for further work.

In **Appendix 1**, I examine what offset reflections can tell us about the crack structure of reservoirs. I conclude that, whilst offset reflected amplitudes contain information about crack density and content, they are difficult to measure in practice [Yardley, Graham & Crampin 1991].

1.4 ABBREVIATIONS USED IN THIS THESIS

AIT	Analytical independent rotation technique
AST	Analytical synchronous rotation technique
AVO	Amplitude versus offset
AR	Aspect ratio
CMP	Common midpoint
DPM	Double source propagator matrix (estimation technique)
DTS	Direct time series (estimation technique)
ε	Crack density
EDA	Extensive-dilatancy anisotropy
EOR	Enhanced oil recovery
IL	Inline
LTT	Linear transform technique (estimation technique)
NMO	Normal moveout
PD	Polarization diagram (Hodogram)
PTL	Periodic thin layer
qP	Quasi-*P*-wave
qSR	Quasi-shear-wave polarized at (R)ight angles to crack normals
qSP	Quasi-shear-wave polarized (P)arallel to crack normals
*qS*1	Leading (faster) split quasi-shear-wave
*qS*2	Second (slower) split quasi-shear-wave
SEGY	Industry standard format for transfer of seismic data
Vp	*P*-wave velocity
Vs	Shear-wave velocity
VSP	Vertical seismic profile
XL	Crossline

CHAPTER TWO

SHEAR-WAVE ANISOTROPY AND THE HYDROCARBON INDUSTRY

2.1 INTRODUCTION

The aim of this chapter is to provide sufficient background information about shear-wave uses, behaviour, processing, and modelling to ensure that the research presented in this thesis can be understood and set in context.

A history of the use of shear-waves in exploration seismology is given by Tatham & McCormack [1991]. Shear-wave seismics were initially studied as it was believed that they would give better resolution than *P*-waves and, when compared with *P*-wave results, would give information about lithology. This work concentrated on *SH*-waves as these do not produce *S*-to-*P* conversions in horizontally layered media; however, the arrivals were not as clear as expected.

In 1976 a consortium of 13 companies (the Conoco Group Shoot) started a two year project to gather shear-wave data from 20 sites in the USA. The results of the anisotropic analyses of these data sets were presented at the 1986 SEG meeting [e.g. Alford 1986; Becker & Perelberg 1986; Lynn & Thomsen 1986; Willis, Rethford & Bielanski 1986]. By this time workers such as Crampin [1985a] were suggesting that shear-wave anisotropy, the cause of the apparent low quality of shear-wave data, was in fact the source of useful information. Since the mid-1980s, many applications of shear-wave anisotropy to the hydrocarbon industry have been published. These have been summarised by Crampin & Lovell [1991].

2.2 WHY ARE ROCKS ANISOTROPIC?

Rocks are anisotropic if they have different elastic properties in different directions. Rocks may be anisotropic for a variety of reasons; these have been described by Crampin, Chesnokov & Hipkin [1984]. The two principal reasons discussed in this thesis are thin layers, and aligned cracks or fractures. The significance of layering (e.g. sequences of geological beds) has been recognised for

many years [Postma 1955]. This is called thin layer anisotropy and can give directional shear-wave velocity variations between ray paths normal to and parallel to the layers of up to 20%. [Percentage anisotropy is given by $((V_1-V_2)/V_1)\times100$; where V_1 and V_2 are the fastest and slowest shear-wave velocities through the medium]. Thin layer anisotropy is commonly present in sedimentary basins [Bush & Crampin 1991].

Shear-wave anisotropy attributed to aligned cracks, or fractures, is typically between 1% and 5%. Fracturing can be caused by: far field compression [Lorenz, Lawrence & Teufel 1991]; folding of beds (fractures can occur along the fold axis which is usually perpendicular to the regional maximum compressive stress [Crampin *et al.* 1986)]. Fracturing may also be caused by down-warping (due to salt-withdrawal structures [Lewis, Davis & Vuillermoz 1991] or loading) and faulting [Scott 1977; Stapp 1977].

2.3 MODELLING ANISOTROPIC MEDIA

In this thesis I use the ANISEIS modelling package (version 4.0) [Taylor 1990] to create synthetic seismograms in anisotropic models. The wave equation in an anisotropic medium is:

$$\rho(\partial^2 u_i/\partial t^2) = c_{ijkl}(\partial^2 u_k/(\partial x_j \partial x_l)); \qquad (2\text{-}1)$$

where ρ is the density, u_k is the displacement in the kth direction and c_{ijkl} is a fourth order tensor of elastic constants in which $i,j,k,l = 1,2,3$. In general the solution gives three body waves; one with mostly longitudinal motion *qP* (the quasi *P*-wave) and two with mostly transverse motions *qS1* and *qS2* (the fast and slow quasi-shear-waves).

ANISEIS uses an extension of the anisotropic reflectivity technique of Booth & Crampin [1983] to solve the wave equation in anisotropic structures. This is a full waveform technique and the synthetic seismograms produced contain all arrivals. The reflectivity technique was originally developed by Fuchs [1968] and Fuchs & Müller [1971] to calculate synthetic seismograms for modelling earthquakes in isotropic media and is limited to modelling plane layered structures.

Application of the reflectivity technique to the modelling of seismic data means

that the spherical wave (from a point source in an isotropic[1] medium) or the cylindrical wave (from a line source in an isotropic medium) may be decomposed into plane waves. The plane waves are transformed through the layered structure using propagator matrices [Gilbert & Backus 1966; Crampin 1970] to find the effective reflectivity of those parts of the model above and below the source. This determines the excitations of the plane wave modes in any component of the model. The curved wavefront solution is determined by integrating the plane wave solutions of the wave equation. Three-component coupling occurs between the *qP*, *qS1* and *qS2* waves in anisotropic media and this integral should be evaluated over both components of the horizontal wavenumber. However, this is time consuming and for weak anisotropy (<10%) it is possible to evaluate the integral in the sagittal plane only. [The sagittal plane is the vertical plane containing the source and receiver.] ANISEIS has the facility to perform both the two dimensional and three dimensional integration and there is negligible difference for weak anisotropy [P.Wild, personal communication].

Source and receivers can be placed anywhere in the model allowing reflection, VSP and even crosshole geometries to be modelled. If the source is placed at the free surface (the default position), it is modified so that only contributions from waves directed into the model are calculated. This modification can be overcome by placing the source just under the surface.

ANISEIS can generate seismograms for three types of sources: an explosion; a vertical force; and a horizontal force and provides six basic pulse shapes, which can be modified by damping factors. In this thesis I use the horizontal force option which generates a unit force in any specified (horizontal) direction.

ANISEIS can calculate models with up to 20 layers (including the isotropic source layer and an isotropic halfspace at the base of the model). Version 4.0 allows 20 three-component receivers and calculates up to 1024 samples per trace.

---

[1]For simplicity ANISEIS requires that point sources must be placed in an isotropic media. If an isotropic source layer is not specified, ANISEIS inserts an extremely thin source layer (<1m), which is chosen to minimize high incidence reflections. Inward reflections are suppressed within this source layer and its presence does not affect the seismograms.

Alternatives to ANISEIS

Batakrishna Mandal of MIT has written a program which also uses the reflectivity technique and produces results very similar to ANISEIS. However, this program is not commercially available. Several other anisotropic modelling algorithms exist including: finite difference and finite element methods which are expensive in computer time; and ray tracing, which is invalid near singularities (see Section 2.4). Leon Thomsen (Amoco) set up the AMC to compare the results of these codes for VSP and reflection geometries in anisotropic models. Most gave similar results (displayed at the SEG meeting, San Francisco 1990); however, no quantitative comparison was performed to determine which gave the correct results and no publication has been forthcoming.

Creating anisotropic materials in ANISEIS

ANISEIS can calculate synthetic seismograms for models which are anisotropic due to the presence of cracks and/or thin layers. The elastic constants of a layer can be rotated about any axis. This can give combinations of dipping cracks and thin layers with the full range of anisotropic symmetries and up to 21 independent elastic constants. Media with 21 independent elastic constants have triclinic symmetry and the following stiffness tensor [Crampin 1984a]:

c_{1111}	c_{1122}	c_{1133}	c_{1123}	c_{1131}	c_{1112}
c_{2211}	c_{2222}	c_{2233}	c_{2223}	c_{2231}	c_{2212}
c_{3311}	c_{3322}	c_{3333}	c_{3323}	c_{3331}	c_{3312}
c_{2311}	c_{2322}	c_{2333}	c_{2323}	c_{2331}	c_{2312}
c_{3111}	c_{3122}	c_{3133}	c_{3123}	c_{3131}	c_{3112}
c_{1211}	c_{1222}	c_{1233}	c_{1223}	c_{1231}	c_{1212}

Symmetry in the anisotropic medium reduces the number of independent elastic constants. In this thesis, the following symmetries are frequently encountered: isotropic (2 independent elastic constants); hexagonal (5 independent elastic constants); and orthorhombic (9 independent elastic constants). For isotropic media the above tensor can be expressed in terms of Lamés' constants and the non-zero elastic constants are: $c_{2211} = c_{3311} = c_{3322} = \lambda$; $c_{2323} = c_{3131} = c_{1212} = \mu$; $c_{1111} = c_{2222} = c_{3333} = \lambda+2\mu$.

ANISEIS uses the formulations of Postma [1955] and Hudson [1980, 1981] to calculate the elastic constants of materials with thin layer and crack anisotropy respectively. In the long wavelength limit a regular periodic sequence of thin layers can be modelled by alternating two isotropic plane layers [Postma 1955]. This gives a material with periodic thin layer (PTL) anisotropy. In this study I model all thin layer anisotropy with PTL materials. There is no limit to the strength of PTL-anisotropy that can be used.

Hudson's formulations [1980, 1981] (based on the scattering of elastic waves by cracks), as adapted by Crampin [1984b], show that the effective elastic constants for a material with aligned cracks are:

$$c_{ijkl} = c^0_{ijkl} + c^1_{ijkl} + c^2_{ijkl}; \qquad (2\text{-}2)$$

where: c_{ijkl} is the fourth order tensor of elastic constants of the cracked medium; c^0_{ijkl} are the elastic constants of the rock matrix and c^1_{ijkl} and c^2_{ijkl} are the first and second order perturbations due to the presence of the cracks. This formulation is valid for thin penny shaped cracks and assumes that: the crack radius is much less than the seismic wavelength; the cracks are randomly distributed within the scale of the seismic wavelength; and the cracks are disconnected with a crack density, $\varepsilon \ll 1$ (where $\varepsilon = Na^3/V$; N is the number of cracks of radius a in a volume V). For thin cracks, with aspect ratios (AR) less than about 0.2, percentage anisotropy is approximately given by $\varepsilon \times 100$. [The aspect ratio is the ratio of crack thickness to diameter.] Hudson's formulations are strictly valid for $\varepsilon \leq 0.1$ (approximately 10% anisotropy) and AR$\leq$0.2. The following section contains a discussion on the validity of using Hudson's formulations to model real crack structures.

2.4 SHEAR-WAVE BEHAVIOUR IN ANISOTROPIC MEDIA

In this section I show how shear-waves behave in layered and cracked media produced using ANISEIS. The terminology for describing wave propagation in anisotropic media is given by Crampin [1989]. The behaviour of shear-waves in anisotropic media is complicated. I will restrict this discussion to cases which show

behaviour that is relevant to later chapters. I use three different anisotropic media:

a) a medium with aligned vertical cracks. Fractures in the Austin Chalk (studied in Chapters Five to Seven) are subvertical [Corbett, Friedman & Spang 1987]. This medium has hexagonal symmetry with a horizontal symmetry axis, perpendicular to the crack strike.

b) A medium with horizontal PTL-anisotropy. The geological layers in the study area in Chapters Five to Seven are subhorizontal [Kuich 1989]. This medium has hexagonal symmetry with a vertical symmetry axis.

c) A combination of the above media as found in some sedimentary basins [Chapter Six; Bush & Crampin 1991]. This medium has an orthorhombic symmetry.

Figure 2.1 shows the variation in body wave velocities with incidence angle in two orthogonal vertical symmetry planes for these three cases. For a general direction of propagation there are usually three arrivals: one *P*-wave; and two shear-waves. In three dimensions these arrivals form continuous surfaces or sheets. The two shear-wave sheets generally travel at different velocities and have different (orthogonal) polarization directions to each other. The shear-wave arrivals may be labelled in two ways:

a) by the polarization direction of the shear-waves in the sheet: *qSR* for the sheet with polarizations at right angles to the crack (or layer) normals; and *qSP* for the sheet with polarizations parallel to the crack (or layer) normals.

b) According to the speed of the arrival for a given direction: *qS1* and *qS2* for the first and second arrivals respectively.

The important things to note in Figure 2.1 are:

1. The shear-wave velocities are dependent[2] on azimuth and incidence angle in anisotropic media.

2. For some directions of propagation the two shear-wave sheets meet. Such

---

[2] *P*-wave velocities are also directionally dependent in anisotropic media. This property is not used, as it is easier to quantify anisotropy along a single ray path using the difference between two shear-wave arrivals than by using absolute arrival times [Jituboh *et al.* 1991]. Crampin [1985a] also argues that shear-waves, having two arrivals, contain more information about the anisotropic structure than *P*-waves (for instance, differential attenuation of the two shear-waves may give information on crack content.

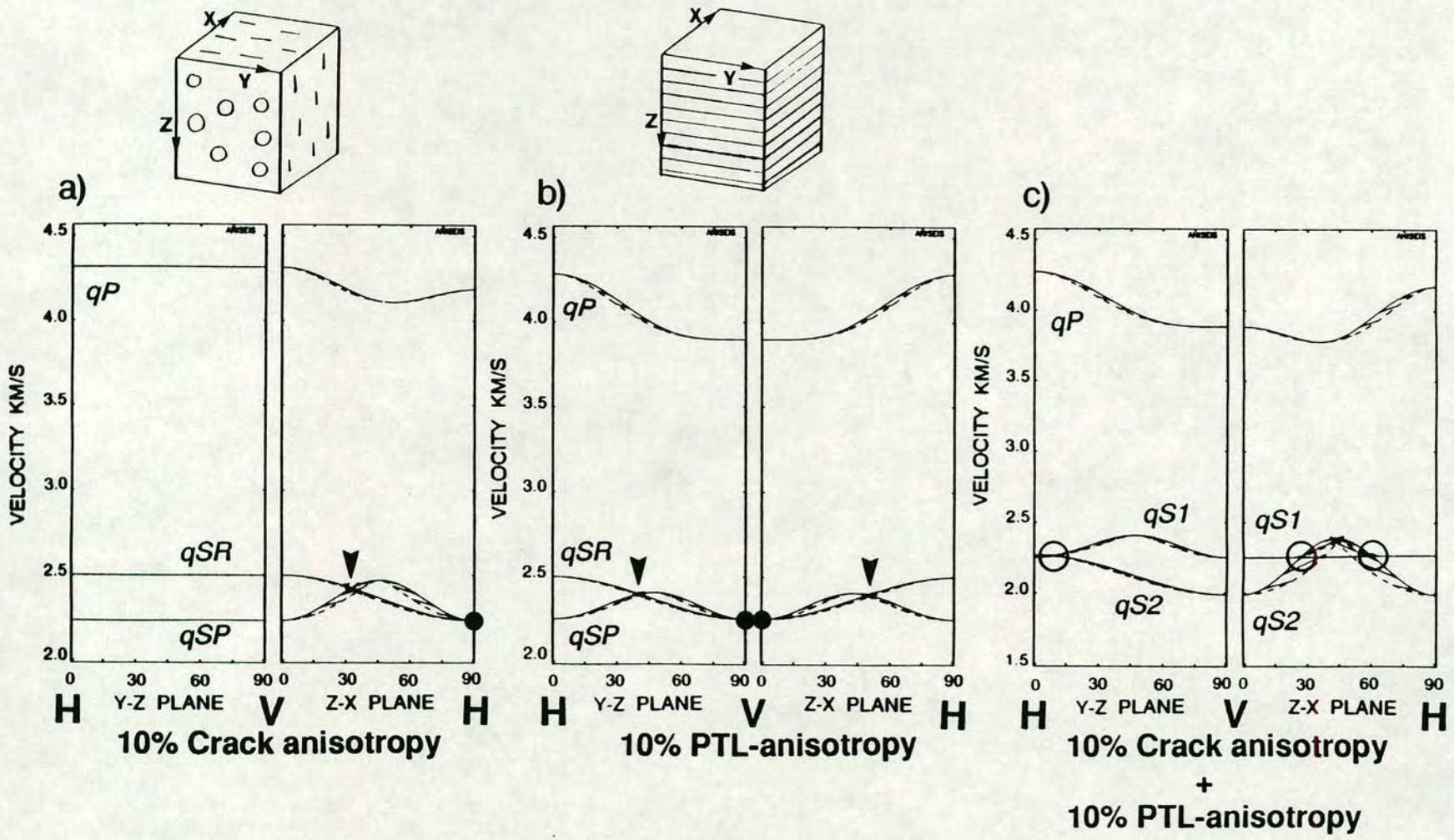

FIGURE 2.1: Group (dashed lines) and phase (solid lines) velocities for body waves for 10% crack anisotropy, 10% PTL-anisotropy and a combination of 10% crack- and 10% PTL-anisotropy (orthorhombic symmetry) showing the behaviour of body wave velocities with incidence angle in the Y-Z and Z-X planes. The cracks are water-filled. **V** and **H** indicate vertical and horizontal propagation respectively. Line singularities are marked by arrows; kiss singularities are marked by black dots; and point singularities are marked by open circles.

directions are called *singularities*. There are three types of singularity: the *line singularity*, where the shear-wave sheets cross along a line (either side of which, the *qS1* polarization is different); the *kiss singularity*, where the sheets touch tangentially; and the *point singularity*, where a line singularity has pulled apart so that the sheets only cross at points. It is very useful to locate singularities in field data: the position and type of singularities give valuable constraints in modelling. I have marked the positions of singularities in Figures 2.1 and 2.2.

3. The group and phase velocities are, in general, not parallel to each other.
4. The behaviour of split shear-waves in orthorhombic media is more complex with several point singularities.

In Figure 2.2, I show equal area plots [see Wild & Crampin 1991] for the same materials as above. These plots show the polarizations and time delays for a hemisphere of propagation directions projected onto a horizontal surface. [For VSP geometries the horizontal plane is a convenient, fixed, reference plane in which to display measured shear-wave polarizations and time delays.] Such displays are useful for matching field measurements to the polarizations and time delays of synthetic materials.

Figure 2.2 shows that the *qS1* polarization, and the time delay between the two arrivals, vary with azimuth and incidence angle. This means that rays from different azimuths and offsets (or to different levels in a deviated well) can have quite different *qS1* polarizations and time delays, even for propagation through a single anisotropic medium. Similarly, *qS1* polarizations and time delays will be different for vertical propagation through media in which the cracks or thin layers dip. [In Figure 4.25, I show equal area plots for media with a combination of cracks and dipping PTL-anisotropy.] I shall now describe the important features of equal area plots for the three materials discussed above.

Crack anisotropy: for vertical cracks there is a band of polarizations parallel to the crack strike (Y-direction). This band is bounded by line singularities. The largest delays between the two shear-wave arrivals occurs for propagation parallel to the cracks. This means that vertically travelling shear-waves in VSPs will undergo maximum splitting.

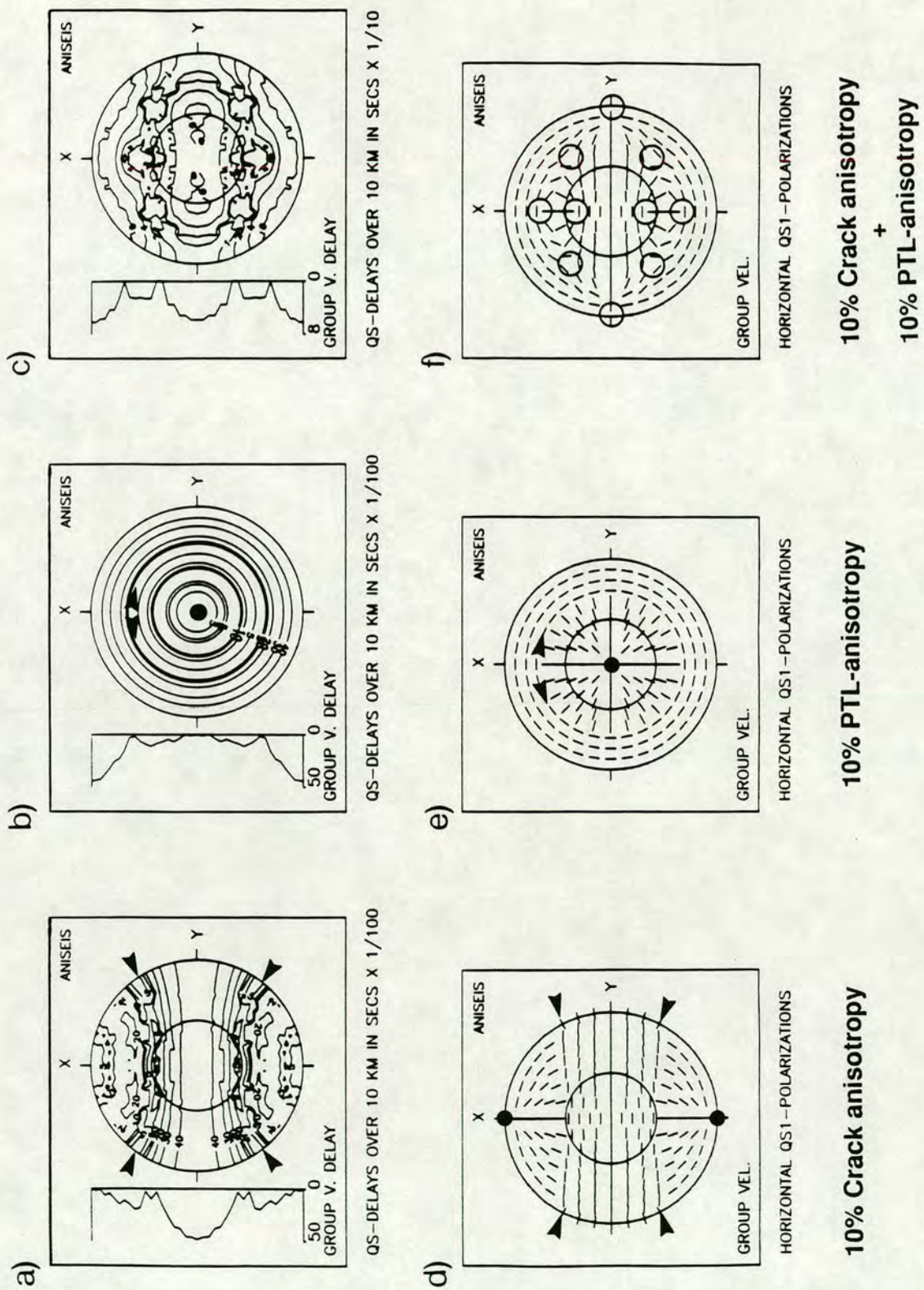

FIGURE 2.2: Equal area plots of group velocity delays between the fast and slow split shear-waves (a), b) and c)) and polarizations of the leading split shear-wave (d), e) and f)) for all azimuths and angles of incidence for the same materials as shown in Figure 2.1. The centre of each plot represents vertical propagation and the outer limits of the plots represent horizontal propagation. The small circle represents the *shear-wave window* (see Section 3.3). Line singularities are marked by arrows; kiss singularities are marked by black dots and point singularities are marked by open circles. The contours are not smooth as the group velocity surfaces are complex and show rapid variations of wave type and polarization, particularly in the neighbourhood of point singularities.

Thin layer anisotropy: for horizontal thin layers the *qS1* arrival has a radial polarization except for near-horizontal propagation, outside the line singularity. For vertical propagation there is a kiss singularity and therefore no splitting will be observed for vertically propagating waves in VSPs. Maximum time delays are for subhorizontal propagation.

Combinations of crack and thin layer anisotropy: The plots become more complex when the two types of anisotropy are combined. The positions of the point singularities depends on the relative strengths of the two types of anisotropies. [The positions of these point singularities for a wide range of material has been catalogued by Wild & Crampin 1991.]

The exact behaviour of shear-waves is not only dependent on crack properties (for example aspect ratio and crack content affect the positions of the singularities [e.g. Bush 1990; Douma & Crampin 1990; Crampin 1988, 1993a]) but also on the isotropic matrix properties.

Can ANISEIS model real reservoir conditions?

In a real reservoir cracks, and fractures, will not be perfectly aligned, uniform penny shaped features as described in Hudson's formulations. Modelling is based on the assumption that an equivalent anisotropic medium can be calculated to match the elastic constants of the real rock. Hudson's formulations can be used to generate equivalent media for rocks which are anisotropic due to cracks or fractures as long as the conditions listed in Section 2.3 are met. The crack parameters used in the model represent the parameters needed to generate an anisotropic medium equivalent to the real rock. In general these, whilst matching elastic constants, will not match crack or fracture dimensions in the reservoir. However, a larger crack density in the models implies a larger crack or fracture density in the real rock. The orientation of Hudson cracks will also be that of the real cracks or fractures. Therefore, ANISEIS can produce a match of elastic constants with the real rock, but it does not allow a direct assessment of the physical dimensions of cracks in the rock.

Fluid connection between cracks

One potential problem with using ANISEIS to model field data is that Hudson cracks are not connected, whereas in a productive reservoir fluid must be able to flow. Thomsen [1991] presented an alternative theory to Hudson in which cracks were inserted into a porous medium in which the cracks and pores are hydraulically connected. Tatham [1985] suggests that at seismic frequencies cracks behave as though they are unconnected. This means that isotropic porosity has no affect (other than changing the bulk properties of the rock) and it is valid to use Hudson's formulations. At present there is no consensus that any theory replicates *in situ* rock properties. Rathore *et al.* [1992] and Rathore & Fjær [1992] tried to compare Hudson's and Thomsen's theories using synthetic sandstones with known crack parameters. However, in the test samples the crack size was the same order as the seismic wavelength. Neither theory is valid in such cases.

2.5 PROCESSING METHODOLOGY

Now that I have summarised shear-wave behaviour in anisotropic media it is possible to outline the processing, modelling and interpretation methodology used in this thesis. This is similar to that described by Wild *et al.* [1993] and is shown in Figure 2.3.

Experiment Design and Field Acquisition

The first stage in the acquisition of shear-wave data is experiment design; this should be tested by premodelling as done by MacBeth *et al.* [1993]. Experiment design depends on the structure at a given site and the parameters which need to be determined. If cracks or fractures are known to be vertical and any thin layer anisotropy has a vertical axis of symmetry, then a zero-offset VSP will give the critical information on crack strike and density (Section 2.4). However, if the structure is complex, multi-azimuth multi-offset VSPs are needed to allow modelling of the full structure. The data analyzed in this study were collected before I became involved in the experiments and it was not possible to design the optimum acquisition geometry.

It is usual for nine-component data (i.e. three surface source orientations: inline;

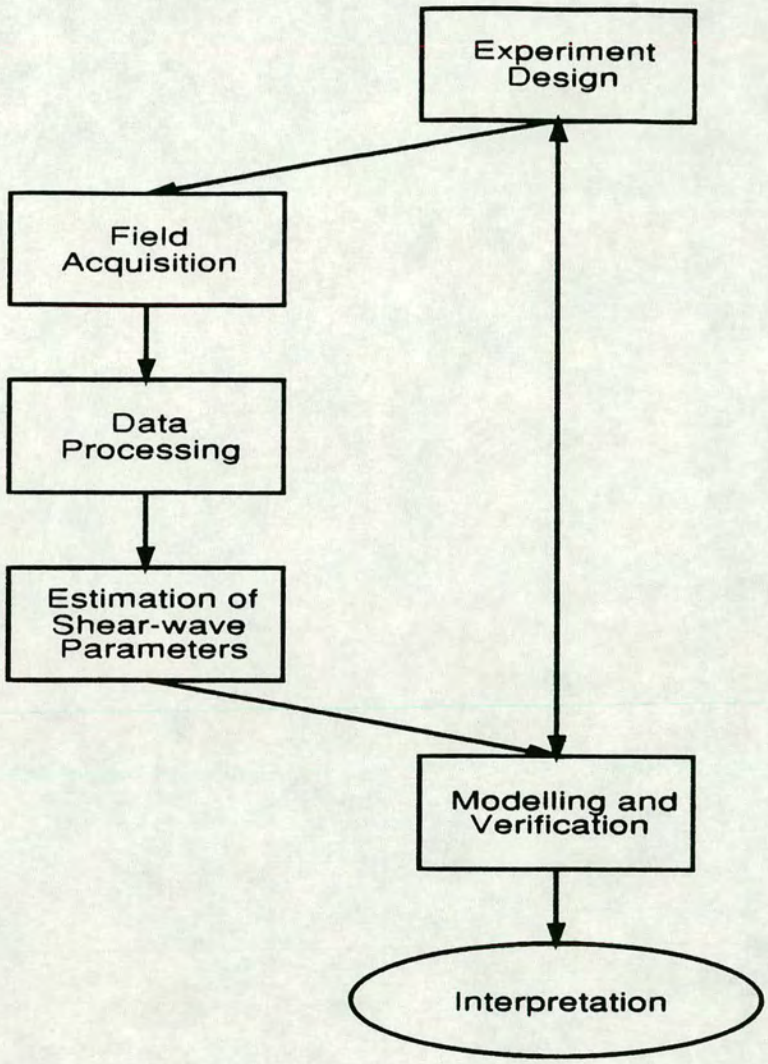

FIGURE 2.3: Flow chart showing steps in the acquisition, processing and modelling of shear-wave data.

crossline; and vertical, recorded on three geophone components) to be recorded, although, many zero-offset VSP studies only examine four-component data (i.e. two horizontal shear-wave sources recorded on two horizontal geophone components).

Data Processing

Anisotropy estimation techniques are used to extract polarization and time delay information from the shear-wave arrival. These techniques operate over the whole shear-wave arrival, and data processing is kept to a minimum to prevent distortion of the waveform. However, several steps are necessary before estimation techniques can be applied; these are as follows:

1. stacking along the same source-receiver ray path (with visual quality control to remove bad traces);
2. band pass filtering to reduce noise;
3. rotation of geophones into a known coordinate system. The rotation is based on gyro-data or the *P*-wave arrival.
4. Some estimation techniques require the removal of the upgoing wavefield. This is done using an FK filter which does not distort the waveform [Campden 1990].

Deconvolution is not necessary as the estimation techniques act over the whole arrival. Kramer [1991] proposed a 3-D deconvolution operator. However, his estimates of polarization angle and time delay were not significantly improved by application of this operator.

After these processing steps, the anisotropy estimation techniques, described in Section 2.7, are applied. I use all the estimation techniques on each data set. This is because a comparison of the results from each techniques can highlight changes in the anisotropic structure (Chapter Four) and errors in source and geophone polarities (Section 5.4.1). I used Spectrum's GEOWELL VSP processing package for routine processing, such as filtering and trace sorting.

Modelling and Verification

Before the results of the estimation techniques can be interpreted the structure must be modelled. This is because *qS1* polarizations and time delays vary not only

with anisotropic structure, but also with ray path (Section 2.4). This means that *qS1* polarizations cannot be directly interpreted in terms of crack strike. Modelling is an iterative process, performed until there is a good match between the observed and modelled seismograms. An isotropic model is created to match the arrival time of the fast shear-wave. [In Hudson's crack model the maximum velocity is that of the isotropic matrix, the addition of cracks slows the second arrival.] Perturbations to this structure, due to the presence of aligned cracks or thin layers are then added, dependent on geological information from the site.

Interpretation

Once a model has been produced for a site this may be interpreted in terms of the anisotropic structure of the rockmass at the site. There is no direct link between the model crack parameters and reservoir structure as discussed in Section 2.4. However, fracture strike and density can be inferred from model parameters.

2.6 FIELD ACQUISITION OF SHEAR-WAVE DATA

Shear-wave generation requires the source to generate a component of horizontal motion and a number of methods have been used to accomplish this. I now describe the methods used to generate the data presented in this thesis.

OMNIPULSE source

Bolt Technology Corporation's OMNIPULSE multimode generator was used to collect the data presented in Chapter Four. OMNIPULSE is essentially a land airgun attached by a pivot to a baseplate which is in contact with the ground. Marathon Oil Company extensively tested this source [Tinkle *et al.* 1989]. The airgun assembly is tilted to the left and fired, reaction to the upward moving piston generates an impulsive force on the ground. The airgun is then tilted by the same angle to the right and fired again. [The tilt angle may be up to 45° but is governed by baseplate coupling with the ground at the site in question.] The shear-waves from these two shots have opposite polarities whereas the polarity of the compressional wave remains constant. Subtracting traces from the left and right shots enhances the shear energy

whilst cancelling out the *P*-waves. Adding the two traces cancels the shear-waves to give a *P*-wave source. The source generates a force of up to 8.8×10^6N with each shot and for deep geophone levels, in VSPs, many shots are stacked to get a clean signal. The OMNIPULSE can be used as a *P*-wave source with the airgun vertically above the baseplate.

ARIS source

The ARIS (Arco impulsive source) has a tilting mechanism similar to the OMNIPULSE but the impulsive energy is provided by a 2200kg weight which is forced down onto a metal baseplate by compressed air and can generate energies up to 2×10^5Nm. The firing assembly can be tilted up to 30° in any direction (15° is commonly used) and data from opposite hits are processed in a similar way to that from the OMNIPULSE. During firing most of the weight of the truck rests on the baseplate to ensure good coupling.

VIBROSEIS source

VIBROSEIS sources have been used to generate shear-waves since the 1960's [Cherry & Waters 1968]. A sweep through frequencies over periods of up to 30 seconds is used to produce a controlled waveform. The recorded seismograms are a convolution of: the sweep signal; the earth's impulse response; and an unknown wavelet[3]. The seismograms are then crosscorrelated with the reference sweep signal to compress the pulse to give a mixed-phase wavelet. The acceleration of the baseplate and reaction mass are used in a feed back loop so that the motion of the baseplate closely follows the reference sweep. The far field wavelet is given by the time derivative of the baseplate force [Miller & Pursey 1954] which is calculated from the weighted sum of the accelerations of reaction mass and baseplate [Sallas & Weber 1982]. However, the baseplate force does not follow exactly the reference sweep and the difference between the true baseplate motion and the reference sweep means that

---

[3]The unknown wavelet includes the unmeasured and unknown electro-mechanical conversion of the known electrical sweep signal into the force applied to the ground by the vibrator plate, the propagating effects in the earth, and the recording system response.

the compressed wavelet is not a true representation of the far field signature [Ziolkowski 1991]. This may cause some problems in modelling shear-wave polarization diagrams where an accurate knowledge of the source pulse shape is essential. [Campden [1990] shows how different pulse shapes will give very different particle motions for the same anisotropic model due to the interference of the fast and slow shear-waves.] VIBROSEIS sources can be used in parallel to generate stronger signals.

Repeated firing of any of the above sources at a single location can dig the baseplates into the ground and cause the source signature to change with time.

P-S mode conversions

It is possible to study anisotropy using *P*- to *SV*-wave conversions, which are either converted at a reflector or in transmission at an interface. Generally, wide offsets are needed to generate conversions with sufficient energy, but useable energy is found for conversions within 5° of the vertical [P.Dillon, personal communication]. This method has several advantages [Garotta 1989]: it is cheap; the shear-waves travel through the potentially disturbing near-surface layers only once (for reflection surveys) and can be used to study shear-waves in a marine VSP environment [Ahmed 1989; Campden 1990]. However, there are disadvantages: only one source polarization can be generated; the exact source characteristics are not known; and the shear-waves must be separated from the *P*-waves.

Shear-wave data are recorded using three-component Cartesian geophones. The SEG has proposed a polarity convention for the generation, recording and exchange of three-component data [Pruett 1989]. The agreed standard for geophones is a right handed set, with a tap along a positive axis giving a positive signal on tape. Three-component surface geophones should have arrows showing the correct orientation moulded into the case. Lawton & Bertram [1992] compare several surface three-component geophones and find that the polarity of horizontal components is opposite to the SEG standard in Cartesian geophones and there is no consistency in the colour coding or nomenclature of horizontal components between different geophones.

2.7 ANISOTROPY ESTIMATION TECHNIQUES

The analysis of the vast quantities of data acquired in hydrocarbon exploration has required the development of objective computer algorithms to extract the anisotropy parameters. [The anisotropy parameters are the *qS1* polarization direction and time delay between the two split shear-waves.] Although used extensively in this thesis these techniques are still in their development stage. Whilst it is known that they perform well on noise free synthetic seismograms, their accuracy and sensitivity to changes in anisotropic symmetries is still being evaluated by their originators [Zeng & MacBeth 1993a]. In this section the techniques used in this thesis are described. Table 2.1 gives a summary of the uses and requirements of these techniques. Many alternative techniques exist to those described here; however, none are significantly more sensitive or accurate.

For vertical propagation through vertical cracks a shear-wave will split into two orthogonal components (Section 2.4). Shear-waves propagate with subvertical incidence angles in both near-offset VSPs and in reflection lines and it is believed that cracks are commonly vertical [Crampin 1990]. A number of techniques have been developed to extract the anisotropy parameters for this simple case. These techniques are consequently only valid for such cases.

Commonly two orthogonal source orientations (inline and crossline) are recorded on two orthogonal (inline and crossline) geophone components. The recorded four-component data can then be displayed as a 2×2 data matrix. One row corresponds to the inline geophone traces from the inline and crossline sources, and the other row corresponds to the crossline geophone traces. Ignoring the upgoing wavefield and multiple reflections and considering only direct waves, the recorded data matrix $\mathbf{D}(t)$ for a uniform anisotropic half-space can be expressed as [MacBeth & Yardley 1992]:

$$\mathbf{D}(t) = \{\mathbf{R}^{T}(\theta)\Lambda(t;\tau_1,\tau_2)\mathbf{R}(\theta)\} * \mathbf{S}(t); \qquad (2\text{-}4)$$

where * represents a multiplication in the frequency domain or a convolution in the time domain; $\mathbf{R}(\theta)$ is a standard 2×2 rotation matrix with $\mathbf{R}^{T}(\theta)$ being the transpose matrix. θ is the polarization direction of the leading split shear-wave with respect to

Table 2.1

fold out

Table 2.1: Anisotropic estimation techniques.

Technique		Sources required	Special requirements	When to use?
AST Zeng & MacBeth 1993b	Analytical Synchronous Rotation Technique	2 sources	1. rotated data 2. two orthogonal shear-waves	The standard two source technique. Analytical form of Alford rotation [1986].
AIT Zeng & MacBeth 1993b	Analytical Independent Rotation Technique	2 sources	1. rotated data	Useful to determine if medium polarization changes and at what depth. Also to determine if source and geophone are misaligned.
LTT Li & Crampin 1993	Linear Transform Technique	2 sources	1. two orthogonal shear-waves	For zero-offset unrotated data with a constant *qS1* direction.
DPM Zeng & MacBeth 1993b	Double Source Propagator Matrix Technique	2 sources	1. rotated data 2. upgoing wavefield must be removed 3. orthogonal shear-waves 4. assumes constant source signature and ray path between levels	Use to examine structure below changes in medium polarization.
DTS Campden 1990	Direct Time Series Technique	1 source	1. rotated data 2. orthogonal shear-waves	Use for P-S conversions and to check polarities before AST.

the inline direction. Λ is a diagonal matrix describing the shear-wave travel times and is given by:

$$\Lambda = \begin{bmatrix} \lambda_1 & 0 \\ 0 & \lambda_2 \end{bmatrix}; \qquad (2\text{-}5)$$

where λ_1 and λ_2 define time shift operators and attenuation factors which convolve the source wavelet $s(t)$ such that $\lambda_i * s(t) = A_i * s(t-\tau_i)$. A_i is the attenuation factor and τ_i the travel time of the shear-wave. As the source is an ideal linear source and aligned along the inline and crossline directions $S(t)$ is a diagonal matrix with the principal diagonal given by the scalar source function $s(t)$. The polarization angle θ and the time delay ($\Delta\tau = \tau_1 - \tau_2$) may be found by techniques which decompose $D(t)$ into the three matrices in curly brackets in Equation (2-4).

AST - Analytical Synchronous Rotation Technique

Alford [1986] proposed a numerical search procedure to accomplish the above decomposition. It assumes that any source orientation can be mathematically created by a linear combination of the two sources. The data matrix is rotated until the energy on the off-diagonals is minimum. After rotation, the two sources are directed along the fast and slow directions and no splitting takes place so there is no energy on the off-diagonals. The rotation angle gives the *qS1* polarization direction and the time delay is found by crosscorrelation of the traces on the main diagonals. Here, I use a faster analytical version of this technique (AST) [Zeng & MacBeth 1993b].

This approach is shown in Figure 2.4 for a zero-offset VSP in which vertical cracks strike at $\theta°$ to the inline direction. The shear-waves split on their way from source to receiver and energy is recorded on all four horizontal components of the data matrix. After application of AST (equivalent to rotating the sources and geophones by $\theta°$) energy is only present on the main diagonals. A time delay can be seen between the fast (S1R1) and slow (S2R2) arrivals. As with all the estimation techniques, the calculation is performed over a time window which includes the main shear-wave arrival. This window is picked interactively and in Chapter Four I examine the sensitivity of the estimation techniques to the window length. Figure 2.4 also

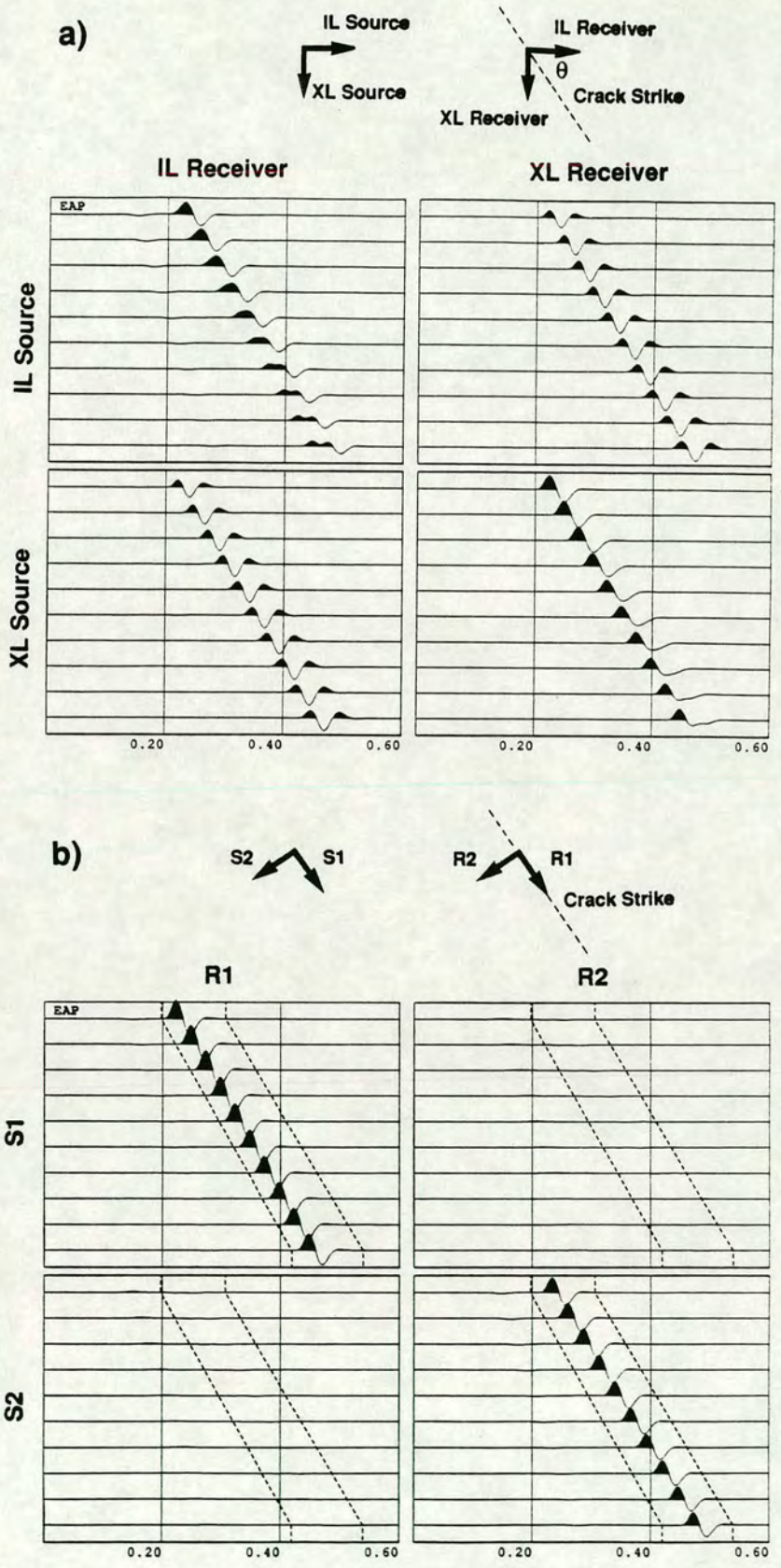

FIGURE 2.4: (a) A plan view of the acquisition geometry and crack strike for a zero-offset VSP together with the recorded 2×2 data matrix. [In a zero-offset VSP the sources are directly above the receivers; however, I have moved the sources to one side in this diagram to make the diagram clearer.] (b) Effective acquisition geometry and 2×2 data matrix after the application of AST. The time delay between the fast (S1R1) and slow (S2R2) shear-waves can be seen. The time window over which AST was applied has been overlaid onto the plot.

shows the SEG convention [Pruett 1989] for relative orientations of sources and receivers that I adopt in this thesis.

This technique is the simplest and most widely used anisotropy estimation procedure. A source balancing routine has been added to this technique [Winterstein & Meadows 1991a; X.Zeng, personal communication] for use when the two sources have different source strengths. This routine equalises the energy on the off-diagonal elements and assumes the data matrix is symmetrical. The source balancing version used here linearly interpolates the rotated traces to give time delay measurements below the sample rate.

AIT - Analytical Independent Rotation Technique

It is inappropriate to use AST if the data matrix is asymmetric [Chapter Three]. The data matrix may not be symmetric below changes in crack orientation [MacBeth & Yardley 1992]. AIT [Zeng & MacBeth 1993b] can be used to estimate the degree of matrix asymmetry. This can be used to see whether it is valid to use AST and to establish at what depth the change in crack orientation occurs. Equation (2-4) can be modified as follows:

$$\mathbf{D}(t) = \{\mathbf{R}^{T}(\theta_G)\Lambda(t;\tau_1,\tau_2)\mathbf{R}(\theta_S)\} * \mathbf{S}(t); \qquad (2\text{-}6)$$

where the difference between θ_G and θ_S determines the asymmetry. AIT is based on work by Igel & Crampin [1990] and MacBeth & Crampin [1991]. This technique can be thought of as independent rotations of the geophone and source frames about the Z-axis by θ_G and θ_S respectively until $\mathbf{D}(t)$ assumes the form of the diagonal matrix $\Lambda(t)$. Where there is no asymmetry θ_G and θ_S are the same and the technique reduces to AST. θ_G and θ_S start to diverge where an abrupt change in crack strike occurs and hence AIT can be used to locate levels for layer stripping [MacBeth & Yardley 1992].

LTT - Linear Transform Technique

For near-offset VSPs it is not possible to rotate the data using horizontal plane *P*-wave arrivals. In such cases LTT [Li & Crampin 1993] can be used. Linear transforms

can be defined as follows:

$$\xi(t) = s_{11}(t) - s_{12}(t); \tag{2-7}$$

$$\eta(t) = s_{21}(t) + s_{12}(t); \tag{2-8}$$

$$\zeta(t) = s_{11}(t) + s_{22}(t); \tag{2-9}$$

$$\sigma(t) = s_{12}(t) - s_{21}(t); \tag{2-10}$$

where s_{ij} are the elements of the data matrix of the recorded time series for the general case where the source directions and geophone components are not parallel. These can be rewritten as:

$$\begin{aligned} \xi(t) &= [qS1(t) - qS2(t)] \cos(\alpha+\alpha'); \\ \eta(t) &= [qS1(t) - qS2(t)] \sin(\alpha+\alpha'); \end{aligned} \tag{2-11}$$

$$\begin{aligned} \zeta(t) &= [qS1(t) + qS2(t)] \cos(\alpha-\alpha'); \\ \sigma(t) &= [qS1(t) + qS2(t)] \sin(\alpha-\alpha'); \end{aligned} \tag{2-12}$$

where α is the angle of the fast direction from the X source direction and α' is the angle of the fast direction from the x geophone component. When the time series $\xi(t)$ and $\eta(t)$ are plotted against each other, the resulting motion is linear (as with $\zeta(t)$ and $\sigma(t)$) and hence the time series $qS1(t)$ and $qS2(t)$ and the angles α and α' can be estimated. If the source direction is known, then the geophone orientation can be calculated. LTT is analogous to AST except that AST assumes source and geophone orientations are fixed and allows the fast direction to change, whereas LTT assumes the polarization direction is fixed but allows the geophones orientation to vary.

DPM - Double Source Propagator Matrix Technique

This propagator matrix technique uses the downgoing wavefield at one level as the source for deeper levels [Zeng & MacBeth 1993b]. This technique assumes that the difference in the recorded shear-wave arrival at two levels is caused entirely by passage through a constant anisotropic symmetry between the two levels. This has the

advantage that any distortions caused in the near-surface (e.g. multiples, *P*-to-*S* mode conversions) can be included as part of the downgoing wavefield and do not have to be excluded from the analysis. However, this assumption places restrictions on the use of DPM:

1) DPM can be used only on near-offset data from undeviated wells.
2) The upgoing wavefield has to be removed.
3) This technique assumes geophones are accurately rotated.
4) Source characteristics must be stable with depth. [This may not be true due to damage to the ground caused by repeated shots.]

DPM is a useful technique for examining anisotropy below the disturbing influences of the surface layers or below suspected changes in crack orientation. Equation (2-4) at the *i*th geophone level can be rewritten with the data matrix at the previous geophone level replacing the diagonal source matrix S(t) as follows:

$$\mathbf{D}_{i+1}(t) = \{\mathbf{R}^{T}(\theta)\Lambda(t;\tau_1,\tau_2)\mathbf{R}(\theta)\} * \mathbf{D}_i(t); \qquad (2\text{-}13)$$

here the equation is written for a single geophone interval; however, the change in the wavefield between two geophone levels (often about 10m) is too small for significant changes to occur and a larger interval is generally used. This expression can be solved analytically for the anisotropy parameters [Zeng & MacBeth 1993b].

DTS - Direct Times Series Technique

Two source techniques are the most stable; however, it is not always possible to have two source orientations, for example, when *P*-to-*S* conversions are studied in a marine environment. DTS [Campden 1990] can also be used to check source and receiver polarities, before the results of the two source techniques can be interpreted (Section 5.4.1). The geophone components are mathematically rotated in 1° increments and the start time of the X-component trace is increased (in increments of the sample interval) until the minimum arithmetic difference between the X- and Y-component traces is found. The values of rotation angle and time delay which give the global minimum are taken to be the *qS1* polarization direction and the time delay.

2.8 RECENT FIELD RESULTS

The study of shear-wave anisotropy may be able to help with determining fracture, and crack location, density, and strike. In this section I review recent successful applications of shear-wave anisotropy. I also comment on other techniques for obtaining the same information.

It is difficult to locate reservoirs by any method. Gas saturated reservoirs may be seen in the amplitude versus offset behaviour of *P*-waves [Ostrander 1984] in reflection seismics. However, shear-wave reflection surveys can provide a direct means of locating fractured zones within the reservoir. Mueller [1991, 1992] analyzed the reflection continuity on slow shear-wave sections to locate regions of high fracture density in the Austin Chalk [see Section 7.2.2]. These were later drilled and found to be productive. Fractures in the core samples recovered from these wells confirmed that the anisotropy was linked to fractures (the polarization of the leading split shear-wave also matched the fracture orientation) and productivity. Li, Crampin & Mueller [1992] found that the amount of shear-wave anisotropy seen in reflection lines is related to reservoir productivity. Lewis, Davis & Vuillermoz [1991] analyzed data from a 3-D three-component reflection survey over a producing field and found correlations between reservoir production and amount of anisotropy.

The determination of fracture size and direction is usually achieved by one of several techniques including borehole televiewers, dipmeters and more recently formation microscanners [Luthi & Southaite 1990]. Formation microscanners invert conductivity data to give crack aperture and strike. These methods give estimates of fracture size and strike local to the borehole. As seen in Mueller's [1991, 1992] work shear-wave seismics can determine these parameters remotely in reflection surveys. Recent work using shear-wave VSPs has detected anisotropy and in some cases the presence of fractures has been confirmed by independent means showing that shear-waves are "seeing" the cracks in the reservoir layer. Cliet *et al.* [1991] found that production rates are proportional to anisotropy. Queen *et al.* [1992] found that percentage anisotropy, observed in VSPs, is related to fracture density at the Conoco Borehole Test Facility.

CHAPTER THREE

EFFECTS OF CHANGING CRACK ORIENTATION WITH DEPTH ON SHEAR-WAVE SIGNALS IN REFLECTION SURVEYS AND VSPs

3.1 INTRODUCTION

Recent publications have shown that changes in crack and fracture orientation can occur with depth. In this chapter, I use synthetic data to show that in such circumstances shear-wave arrivals in VSPs, with geophones in the layer of interest, are easier to interpret than in reflection surveys. This is because the polarization direction of the leading split shear-wave is determined by the last anisotropic medium through which it passed. From this, I conclude that, until more is known about the changes in anisotropic symmetry with depth, VSPs provide a simpler environment in which to experiment.

I use polarization diagrams of the shear-wave arrival to show how multiple splitting, due to passage through two or more layers with different anisotropic structures, distorts the shear-wave arrival. This gives a nonsymmetrical data matrix. Many estimation techniques assume that the data matrix is symmetrical and have been applied blindly to data sets in the past. I show that, in the presence of a changing crack geometry with depth, the most commonly used estimation technique (AST, Table 2.1) gives uniform, but incorrect results. Offset data in reflection lines are further distorted by the effect of transmission coefficients at the reflecting interface invalidating the use of AST.

3.2 DO CRACK ORIENTATIONS CHANGE WITH DEPTH?

Before modelling, I review the evidence for changes in crack and fracture orientation with depth. Luthi & Southaite [1990] use a formation microscanner to measure fracture dip in the basement rock in Connecticut (USA). They find that the fracture dip changes with depth from 60° at approximately 190m to steeper angles at about 1070m (shallower dipping features were also seen at this depth but these were associated with foliation planes).

Evidence for changing crack orientation with depth also comes from shear-wave seismic data. Martin & Davis [1987] and Squires, Kim & Kim [1989] used similar techniques to analyze shear-wave reflection data from the Silo field, Wyoming and the Lost Hills field, California, respectively. Martin & Davis [1987] divided the section into blocks, bounded vertically by reflectors and determined the time interval between reflectors on both the fast and slow shear-wave sections. In some blocks, the two way time between reflectors was smaller on the 'fast' section; in other blocks the 'slow' section had a smaller two-way time. This was interpreted as 90° changes in crack orientation [Martin & Davis 1987; Lewis, Davis & Vuillermoz 1991]. Ohanian & Beckman [1992] also find changes in fracture strike with depth from VSP data and match these to changes in geological structure.

Further changes in fracture orientation with depth are reported by Beckham [1990] who analyzed data from the Pembrook field in Texas. Data from this field had previously been analyzed [Becker *et al.* 1989; Murtha 1989], but the results were inconclusive, possibly because the changes in fracture strike with depth, noticed by Beckham [1990], were not incorporated in the analysis. Winterstein & Meadows [1991a, 1991b] identified a decrease in time delay in VSPs data from the Cymric, Railroad Gap and Lost Hills fields in California after a source-geophone rotation [Alford 1986] had been applied. They inferred that the fracture orientation changed with depth and developed a layer stripping approach to investigate the deeper layers.

3.3 DISTORTION OF THE SHEAR-WAVE SIGNAL

Each shear-wave splits into two components each time it passes into a medium with a different crack orientation. This is illustrated in Figure 3.1. The shear-wave splits into two components as it enters the first cracked medium. On entering the second layer, with a different crack orientation, both split shear-waves split again giving four shear-wave arrivals. The polarizations of the four split shear-waves are now fixed by the crack distribution in the second medium and direct information about the crack parameters of the first layer is hidden. This means that the *qS1* polarization recorded using surface geophones may not be the same as recorded by geophones in the reservoir.

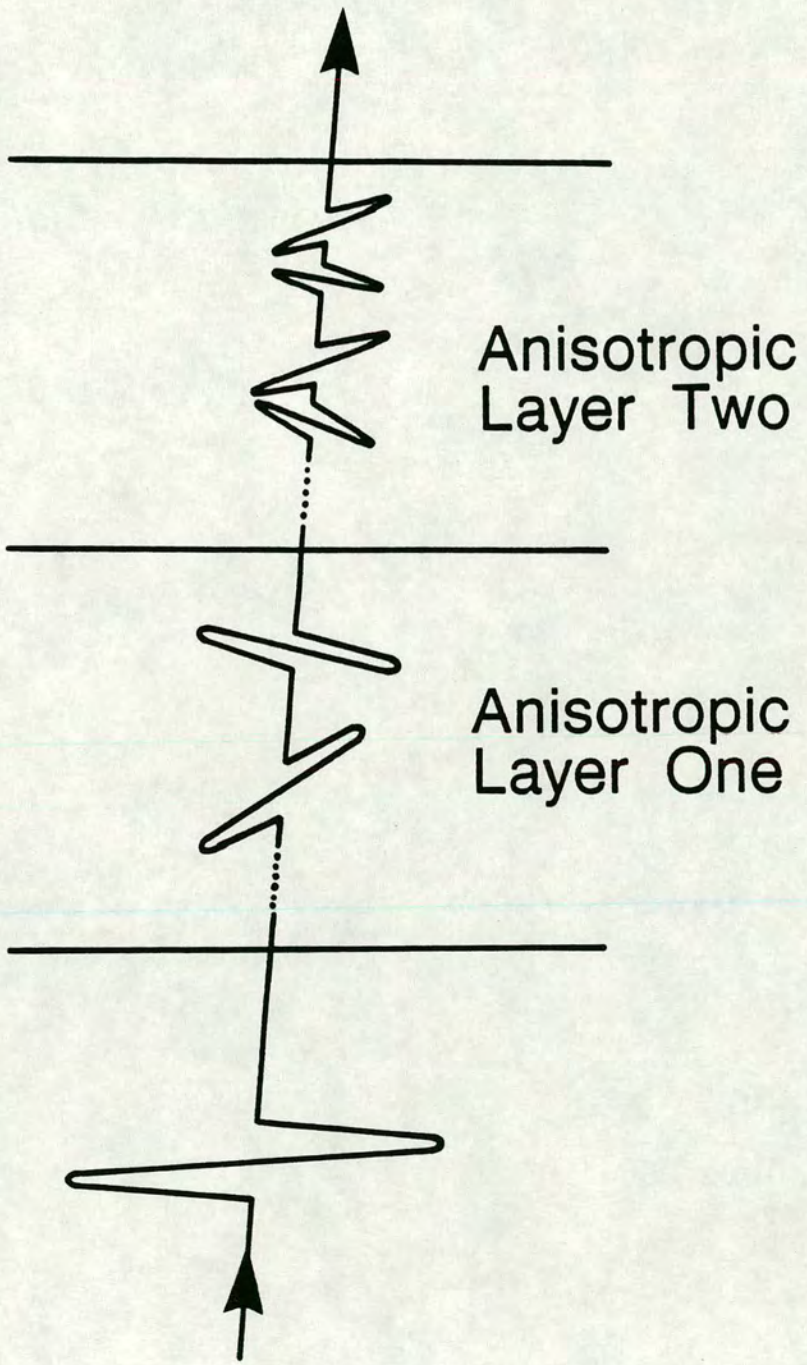

FIGURE 3.1: A schematic illustration of double splitting. A shear-wave entering an anisotropic medium will split into two components. If the split shear-waves then enters a second anisotropic layer with a different crack orientation each of the waves will split into two. This gives a total of four shear-waves. The first shear-wave arrival will be polarized parallel to the cracks in the second layer.

The shear-wave signal is also distorted if recorded at wide offsets in reflection lines. This is due to the difference in *SV* and *SH* transmission coefficients for nonnormal transmission at interfaces. Such distortions occur at the free surface and at internal interfaces. *Shear-wave windows* (for arrivals at the free surface) [Evans 1984] and *internal shear-wave windows* [Liu & Crampin 1990] have been defined, within which the shear-waves remain undistorted. The shear-wave window is the solid angle at the surface bounded by angles of incidence of $\sin^{-1}(Vp/Vs)$, which is about 35° for a Poisson's ratio of 0.25. Irregular topography may mean that, locally, the angle of incidence of the incoming shear-waves is outside the shear-wave window, leading to distortion of the shear-wave signal, even for arrivals which are apparently within the window for a horizontal surface.

Booth & Crampin [1985] describe the distorting effects of *S*-to-*P* mode conversions at a low velocity layer on the interpretation of shear-wave polarizations recorded above small earthquakes. Similar effects may be expected to occur for wide-offset reflection surveys where *S*-to-*P* converted phases can arrive earlier than the direct shear-waves. This could make estimation of the polarization of the leading split shear-wave difficult in reflection surveys.

3.4 MODELLING CHANGES IN CRACK ORIENTATION

Synthetic seismograms were calculated for a series of simple models with vertical cracks to show the effects of changes in crack orientation with depth on shear-waves recorded in VSP and reflection geometries. The modelling in this chapter concentrates on the effects of changing strike with depth; crack dip may also change with depth. Changes in dip and strike both mean that the *qS1* and *qS2* polarizations change with depth. Both situations give rise to similar effects. The models, listed in Table 3.1 and illustrated in Figure 3.2, are consistent with simplified velocity structures from the North Sea and were taken from the Vulcan gas field [Campden 1990].

The models consist of a target layer (CMAIN) whose crack geometry is of interest. Above this are a series of different surface layers, whose thickness, crack strike, and velocity vary between models, and present possible realistic anomalies in crack direction. The crack strike in the CMAIN layer remains constant at R120°T

TABLE 3.1: Model structures.

MATERIAL CONSTANTS

	Isotropic parameters			Crack parameters	
	Density (g/cm^3)	*Vp* (km/s)	*Vs* (km/s)	Crack density ε	Crack strike (R°T)
CLVL1	2.2	2.5	1.44	0.04	75°
CLVL2	2.1	1.5	0.866	0.04	75°
CMAIN	2.3	4.0	2.309	0.04	120°
BASE	2.6	5.0	2.886	-	-

MODEL STRUCTURES

Model 1		Model 2		Model 3		Model 4	
Thickness (m)	Layer	Thickness (m)	Layer	Thickness (m)	Layer	Thickness (m)	Layer
		50	CLVL1	200	CLVL1	50	CLVL2
500	CMAIN	500	CMAIN	500	CMAIN	500	CMAIN
∞	BASE	∞	BASE	∞	BASE	∞	BASE

The BASE layer is a halfspace in all models.

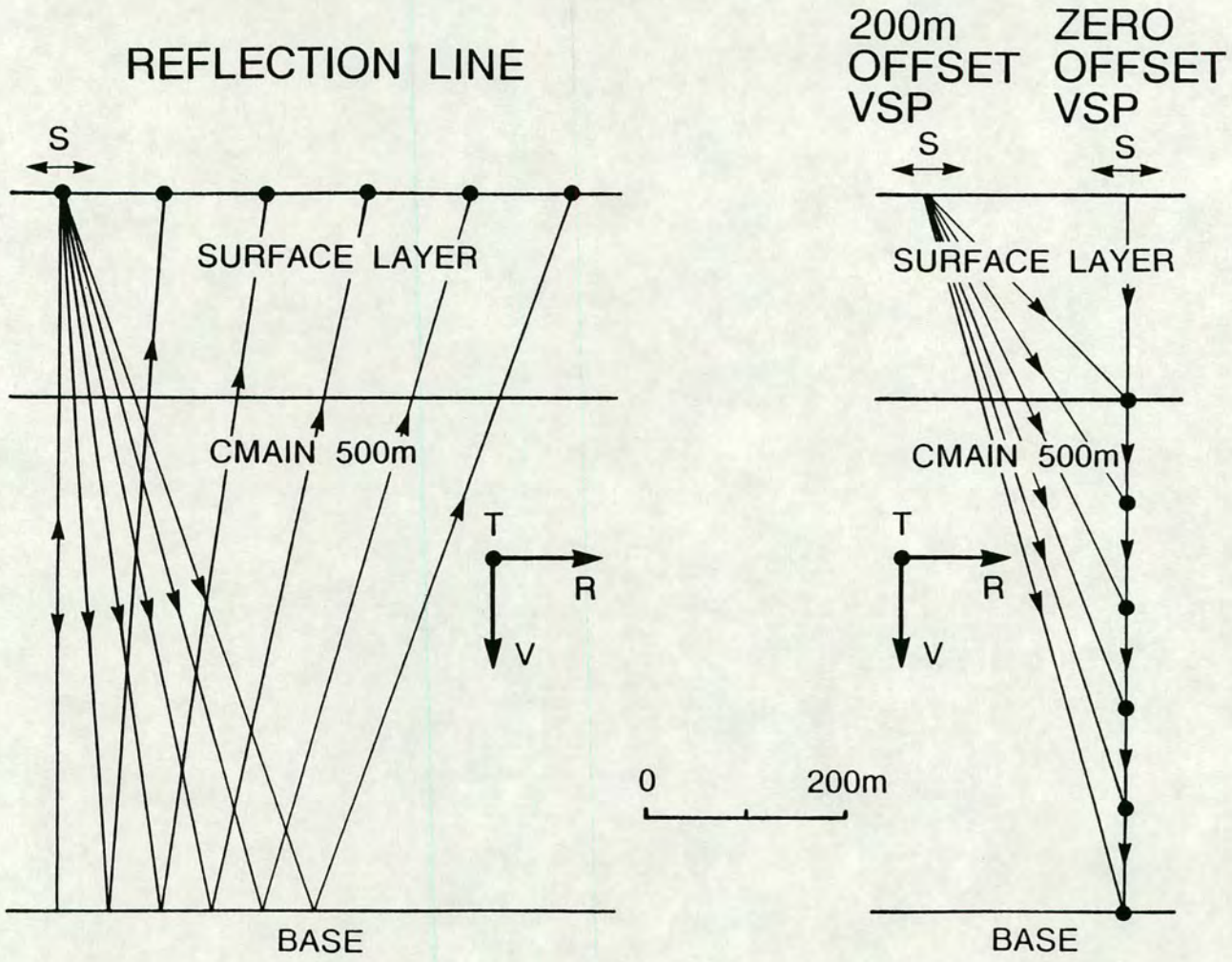

FIGURE 3.2: A schematic illustration of the geometries used for the models. The sources are in the radial direction, the transverse direction is out of the page. All angles are quoted with respect to this coordinate system. The thickness of the surface layer varies between models, but the depth of the geophones in the VSPs remains fixed. The ray paths in the reflection line are all within the shear-wave window.

(where R and T represent the horizontal radial and transverse directions respectively). Crack densities of 0.04 were used throughout. This gives a shear-wave velocity anisotropy of about 4%, similar to that observed in a wide range of geological situations [Alford 1986; Gaiser & Corrigan 1990; Martin & Davis 1987]. A horizontal shear-wave source with a mean frequency of 25Hz was used to generate synthetic seismograms for two azimuths of the acquisition plane relative to the crack strike, and three source orientations for each of the models. A representative selection of these seismograms is presented to show the effects of changes in crack orientation with depth. Synthetic seismograms were calculated for a reflection gather, a zero-offset VSP, and a 200m offset VSP for each model.

3.5 RESULTS

3.5.1 Model 1

Model 1 (Table 3.1) represents a control model with no surface layer, where the shear-waves are only affected by the CMAIN layer. Figure 3.3 shows shear-wave seismograms and polarization diagrams for a reflection gather and two VSP offsets in Model 1. [Polarization diagrams (PDs) are plots of the two horizontal geophone traces for a time window around the shear-wave arrival.] In the case of the reflection line, the seismograms and the PDs show a 0.1s window around the shear-wave arrival that is reflected from the base of the CMAIN layer. In the case of the VSPs, the arrival shown is the direct shear-wave arrival.

The first motions of the leading split shear-waves in the PDs of the reflection line, the zero-offset VSP, and all except the three uppermost geophones of the 200m offset VSP are in the direction of the crack strike within the CMAIN layer. The exceptions (the three uppermost geophones in the 200m offset VSP) are where the polarizations show the anomalous behaviour expected in directions close to a line singularity (see Figure 2.2). The incidence angle of the ray to the first geophone in the 200m offset VSP is 45° (the 200m offset source position to the top geophone in Figure 3.2) and for such incidence angles the fast shear-wave polarization is not parallel to the strike of the cracks. Also, near the shear-wave singularity the time delays are small, as is the path length for the top geophones and the distinctive first motion seen in the deeper

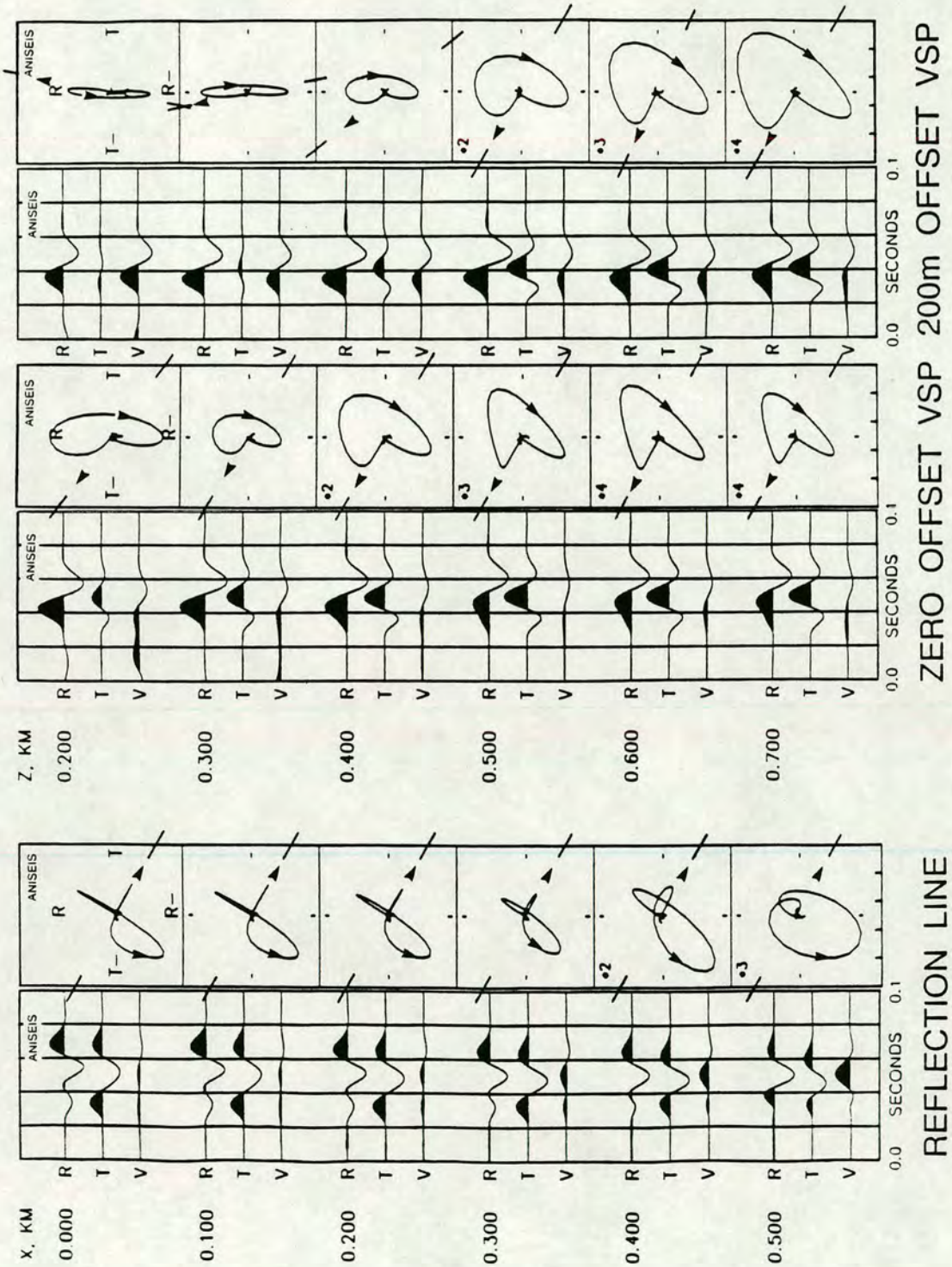

FIGURE 3.3: Normalized synthetic seismograms and PDs for the horizontal plane in Model 1 (control). Source is a radial horizontal force. The PDs are windowed around the main shear-wave arrival and the horizontal geophones are aligned in the R and T directions. From the left, the seismograms and PDs are: a reflection gather; zero-offset VSP; and a 200m offset VSP. The cracks strike R120°T. The crack orientation is clearly seen in the initial polarization of the (faster) split shear-wave arrival in the PDs of the reflection survey, zero-offset VSP and deeper geophones of the 200m offset VSP. The direction of first shear-wave motion in the PDs is marked by an arrow. The numbers in the top left corners of some of the PDs indicates the gain applied to the original signal relative to the unnumbered PDs.

geophones has not had time to build up. Most of the energy therefore, is still in the source (radial) direction. The first and second geophones in the 200m offset VSP show a change from anticlockwise to clockwise rotation. Such changes in direction of rotation are characteristic of ray paths either side of a line singularity (across which the *qS1* polarization changes) in a hexagonally symmetric medium [Douma & Crampin 1990].

The polarity of the first motion in the PDs for the reflection line is reversed with respect to that seen for the VSPs, although still parallel to the crack strike. This phase change is caused by the reflection at the base of the CMAIN layer and is a result of the shear-wave reflection coefficients at a low-to-high velocity interface [Achenbach 1973; Crampin 1987b]. The patterns displayed in the PDs for the reflection line and the VSPs are also different due to the different path lengths in the anisotropic medium. However, the important diagnostic properties of the shear-wave signal are the *qS1* polarization direction (not necessarily the polarity) and the delays between the fast and slow shear-waves, and not the patterns in the PDs. The PD patterns are dependent on the frequency, amplitude, phase, polarization and pulse shape of the incident signal, as well as the polarization directions and time delays through the anisotropic material.

The PDs for the wider offset geophones in the reflection line are distorted. This effect is similar to the distortion caused by nonnormal transmission described in Section 3.3. This distortion occurs because the *SV* and *SH* components of each shear-wave have different reflection coefficients. This occurs even at an isotropic/isotropic interfaces [Achenbach 1973; Crampin 1987b] and can produce effects similar to shear-wave splitting [Appendix 1; Liu, Crampin & Yardley 1990]. In general, in an anisotropic medium, the different reflection coefficients cause each of the incident split shear-waves to split again on reflection. This means that each of the incident shear-waves excites both shear-wave polarizations upon reflection giving a total of four shear-wave arrivals at the surface. For the wider offset geophones in the reflection line, the time delay between the first two arrivals is only developed between the reflector and the surface. This is because these two arrivals only split from each other as a result of the offset reflection. The difference between reflection coefficients increases with angle of incidence. Such anomalies are seen for reflection of

shear-waves with angles of incidence greater than a few degrees when the incident shear-waves are not strictly *SV* or *SH* (see Appendix 1). In a reflection line in a horizontally-stratified earth with isotropic layers, where the source polarizations are usually *SV* and *SH*, such distortions do not occur. However, such distortions are seen in anisotropic cases, where the anisotropic symmetry means that the *qS1* and *qS2* arrivals are not polarized in the inline or crossline directions.

Inclusion of such anomalous signals in common midpoint stacking (CMP) techniques for reflection data gives rise to inaccurate determinations of time delay and polarizations. Thus, CMP techniques may lead to degradation of shear-wave signals at non-vertical incidence reflectors and, perhaps more seriously, at reflections from small offset signals at dipping reflectors. Li & Crampin [1991a, 1991b] present colour displays of instantaneous shear-wave polarization. Examining such plots for reflection gathers allows the seismic processor to determine, for each reflection level, the offset at which such distortions start to degrade the shear-wave signal.

3.5.2 Model 2

Model 2 has a single low velocity anisotropic surface layer of 50m thickness (Table 3.1) in which cracks strike at R75°T, in contrast to the CMAIN layer where the cracks strike R120°T. In this case, The PDs and seismograms for the reflection line are distorted whereas the PDs for the VSPs remain essentially unchanged (Figure 3.4). The upper layer is thin and causes only a small time delay to build up. This does not affect the visual picking of the *qS1* polarization for the deeper geophones in the VSP as a large time delay still builds up in the CMAIN layer.

The PDs for the reflection line are more complicated, as the shear-wave must travel twice through the upper layer. The first observable motion in the PDs for the reflection line in this model (Figure 3.4) lies between the crack orientation in the surface layer and those in the CMAIN layer. The surface layer is thin, and only causes small delays between fast and slow shear-waves within the layer. The visible first motion is a superposition of the fast and slow shear-waves, which have a small time delay (phase difference), and the resulting interference lobe does not lie along the crack strike.

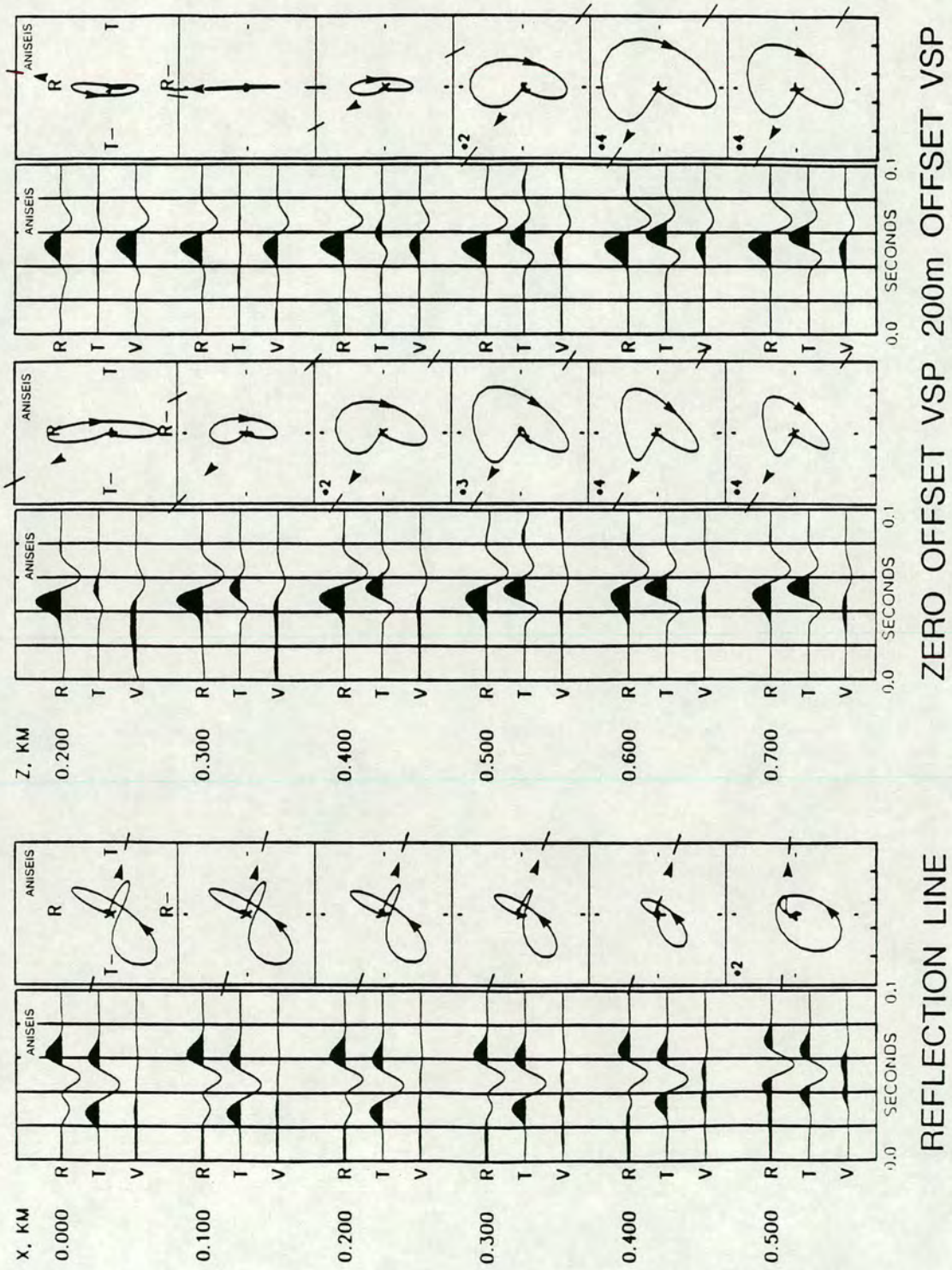

FIGURE 3.4: Model 2 with horizontal radial source. The cracks strike R75°T, in a 50m thick, low velocity surface layer. This shows the behaviour of shear-waves for a reflection survey and zero-offset and 200m offset VSPs.

3.5.3 Model 3

In Model 3 I increased the thickness of the anisotropic surface layer to 200m (Table 3.1, Figure 3.5). The first motions in the PDs for the reflection data align with the crack strike in the surface layer and not the crack strike in the CMAIN layer. This is because the delay between the fast and slow shear-waves in the surface layer is large enough to give a clear initial direction. Therefore the polarizations and delays in the CMAIN layer are effectively obscured. The VSP arrivals are more complex than in previous cases as passage through a 200m surface layer means that two separated shear-waves form the incident wave for the CMAIN layer. The top geophone in the zero-offset VSP is at the base of the surface layer and shows the waveform incident on the CMAIN layer. The relative orientation of the source and the cracks in the two layers means that the first arrival is small for geophones 4,5 and 6. I have marked this arrival by dots in Figure 3.5). This arrival is still polarized parallel to the CMAIN cracks but in the opposite direction. Such a low amplitude arrival is likely to be hidden by noise in field data and I mark the first motion of the main arrival by an arrow. PDs at the shallow geophones in the 200m offset VSP are complicated by the effects of reflections and refractions at the interface and only the deepest geophone clearly displays the properties of the CMAIN layer. Thus the crack orientation in the CMAIN layer can still be picked out by visual inspection of the PDs at the deeper geophones of the VSPs even in the presence of a 200m surface layer, while the PDs for the reflection line are dominated by the surface layer.

3.5.4 Model 4

Model 4 (Figure 3.6) shows the effects of decreasing the velocity of the 50m thick surface layer for the same crack density. The time delay between the split shear-waves in any direction in this layer is larger than in Model 2 (Figure 3.4) because of the larger number of cycles within the upper layer for the given path length. This increases the distortion in the PDs of the reflection line compared to Figure 3.4, but again has only marginal effects on the VSPs.

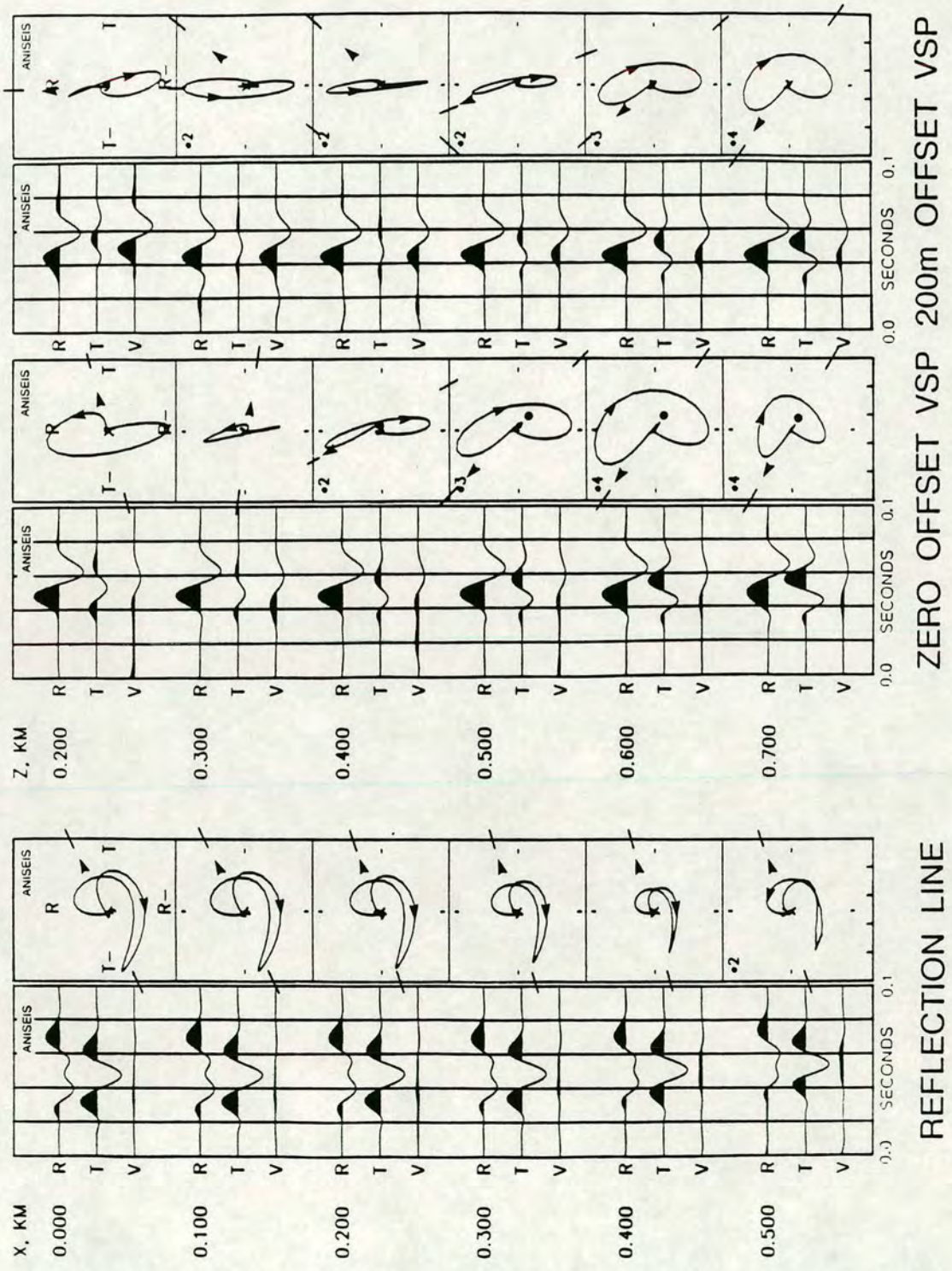

FIGURE 3.5: Model 3 with horizontal radial source. The cracks strike R75°T, in a 200m thick, low velocity surface layer. Note that the shear-wave polarizations for the reflection survey show the crack direction in this surface layer, not in the deeper reservoir layer. The dot, in the PDs for the deeper geophones in the zero-offset VSP, marks a small precursor to the main shear-wave arrival.

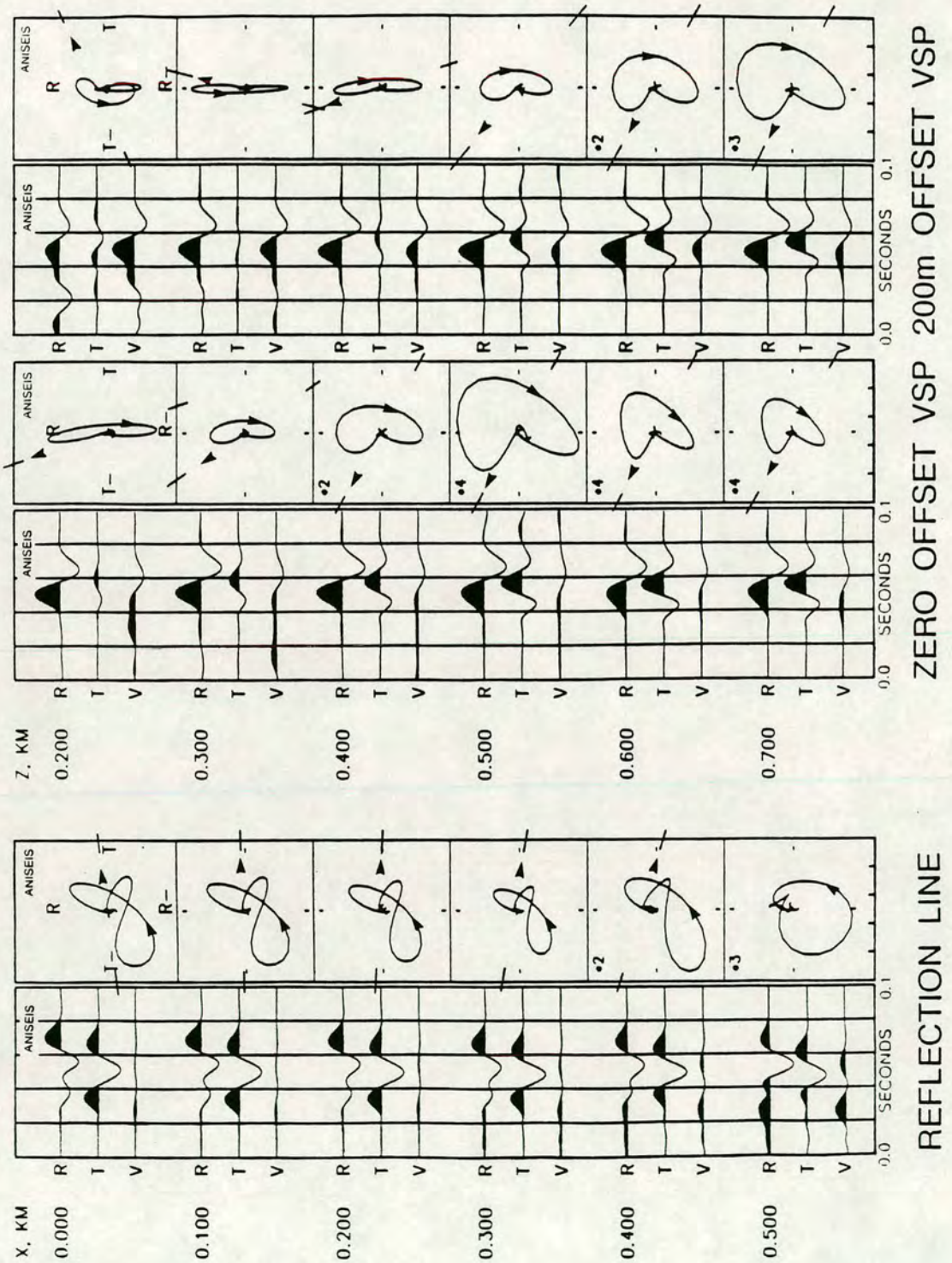

FIGURE 3.6: Model 4 with horizontal radial source. The geometry of the model is the same as Model 2 (Figure 3.4) with a 50m surface layer. The velocity within this layer is smaller than in Model 2 and the PDs for the reflection line show more distortion than in Figure 3.4.

3.6 USING AST WHEN CRACK ORIENTATION CHANGES

I have shown that changes in crack strike above a reservoir mask information about the reservoir layer in surface recordings. Such masking effects are made worse if the upper layer is thick or has a low velocity. Visual picking of the polarization of the first arrival in VSPs is not affected by changes in crack orientation as long as sufficient time delay builds up in the layer of interest. Slack *et al.* [1992] state that shear-wave arrivals can be visually picked if the separation between the first and second arrivals is $\geq\lambda/8$. In this section, I investigate the effect of changing crack orientation with depth on AST (see Section 2.7); a version of the most commonly used estimation technique.

3.6.1 Visual inspection of polarization diagrams

I repeated Model 1 (Table 3.1, Figure 3.7) with the source polarization and geophones aligned parallel to the cracks. This source excites the fast shear-wave. An orthogonal source, aligned perpendicular to the cracks, would excite the slow shear-wave. For vertically propagating shear-waves incident on vertical cracks, positioning the source and geophones like this is equivalent to rotating the data matrix as done by AST. This makes most of the off-diagonal components zero for both the VSPs and the reflection line.

The offset geophones for the reflection line show motion which is not linearly polarized and is visible on both horizontal components. This is due to the splitting on reflection, described above, causing both shear-wave polarizations to be excited. If the wider offset geophones are included in the gather, post-stack rotation of this data yields a maximum energy direction which is a few degrees anticlockwise from the X-direction. However, in processing field data, most rotations are now performed prestack which leads to incorrect rotations of the farthest offset geophones of up to 40°. When the rotated traces are stacked together the signal is degraded by the inclusion of the far-offset traces. Even in this case of a single anisotropic layer, matrix rotations do not yield the correct crack orientation if traces with angles of incidence greater than about 10° (for this velocity structure) are included.

The PDs for the shallow geophones in the 200m offset VSP are also non-linear.

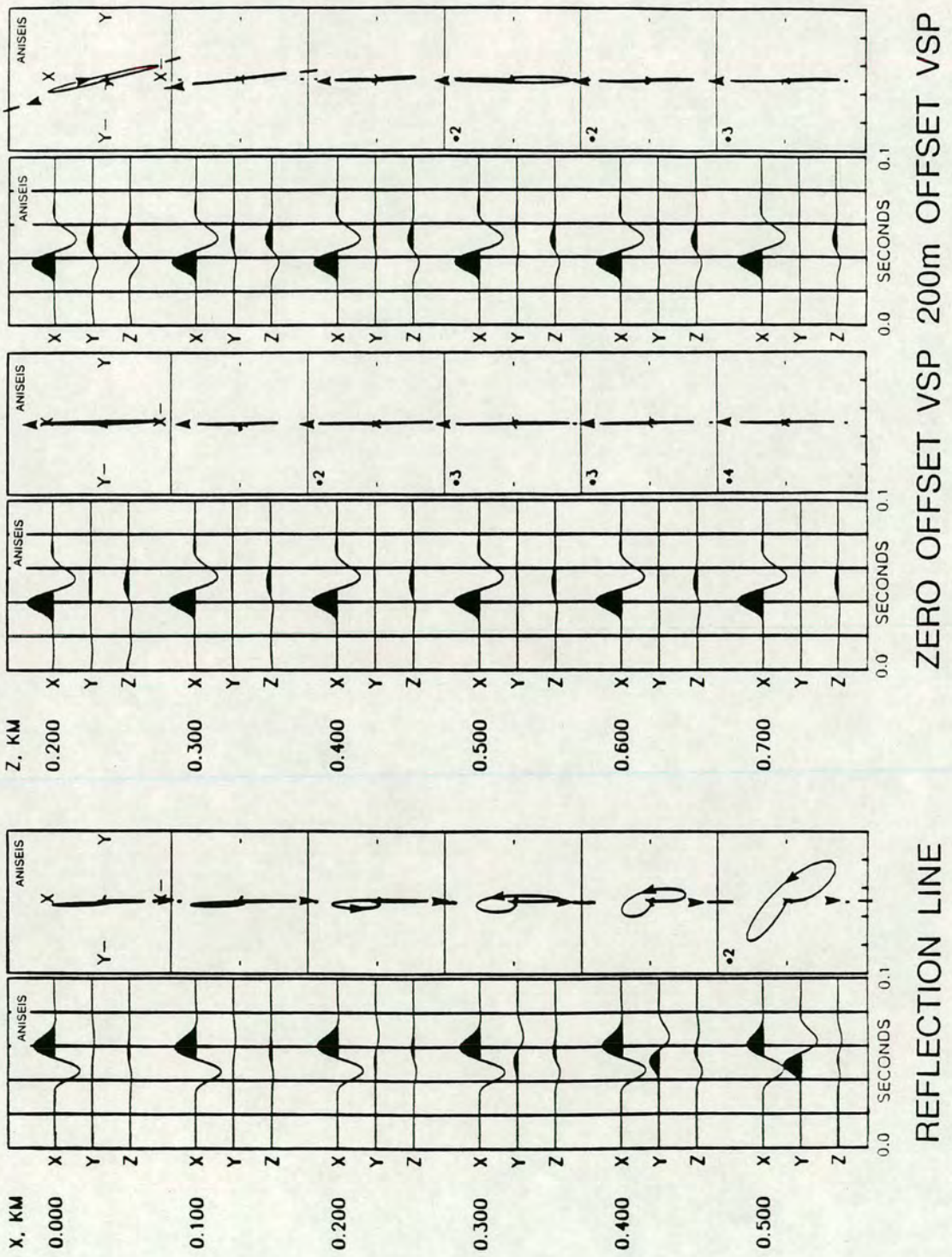

FIGURE 3.7: Model 1 repeated with the source and geophones aligned parallel to the cracks (R120°T). PDs show linearly polarized motions as only the fast shear-wave has been excited (except for wide-offsets where the fast shear-wave is not polarized parallel to the cracks and in the offset reflections where the shear-wave signal is distorted by the reflecting interface). The X-direction is parallel to the source.

The incidence angle to the uppermost geophone in the 200m offset VSP is 45°; the cracks strike at R120°T and in such cases the *qS1* polarization is not parallel to the cracks (Figure 2.2). In the case of Model 1, where the crack strike is constant, this method yields estimates of the crack strike only if ray paths with steep angles of incidence are used.

Model 3 was recalculated with source and geophones aligned parallel to the cracks in the surface layer (Figure 3.8), and to the lower, CMAIN, layer (Figure 3.9). This simulates the possible rotations which may give information about the structure of the CMAIN layer. The PDs for the reflection line in Figure 3.8 are non-linear for all geophones as passage through two layers with different crack orientations excites both shear-wave polarizations. Both the VSPs show motion that is not linearly polarized in the PDs for all geophones in the CMAIN layer, although the time delays between the two split shear-waves for the second and third geophones in the 200m offset VSP are small in Figure 3.8 leading to nearly linear PDs. This is because the ray paths to these two geophones pass close to a line singularity. Figures 3.8 and 3.9 show that the presence of a layer with a different crack orientation means that both shear-wave polarizations are always be excited in deeper layers and no rotation of source and geophones zero the off-diagonals components.

Layer Stripping

The PDs from the zero-offset VSP in Figure 3.8 demonstrate the principle behind the layer stripping approach of Winterstein & Meadows [1991a]. AST is applied to the data to minimize the off-diagonal energy on the first geophones to give linearly polarized arrivals as seen for the shallowest geophone here. If energy is present on the off-diagonal elements, multiple splitting is assumed to have occurred and the deeper data are rotated and time shifted to remove the effects of the upper anisotropic layer. By this method, successive anisotropic layers can be stripped away to reveal the deeper structure. However, it is not clear how to pick the depth at which to start stripping the data. In Figure 3.8, it can be seen that the PD from the second geophone in the zero-offset VSP is also 'nearly linear' due to the short time delays built up in the CMAIN layer by this depth. This second geophone is below the interface where

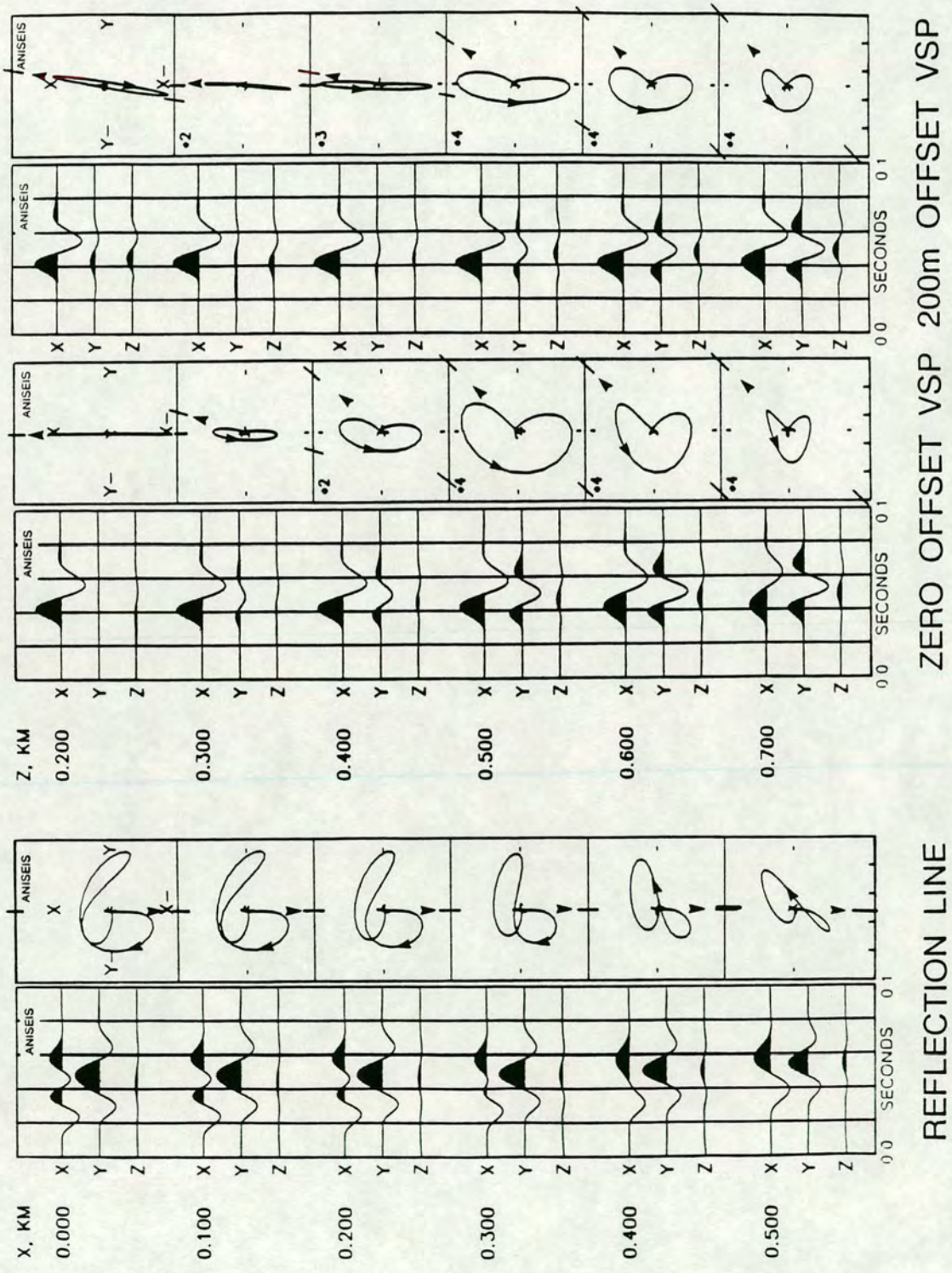

FIGURE 3.8: Model 3 repeated with source and geophones aligned parallel to the cracks in the surface layer (R75°T). The off-diagonal component has only been minimized for the top geophones in the VSPs which lie in the surface layer. The X-direction is parallel to the source.

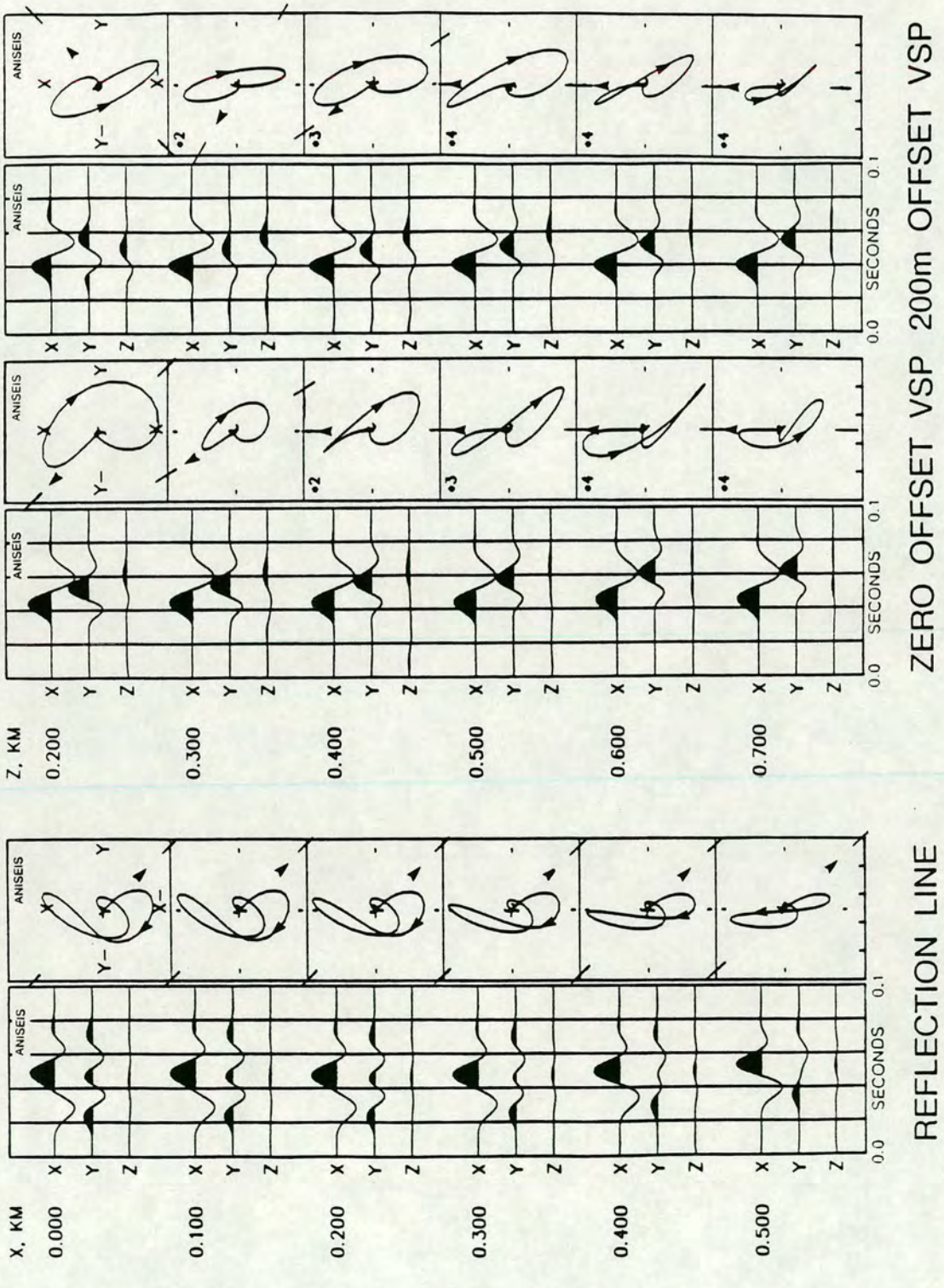

FIGURE 3.9: Model 3 repeated with the source and geophones aligned parallel to the cracks in the CMAIN layer (R120°T). The off-diagonal component has not been minimized at any of the geophone positions. The X-direction is parallel to the source.

layer stripping should take place, but, in noisy data it may be mistaken for a linearly polarized arrival. Tying the depth of layer stripping to geological boundaries may be an answer, but it is not clear yet how anisotropy is linked to lithology. Barthelemy, Tremolieres & Andrieux [1992] suggest that lithological interfaces are not always the same as mechanical interfaces.

MacBeth & Yardley [1992] show that changes in crack orientation do not become apparent in the results of anisotropy estimation techniques (in VSP data) until significantly below the depth of the change in crack orientations and, again, an incorrect depth may be chosen for layer stripping. The effect of choosing the wrong depth for layer stripping is dependent on several factors, including: pulse shape; frequency; percentage anisotropy; and the change in crack strike at the interface. For layer stripping to work the geophone, at which the stripping takes place, must be close enough to the change in crack strike for the estimation techniques not to detect the influence of the second crack orientation. MacBeth & Yardley [1992] show how quickly the estimation techniques respond to a change in crack strike for a variety of pulse shapes and frequencies. If the pulse is an impulse, then the estimation techniques detect the change in crack strike immediately; however, for a 15Hz pulse (a typical frequency found in field data) the estimation techniques do not detect the change in crack orientation until 3ms of delay has built up after the change in crack strike. This means that the point of layer stripping and the actual change in crack strike must be close enough together such that at most 3ms of delay builds up between them. This can be used to decide geophone spacing in field experiments, particularly in the near-surface where geophones levels are usually widely separated.

Layer stripping is likely to be easier in VSPs as the shear-waves pass only once through each layer and so less multiple splitting occurs. VSPs, with recordings from all levels, also give a continuous record of how the shear-waveform changes with depth.

3.6.2 Applying AST to multiply split shear-waves

I have shown, using polarization diagrams, that rotations of the data matrix do not yield zero off-diagonal elements in the presence of a changing crack orientation with

depth. Here, I show how this affects the results of AST for VSP data. AST requires two identical orthogonal shear-wave arrivals (Section 2.7) separated by a time delay. After passage through two layers with different crack orientations there are four arrivals. For this case Equation (2-4) can be rewritten as:

$$\mathbf{D}(t) = \{\mathbf{R}^{\mathrm{T}}(\theta_2)\Lambda_2\mathbf{R}(\theta_2)\} * \{\mathbf{R}^{\mathrm{T}}(\theta_1)\Lambda_1\mathbf{R}(\theta_1)\} * \mathbf{S}(t); \qquad (3\text{-}1)$$

using the same notation as in Section 2.7. θ_1 and θ_2 are the crack strikes in the first and second anisotropic layer. In general, the data matrix in Equation (3-1) is not symmetrical [MacBeth & Yardley 1992]. I applied AST to synthetic seismograms calculated for the Winterstein & Meadows [1990a] model of the Lost Hills field (Figure 3.10). AST gives correct answers for the polarization direction and time delay in Layer 1, once sufficient time delay has built up. In the second medium AST finds a minimum in the energy on the off-diagonal components. This minimum is created by the superposition of four arrivals and does not indicate the crack strike or time delay. The stability of the results should not be taken as evidence for the estimation technique working. These results were shown by Yardley & Crampin [1990]. Results are similar for reflection data, except that the shear-wave signal is more distorted as it contains eight arrivals [MacBeth & Yardley 1992].

MacBeth & Yardley [1992] give a detailed account of how AST and AIT behave in the presence of changing crack orientation with depth. We found that estimation techniques continued to give the polarization angle of the first layer for some distance into a second layer with a different crack orientation. The solutions for polarization direction then diverged from the crack strike in the first layer. The crack strike in the second layer is only determined by the estimation techniques if the time delay in the second layer is greater than the pulse length.

3.7 CONCLUSIONS

From this work, I conclude that changes in crack orientation with depth mean that it is not possible to extract information about deep layers by visual inspection of polarization diagrams in reflection data. It is possible to identify the *qS1* polarization

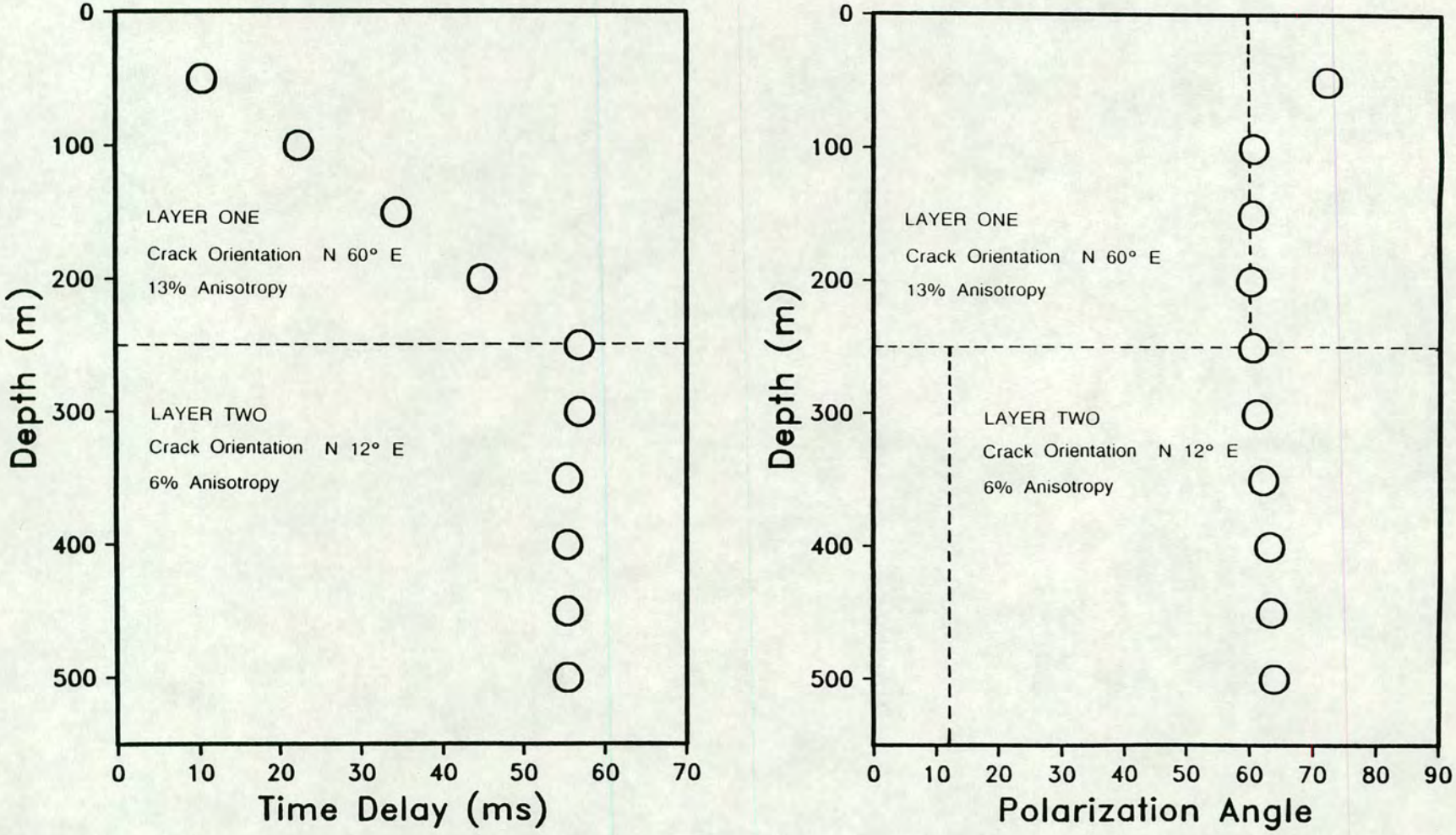

FIGURE 3.10: Results from a source-geophone rotation [Alford 1986] from synthetic zero-offset VSP data for a model with two crack orientations (shown by the vertical dashed line). The model is based on the structure for the Lost Hills field determined by Winterstein & Meadows [1990a]. In the second layer the time delays and polarizations are not resolved due to the double splitting of the shear-waves at the interface.

and time delay by visual methods in VSP data as long as sufficient delay ($\lambda/8$) can build up after the change in crack orientation. Clear first arrivals do not develop if the anisotropy is weak or if the layers with different crack strikes are thin. Many workers report that most anisotropy is in the near-surface [Becker *et al.*1990; Bush 1990; Winterstein & Meadows 1991a, 1991b]. Therefore sufficient time delays, to allow visual picking of arrivals, may never build up in deeper layers. Where sufficient delays do not build up after a change in crack strike the visible first arrival is a superposition of several arrivals and, if picked, gives an incorrect polarization estimate.

Estimation techniques that require that there are only two orthogonal shear-waves give incorrect results for both VSPs and reflection data. The break down of the estimation techniques can be identified by the presence of energy on the off-diagonal elements of the rotated data matrix. Recently propagator matrix techniques (e.g. DPM, Section 2.7) and layer stripping techniques [MacBeth *et al.* 1993; Winterstein & Meadows 1991a, 1991b] have been introduced to overcome this problem. It is not clear whether such techniques are effective on field data as it is difficult to confirm their results.

Reflection from an interface creates further shear-wave arrivals (if the signal does not propagate vertically or is not polarized strictly *SV* or *SH*). This leads to apparent shear-wave splitting and contaminates any CMP stacking of reflection data even for relatively steep angles of incidence.

I have used simple models in this investigation. More complex models (with dipping cracks and thin layer anisotropy) only confirm the conclusions of this chapter: as VSPs allow recording at all levels, they provide a simpler, more controlled environment in which to investigate shear-wave anisotropy than reflection surveys.

CHAPTER FOUR

THE LOST HILLS VSP, KERN COUNTY, CALIFORNIA: A CASE STUDY

4.1 INTRODUCTION

The Lost Hills field is situated at the southern end of the San Joaquin Valley, California. The San Joaquin Valley is one of America's leading oil and gas producing regions and has 22 oil fields containing in excess of 100 million barrels [Thurston, Mason & James 1987]. Recently, hydrocarbon recovery has concentrated on enhanced oil recovery projects [Mason 1988], for which knowledge of reservoir fracture parameters is important. Shear-wave VSPs in the upper 760m of the structure indicate that the *qS1* polarization is parallel to induced hydraulic fractures [Winterstein & Meadows 1991a] and that shear-waves can detect hydraulic fractures [Meadows & Winterstein 1992]. In this chapter, I process and model data from a zero-offset VSP from this field in an attempt to evaluate the fracture structure of the reservoir. This VSP has geophone levels between 1.1km and 2.3km and is below the depth range investigated by Winterstein & Meadows [1991a].

Squires, Kim & Kim [1989] inferred 90° changes in fracture orientation around this well to account for decreases in time delay with depth. Here, I use VSP data to present a new interpretation. The results of the estimation techniques indicate that the polarization direction of the medium does change with depth, but not by 90°. Previous interpretations were based on inappropriate application of estimation techniques in the presence of multiple splitting. This chapter represents a case study of the distorting effects of changes in crack orientation with depth as discussed in Chapter Three. The *qS1* polarization direction, at depth, is N58°E and is consistent with regional stress directions and known fracture orientations [Winterstein & Meadows 1991a]. This suggests that the anisotropy is caused by features (probably fractures) aligned with the regional stress field. I am unable to resolve anisotropy in the reservoir layer.

A single zero-offset VSP with geophone levels between 1.1km and 2.3km does not allow a unique model to be developed. I therefore calculate a range of physically

plausible models which account for the results of the estimation techniques. Using these models, I show how the estimation techniques are affected by changes in crack orientation and source characteristics.

4.2 STRUCTURE OF LOST HILLS ANTICLINE

Figure 4.1 shows the location of the Lost Hills anticline, the formation of which has been described by Medwedeff [1989]. Medwedeff used growth fault bending theory, in the presence of compression normal to the San Andreas, to model the formation of the anticline. The current relative motion of the North American and Pacific plates is approximately 10° clockwise from the strike of the San Andreas fault [Pollitz 1986]. The San Andreas fault, which is 30km to the southwest, has a low shear strength [Zoback *et al.* 1987] and relieves the component of stress parallel to the fault by movement along the fault. This leaves a compression directed along N50°E, normal to the fault. This is confirmed principally by borehole breakout studies, and also by focal mechanism, hydraulic fracturing and geological studies of the region for the World Stress Map Project [Zoback 1992].

Figure 4.2 shows a southwest-northeast section through the anticline from Medwedeff [1989] with the location of the VSP marked. Slip began approximately 8Ma ago (upper Miocene) during the deposition of the Etchegoin formation (the later Etchegoin deposits onlap the anticline structure) and occurred along a detachment at the base of the Tertiary. Deposition of sediments then occurred at a similar rate to the uplift of the anticline structure. This means that sediments at a given depth, throughout the anticline, have experienced similar compression due to overburden and seismic velocity is depth dependent, rather than formation dependent. This is confirmed by velocity modelling which shows that velocity has to be depth dependent to match the two way times to seismic interfaces in reflection profiles [Medwedeff 1989]. A 24km gravity profile [Barton 1948] across the structure, perpendicular to the fold axis, is flat. If density was related to geological formation the anticline would be apparent on the profile. This confirms that there is little lateral density variation, even across the dipping limbs of the anticline.

The zone of interest in this well is between the Lower Reef Ridge and the

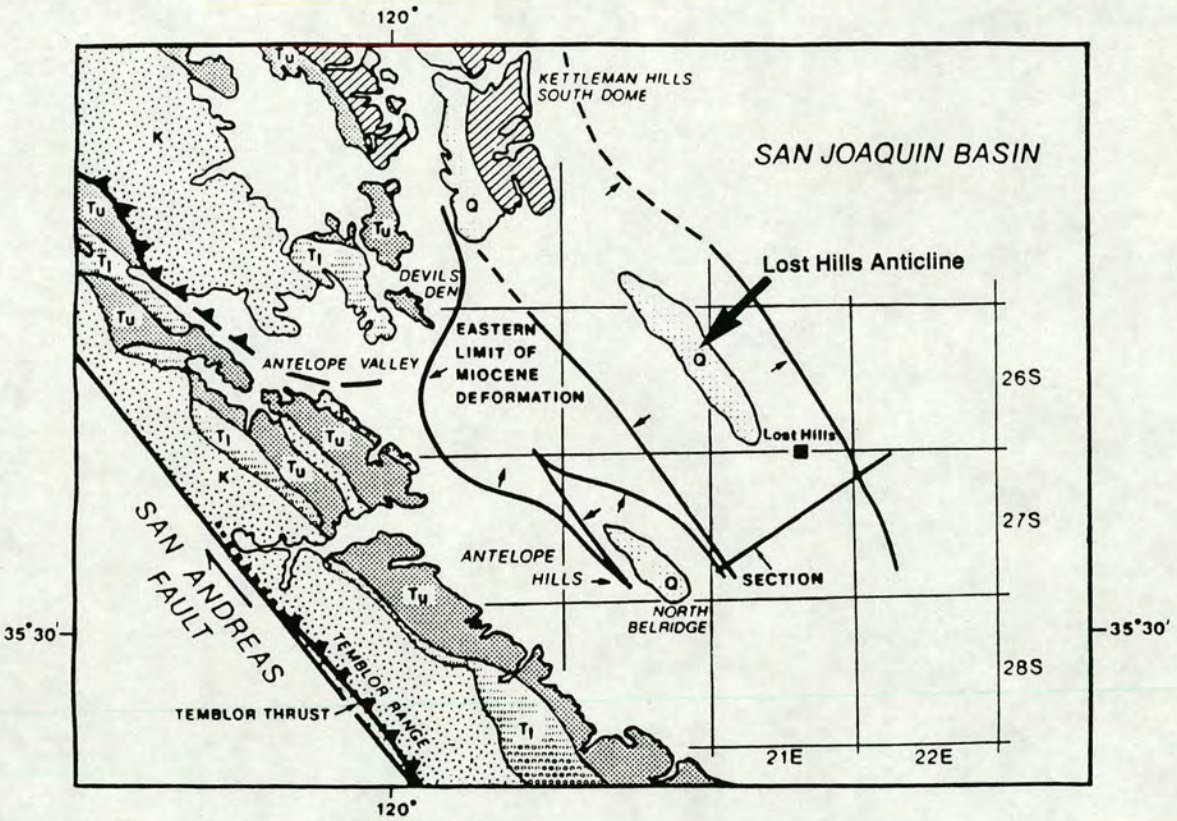

FIGURE 4.1: Map showing the location of the Lost Hills field (taken from Medwedeff [1989]) with respect to the San Andreas fault. The maximum compressive stress acts normal to the San Andreas fault and was responsible for the formation of the anticline [Medwedeff 1989].

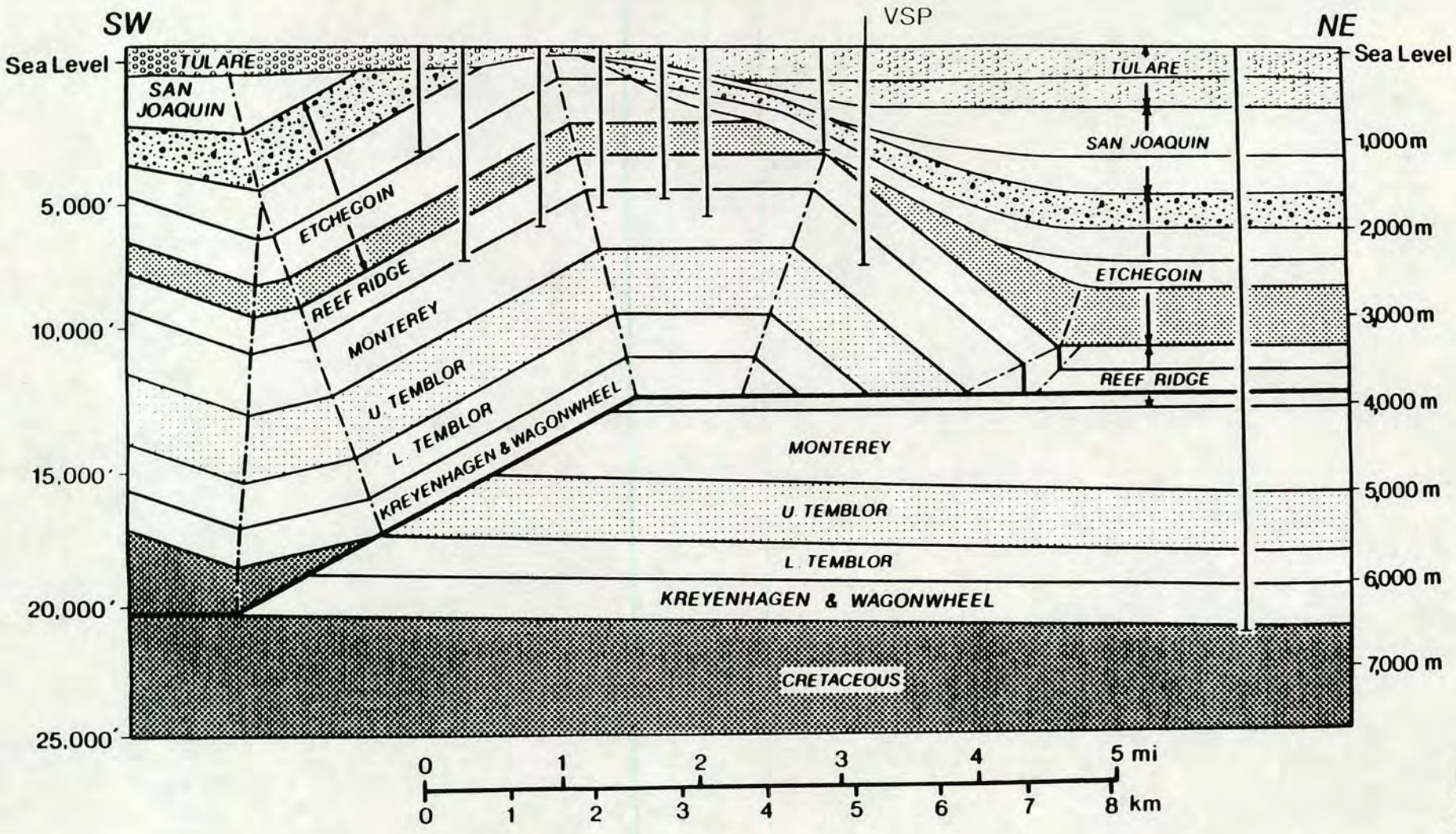

FIGURE 4.2: SW-NE section through the Lost Hills anticline taken from Medwedeff [1989]. The approximate position of the VSP analyzed in this chapter has been marked on the NE flank of the anticline. The zone of interest is in the upper Monterey formation.

McDonald Shale (part of the Monterey formation, Figure 4.2). The Monterey and Reef Ridge formations are shales and siliceous shales [Dibblee 1973] and dip at approximately 42° to the northeast [Medwedeff 1989]. These deposits were laid down in a marine environment [Bandy & Arnal 1969]. During the deposition of the Etchegoin formation (Upper Miocene to Lower Pliocene) the basin was cut off from the sea, then silted up [Bartow 1987] and the upper Etchegoin deposits are shallow water deposits. Above the Etchegoin formation are the San Joaquin pebble conglomerates. The youngest formation is the Pliocene Tulare which is a horizontally bedded mixture of siltstone, sandstone and conglomerate [Medwedeff 1989]. According to Winterstein & Meadows [1990b], the Tulare formation at the Cymric and Railroad Gap oil fields, 15km to the south, contains particles from fine grains to cobble size with interbedded shales.

Hydrocarbon reservoirs are found in many of the formations within the Lost Hills anticline from the Tulare down to the Temblor formation [Land 1984]. The growth history of the anticline means that metamorphic processes are more dependent on depth of burial rather than stratigraphic position and most of the productive regions lie at similar depths [McGuire *et al.* 1983]. Both oil and gas are produced in the Lost Hills field with annual production in 1982 standing at 3.4 million bbl of oil and 20.5tcf of gas from fractured reservoirs in the Monterey formation [Land 1984]. Squires, Kim & Kim [1989] use VSP data from this well and a surface reflection line to conclude that reservoirs in this field are characterized by anomalously low *Vp/Vs* ratios. The *Vp/Vs* ratio is 1.65 for the zone of interest in this well. Low *Vp/Vs* ratios were interpreted as indicating diagenetic alteration to an almost all quartz lithology. Fracturing occurs during recrystallization after this diagenetic process [Squires, Kim & Kim 1989]. Analysis of core by Mobil Oil Company [Squires, Kim & Kim 1989] from wells within the field gives a predominant fracture orientation of N45°E for the zone of interest.

4.3 ANISOTROPY STUDIES IN THE LOST HILLS

Squires, Kim & Kim [1989] used data from a shear-wave reflection profile (see Section 3.2), which intersected the well, to infer that the fracture direction within the

anticline is usually NW, but was NE in the zone of interest in this well. However, they encountered difficulties in determining instrument polarities [Kim 1989]. They also found an anomalously large time delay between the *qS1* and *qS2* arrivals in the zone of interest.

Winterstein & Meadows [1991a] determined induced fracture directions in the Lost Hills field by analysis of shear-wave VSPs and tiltmeter surveys from three boreholes. In one borehole fracture orientations of N53°E and N56°E were determined from tiltmeter data and N58°E and N59°E from VSP data for two different depth regions. The other two wells, one with VSP data and one with tiltmeter data, gave fracture strikes of N40°E and N59°E respectively, although the wells were less than 200m apart. [Fracture dip was not noted by Winterstein & Meadows [1991a]; however, vertical cracks were required in their models to get a good fit of modelled and observed data.] They layer stripped (see Section 3.6.1) one VSP data set and found an approximately constant shear-wave velocity anisotropy of 3% and fracture orientation of N59°E for the entire depth range (30m-640m, 100ft-2100ft) except for within two layers. These anomalous layers were a thin near-surface layer and the interval between 274m (900ft) and 365m (1200ft) where the fracture orientations were approximately N5°E and N120°E respectively. Multi-offset multi-azimuth data were also acquired at a single geophone level, 609m (2000ft). They modelled the resulting shear-wave polarizations using a single layer with vertical cracks striking N55°E and weak thin layer anisotropy dipping at 10° towards N70°E (part of the rock strata dips at approximately this angle). Their model does not take into consideration ray bending due to changes in velocity with depth or the changes in fracture strike with depth. Further analysis of these data sets using both propagator matrix and layer stripping techniques confirmed changes in fracture orientation with depth [Lefeuvre, Winterstein & Meadows 1991].

Choi & Gangi [1991] processed the VSP data set analyzed in this chapter and determined a *qS1* polarization angle of N45°E and a slight decrease in time delay from about 44ms to 38ms through the depth range using an Alford [1986] rotation. They associate scattered results and the decrease in time delay with problems of source-amplitude balancing and movements in source location respectively. After their

source imbalance correction, there is still substantial energy in the off-diagonal sections. This implies that they have not been able to determine the fracture strike (see Section 3.6.1). Choi & Gangi [1991] state that their determination of polarization angle is supported by the N45°E fracture orientation from core data in the reservoir layer [Squires, Kim & Kim 1989]. However, the delay they detect is entirely built up above the VSP section and they show no evidence of further delays in the reservoir layer. Squires, Kim & Kim [1989] do not state which wells in the field the core data came from. With such a complex geological structure it is not known if fracture directions are laterally invariant within the reservoir layer.

4.4 DATA ACQUISITION

The nine-component VSP analyzed here was acquired by Kim Tech (now Production Geophysical Services) in 1986. The acquisition geometry for this VSP in the Trueman Fee #162 well is shown in Figure 4.3. The source offset is 155m at an azimuth of N253°E from the well head. Two orthogonal source orientations (inline and crossline) were acquired using an OMNIPULSE source on separate runs of the sonde. The well is cased and is slightly deviated (up to 4.5° at depth). Well deviation, determined by gyro-data, is also shown in Figure 4.3. There were 42 geophone levels between 1097m (3600ft) and 2347m (7700ft) at 30m (100ft) intervals. *P*-wave data, with the OMNIPULSE airgun in the vertical position, were also recorded for seven geophone levels in the upper part of the well between 152m (500ft) and 1066m (3500ft) at 152m (500ft) intervals. Gearhart Inc. three-component 10Hz geophones were used.

Well deviation means that the sagittal plane rotates through 12° between the shallowest and deepest geophone levels and the source orientations for the deeper geophone levels are not strictly inline and crossline.

The number of shots fired at each level depended on the depth and received signal quality and was as follows (level 1 is the shallowest):

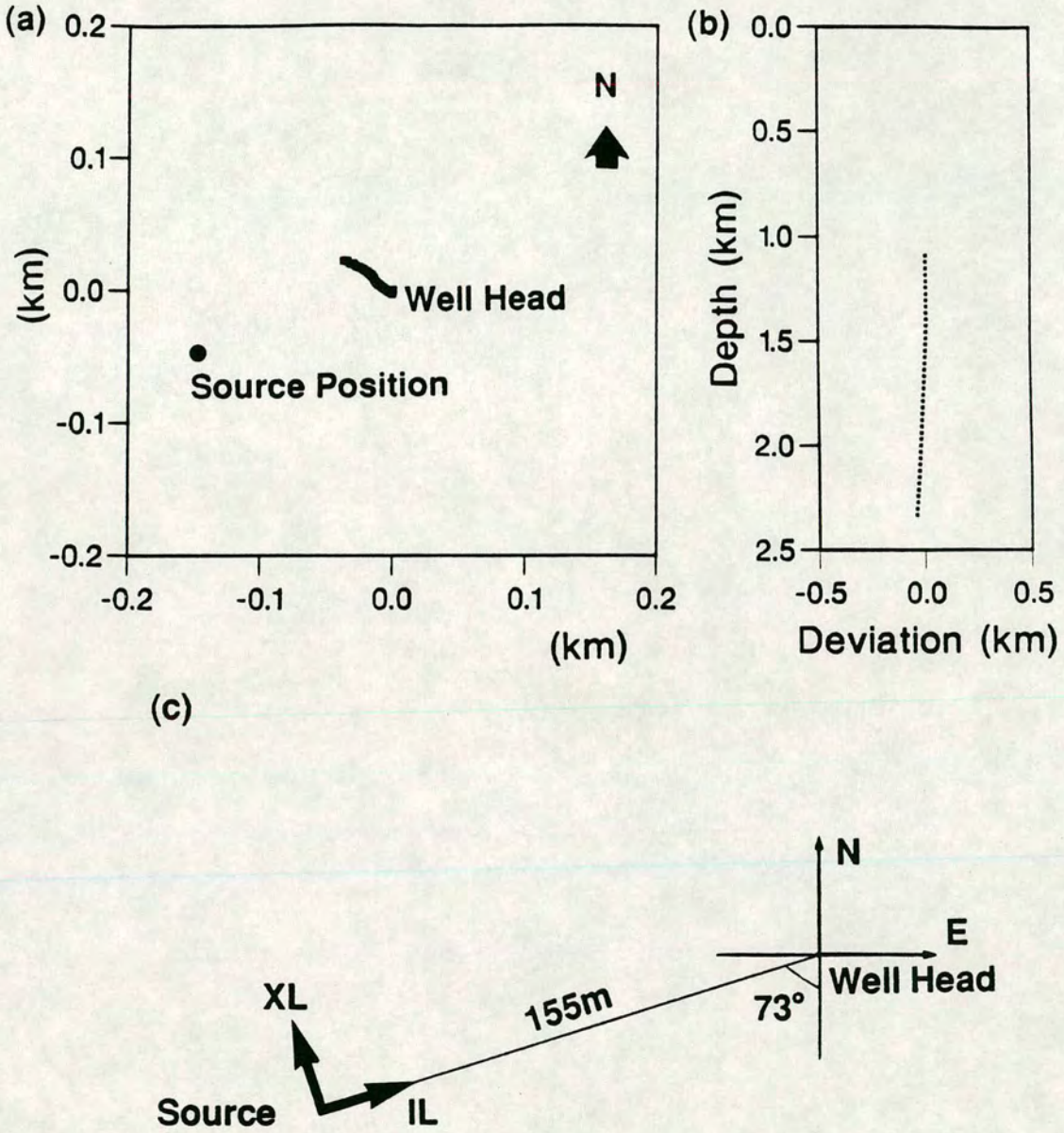

FIGURE 4.3: Experiment geometry and well deviation: (a) Shows a plan view of the source offset and well deviation. Well deviation of up to 4.5° in the lower part of the well means that the sagittal plane rotates by 12° with depth; (b) shows geophone levels in the plane of maximum deviation; (c) shows source offset, azimuth and directions.

Geophone levels	Inline source	Crossline source
1-9	8	11
10-18	12	11
19-34	20	11
35	30	11
36-42	30	30

Each shot was repeated, with the airgun firing to the left and to the right. The source location had to be changed on several occasions during the experiment due to damage to the ground caused by the source. Each change in source location was between two and three metres.

4.5 DATA PROCESSING

In this section I describe the processing (see Section 2.5) of the VSP data prior to application of the estimation techniques. I also display the processed data.

Unstacked SEGY data were provided on magnetic tape, together with gyro-data logs. I wrote an interactive graphical trace stacking program for *VAX*-workstations which allowed all traces from a given geophone component at each level to be inspected before stacking. Some traces were dominated by high frequency noise bursts and a 70Hz low pass filter was applied to all the data to eliminate this noise to allow visual quality control during stacking.

Right shots were then added and subtracted from the left shots to give *P*-wave and shear-wave sources respectively, as described in Section 2.6. This gave shear-wave source orientations of N17°W (crossline) and N73°E (inline). Geophone components were rotated (see Section 4.5.1) into north, east and vertical components, using gyro-data, to give a fixed reference system in which to interpret the shear-wave polarizations. The recorded shear-wave signal has a peak frequency of 10Hz and a 3 to 25Hz frequency domain band pass filter was applied to reduce noise. A 3 to 40Hz band pass filter was applied to the *P*-wave sections. These filters were designed after inspection of the amplitude spectra from windows about the shear- and *P*-wave arrivals and reduced the scatter in the estimation technique results.

As I use propagator matrix estimation techniques (Section 2.7) on this data I

applied an FK filter which only passed the downgoing wavefield between 0 and 30Hz and removed the upgoing wavefield.

4.5.1 Rotation of the three-component data

Rotation of the three-component data based on gyro-data did not give rotations of the horizontal plane PDs that were consistent between levels. It is important to know the orientation and polarity of the geophone components and sources so that the *qS1* polarization can be interpreted. Here, I determine the correct geophone coordinate system.

According to the observers' logs, the X-component geophone (attached to the gyro-tool) was recorded in Channel 5 of the recording instrument and the Y-component was recorded in Channel 7. The logs do not state whether the geophones formed a left-handed or right-handed set. Production Geophysical Services and Geosource, contacted by M.A.Meadows of Chevron [personal communication], were unable to reach agreement on the geophone arrangement. Here, a right handed set (SEG convention) is assumed, with the positive Z-component downwards. [The first break of the *P*-wave arrival from the impulsive OMNIPULSE source gives a positive signal on tape indicating that positive Z is downwards.]

Figure 4.4a shows the unrotated horizontal plane polarization diagrams, together with the initial rotation based on the gyro-data (Figure 4.4b). Whilst the pattern in the PDs is consistent between levels the orientation is incorrect. This error was noticed independently by D.F.Winterstein & M.A.Meadows [personal communication] who have also examined this data set. However, their solution was different from mine. I assumed that this error in rotation was due to incorrect wiring in the field (a common mistake [M.C.Mueller, personal communication]). The simplest possibility is that the X-component was actually recorded in Channel 7 and the Y-component in Channel 5. The rotation is successful if the geophone components are swapped (Figure 4.4c). The solution chosen by D.F.Winterstein & M.A.Meadows is similar but assumes a left handed geophone set and gives horizontal plane PDs which are rotated 180° from the ones shown here. Rotations of 180° are relatively unimportant in analyzing shear-wave splitting as the *qS1* and *qS2* polarizations, and time delays are preserved.

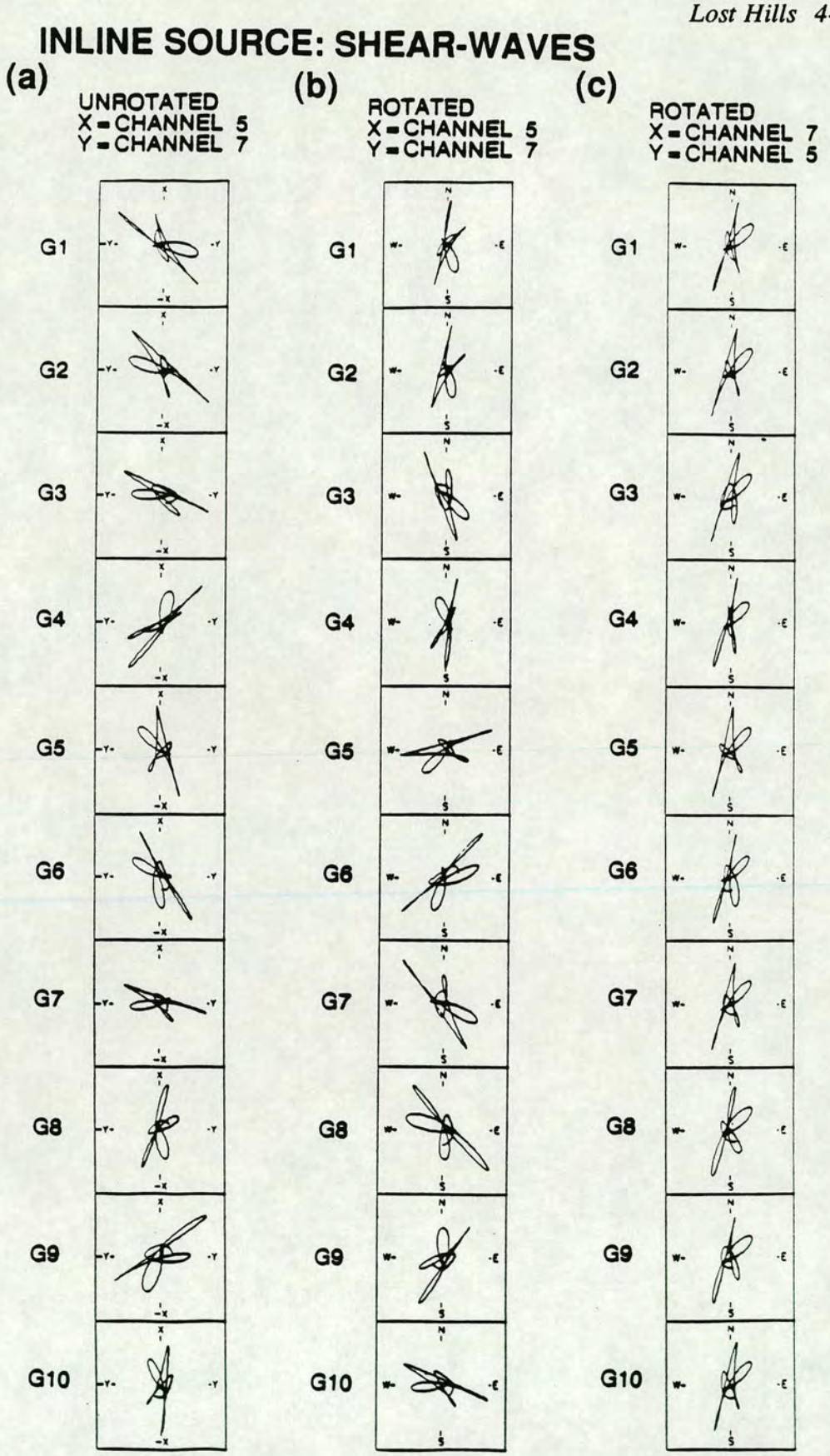

FIGURE 4.4: Horizontal plane shear-wave polarization diagrams; (a) unrotated geophones showing consistent shapes but inconsistent alignments; (b) PDs for geophones rotated according to the observers' logs, again showing inconsistent alignments; and (c) PDs for geophones rotated after the X- and Y-channels have been switched.

The 155m source offset means that the first few geophone levels show enough energy on the horizontal components to verify which rotation is correct. Figure 4.5 shows the horizontal and sagittal plane PDs for the incident *P*-wave arrival. The solution used here gives a first motion in the positive radial direction (away from the source) as expected for an impulsive source. D.F.Winterstein & M.A.Meadows did not perform analysis of the *P*-wave arrivals and their solution gives an incident *P*-wave from the east.

4.5.2 The data after processing

The data, after band pass filtering and rotation are shown in Figures 4.6 to 4.8. The noise level is low. There is little upgoing energy, implying that there are no sharp velocity contrasts. There is little *P*-wave energy on the shear-wave sections (including the vertical component). This shows that the subtraction of the left from right shots was successful in cancelling out the *P*-wave signal and that the source is repeatable left to right. The downgoing arrival has several cycles indicating the presence of multiple energy created in the near-surface [S.A.Raikes, personal communication]. There is little change in the shear-waveform with depth.

For all subsequent work I reversed the polarity of the crossline geophones components to match the convention used in this thesis (see Figure 2.4). This is equivalent to having a crossline source orientation of N163°E and makes comparison of field and modelled data easier. The PDs in Figure 4.9 display elliptical motion indicating that shear-wave splitting has occurred in shallower layers. The initial motion (indicated by arrowheads) is similar for both source directions, as expected for shear-waves travelling in an anisotropic medium.

4.5.3 Near-surface data

The seven near-surface geophone levels allow some information to be gained about the upper 1km of the structure as the vertical OMNIPULSE source produced direct shear-wave arrivals. I rotated the data into the radial and transverse directions by finding the maximum energy direction (over a 160ms window) of the *P*-wave arrival in the horizontal plane. At these depths there is significant *P*-wave energy in

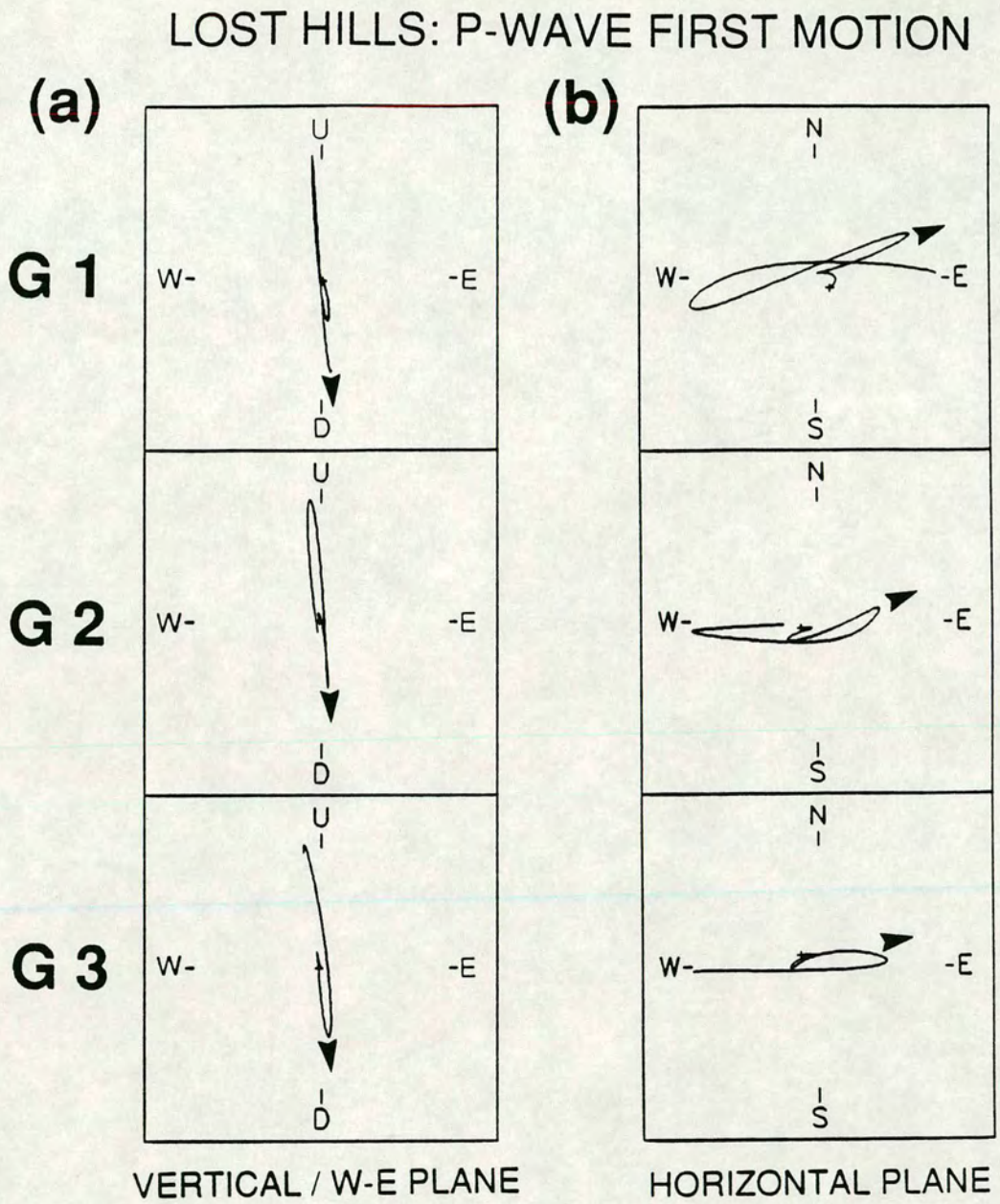

FIGURE 4.5: Polarization diagrams for the first three *P*-wave arrivals rotated after the X- and Y-channels have been switched. The first motion is downgoing and a few degrees north of east, which is consistent with an impulsive source located at N253°E.

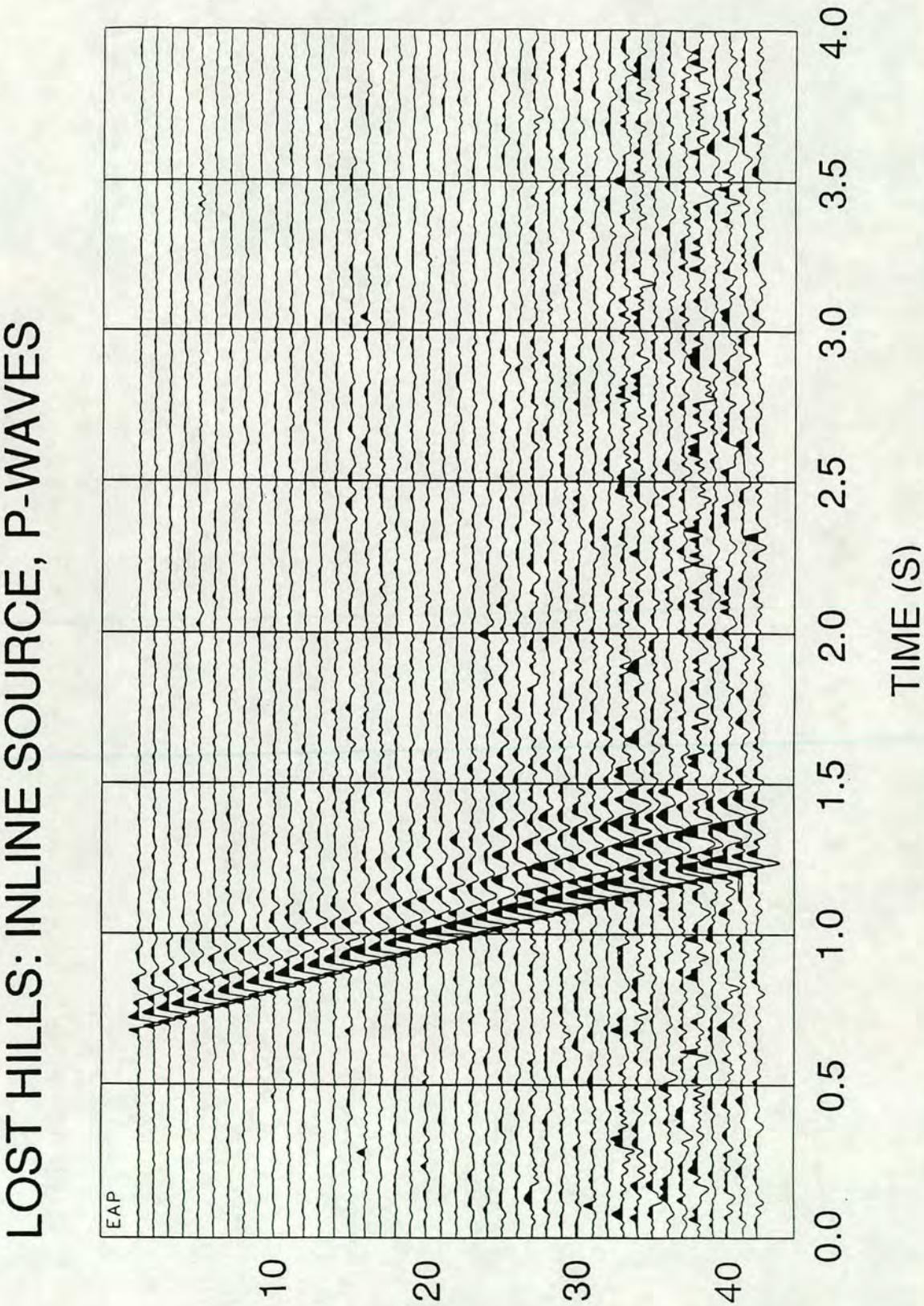

FIGURE 4.6: Vertical component *P*-wave arrival after addition of the left and right shots from the inline OMNIPULSE source. The downgoing arrival has a consistent pulse shape with depth and there is little upgoing energy.

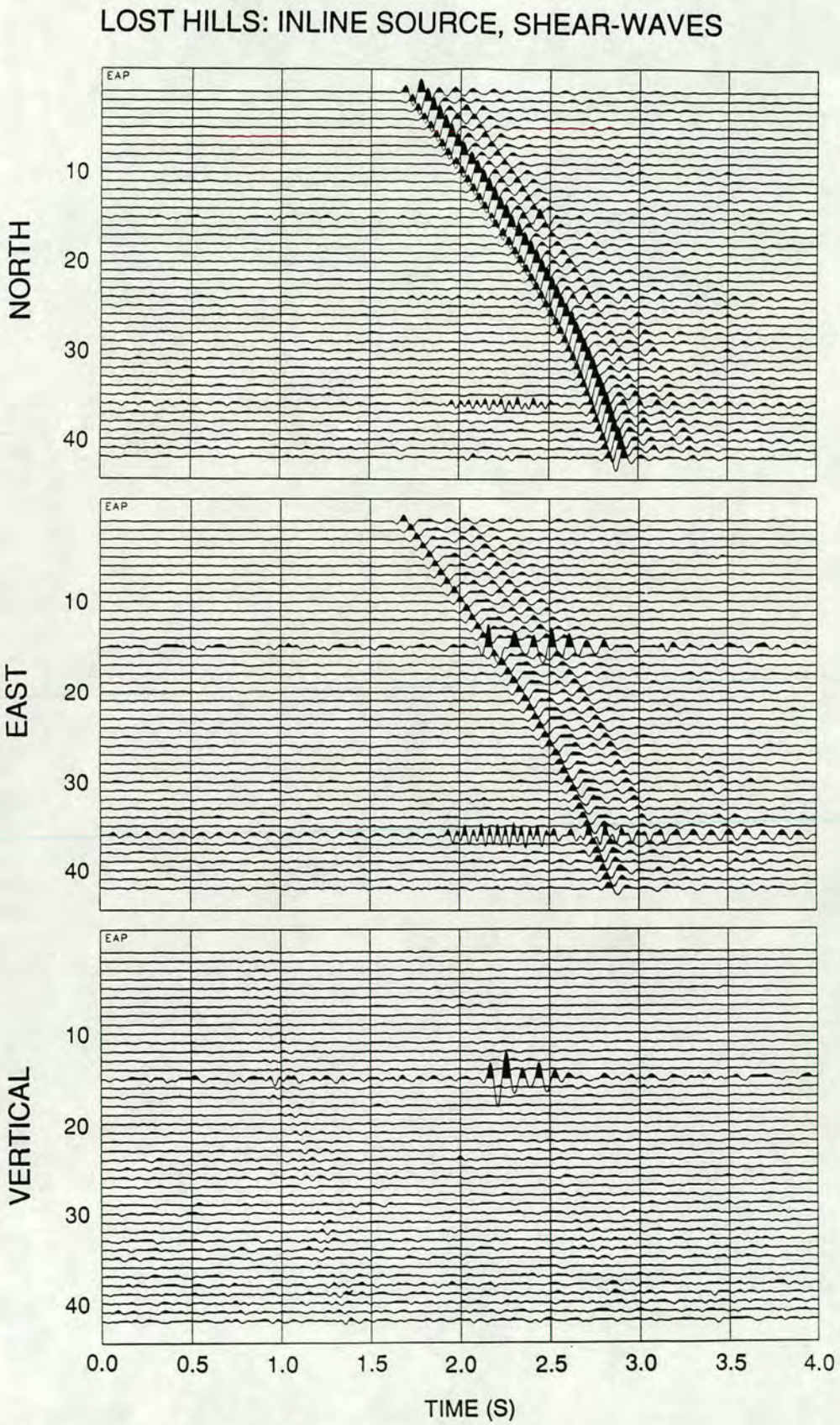

FIGURE 4.7: North, east, and vertical shear-wave sections from the inline source after left and right shots have been subtracted. The relative amplitudes of each component at a given geophone level are correct. Examination of the vertical component shows how well the compressional energy has been cancelled out. There is little change in arrival shape with depth and little upgoing energy.

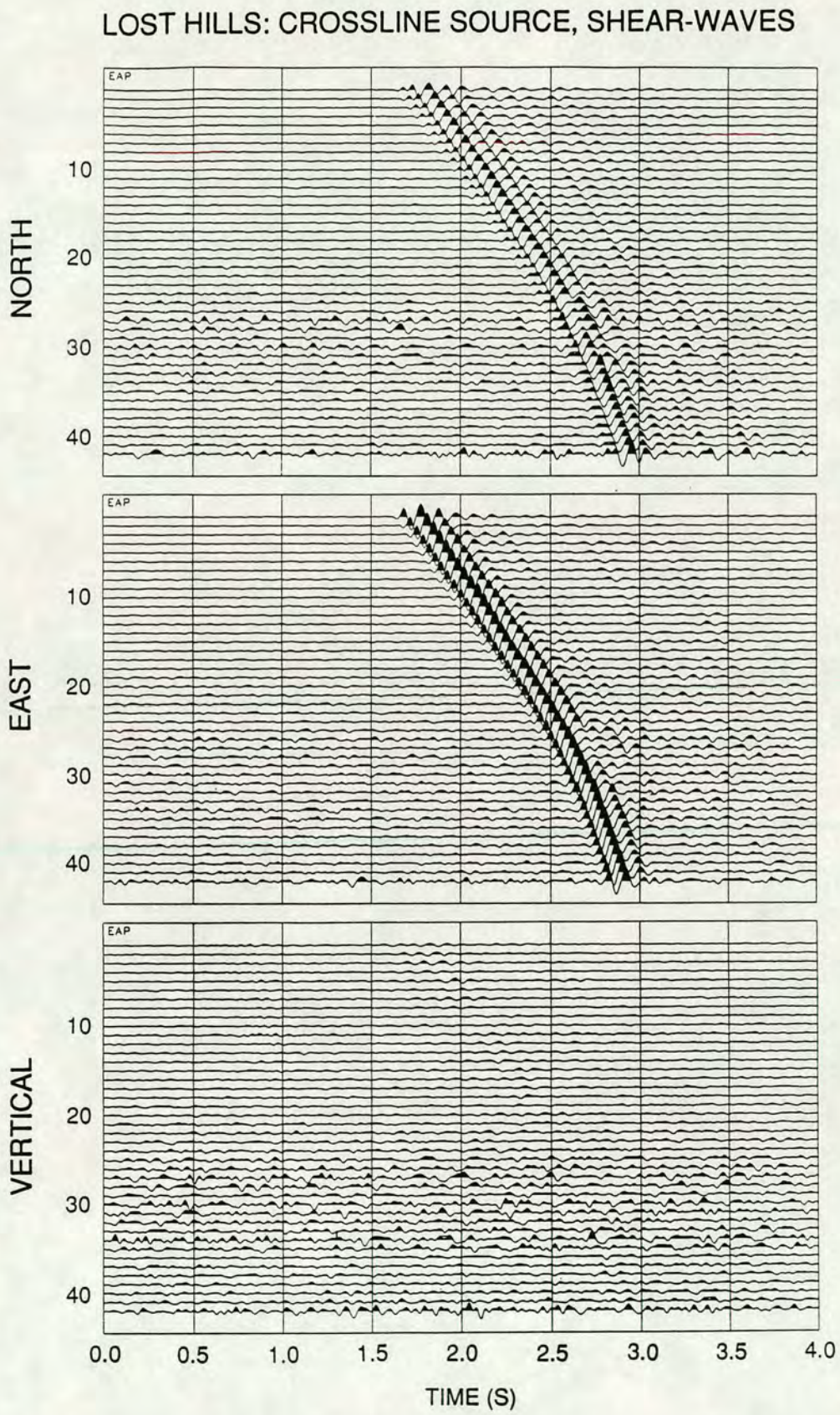

FIGURE 4.8: North, east, and vertical shear-wave sections from the crossline source, after subtraction. The relative amplitudes of each component at a given geophone level are correct.

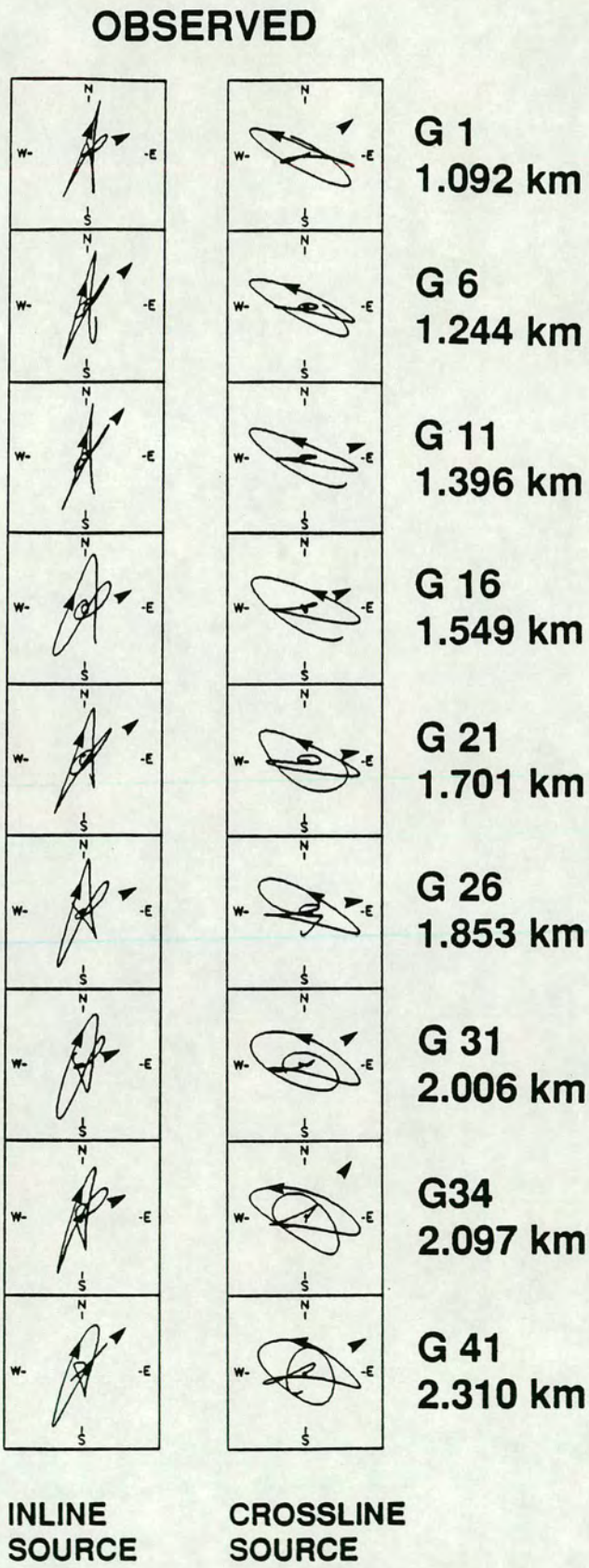

FIGURE 4.9: Selected horizontal plane polarization diagrams for a 300ms window about the downgoing shear-wave arrival after processing. The approximate polarization of the first arrival and direction of motion are marked with arrows. There is a gradual change in shape of the polarization diagrams with depth.

the horizontal plane.

The seismograms show that there are two close shear-wave arrivals (Figure 4.10); the first, which is linearly polarized, is a *P-S* conversion within the top 350m. The interface which gives rise to this *P-S* conversion is probably the same as that which gives rise to the multiple seen in the direct shear-wave sections (Figure 4.7). The second shear-wave arrival is the direct one. [Arrival times can be correlated to those of the shallowest geophone level in the main section (Figure 4.7) which is only 30m (100ft) deeper than the deepest geophone level in Figure 4.10.] Horizontal plane PDs for this arrival (Figure 4.10) are noisy. However, for the deeper arrivals, where the ray paths are close to vertical the shear-wave energy is directed towards the northeast, rather than N73°E (radial) as expected for a *P-SV* conversion in an isotropic medium. This may imply the presence of anisotropy in the near-surface; however, data quality is poor and no firm conclusions can be drawn.

4.5.4 Interval velocities and Vp/Vs ratio

The downgoing shear-wave and *P*-wave arrivals were timed using the GEOWELL package. Arrival times were inverted to give the interval velocities shown in Figure 4.11. Arrival times were also picked from the near-surface records; these are of poor quality and are scattered. The shear-wave arrival times are those for the *qS1* arrival (determined in Section 4.6.2) as this gives the isotropic matrix velocity (Section 2.5).

The shear-wave velocities vary smoothly with depth down to about 2km where there are sharper increases in velocity which correspond to the position of the zone of interest [Squires, Kim & Kim 1989]. Similar behaviour is seen in the *P*-wave velocities; however, they show a wider variation at depth. The calculated *Vp/Vs* ratio shows the same behaviour as found by Squires, Kim & Kim [1989] with a decrease in the zone of interest which may be an indicator of the presence of a reservoir in this field.

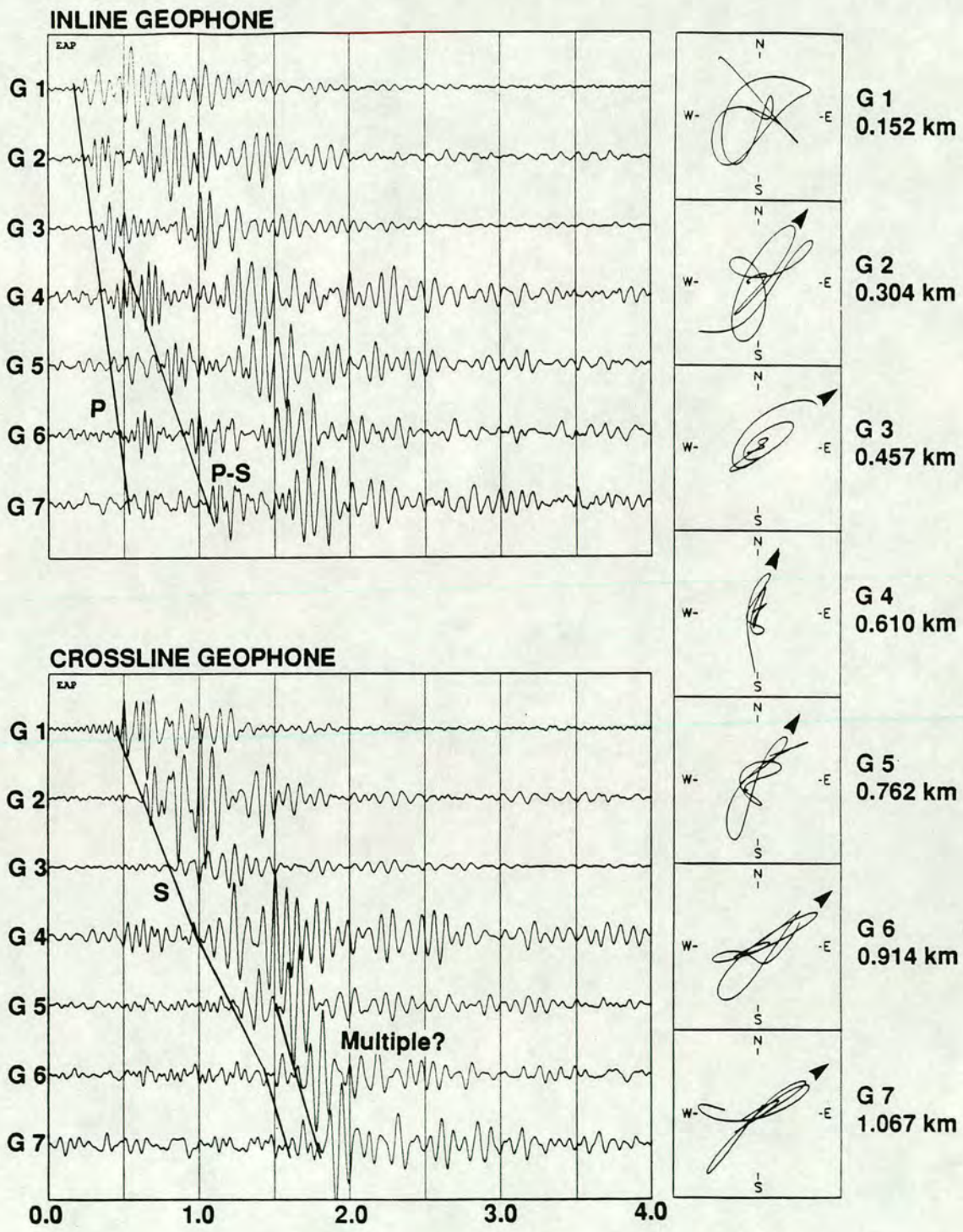

FIGURE 4.10: Horizontal component geophone recordings of the seven near-surface *P*-wave shots, band pass filtered between 5 and 30Hz to enhance the shear-wave arrival. I have marked on the *P*-wave and shear-wave arrivals on the sections on which they are most clearly visible. There is a large amplitude shear-wave arrival following the direct shear-wave arrival and this may be a multiple. The figure also shows horizontal PDs for a 220ms window about the direct shear-wave arrival with approximate first motions marked. The presence of mode conversions and multiples make picking first arrivals difficult. [The *P*-wave arrival for Geophone 4 is not linear, meaning that the rotation is poor for this level.]

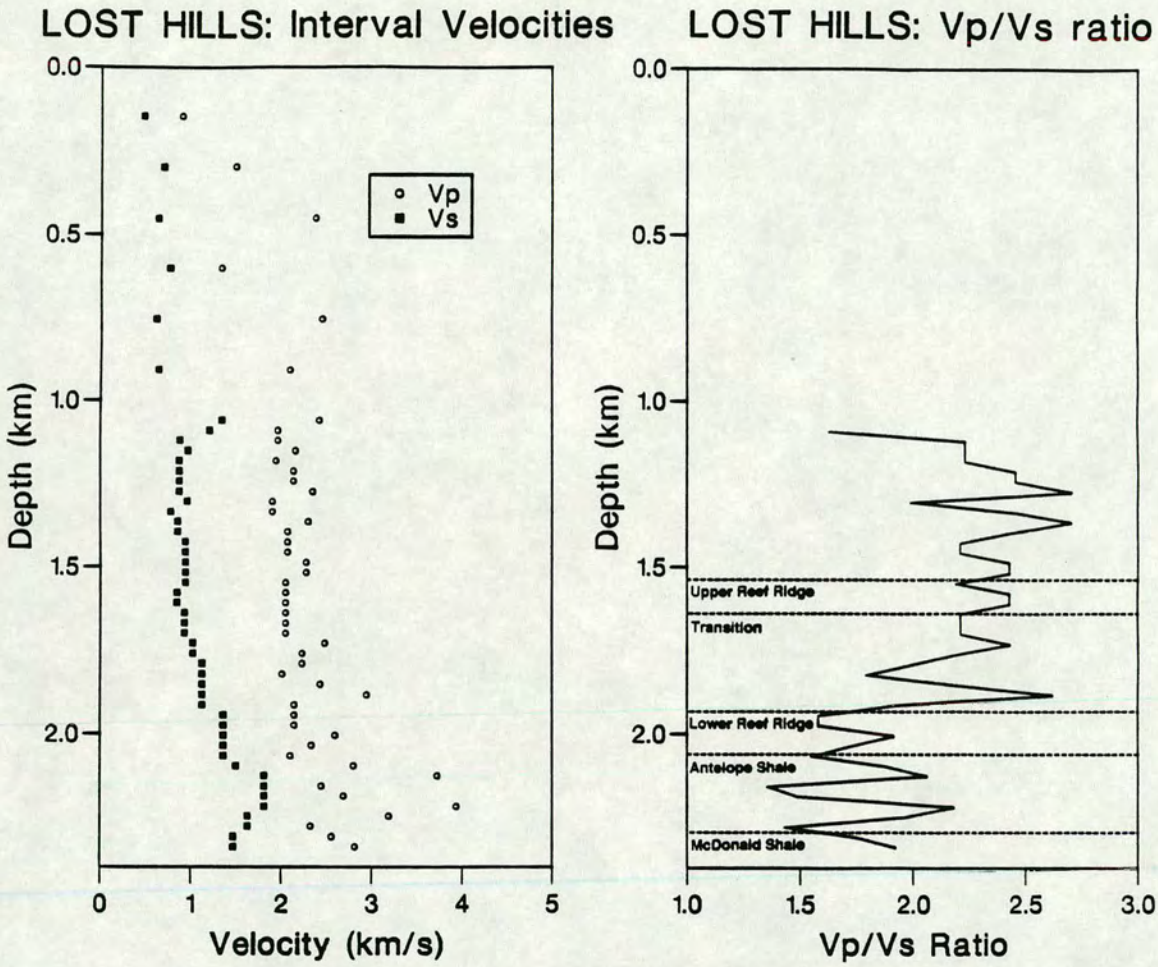

FIGURE 4.11: (a) Shear-wave and *P*-wave interval velocities between geophone levels. (b) *Vp/Vs* ratio showing a decrease in the zone of interest. Interfaces positions are those given by Squires, Kim & Kim [1989].

4.6 EXTRACTION OF ANISOTROPY PARAMETERS

It is difficult to determine the direction of first motion and time delays between split shear-waves by visual analysis of polarization diagrams. This can be seen by trying to pick first motions visually in Figure 4.9. Here, I apply the estimation techniques described in Section 2.7.

4.6.1 Direct time series technique (DTS)

I used the single source technique DTS as it is unaffected by differences in source strength between the two source orientations [Choi & Gangi [1991] suggested that source balancing errors caused scatter in their estimation of polarization and time delay for this data set].

The main shear-wave arrival contains multiple energy and I ran DTS over several window lengths to see if inclusion of multiple energy changed the estimates of time delay and polarization angle. The window start time was interactively picked just before the first break and seven window lengths from 0.15s to 0.45s were tested. Results were stable once the window contains most of the main arrival (>0.2s). [See Figure 4.14 for a similar analysis on AST.] The low amplitude multiples following the main arrival do not significantly affect the results. Figure 4.12 shows the results for a 0.26s window, which just encompasses the main downgoing arrival. The polarization angle for the inline source is approximately constant at N47°E. For the crossline source, the *qS1* polarization angle is N45°E in the upper section and falls to N41°E for the 11 deepest levels. The polarization angle is independent of source direction as expected for passage through an anisotropic medium.

The time delays for each source orientation show similar behaviour, with approximately 45ms of delay for the upper half of the section. The time delay then decreases to 38ms at the deepest levels. Choi & Gangi [1991] attributed the decrease in delay, which they detected using Alford's rotation [1986], as being due to the changes in source location. The positions where the source locations were changed are marked on Figure 4.12. The source position for the inline and crossline runs changes at different depths; however, the time delay behaviour is similar for each source orientation. In addition, geophone levels 1 to 16 and 34 to 42 for the inline source

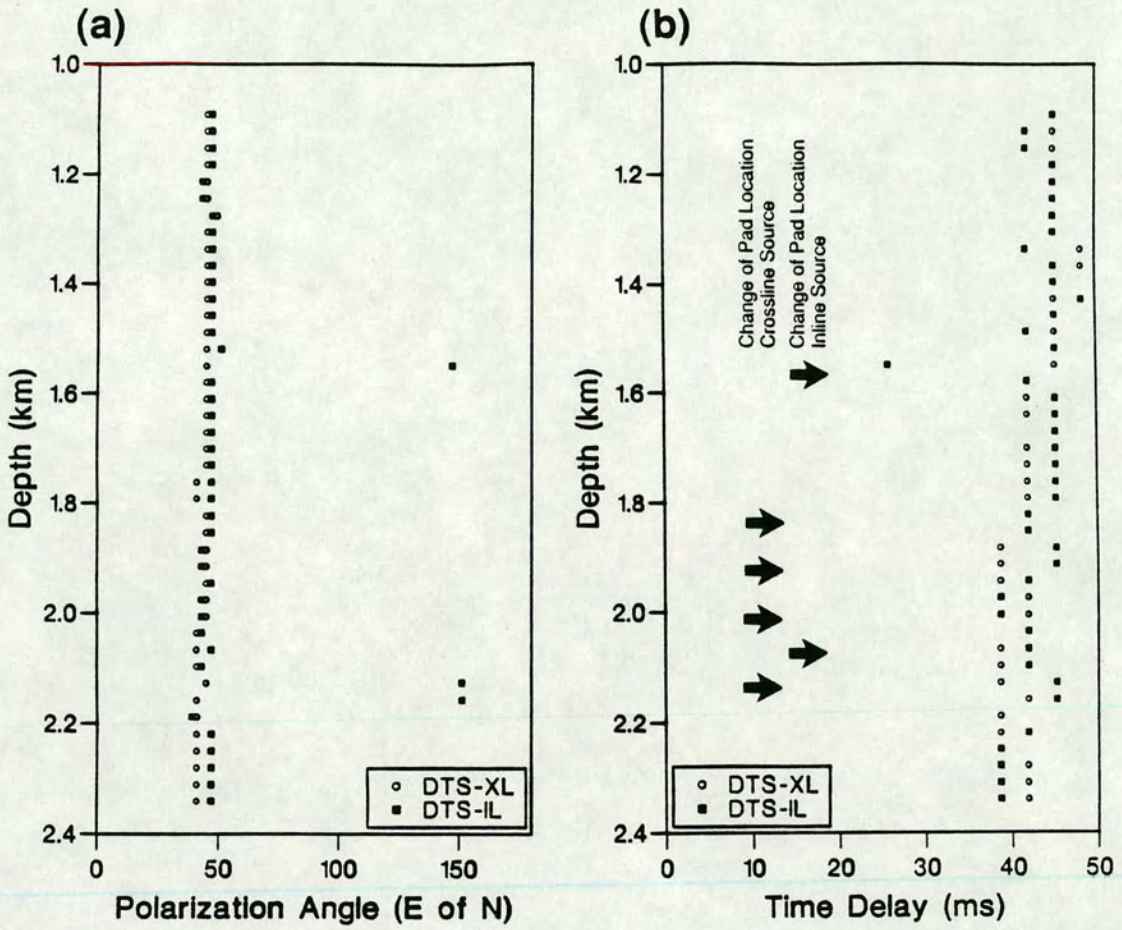

FIGURE 4.12: Estimates of polarization angle of the leading split shear-wave and time delay using DTS, applied in turn to the inline and crossline sources. The geophone levels at which the source pad was moved on each run are marked on the time delay plot.

were shot at the same source location and the decrease in time delay is still present. The decrease is therefore due to the properties of the rockmass along the ray path rather than changes in source location. To confirm this, seismograms for the anisotropic model developed in Section 4.7.2, were recalculated with different offsets for the inline (151m) and crossline (155m) source orientations. [In the field the source positions for the two runs were less than 4m apart, except for the 2.133km (7000ft) level.] The results for DTS on the synthetic seismograms were identical from both source positions, and are not shown here. For this geometry, lateral changes in source position of 4m do not affect the results of DTS. Modelling, of course, cannot take account of very local differences in near source structure.

I also used this model to examine the effect on the estimation techniques of the orthogonal sources not being aligned in the radial and transverse directions. When the estimation techniques are run on data from orthogonal sources which are out of the radial and transverse directions by less than ±2° the results are unaffected. Source misalignments greater than 2° do affect the results of the estimation techniques. I have no information to indicate that the sources were misaligned. If the misalignment of the orthogonal sources (or geophones) is by a known amount it is easy to correct this before using the estimation techniques by mathematical rotation of the data set. I use this here as I deliberately rotated the geophones into a northsouth-eastwest (rather than radial-transverse) coordinate system to make the PDs more readily interpretable.

I assume that the sources are exactly 90° apart. Errors in orientation of the two sources leading to nonorthogonal sources have been investigated by Zeng & MacBeth [1993a]. They show that small errors in the relative directions of the two sources (θ°) only give rise to small errors to the determined *qS1* polarization (θ°/2).

4.6.2 Double source rotation techniques (AST and AIT)

Ghose & Takahashi [1991] found that geophone response varies with tool orientation in the well and that mathematical rotation of the recorded data matrix, used in AST and AIT, is not valid. However, when DTS was applied to data from different runs of the sonde, results for the two runs are the same even when the tool has different in-hole orientations (Figures 4.12 and 4.13). For this data it appears that

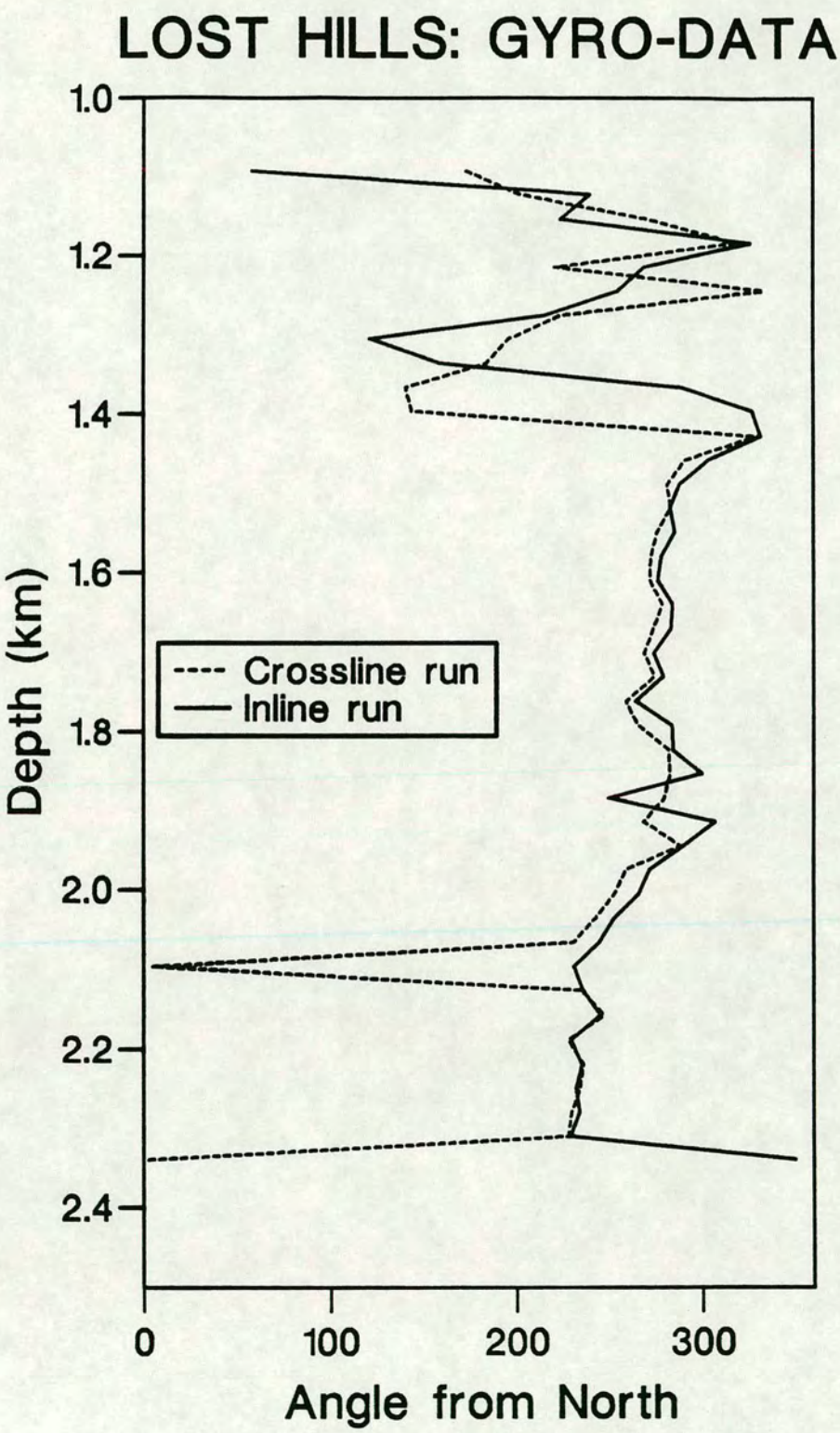

FIGURE 4.13: Direction of one component of the geophone tool, taken from gyroscopic data for successive runs of the tool. The tool orientation is remarkably consistent between the two runs, this could be due to a slightly oblique shape of the casing causing the sonde to have a preferential alignment as it is drawn up the well.

geophone response is not a function of tool orientation and rotation of the data matrix is valid. This is further confirmed by the consistent results of the estimation techniques with depth even though the tool position and orientation is different for each estimate.

The effect of window length on AST and AIT was investigated for windows from 0.15s to 0.6s. Results from AST for four windows are displayed in Figure 4.14. For windows that include most of the main shear-wave arrival, and longer, results are independent of window length. For this data set, inclusion of the multiples in the later part of the arrival does not affect the determination of time delay and polarization. AIT was similarly unaffected by window length.

Figure 4.15 shows results for both AIT and AST for a 300ms window. AST gives a constant polarization angle with depth of about N45°E, similar to that determined separately for each source by DTS. The source and geophone estimates from AIT oscillate about this direction. The oscillations are smooth variations with depth and are therefore not likely to be due to changes in source position or source balancing problems which would give rise to abrupt changes. Divergence in the source and geophone polarization estimates of AIT can indicate a change in crack orientation [MacBeth & Yardley 1992].

A decrease in time delay is seen, from 42ms for the upper 15 geophone levels to 38ms at the deepest levels. The similarity between single- (DTS) and double-source (AST) estimation techniques indicates that any difference in source strength does not affect the results of AST. Zeng & MacBeth [1993a] show large mismatches in source strength (>50%) are required to produce small (5°) changes in the estimates from AST and AIT, and this is confirmed in field examples in Chapter Five.

The four-component data matrix after AST is shown in Figure 4.16 with the position of the computation window (300ms) marked. The main diagonals contain most of the energy. The pulse shape changes slightly with depth. Some energy remains on the off-diagonal components. Although AST finds relatively constant values for time delay and polarization, these may be an artefact caused by assuming only two shear-wave are present (Section 3.6.2).

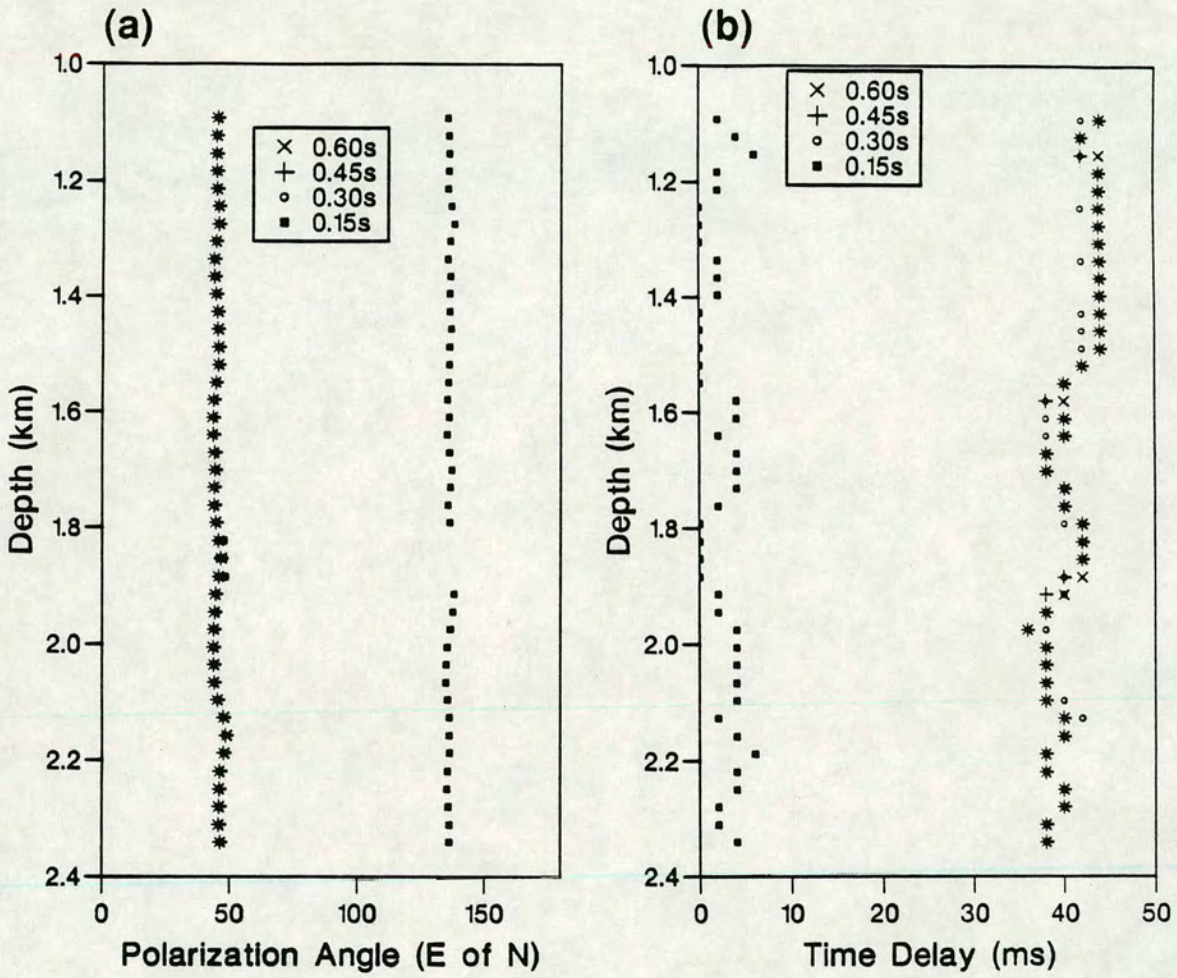

FIGURE 4.14: Estimates of polarization angle and time delay using AST for window lengths from 0.15s to 0.60s. The results are stable for all but the shortest window length.

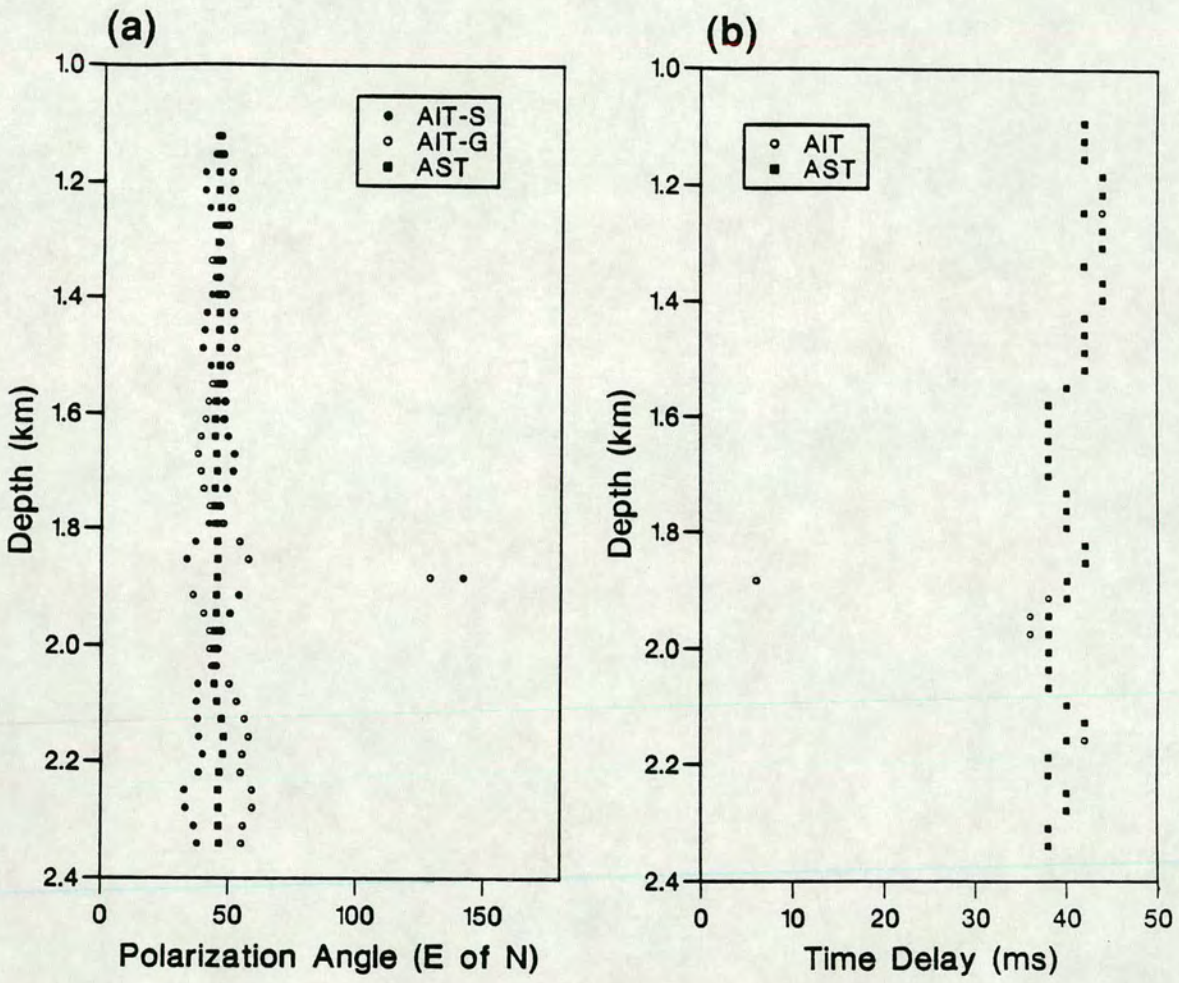

FIGURE 4.15: Estimates of polarization direction and time delay using both AST and AIT for a 0.3s window. The source and geophone polarization directions determined by AIT oscillate around that found by AST. Both techniques show a slight decrease in time delay with depth.

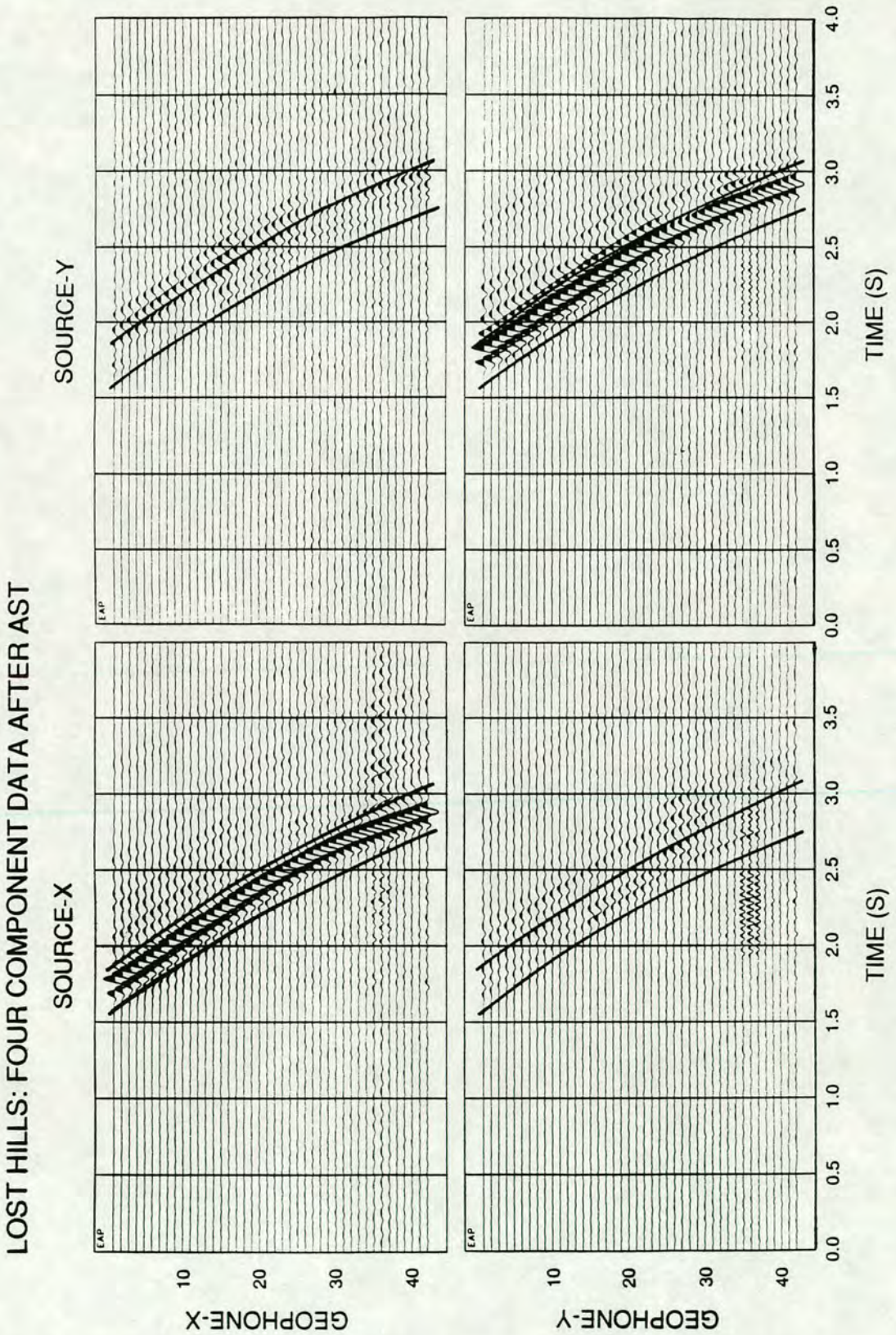

FIGURE 4.16: Four-component data matrix for the Lost Hills data after AST. The approximate position of the window over which the polarization direction was determined is marked. Some energy remains on the off-diagonal sections.

4.6.3 Propagator matrix techniques

The presence of energy on the off-diagonal components after AST indicates a change in medium polarization direction with depth and I now apply techniques which can cope with such changes. DPM (Section 2.7) was run on this data set; however, the results were very scattered and are not shown. This may be due to the different position of the source for the inline and crossline runs. I also applied a single source version of DPM (SPM) [Zeng & MacBeth 1993b] as this is not affected by the different position of the source on the two runs.

SPM was run over a range of geophone intervals from one interval (30m) to 10 intervals (300m). The results were scattered for short calculation intervals as the waveform only changes slowly with depth. Results were also scattered for large intervals as the assumption that the rays to the top and bottom of the range travel the same ray path, apart from between the geophones, does not hold for this 155m offset VSP. Figure 4.17 shows the results of SPM calculated over 6 geophone levels for a 0.7s window. This window includes the main arrival and the multiple energy (Section 2.7). The *qS1* direction for the inline source is N58°±6°E and N59°±5°E for the crossline source. The lateral changes in the source position have little affect on this single source technique.

4.6.4 Layer stripping

The depth at which any multiple splitting occurs is not known. The source and geophone estimates diverge at the top geophone and a change in medium polarization could occur at this level. I now apply layer stripping (see Section 3.6.1) at this level.

Layer stripping is highly sensitive to: errors in source positions [Winterstein & Meadows 1991a]; the parameters used for layer stripping; and the depth at which stripping is initiated [C.Macbeth, personal communication]. I therefore applied layer stripping to each of the top three geophones for a range of anisotropy parameters.

Both AST and AIT give polarization angles of N45°E, giving no freedom to alter this parameter. There is more scatter in the time delay estimates, also the amount of time delay needed for the layer stripping may alter with depth as the incidence angle changes. I used a range of time delays from 32ms up to 50ms in steps of 1ms, and

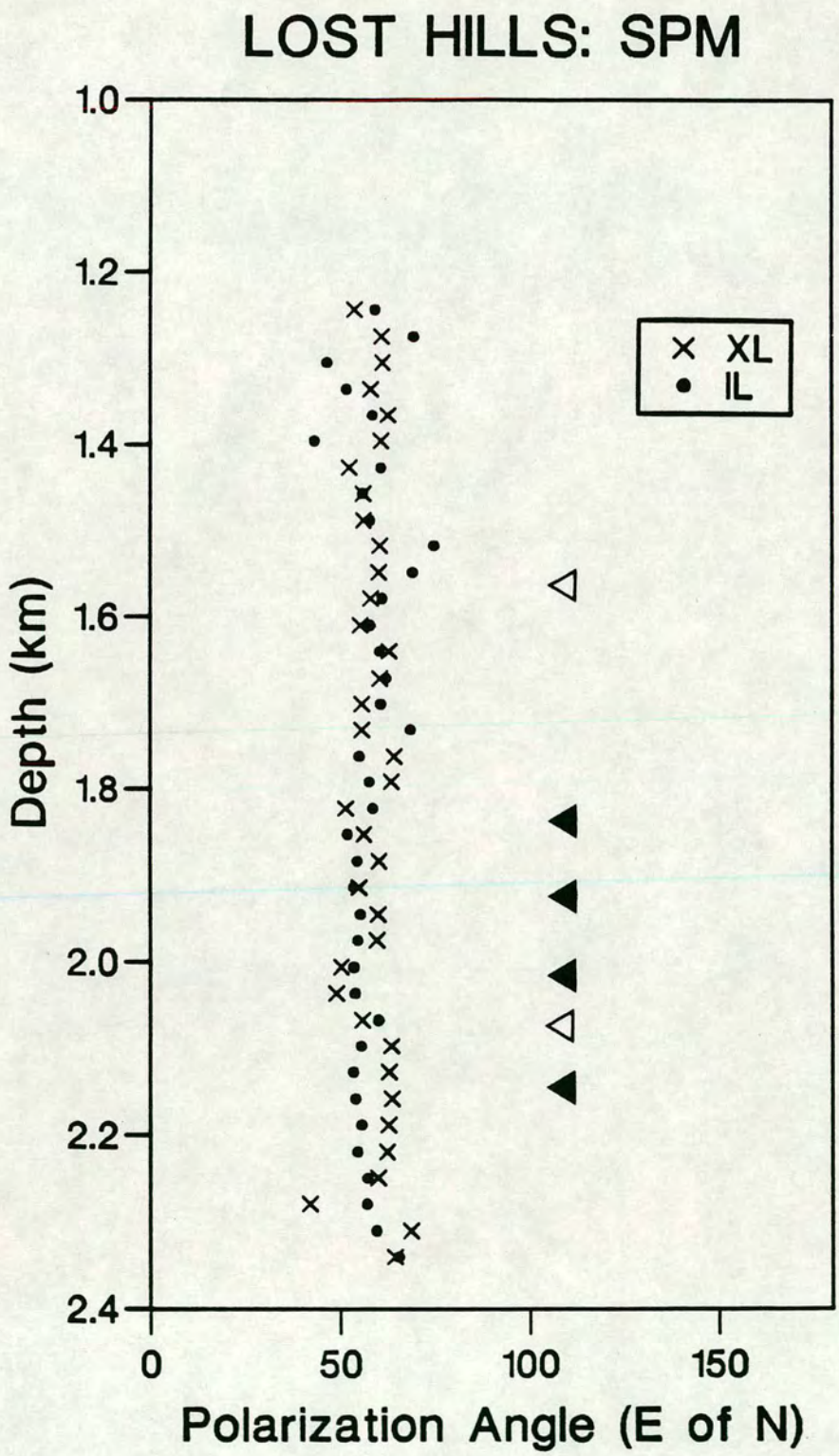

FIGURE 4.17: Results of a single source propagator matrix technique (SPM) applied to both inline and crossline sources. The results are N58°±6°E and N59°±5°E for the inline and crossline sources respectively. The open triangles mark changes in source location on the inline run and the closed triangles mark changes in source location on the crossline run. [SPM is a single source version of DPM: Table 2.1, Section 2.7.]

steps of 0.2ms around 42ms. For layer stripping to be successful the source and geophone estimates of AIT should be coincident after layer stripping; however, this occurred for all chosen time delays. Sample results of AIT after layer stripping are shown Figure 4.18. The source and geophone estimates are coincident; however, the polarization angle is not constant with depth. Further changes in medium polarization within the section should be identified by a second divergence in the source and geophone estimates of AIT. However, there is no obvious level to apply a second layer stripping operator.

Applying the original layer stripping operator at deeper levels is not valid as the source and geophone AIT estimates are not coincident. As layer stripping was not successful at the top of this section it may mean that the medium polarization changes above the VSP section. [Off-diagonal energy for the shallowest levels after AST suggests that it does.] Layer stripping should be applied at shallower levels, but the absence of data from the top 1.1km of the well prevents this.

4.6.5 Note on Yardley & Crampin 1990

Yardley & Crampin [1990] give a result of N55°E for the fast direction as determined using DTS on this data set. The source directions used in that calculation were north and east as given in the observers' logs; however, the true source directions are N17°W (crossline) and N73°E (inline) [S.Squires, personal communication]. This caused Yardley & Crampin [1990] to produce polarization estimates 10° clockwise of the value presented here.

4.6.6 Discussion of results

DTS, AST and AIT give estimates of 42ms and N45°E for the time delay and *qS1* polarization. This magnitude of time delay is similar to that seen in other data from California, by Winterstein & Meadows [1991b] and by myself (using data owned by the Japan National Oil Corporation) in VSP data from central California. In both cases the time delay is built up in the top few hundred metres. The polarization results are relatively consistent with the first motions seen in the observed shear-wave arrivals and indicate that the *qS1* polarization direction is in the NE quadrant. There is no

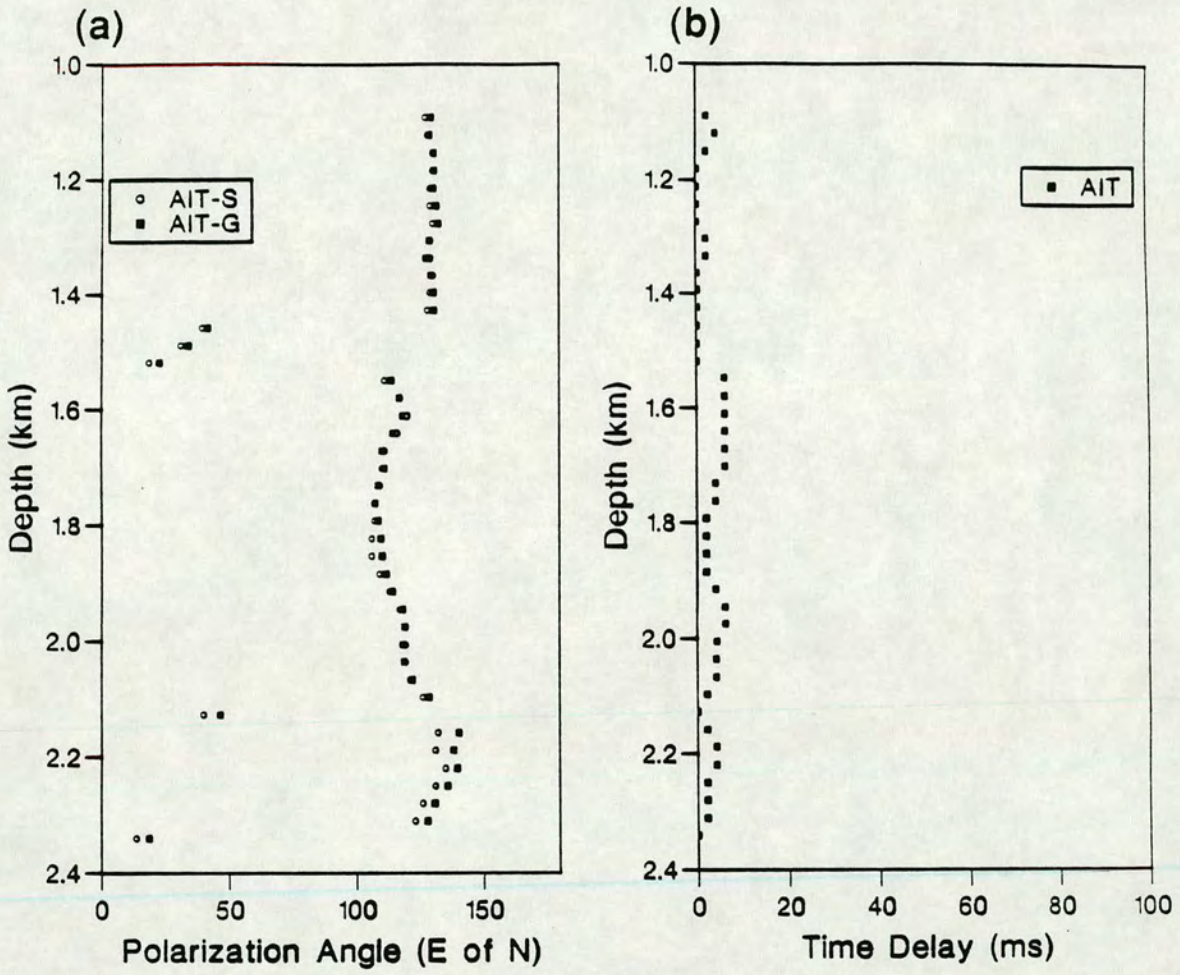

FIGURE 4.18: Results of AIT applied after the data have been layer stripped. The parameters used in the layer stripping were N45°E and 42ms. The source and geophone estimates from AIT have closed up. The determined polarization angles are not constant with depth.

indication of a further build up in time delay in the reservoir region.

The oscillation of the source and geophone estimates for AIT, together with the presence of off-diagonal energy after AST, implies that multiple splitting has occurred. This conclusion is further supported by the decrease in time delay which can be caused by changes in crack orientation with depth [Winterstein & Meadows 1990a; Yardley & Crampin 1990; Section 3.6.2]. Layer stripping at the top of the VSP section is not successful and implies that any change in medium polarization occurs above 1.1km. SPM gives polarization directions around N58°E which is consistent with hydraulically-induced fracture directions in this field [Winterstein & Meadows 1991a].

If multiple splitting has occurred, then the AST results are invalid as the data matrix is not symmetrical. To test this I extracted the 'fast' pulse from the inline and crossline source directions by rotation of the horizontal geophone components by the angle determined using AST. If the AST results are valid the pulses should have the same shape; however, they are slightly different (Figure 4.19).

The results indicate that the polarization direction of the medium changes above the geophone section, but there is considerable non-uniqueness in the interpretation. In Section 4.7.2, I outline two probable structures which I then model to determine which is the most likely.

4.7 MODELLING

The lack of data coverage at this site means that only approximate models can be developed. I now use ANISEIS to develop velocity models which explain the features seen in the observations and the results of the estimation techniques. ANISEIS can only model horizontally layered structures. The upper structure is horizontal (down to 800m, Figure 4.2), below this layers dip more steeply until they dip at 42° (below 1.5km). Borehole information shows that the geological and seismic interfaces are the same [Squires, Kim & Kim 1989]. However, the lack of substantial upgoing energy and the lack of abrupt changes in the shear-wave signal show that the geological interfaces are seismically weak and do not distort the shear-wave signal (see Section 4.7.1). Horizontal gravity profiles and velocity modelling show that density and velocity are laterally invariant. As the interfaces are seismically weak, the effects of

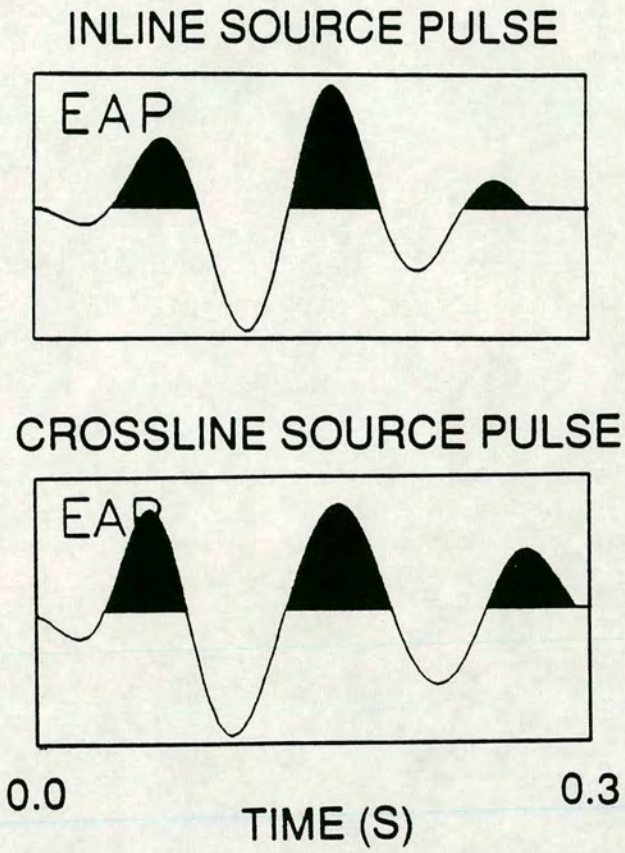

FIGURE 4.19: Pulse shapes along the fast shear-wave direction obtained from the signal recorded from the inline source and the crossline source at the shallowest geophone. The rotation to extract the signal was based on the results of AST at this geophone level. There are slight differences in pulse shape.

dipping layers and shales can be modelled by the inclusion of dipping PTL-anisotropy.

4.7.1 Isotropic velocity model

I developed an isotropic model to match arrival times for the full depth range before introducing anisotropy. The velocity structure was based on the interval velocities shown in Figure 4.11. An iterative method was then used to calculate the velocities for the model layers [Pujol, Burridge & Smithson 1985; coded by D.Campden]. The layer boundaries in the deeper structure are the boundaries of the geological units [Squires, Kim & Kim 1989]. The velocities in the top 1.1km are poorly constrained (due to the near-surface data quality) and I divided this section into two layers. [No logs were available and the seismic data are insufficient to create a more complex model.] The isotropic structure is shown in Figure 4.20 along with ray tracing through the structure. Arrival times between modelled and observed data are compared in Figure 4.21: the match is good. The real data set is the *qS1* section taken from the inline source determined by AST. As only approximate models are sought here, it is sufficient to use densities calculated from *P*-wave velocities as described by Gardner, Gardner & Gregory [1974]. Model parameters are shown in Table 4.1. Multiples are suppressed in all models.

Pulse shapes for modelling

To model shear-wave particle motions it is necessary to know the source signature. I contacted the Bolt Technology Corporation and MIT (who, along with Marathon Oil, carried out some of the testing of the OMNIPULSE source), but they were unable to supply a sample source signature in a digitized form to help with modelling. I hoped that a reference pulse could be compared with the observed one, so that differences could be attributed to the anisotropic above the shallowest geophone. However, the source signature is dependent on ground coupling and near-surface structure at the site and a reference pulse supplied from another site may not be useful. I used the *qS1* arrival from Geophone Level 1 (determined by AST) as the pulse in the models as this will be a good approximation to the true pulse.

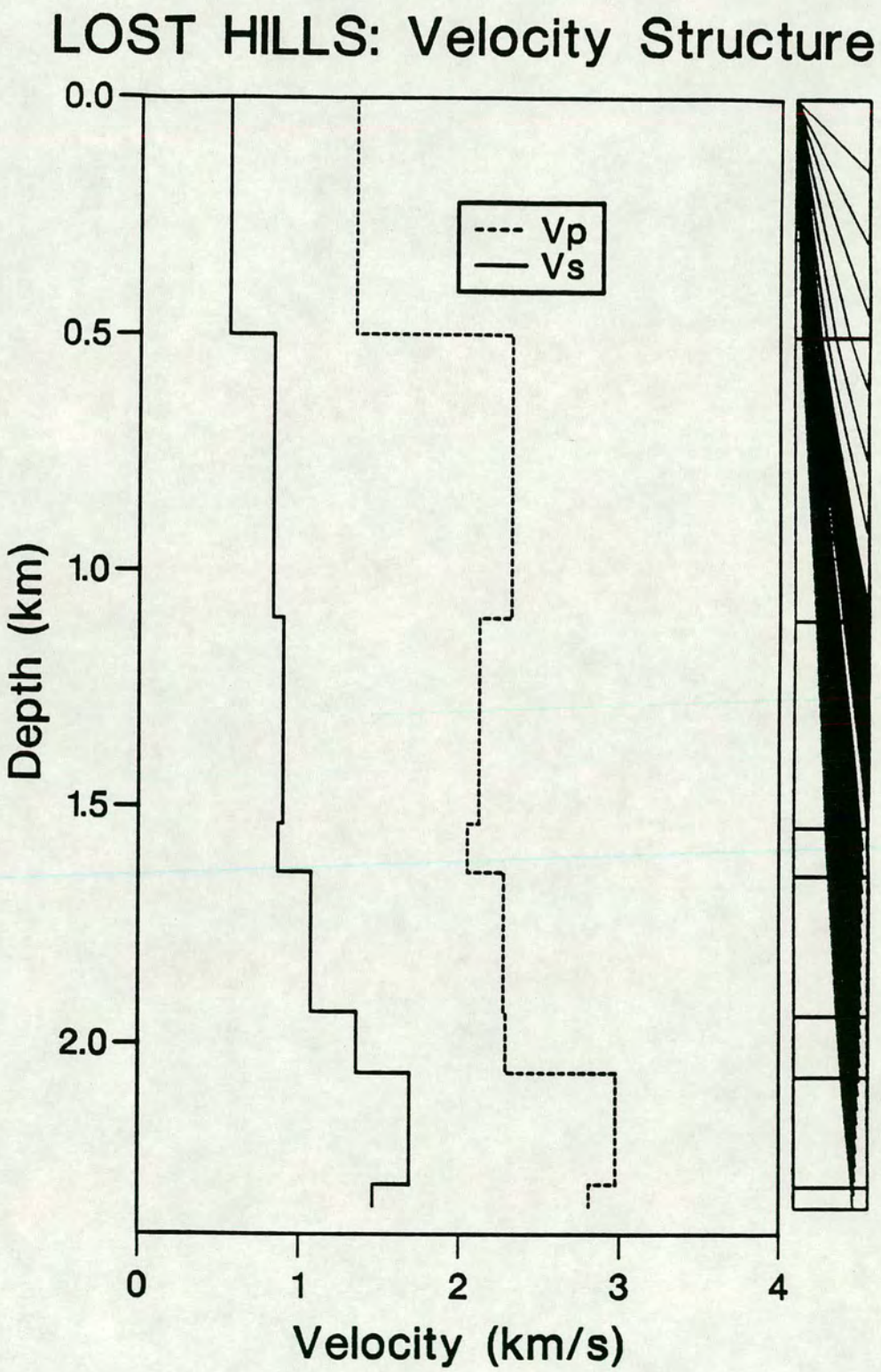

FIGURE 4.20: Isotropic *P*-wave and shear-wave velocity structure inverted from arrival times, together with results of ray tracing through the structure.

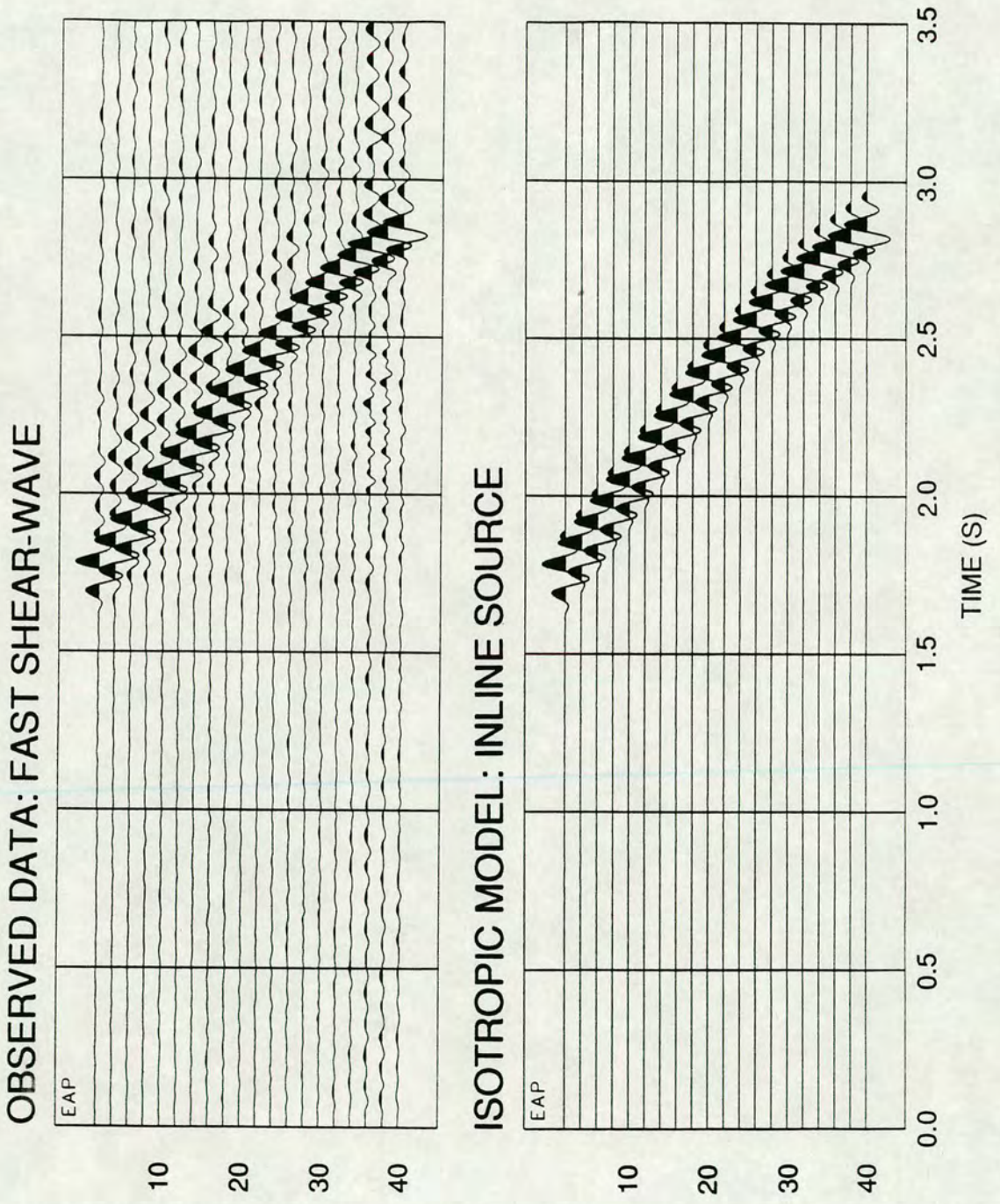

FIGURE 4.21: Comparison of synthetic and modelled seismograms between the observed fast shear-wave and the isotropic model for every second geophone down to geophone 40. A good match of arrival times has been achieved.

TABLE 4.1: Model structure for the Lost Hills VSP.

	Thickness (km)	Density (g/cm^3)	*Vp* (km/s)	*Vs* (km/s)
Layer 1	0.500	1.95	1.344	0.5564
Layer 2	0.600	2.15	2.320	0.835
Layer 3	0.436	2.10	2.121	0.899
Layer 4	0.102	2.09	2.050	0.866
Layer 5	0.294	2.14	2.276	1.074
Layer 6	0.128	2.14	2.290	1.358
Layer 7	0.234	2.29	2.979	1.689
Layer 8	Halfspace	2.26	2.811	1.464

Apparent anisotropy caused by internal shear-wave windows

It is not appropriate to use ANISEIS to model this structure if the dipping interfaces (up to 42°) give rise to apparent splitting due to the effects of internal shear-wave windows (see Section 3.3). I can get a rough idea of the effects of transmission across the geological interfaces in the Lost Hills by calculating the *SV* and *SH* transmission coefficients for my Lost Hills model (Table 4.1). [These effects are likely to be overestimates as such large sections have been blocked together.] Velocity contrasts, below 800m where the interfaces dip, are small. *SV* and *SH* transmission coefficients diverge only for incidence angles greater than 50°. This further confirms that it is valid to use ANISEIS to generate a 1-D model of this structure.

4.7.2 Anisotropic models

I now develop a range of anisotropic models to account for the observed features of the data and the results of the estimation techniques. I contacted Mobil to see if they could supply borehole data on fracture directions in this well, to help constrain the modelling, but they were unable to track down the required information.

What causes the anisotropy?

Up to this point I have interpreted the *qS1* directions in terms of the polarization direction of the medium. Before modelling I must decide what type of anisotropy to add to my model. Part of the structure consists of shales, which can give rise to thin layer anisotropy [Kaarsberg 1968]. The observed time delay is built up above the top geophone where the structure is horizontal. Horizontal thin layer anisotropy does not cause splitting for vertically travelling waves (Section 2.4). As some layers are known to be fractured [Squires, Kim & Kim 1989] I will start modelling by using Hudson cracks. It is possible that any cracks or fractures dip; however, this VSP does not give a sufficient range of incidence angles and azimuths through the structure to investigate dipping crack structures. The *qS1* polarization direction is parallel to the crack strike for a wide range of crack dips (Section 2.4) and changes in *qS1* polarization (along a single ray path) due to changes in crack dip can be modelled by changes in crack strike. Therefore, I will use vertical cracks in all my models.

Fractures open parallel to the maximum principal compressive stress with their normals parallel to the minimum principal stress. Here the *qS1* polarization (and known fracture orientation) is parallel to the regional maximum compressive stress. In sedimentary sequences the minimum compressive stress is typically horizontal [Breckels & Van Eekelen 1982], therefore fractures will form in the vertical plane parallel normal to the San Andreas fault. Anisotropy may also be caused by pore-space and micro-cracks in the rockmass aligned by the stress field. This is called *extensive-dilatancy anisotropy* (EDA) [Crampin, Evans & Atkinson 1984]. However, the exact nature of the azimuthal anisotropy does not affect the modelling as the crack parameters specified in ANISEIS only generate an equivalent medium.

The estimation techniques indicate that the polarization direction of the medium changes with depth. Fracture alignment, the probable cause of anisotropy, is stress controlled (as is EDA). Warpinski & Teufel [1991] find that stress can change locally as a result of geology and structure. Changes in the dip of the structure (at around 800m) may, therefore, be the cause of the change in polarization direction with depth.

Outline of structures to be modelled

I now outline two likely structures, based on the available information, to account for the features of the estimation techniques.

Case 1. The decrease in time delay is a result of a 90° change in crack orientation, similar to those found by Squires, Kim & Kim [1989]. This model means that I have to ignore the SPM results. As SPM is difficult to check and there are no other data from this well to suggest a N58°E fracture orientation it is possible to do this. Also Squires, Kim & Kim [1989] report N45°E fractures in this area consistent with the dominant direction determined by AST. The *qS1* direction is invariant with depth, even though the sagittal plane is not constant, implying crack anisotropy. [The *qS1* polarization in PTL media is dependent on the orientation of the sagittal plane with respect to the medium (Section 2.4).] The off-diagonal energy after AST is difficult to explain but may be produced as a result of different inline and crossline source signatures. The same source truck was used in each case, but at slightly different locations and local coupling effects may change the source characteristics.

Case 2. The off-diagonal energy is a result of multiple splitting (Section 3.6.2) somewhere in the top 1.1km of the structure and is caused by a change in crack strike (not 90°). This is also suggested by the failure of layer stripping within the section. The crack strike at depth is N58°E as determined by SPM. These results are consistent with those of Winterstein & Meadows [1991a]. The decrease in time delay and consistent polarizations with depth are a product of AST being applied to multiply split shear-waves as seen in Figure 3.11.

4.7.3 Modelling: Case 1: 90° changes in crack strike

Squires, Kim & Kim [1989] suggested that there are 90° changes in fracture strike at this location and I now model this case. Cracks were introduced into the isotropic model (Table 4.1) so that the delays and polarizations seen in the anisotropy estimation techniques were matched. This meant using a crack density of 0.0283 in the top 1.1km with a strike of N45°E, and 0.0059 below this with a strike of N135°E, to match the decrease in delay. I put the change in crack strike (which causes the reduction in time delays) at 1.1km as I have no information about the upper structure; it may occur at shallower depths. This does not lead to any multiple split shear-waves as the two crack orientations are exactly 90° apart. Water-filled cracks with an aspect ratio of 0.01 were used. The source offset is 155m and 20 geophones at 61m (200ft) spacing were placed in the model from 1.092km (3600ft).

Figure 4.22 shows the results of AST and AIT from this model: firstly with the same pulse shape used for the inline and crossline sources (Figure 4.22a and 4.22b); and secondly with different pulse shapes for the inline and crossline sources (Figure 4.22c and 4.22d). The polarization angle and time delay seen in the real data has been reproduced (except for the oscillations in the source and geophone estimates for AIT) when the same pulse shape is used for both source directions.

I also used different pulse shapes for each source orientation to see if this would lead to energy on the off-diagonal components after AST. The pulse shapes are shown in Figure 4.19 and are from the top geophone level of the observed inline and crossline shear-wave data after rotation based on the results of AST. The results also match the field data, except that the source and geophone estimates from AIT have

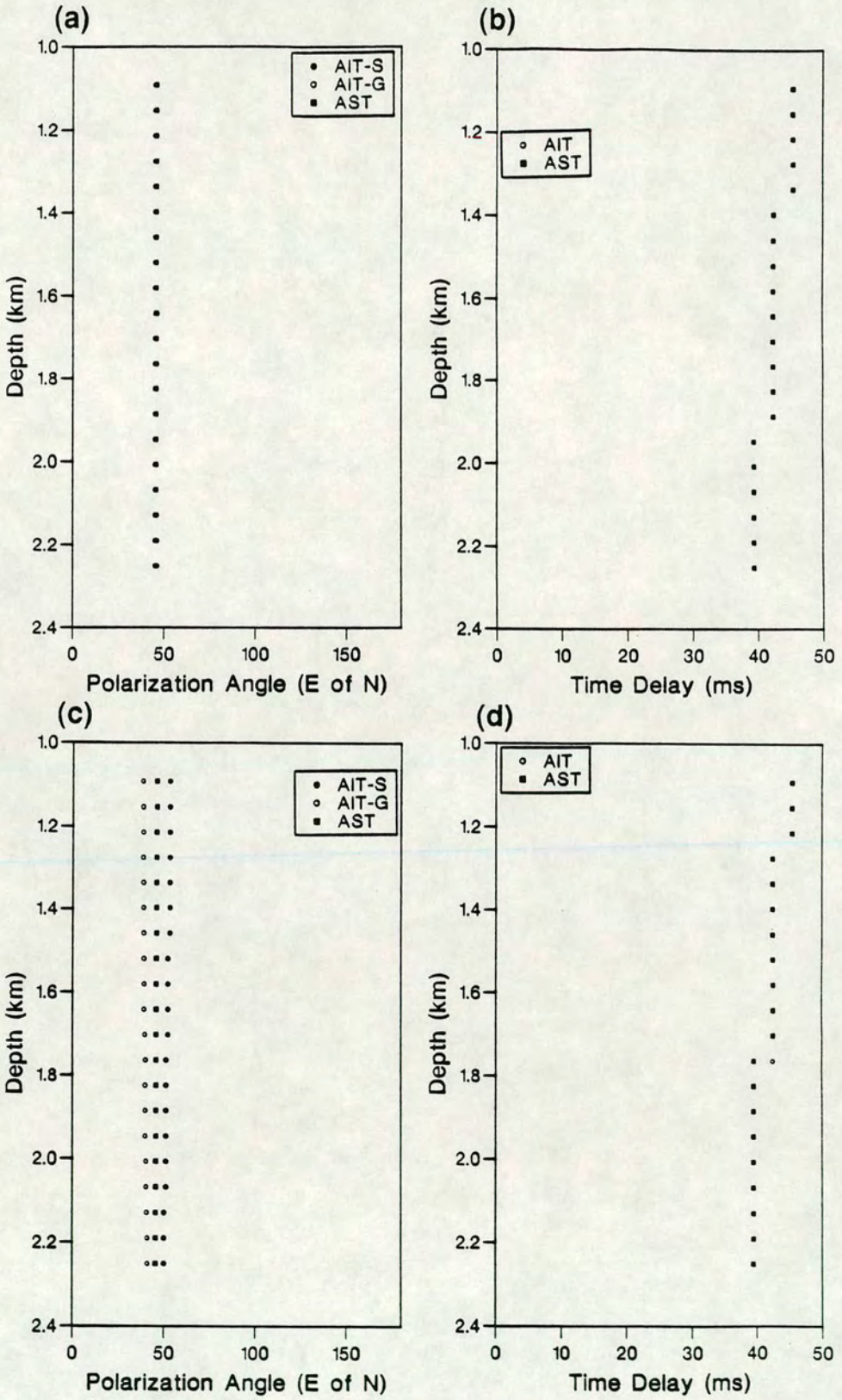

FIGURE 4.22: Results of AST and AIT applied to data from a 155m offset synthetic VSP with crack direction of N45°E in the top 1.1km and N135°E in the remainder. Models were first calculated with the same pulse shape used for the inline and crossline sources ((a) and (b)), then with different pulse shapes for the inline and crossline sources ((c) and (d)). See text for anisotropic parameters.

pulled apart. The fact that AST produces the same result from the two different pulses means that the changes in pulse shape (of the magnitude used here) does not lead to significant off-diagonal energy after AST. I have no justification for using pulses which are more dissimilar than those used here, which were extracted from the field data.

DTS was also run on both these data sets, but, as it works independently on each source direction, changes in pulse shape did not affect it.

Modelling of the deviated VSP

I now do further modelling of Case 1, taking into account that the well was deviated. The basic model is as above; however, the geophones are now positioned exactly as in the field, with a slight decrease in offset with depth and a swing in the sagittal plane orientation with depth by 12°. To do this I ran six models, each with a different crack strike relative to the model sagittal plane. Seismograms from these models were rotated and combined to give the complete VSP data set.

As in the above modelling, different pulse shapes were used for the inline and crossline sources. [These were extracted from the field data and are shown in Figure 4.19.] The match between modelled and observed PDs (Figure 4.23) is very good for the shallower geophones. The quality of the match decreases with depth. This may be due to changes in pulse shape during the experiment as the ground beneath the source becomes damaged. However, the match will also decrease if field data have undergone multiple splitting.

The results of the estimation techniques on these modelled data are shown in Figure 4.24. The polarization estimates are constant even with a change in crack orientation with respect to the sagittal plane. Estimates agree well with the observed results except for the source and geophone estimates of AIT which do not oscillate here.

Dipping PTL-anisotropy at depth

Dipping shales are known to be present and I checked to see if their presence can produce a 90° change in the *qS1* polarization direction. Figure 4.25 shows some

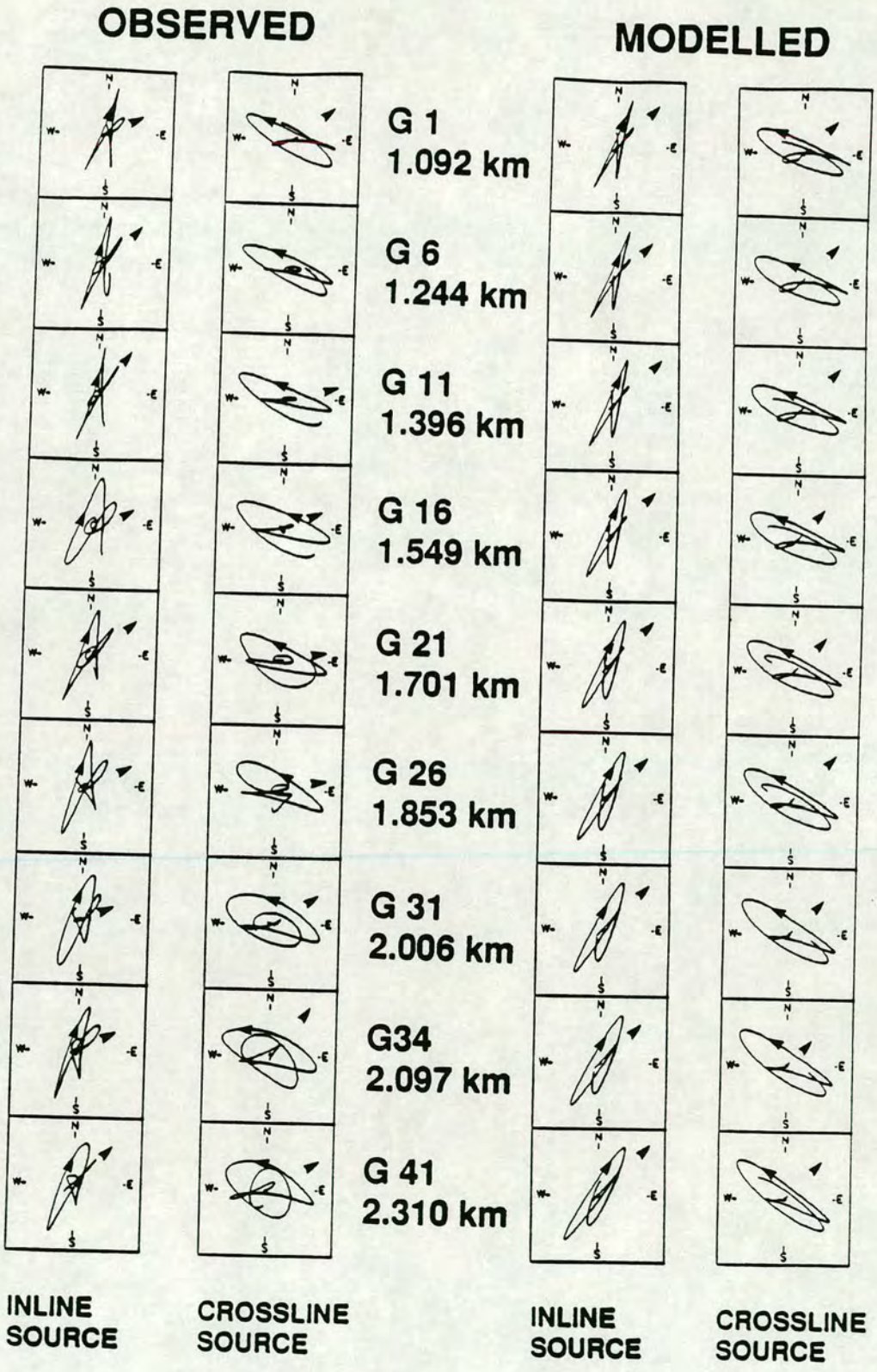

FIGURE 4.23: Observed and modelled horizontal plane polarization diagrams for the model with a deviated well in a structure where the crack strike changes by 90°. A good match has been achieved for the upper geophone levels; however, the match is less good at depth.

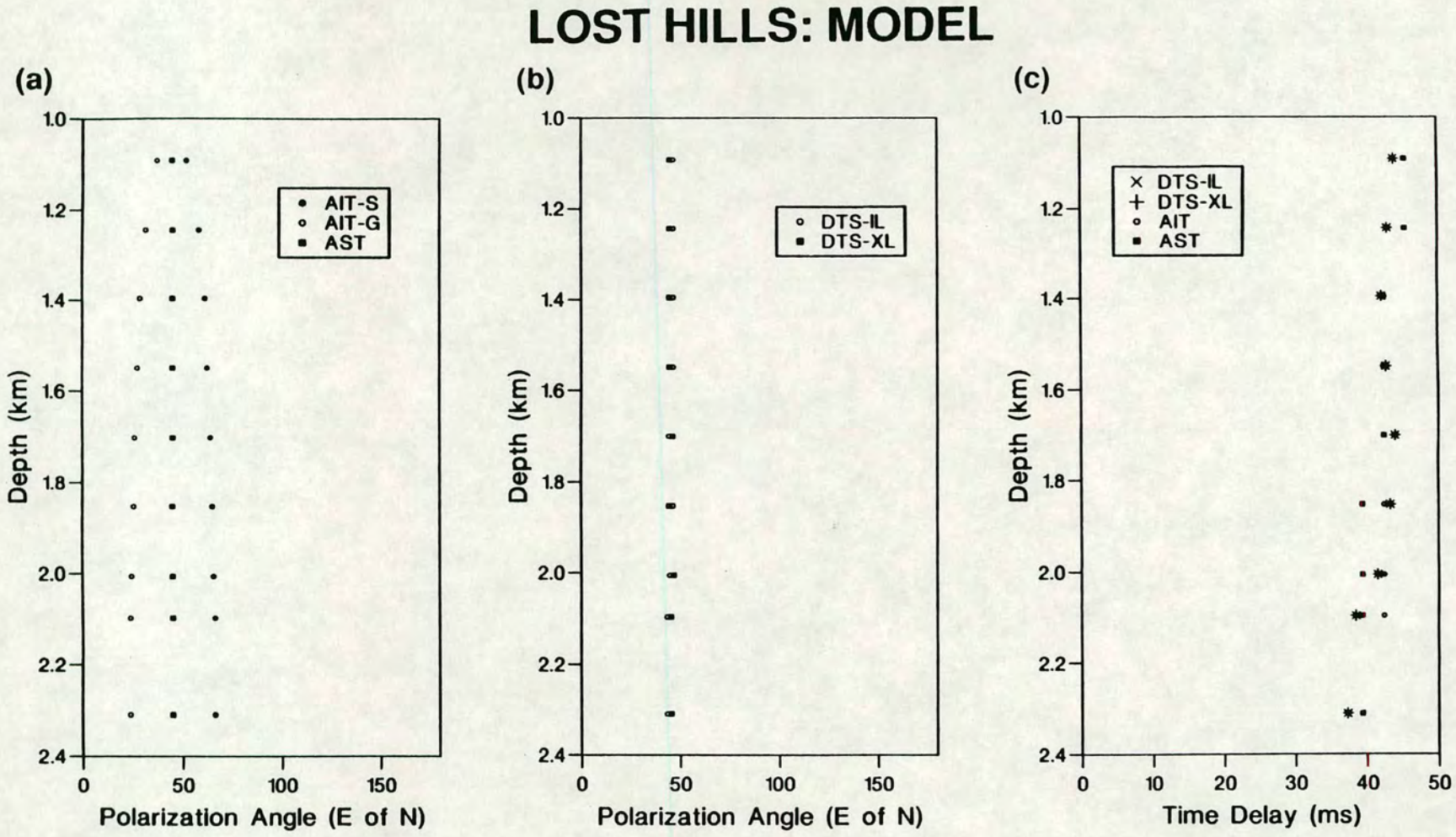

FIGURE 4.24: Results of the anisotropy estimation techniques on the modelled data shown in Figure 4.23. The decrease in time delay and the behaviour of the results of DTS and AST on the field data have been matched. The source and geophone estimates of AIT diverge from the AST result.

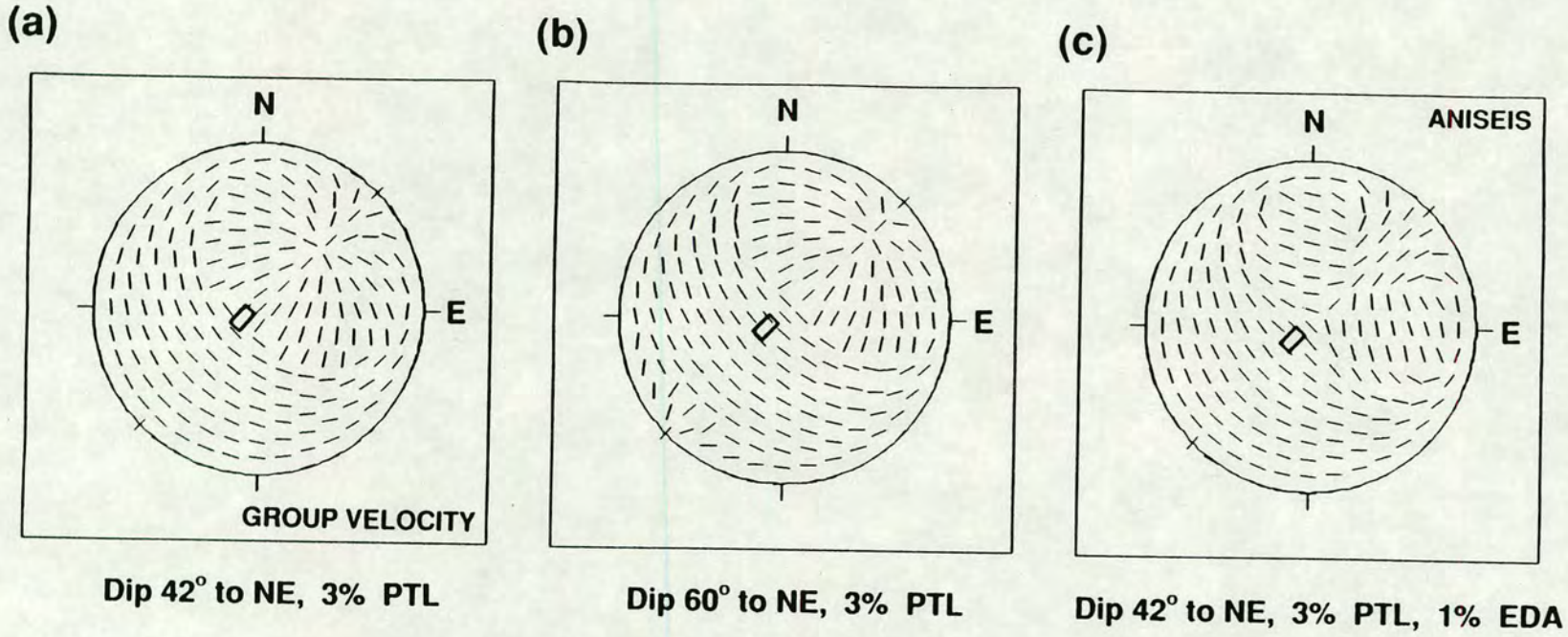

FIGURE 4.25: Equal area diagrams of the polarization direction of the fast split shear-wave for downgoing arrivals. The deeper structure at the Lost Hills dips steeply, but this is not sufficient to get near vertical ray paths with fast polarization directed along N135°E. This can be achieved by (b) increasing the dip in these layers or (c) by adding cracks which strike at N135°E. The boxes show the section of the equal area plot sampled by this VSP geometry.

possibilities. Figure 4.25a shows an equal area plot of qS1 polarizations for PTL-anisotropy dipping at 42° to the NE [Medwedeff 1989]. However, this does not give N135°E polarizations close enough to the vertical for this model. The desired polarization can be achieved if the incidence angle of the ray through the PTL medium is wider (Figure 4.25b). In reality this will happen as rays go through this layer at wider angles due to the dipping structure. I ran a model with steeply dipping thin layer anisotropy below 1.1km; however, the *qS1* polarization direction did not remain constant with depth. This is because the *qS1* polarization direction is dependent on the direction through the medium for PTL-anisotropy (Section 2.4). In this model (as in the field data) well deviation causes the propagation direction to vary.

The dipping shales in the deeper structure are likely to play a part in the anisotropic structure and in Figure 4.25c I show that a combination of cracks and dipping PTL-anisotropy can give a polarization direction of N135°E. However, to get a constant polarization direction with depth the crack anisotropy must dominate.

Conclusions of modelling Case 1

I believe that any change in *qS1* polarization is not by 90° because:

1) this does not match the propagator matrix results;
2) it does not give off-diagonal energy after AST;
3) even with different pulse shapes for each source direction the match in PDs degenerates with depth implying multiple splitting.

4.7.4 Modelling: Case 2: change in crack strike (not 90°)

Now I model the effect of inserting a layer in the upper structure with a different crack orientation as found by Winterstein & Meadows [1991a]. As I have little information on which to base a new model I show the effect of this by inserting a layer, with a different crack strike, into the undeviated Case 1 model. [I therefore do not expect a match of time delays and polarizations with the field data, but I do expect the results of the estimation techniques to show features similar to the field results.] The crack strike in the 200m thick layer between depths of 300m and 500m is now N120°E. The results of AST, AIT and DTS on this model are shown in Figure 4.26.

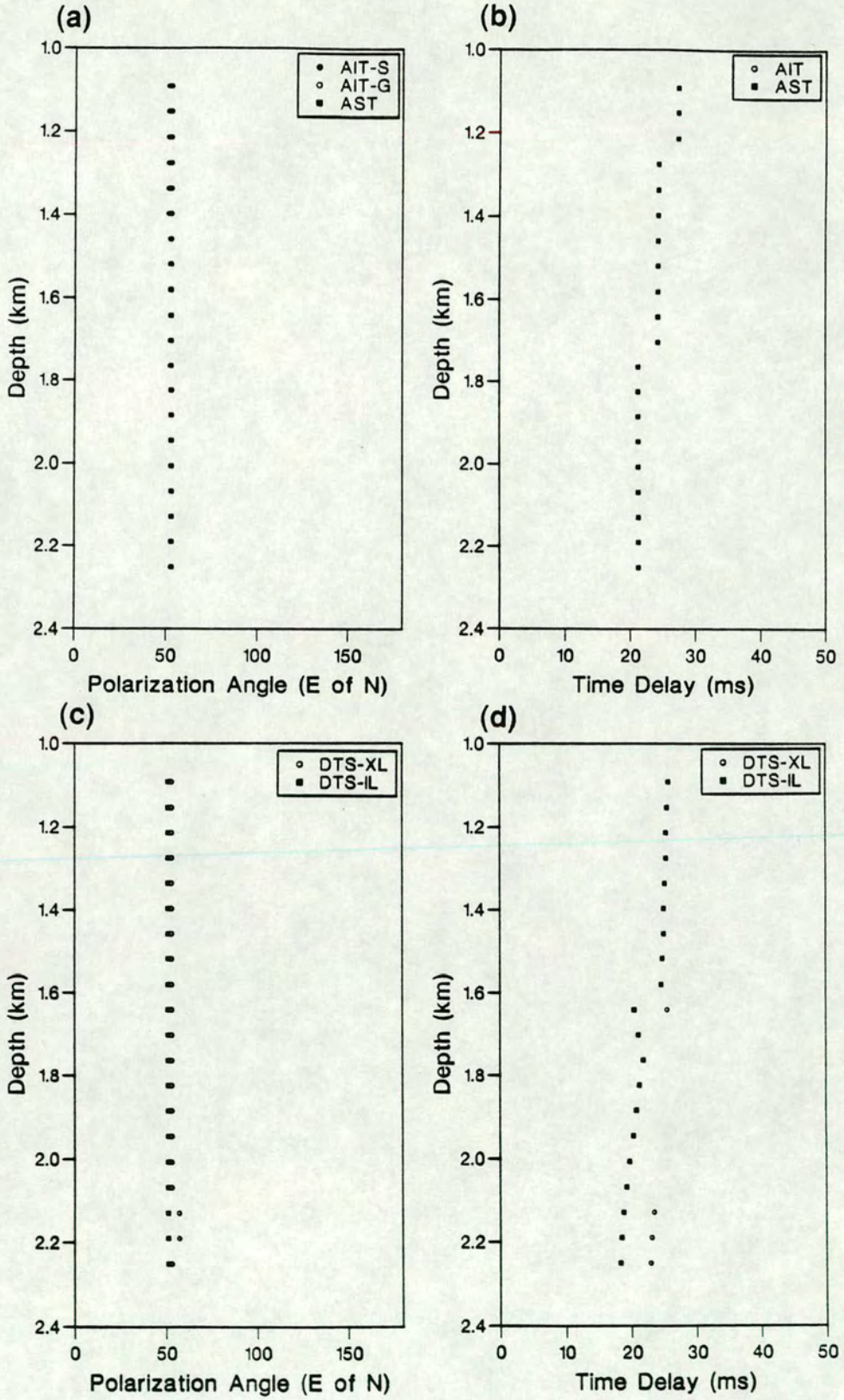

FIGURE 4.26: Results of the estimation techniques applied to a similar model as used for Figure 4.22, but now the model has a 200m thick layer starting at 300m depth with a crack direction of N120°E and 2.8% shear-wave anisotropy.

All techniques give similar results which are consistent between depth levels.

I extracted the pulses from the two shear-wave sources based on a rotation by the angle determined using AST (as done for the field data in Figure 4.19). The pulses are slightly different (Figure 4.27) as found in the field data. This shows that a change in crack orientation above the section of interest may lead to consistent results from the anisotropy estimation techniques, which do not give a true indication of the crack strike.

Results from this model match all the features seen in the field data (including the difference in *qS1* direction and AST result) except the oscillations in AIT polarization estimates. Non-coincident source and geophone polarizations can be due to multiple splitting [MacBeth & Yardley 1992]. Our modelling showed that the source and geophone estimates can oscillate after a change in medium polarization direction, although such frequent oscillations were not seen. The exact behaviour of source and geophone estimates will be dependent on the exact pulse shape and model parameters.

4.8 CONCLUSIONS

The modelling has shown that the most likely explanation of the decrease in time delay is that it is an artefact of the estimation techniques being applied to data containing multiply split shear-waves. I therefore believe that the interpretations of Squires, Kim & Kim [1989] and Choi & Gangi [1991] are based on applying AST in invalid circumstances.

In the neighbourhood of this well there is a change in crack strike in the top 1.1km of the structure. The main features of the observations can be modelled by stress aligned cracks. Propagator matrix techniques give a crack strike of N58°E which is consistent with the known stress regime [Zoback 1992] and with hydraulically induced fractures in other wells in the Lost Hills field [Winterstein & Meadows 1991a].

A zero-offset VSP does not provide enough information to give a unique interpretation of the anisotropic structure at a site other than where the structure is composed solely of horizontal layering with no dipping crack induced anisotropy. If changes in the polarization direction of the rockmass are thought to occur in the

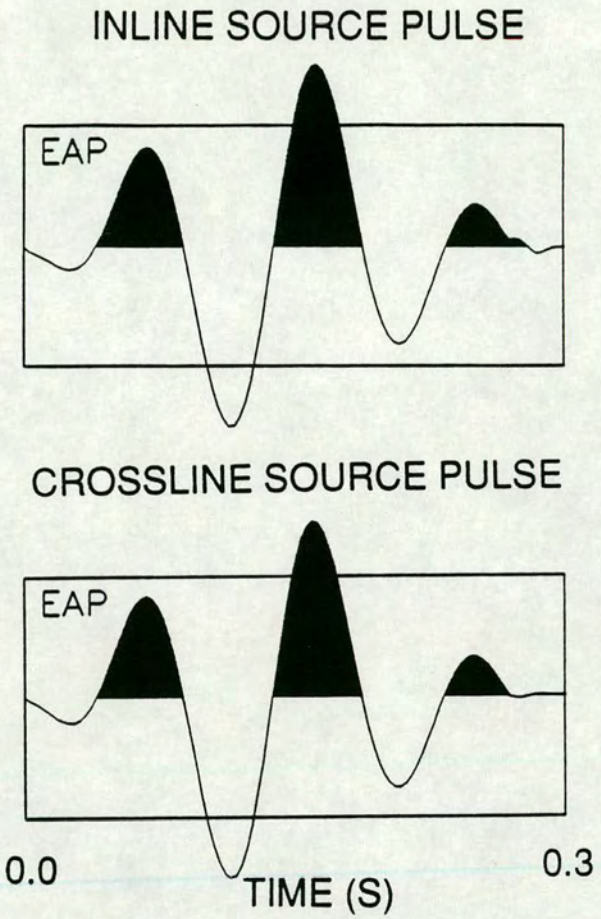

FIGURE 4.27: Source pulses from the model described in Figure 4.26 obtained from the signal recorded from the inline source and the crossline source at the shallowest geophone. The rotation to extract the signal was based on the results of AST at this geophone level. There are slight differences in pulse shape.

near-surface, the VSP should be continued into the near-surface so that such techniques as layer stripping can be applied.

Results of the estimation techniques are stable if the time window for calculation of anisotropy parameters contains the main downgoing arrival. It may be that on other noisier data sets window length is more crucial.

CHAPTER FIVE

SHEAR-WAVE ANISOTROPY IN THE AUSTIN CHALK, TEXAS: PROCESSING

5.1 INTRODUCTION

In Chapter Four the analysis of shear-wave anisotropy and crack structure in the Lost Hills field was hampered by poor data coverage and a complex structure leading to multiple shear-wave splitting. In the following three chapters, I analyze VSP data from three sites along the Austin Chalk trend in Texas. Two of these sites have multi-offset data and the structure is composed of subhorizontal layers. I will concentrate my study on the Austin Chalk, in which reservoir productivity is governed by local fracture distributions. The Austin Chalk lacks obvious structural traps and previous work [Mueller 1991, 1992] has shown that fractured reservoirs can be located using shear-wave anisotropy. Information about fracture orientation is important for orientating horizontal wells which try to link the maximum number of fractures. There has been a recent boom in activity with over 80% of the horizontal drilling in the US taking place in this region [Mueller 1992].

In 1992 Texas accounted for about 26% of US production [Oil & Gas Journal **90**, (52), 1992] and this is an economically important area in which to study the link between anisotropy, fractures and reservoir productivity. One of my study sites (Burleson County) contains a producing fractured reservoir and my aim is to determine whether the anisotropic structure of this reservoir is different to that at the two non-producing sites.

In this chapter the data are processed to yield the anisotropic parameters. Source and geophone polarities are unknown at these sites and I use the estimation techniques to determine these uniquely. Polarization directions of the leading split shear-wave are found to be parallel to known fracture and stress directions. Most of the observed time delay is built up in the near-surface with little indication of further anisotropy at depth. Shear-wave data created from a *P*-wave source are also processed to yield similar results. Results from this chapter are modelled in Chapter Six, and in Chapter Seven

I use reflected shear-wave amplitudes to examine the anisotropy in the chalk layer.

5.2 GEOLOGICAL AND GEOPHYSICAL BACKGROUND

5.2.1 Tectonic setting and stress regime

The data analyzed in this chapter come from the three sites marked in Figure 5.1. The sites lie in an intraplate basin and the general tectonic setting has been described by Zoback & Zoback [1991]. Figure 5.1 also shows the maximum compressive stress directions for the region. These were determined for the World Stress Map Project [Zoback 1992] using different techniques including borehole breakouts, hydraulic fractures, geological information, earthquake source mechanisms and *in situ* stress measurements. Although each technique is limited to a specific depth range (e.g. breakout studies are limited to the depths of boreholes), they give consistent results and, in general, stress directions are consistent over large areas. This region is undergoing extension directed towards the Gulf of Mexico and the maximum compressive stress is parallel to the coast. Away from the coastal areas the stress is dominated by the midplate ENE compression.

The strata are uniform subhorizontal layers (Figure 5.2) which dip by between 2° and 5° towards the coast [Kuich 1989]. There are some deep basement arch features (e.g. the Pearsall Arch) over which the deeper sediments thin.

5.2.2 Geological background

Many of the formations in this region form reservoirs; however, the subject of this study is the Upper Cretaceous Austin Chalk. The Austin Chalk was deposited in thick layers in a marine environment with the depth of water increasing towards the Gulf of Mexico, away from the current chalk outcrop. Chalks deposited in deep water are expected to have uniform facies [Stapp 1977]. The Austin Chalk is a very fine grained carbonate mud containing coarse skeletal remains [Corbett, Friedman & Spang 1987]. Fracture development in the Austin Chalk has been analyzed by Corbett, Friedman & Spang [1987] who examined surface outcrops and well data. They found that the chalk is composed of three units: an upper massive brittle chalk (the Big House Chalk); a central ductile chalk-marl and a lower massive brittle chalk (the Atco Chalk). These

FIGURE 5.1: a) A map (after Corbett, Friedman & Spang [1987] and Kuich [1989]) showing the location of the three sites analyzed. The shaded area is the Austin Chalk outcrop. b) Maximum horizontal stress directions for the study area, taken from the World Stress Map Project [Zoback 1992].

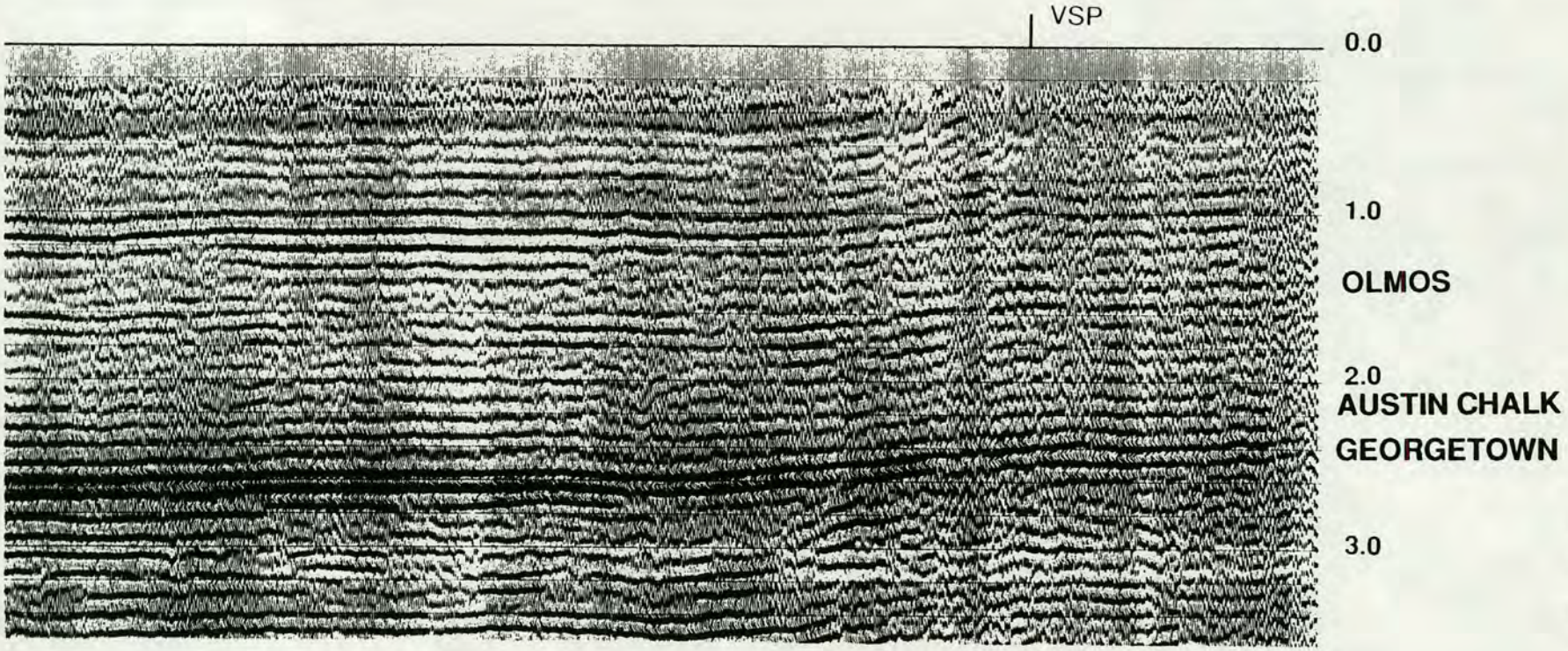

FIGURE 5.2: Representative shear-wave section from Texas. This example is the slow shear-wave section from Amoco's line 17 in Dimmit County and was processed by Li [1992]. The position of the Stumberg Jr. #1 VSP, processed in this chapter, is marked. Horizontal trace separation is 25m.

units are up to 75m thick in the Giddings field [Kuich 1989].

Subsurface porosity lies in the range 5-16% [Dravis 1979]; however, the chalk is impermeable and reservoir productivity is governed by the presence of fractures. High fracture densities can be correlated with thin chalk beds [Corbett, Friedman & Spang 1987]. Fractures are dominantly extensional and result from down-warping due to later deposits (with the fracture strike perpendicular to the dip of the beds) and from faulting [Scott 1977; Stapp 1977; Reaser & Collins 1988]. Normal faulting occurred in the basin as a result of the coastward extension. Original fault movement took place in the Late Cretaceous with further major movements in the late Oligocene or early Miocene [Weeks 1945]. The uniform nature of the faulting indicates that the stress field is regional.

Cores and fracture identification logs show that fractures tend to be subvertical and occur in swarms, principally in grabens [Corbett, Friedman & Spang 1987]. The largest fracture densities occur in the brittle chalk units (four times as much as in the chalk-marl) and can extend through the entire units, generally terminating in the marl. Fracture intensities lie in the range 0.1 to 10.5 fractures per horizontal metre. The fractures are between 0.01 and 1.0mm wide and are usually filled with sparry calcite [Corbett, Friedman & Spang 1987]. Two orthogonal fracture sets are usually present: one parallel and one perpendicular to the strike of the bedding. In the Giddings field (SW of Burleson) the dominant fractures trend NE-SW [Kuich 1989; M.C.Mueller, personal communication] and there is poor reservoir communication in perpendicular directions.

5.2.3 Anisotropy Studies in the Austin Chalk

Several studies on shear-wave anisotropy in this region have recently been published. Alford [1986] analyzed reflection data from Dilley and found a progressive increase in time delay with depth, implying that no multiple splitting had occurred. The *qS1* polarization direction determined by Alford [1986] was along the Austin Chalk trend [M.C.Mueller, personal communication]. Li [1992] and Li, Crampin & Mueller [1992] analyzed three reflection profiles from South Texas and found that the amount of anisotropy could be broadly correlated to productivity. Becker *et al.* [1990]

found 7-8% anisotropy in the Austin Chalk at Marcelina Creek from VSP data and inferred a fractured direction of N60°E at a depth of 2.5km.

Mueller [1991, 1992] analyzed reflector continuity on slow shear-wave sections in the Giddings field. Dimming of the reflector was interpreted as a change in the reflection coefficient due to the presence of fracture swarms (see Section 7.2.2). A horizontal well was drilled to link these amplitude anomalies and they were found to be productive fractured reservoirs. Core samples showed that the fractures were open at depth and parallel to the *qS1* direction [M.C.Mueller, personal communication]. The fracture strike in this experiment was found to be EW rather than the SW-NE fracture strike further south in the Giddings field [Kuich 1989].

In general these studies have shown that the *qS1* polarization direction is parallel to the regional fracture and stress direction. The time delay is built up in the near-surface [e.g. Mueller 1991; Li 1992] and gives a near-surface anisotropy of 2-3%.

5.3 DATA ACQUISITION AND PROCESSING

In this section I describe the data acquisition at each site and how that data was processed to reach the state where the anisotropy estimation techniques can be applied. Processing follows the sequence laid out in Section 2.5.

5.3.1 Dimmit County: Acquisition and processing

In January 1986 Geosource Inc. acquired zero-offset nine-component VSP data from Amoco's Stumberg Jr. #1 well in Dimmit County using VIBROSEIS sources. Each source had a slightly different location:

Source type	Offset (m)	Azimuth (N°E)
P-wave	174	112
Inline shear	162	113
Crossline shear	149	114

Geophone levels were at 152m (500ft) intervals from 152m (500ft) to 1524m (5000ft) and then at 30m (100ft) intervals. In all, 151 geophone levels were recorded. The initial target of the well was the Smackover formation at about 5.8km (19000ft);

however, this proved to be dry [Morris & Raring 1987]. I examine only the top 50 levels (down to 2743m (9000ft)) as this range includes the Austin Chalk. Acquisition parameters are shown in Table 5.1.

The dominant frequency of the signal is about 12Hz and I applied a 3-33Hz band pass filter. It was not possible to determine the orientation of the horizontal geophone components as the offset was too small to give significant *P*-wave energy on the horizontal components. In addition, well deviation in an unknown direction (but <2°) means that the radial direction may not be constant with depth and does not give a fixed reference frame for rotation.

5.3.2 Devine Test Site: Acquisition and processing

The BP test site data, analyzed in this chapter, were acquired in June 1989 by Downhole Seismic Services (DSS); a Western Atlas company. Nine-component data were collected using an ARIS source. The acquisition geometry is shown in Figure 5.3. All wells and source positions lie along the same NW-SE line. Recordings were made simultaneously in all three wells from each source position. This gives a total of nine VSPs, each with two orthogonal shear-wave source orientations (inline and crossline). Acquisition parameters and geophone levels are shown in Tables 5.1 and 5.2 respectively. Data quality control and stacking of traces for each level were done in the field and meant that levels producing poor records could be reshot during the experiment [Raikes, BP internal report]. Well logs were provided from W9.

Initial processing of the shear-wave data was carried out by S.A.Raikes (BP), who processed the ARIS data to give the shear-wave signal. [Subtracting left from right shots gave the crossline source and subtracting forwards from backwards shots gave the inline source.] Raikes also rotated the offset data in the horizontal plane into inline and crossline components using *P*-wave arrivals. Analysis of well logs from all three well [Raikes 1991; Miller, Costa & Schoenberg 1992] shows that the geological structure (below 150m) at Devine over the 300m between W4 and W9 is laterally invariant. I therefore divided the VSP data into four offset groupings to ease processing. These are as follows (the names are derived from the well number and source location; see Figure 5.3):

TABLE 5.1: Acquisition parameters.

	DIMMIT	DEVINE	BURLESON
Source type	VIBROSEIS	ARIS	VIBROSEIS
Number of sources			
P-wave	2	1	2
Shear-wave	1	1	2
Number of shots/sweeps			
P-wave	?	4	4
Shear-wave	?	2	12
Sweep frequency (Hz)			
P-wave	10-80	-	8-56
Shear-wave	6-45	-	8-56
Sampling interval (ms)	2	2	2
Geophone characteristics	10Hz 90% damping	? 70% damping	14Hz 69% damping

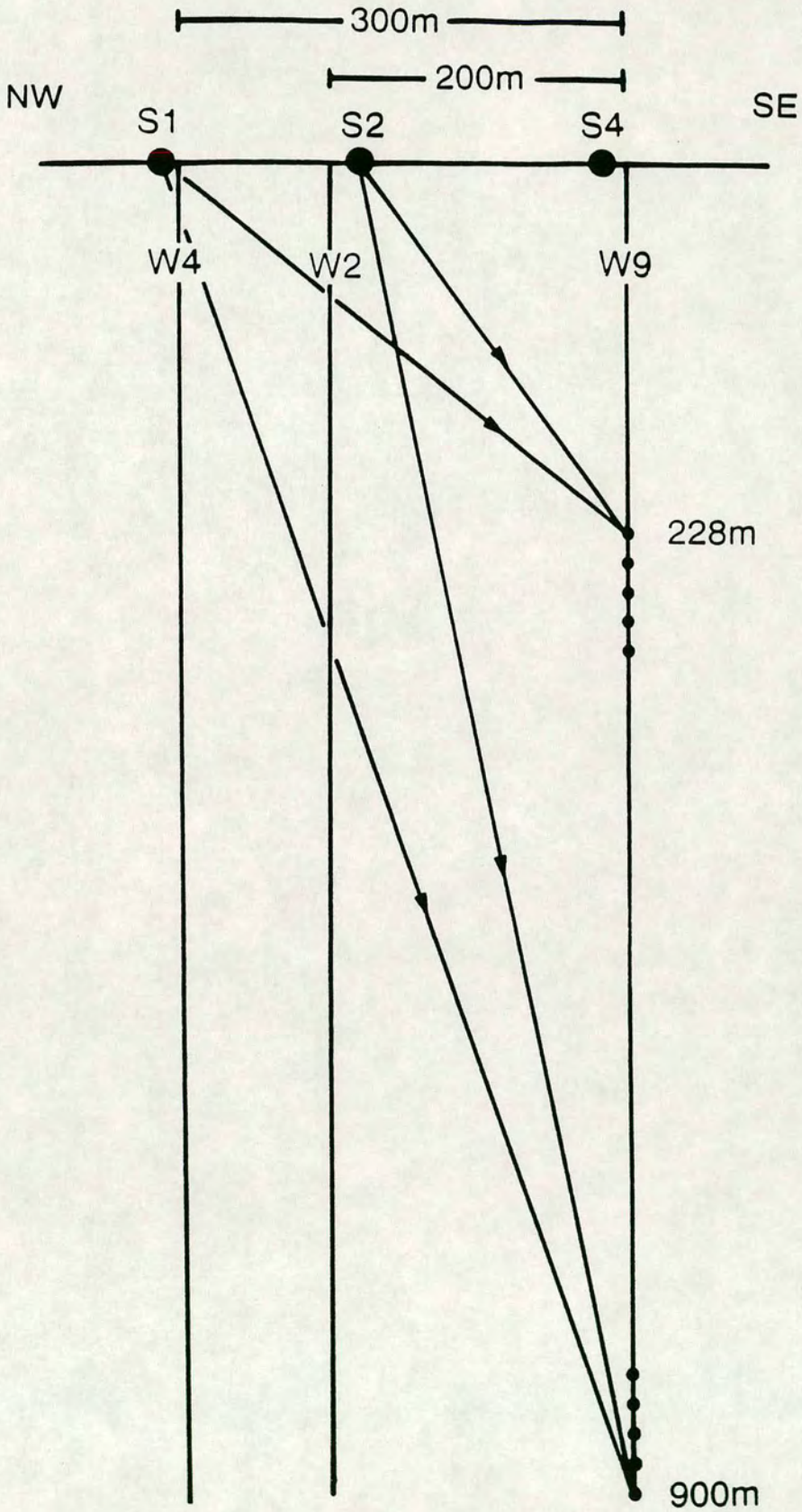

FIGURE 5.3: Cross section through the BP Devine test site showing the source (S) and well (W) geometry used in this study. The wells lie along a single NW-SE azimuth. See Table 5.2 for geophone locations. Recordings were made in all wells from each source position.

TABLE 5.2: Geophone depths at the BP Devine test site.

	W4S1	W2S2	W9S4	W2S1	W4S2	W2S4	W9S2	W4S4	W9S1
Levels	99	93	86	85	83	82	89	80	89
Offset	12m	19m	15m	112m	119m	184m	181m	284m	312m
					Depths (feet)				
	25								
	50	50							
	75								
	100	100							
	150								
	200	200							
	250								
	300	300							
	350								
	400	400							
	450								
	500	500							
	550								
	600	600							
	650								
	700	700							
	750	750		750	750		750		750
	775	775		775	775		775		775
	800	800		800	800		800		800
	825	825	825	825	825	825	825	825	825
					Then at 25ft (8m) intervals				
	2800	2800	2800	2800	2800	2800	2800	2800	2800
		2825	2825	2825		2850	2825		2825
		2850	2850	2850		2850	2850		2850
			2875				2875		2875
			2900				2900		2900
			2925				2925		2925
			2950				2950		2950

Geophone depths are quoted in feet as this gives a better impression of geophone spacing.

Offset (m)	VSP
zero	W4S1 W2S2 W9S4
115	W2S1 W4S2
185	W9S2 W2S4
300	W9S1 W4S4

In each of the non-zero-offset groupings one of the VSPs has a positive radial direction to the NW and the other to the SE. [The positive radial direction is directed from the source towards the receiver.]

Examples of rotated seismograms from each of the non-zero-offset groupings are shown in Figures 5.4 to 5.7. Usually, the main shear-wave arrival has two cycles but is followed by low amplitude multiples. Most of the shear-energy is on the component parallel to the source polarization indicating only small amounts of splitting. The shallowest arrivals from the 300m offset inline sources are distorted. This is due to mode conversions at interfaces for wide incidence arrivals. There is a localised layer with an anomalous velocity under S4 [S.A.Raikes, personal communication] and this gives rise to large amplitude multiples for W4S4 (300m offset, Figure 5.7), particularly for the deepest geophone levels for the crossline source. Examples of polarization diagrams from each offset are shown in Chapter Six (Figures 6.5 to 6.7) and are generally elongated ellipses showing little splitting.

Figures 5.4 to 5.7 show that reflected energy is present in the data and to remove this I applied an FK filter that passed the entire downgoing signal between 3 and 40Hz. At some levels there are anomalously large signals (e.g. around level 70 in W9S2 for the crossline source, Figure 5.5) and to prevent smearing of these signals between levels each trace was individually normalized before the filter was applied. Normalization was based on the maximum amplitude in a 300ms window around the shear-wave signal. After filtering the data were rescaled to restore the correct relative amplitudes between components. Figure 5.8 shows that this reduces the scatter in the estimation techniques results. The dominant frequency of the signal is 18Hz.

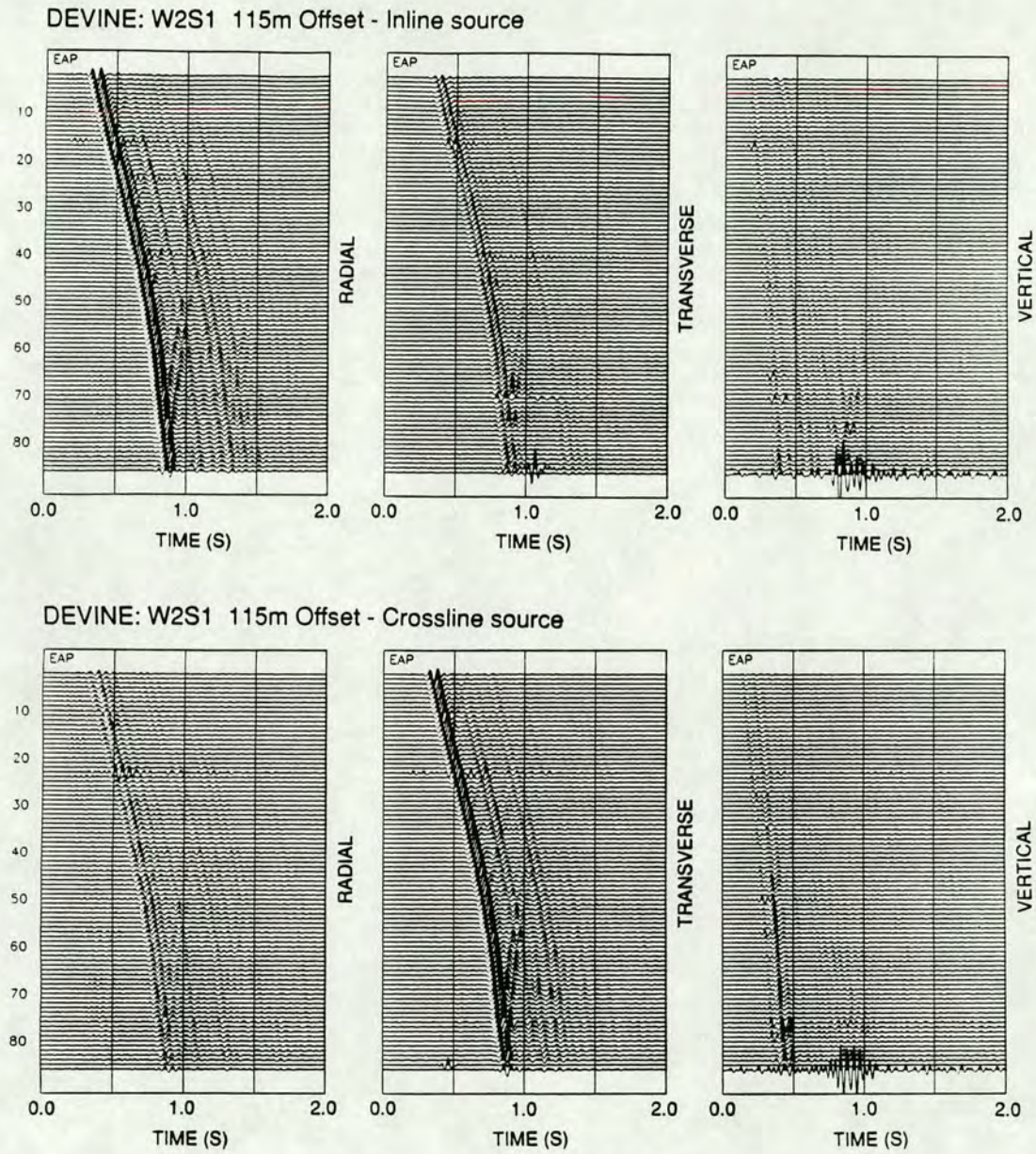

FIGURE 5.4: Three-component seismograms for one of the 115m offsets at Devine. At a given level the seismograms from the inline source are scaled relative to the radial component and relative to the transverse component for the crossline source. There is energy on the off-diagonal horizontal sections indicating anisotropy.

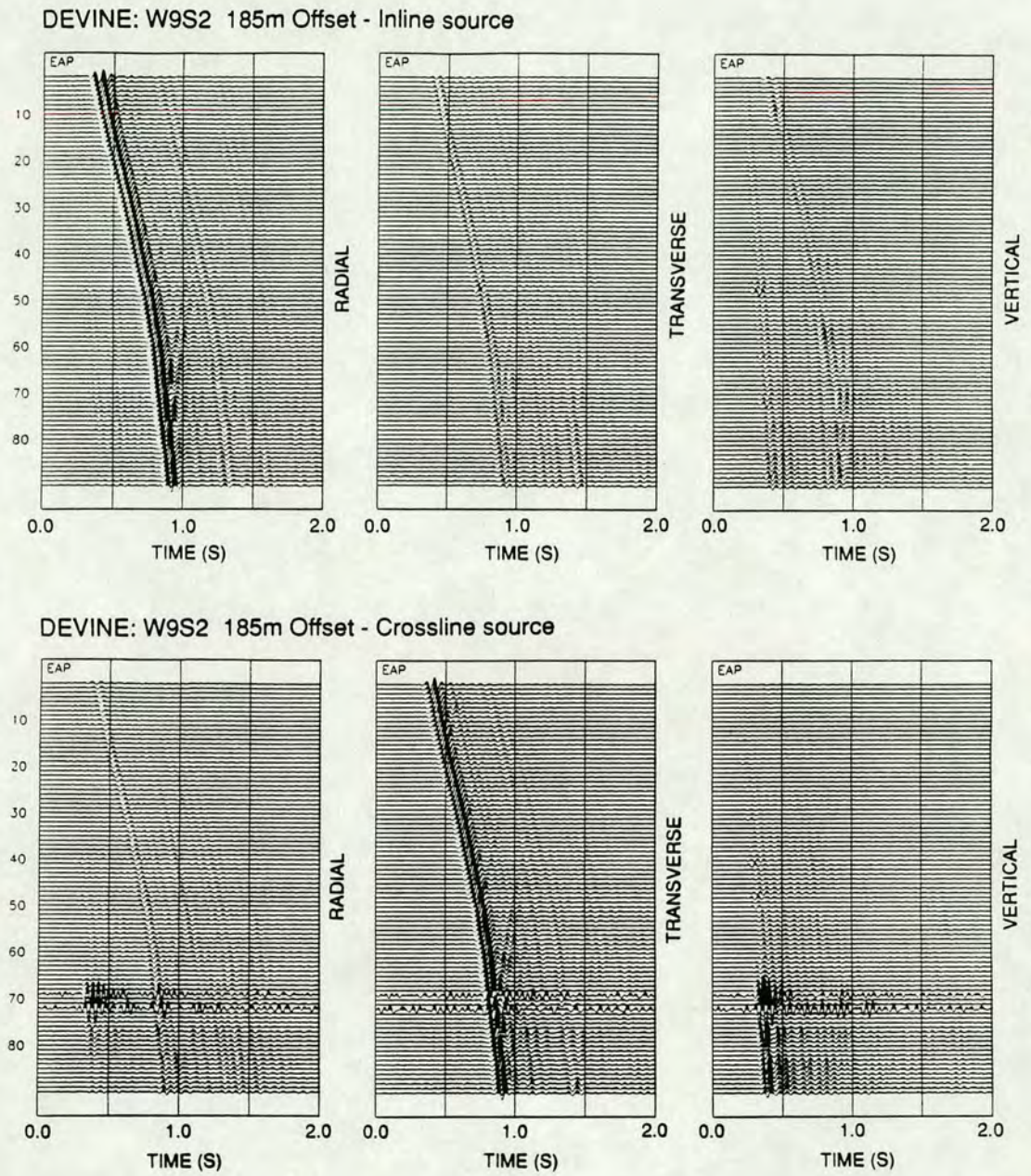

FIGURE 5.5: Three-component seismograms for one of the 185m offsets at Devine. At a given level the seismograms from the inline source are scaled relative to the radial component and relative to the transverse component for the crossline source. There is some energy on the off-diagonal horizontal sections indicating anisotropy.

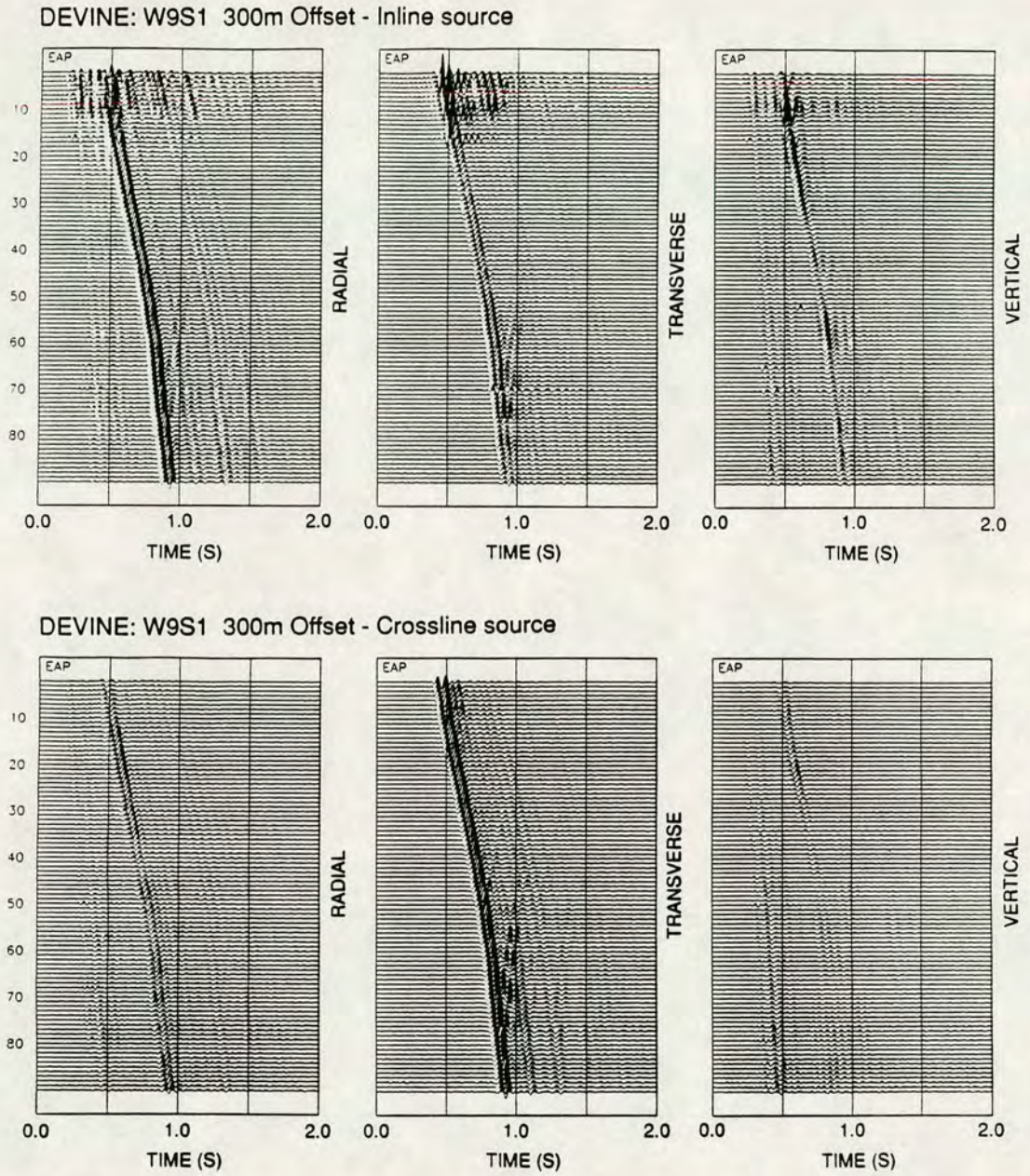

FIGURE 5.6: Three-component seismograms for W9S1 at Devine. At a given level the seismograms from the inline source are scaled relative to the radial component and relative to the transverse component for the crossline source. Shallow levels are distorted by mode conversions for the shallow levels for the inline source.

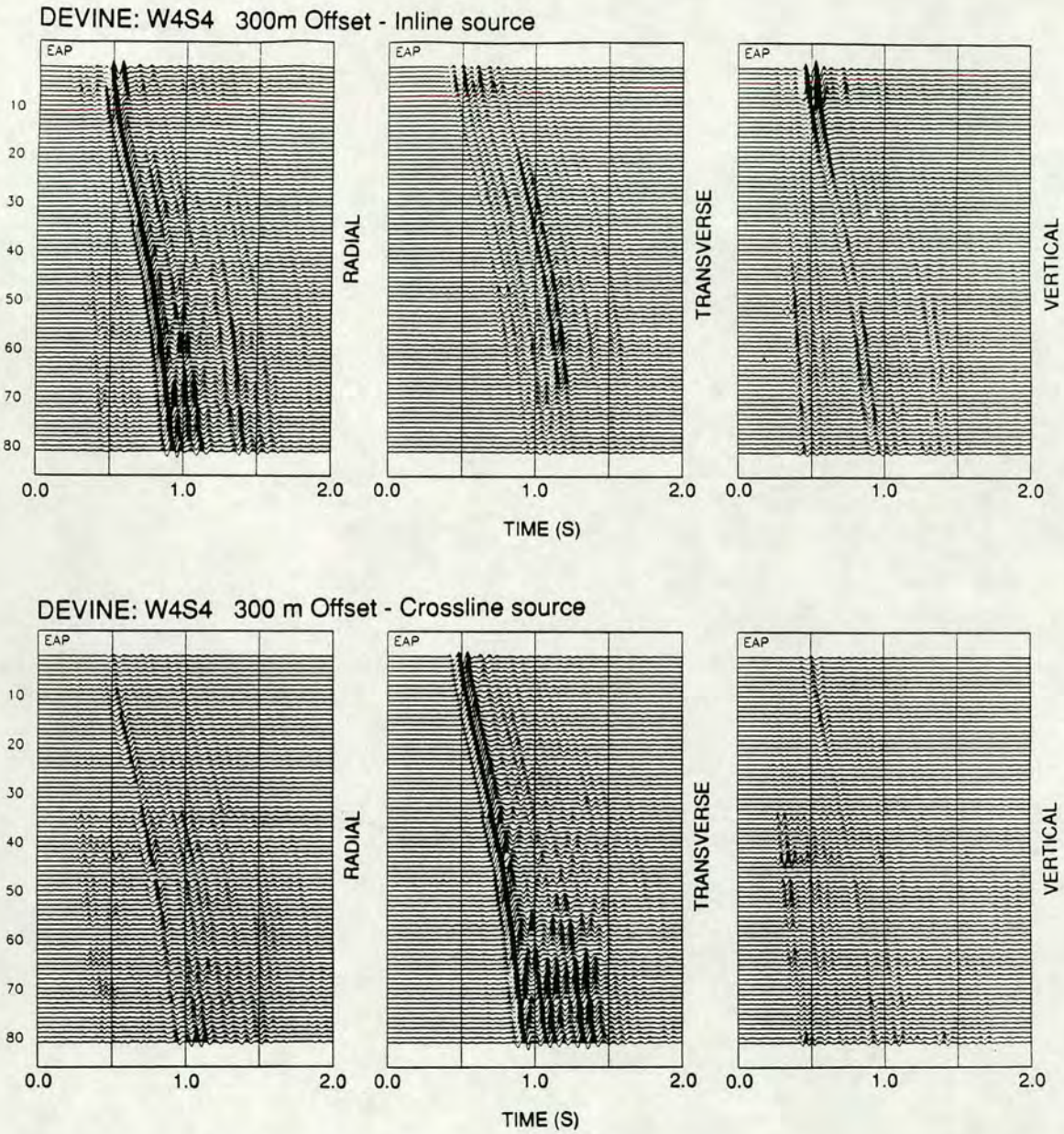

FIGURE 5.7: Three-component seismograms for W4S4 at Devine. At a given level the seismograms from the inline source are scaled relative to the radial component and relative to the transverse component for the crossline source. Multiple energy is present, particularly at depth from the crossline source.

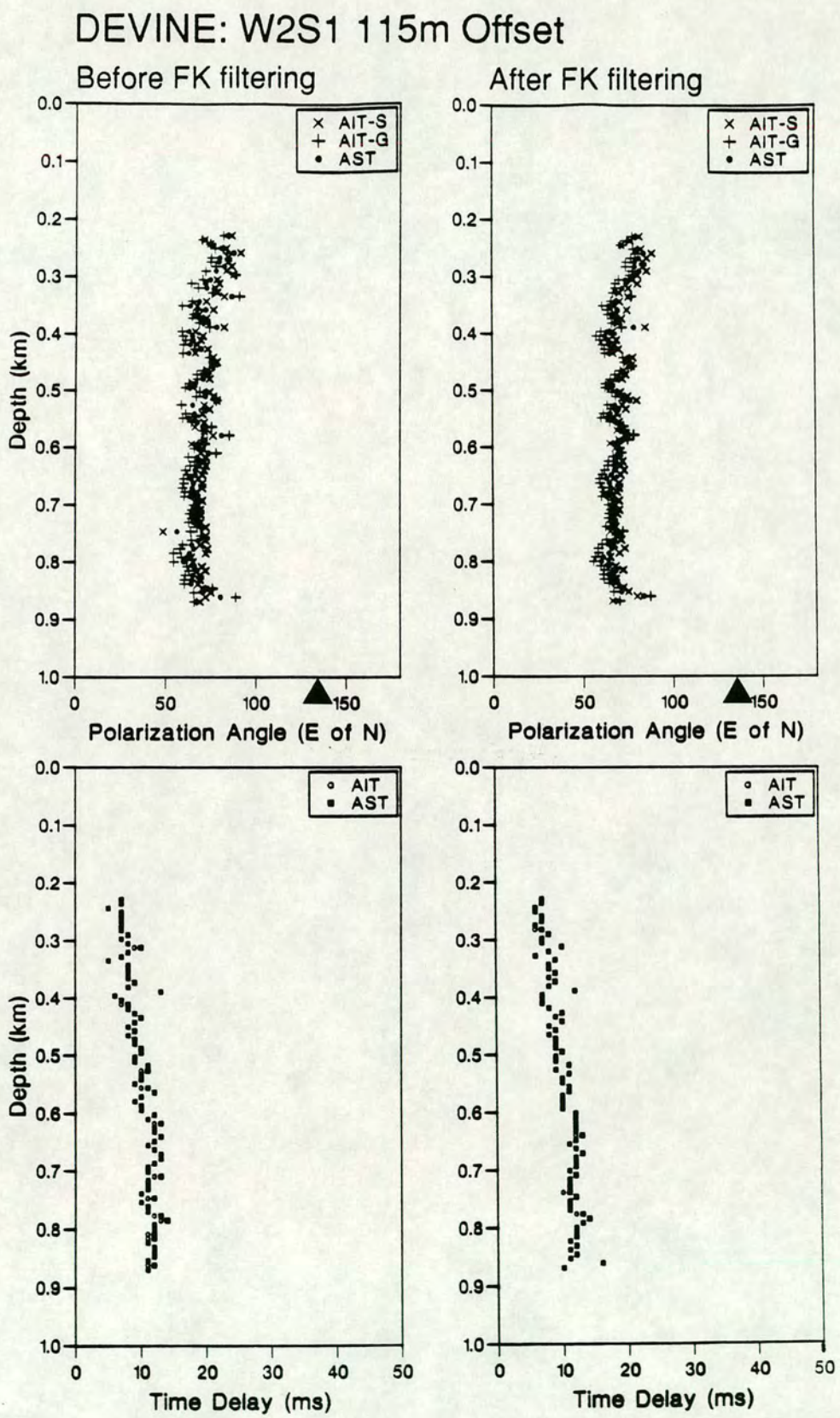

FIGURE 5.8: Test of FK filtering on the results of two anisotropy estimation techniques, AST and AIT. The filtering has reduced the scatter on both estimates of polarization angle and time delay. The radial direction is marked by a triangle.

5.3.3 Burleson County: Acquisition and processing

In November 1986 DESCO (Downhole Exploration Service Company) acquired VSP data from Amoco Producing Company's A.B.Childers #2 well in Burleson County. Nine-component data were shot at four offsets along the same SW-NE azimuth (Figure 5.9) using VIBROSEIS sources. The acquisition parameters and geophone levels are shown in Tables 5.1 and 5.3, respectively.

Data from this well were supplied on three field tapes. I separated the data into source type, offset and component files using the GEOWELL processing package. I cut the trace length from 6 seconds to 4 seconds to make handling easier. The *P*-wave data were band pass filtered from 5-50Hz and rotation matrices were calculated based on the maximum energy direction in the horizontal plane for a 200ms window about the arrivals. I then rotated the offset shear-wave data into radial and transverse orientations, using these rotation matrices, to give the standard geophone arrangement shown in Figure 2.4. The dominant frequency of the shear-waves is 13Hz and I band pass filtered the shear-waves between 5 and 35Hz.

Figures 5.10 and 5.11 show seismograms from two of the offset source locations. The data quality is generally good but some levels are noisy; the noise is mostly caused by spikes in the data before crosscorrelation [S.A.Raikes, personal communication]. [The presence of bad levels meant that I could not apply FK filtering as it requires a constant geophone spacing. Figure 5.8 showed that for the Devine data, whilst FK filtering helps, it does not dramatically enhance the results of the estimation techniques.] The rotations in the horizontal plane were successful. This is seen by the absence of *P*-wave energy on the transverse components. [Shear-wave sources create some *P*-wave energy which is generally apparent on the horizontal components at offset.] For the 700m (VSP3) offset (Figure 5.10) there is little energy on the off-diagonal horizontal sections indicating little anisotropy. Shear-wave energy is seen on both horizontal components for each source at the 1524m offset (Figure 5.11), implying splitting has occurred.

Figure 5.12 shows selected horizontal plane PDs for the depth range 1780m to 2316m for all offsets. For VSP1, the arrivals are elliptical. In VSP2, the PDS for the shallower arrivals are elliptical but become linear at depth. In VSP3, the arrivals are

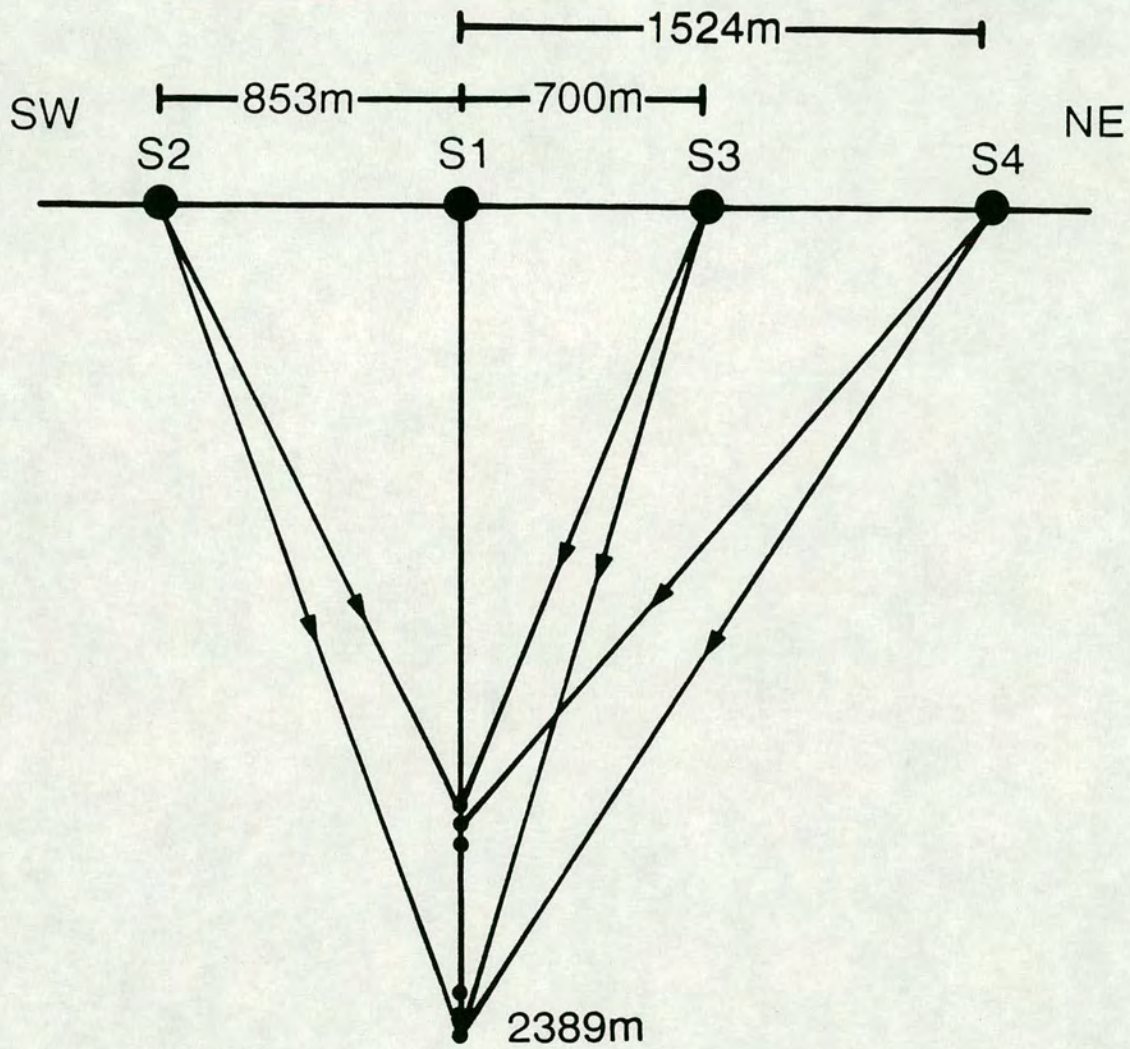

FIGURE 5.9: Cross section through Amoco's A.B.Childers #2 well (Burleson County) showing the source offsets. The wells lie along a single SW-NE azimuth. See Table 5.3 for geophone locations.

TABLE 5.3: Geophone depths in the A.B.Childers #2 well, Burleson County.

	VSP1	VPS2	VSP3	VSP4
Levels	62	56	55	51
Offset	0m	853m	700m	1524m
		Depths (feet)		
	700	700		
	1700	1700		
	2700	2700		
	3700	3700		
	4200	4200		
	4700	4700		
	5200	5200		
	5680	5680	5680	
	5720	5720	5720	
	5760	5760	5760	
	5800	5800	5800	
	5840	5840	5840	5840
		Then at 40ft (12m) intervals		
	7600	7600	7600	7600
	7640		7640	7640
	7680		7680	7680
	7720		7720	7720
	7760		7760	7760
	7800		7800	7800
	7840		7840	7840

Depths are quoted in feet as this gives a better impression of geophone spacing.

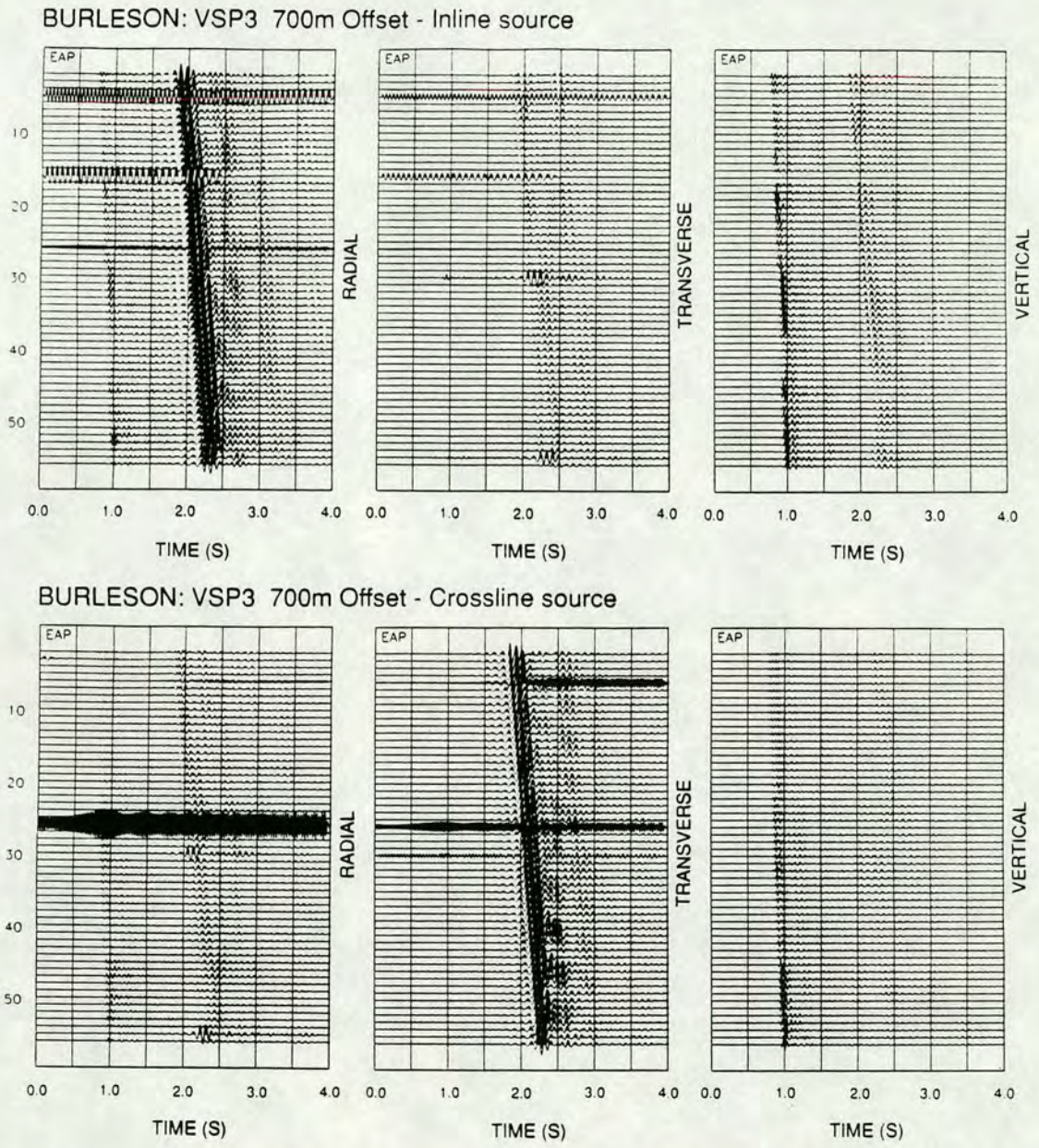

FIGURE 5.10: Three-component seismograms for the 700m offset (VSP3) in Burleson County. These have been scaled relative to the radial component for the inline source and relative to the transverse component for the crossline source. Little energy is seen on the off-diagonal horizontal sections implying linearly polarized shear-wave motions.

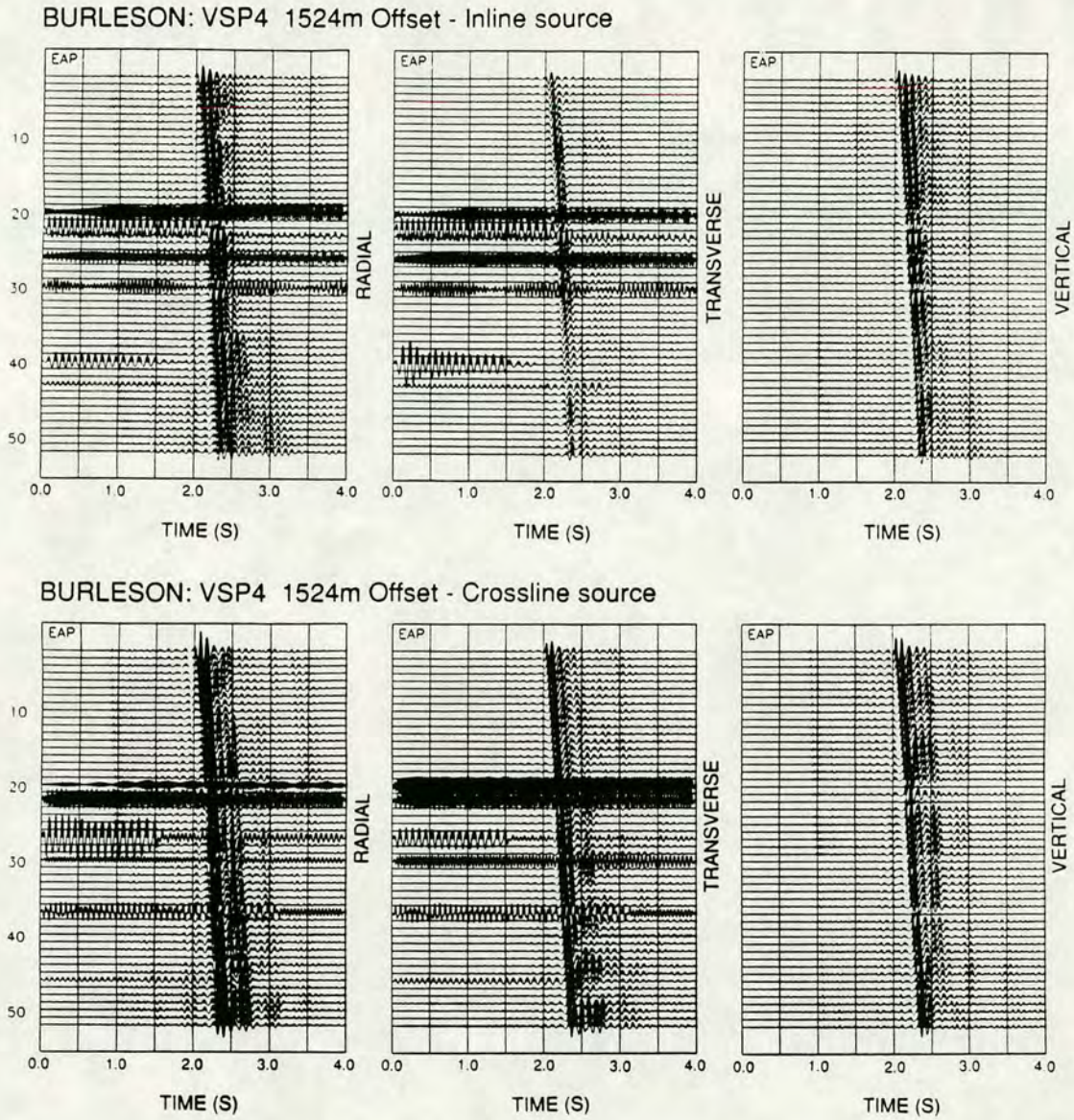

FIGURE 5.11: Three-component seismograms for the 1524m offset (VSP4) in Burleson County. These have been scaled relative to the radial component for the inline source and relative to the transverse component for the crossline source. Some energy is seen on the off-diagonal horizontal sections implying anisotropy.

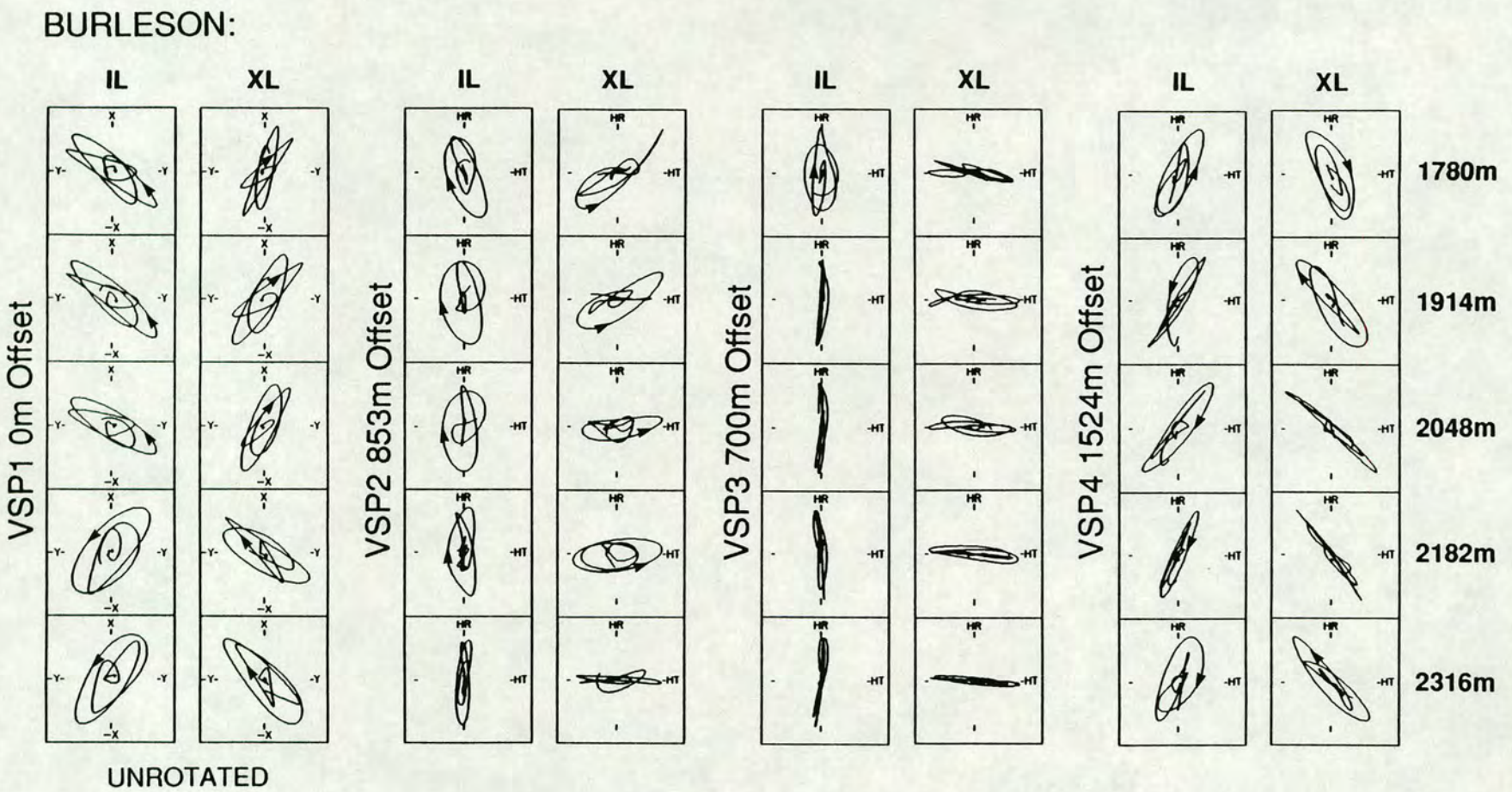

FIGURE 5.12: Selected horizontal plane polarization diagrams for each of the offsets in the Burleson data. The geophones from the zero-offset VSP are unrotated. Where there is a bad trace at the required depth the next level has been displayed instead. The direction of motion is marked by an arrow on elliptical motions. The polarization diagrams for the VSP3 show linear motion as expected from small amounts of energy on the off-diagonal sections in Figure 5.10.

linearly polarized, with the energy along the source direction (as seen in the seismograms). VSP4 has elliptical motions in the shallower and deeper levels with linearly polarized motions for intermediate depths. The motion in the polarization diagrams for VSP4 changes direction with depth from anticlockwise to clockwise for the inline source. This type of behaviour is similar to that seen for ray paths either side of singularities (see Sections 2.4 and 3.5.1).

5.4 EXTRACTION OF ANISOTROPY PARAMETERS

The small degree of splitting encountered in these data sets means that there are no distinct first arrivals, particularly for the non-impulsive VIBROSEIS data. I now apply the anisotropy estimation techniques, described in Section 2.7, to extract the anisotropy parameters. All plotted estimates of polarization angle are rotated into a fixed northsouth-eastwest reference frame so that polarization directions may be compared between sites. I also mark the radial direction on relevant figures with an arrow for reference.

5.4.1 Source and receiver polarities

There is some doubt as to the polarity of the sources and geophones used to acquire both the Devine and Burleson data. This must be resolved before the results of estimation techniques can be interpreted. MacBeth, Zeng, Yardley & Crampin [1993] show how AIT can be used to determine whether the source and geophones are misaligned. I now show how a combination of the estimation techniques can be used to determine uniquely the correct polarities of source and geophones. Let us suppose that in the field both the source and the geophones formed right-handed (RH) sets. If polarities are unknown, there are four possible forms in which the data could appear. These are shown below, other possible reversals in polarity lead to 180° differences in polarization estimates and repeat those listed.

Geometry		Estimation Technique		
Source	Geophone	AST	AIT Source	AIT Geophone
RH	RH	θ	θ	θ
RH	LH	90	θ	180-θ
LH	RH	90	180-θ	θ
LH	LH	180-θ	180-θ	180-θ

If the medium polarization is θ, AST and AIT will record the results shown above for all possibilities. The estimates for both techniques will coincide only for the top and bottom case meaning that the correct geometry is one of these two. To determine which is correct DTS is then applied to the data:

Geophone Geometry	DTS
RH	θ
LH	-θ

The correct polarities of sources and receivers are found only when estimates of AST, AIT and DTS all coincide. Correct polarities can also be found if multiple splitting occurs, even though this causes the AIT estimates to pull apart. In Section 4.6.1, 4.6.2 and 4.7.2, I showed, using field and model data, that AST and DTS give the same estimate even in the presence of multiple splitting. Inspection of the above tables show that only AST and DTS estimates are needed to give a unique solution for source and geophone polarities. [In the case of multiple splitting the estimated angle, θ, will not be the polarization direction of the medium.]

I used this method for the Devine and Burleson data sets. There was no polarity information for Devine and the correct solution was found by reversing the horizontal component geophone components from the crossline source. This is equivalent to reversing the direction of the crossline source. Therefore, in the data that I received, the source set and the geophone set were not both right-handed or both left-handed. [The polarity of the shear-wave source depends on the order of subtraction of the left

and right shots from the ARIS source and can be reversed in processing.]

For the Burleson data observers' notes show that the three-component geophone tool formed a right-handed set with positive Z downwards; but source polarities were not recorded. For this data it was not necessary to change the source or receiver polarities.

5.4.2 Dimmit County: Anisotropy parameters

The horizontal plane shear-wave PDs are linear (Figure 5.13) with the energy from the inline source being perpendicular to the energy from the crossline source. This implies that, either the structure is isotropic, or that the acquisition system is aligned close to the fast or slow direction so that each source orientation only excites one shear-wave. I rotated the data in the horizontal plane to put all the energy from the inline source onto the radial geophone component (Figure 5.14) and the crossline energy onto the transverse component. The rotation was based on a 300ms window about the downgoing shear-wave arrival. The arrivals were then interactively timed on the maximum amplitude of the arrival and the delay between the two shear-waves calculated.

I also applied LTT to this unrotated data set. To do this I must assume that the polarization direction of the medium is invariant with depth. This is reasonable as the region is geologically simple, with a uniform stress regime, and previous work by Alford [1986] suggests this to be the case. Results of direct timing and LTT are shown in Figure 5.15. Isotropic modelling of the upper layer (not shown here) shows that the large time delay in the near-surface (approximately 20ms) is due to the 13m difference in inline and crossline source positions. The effect of the difference in source positions decreases with depth and does not cause the time delay below 1km, where the crossline polarization is the fastest. LTT gives a fast direction, below 1.0km, of N25.2°±9.9°E (only 1° from the crossline source direction). The time delay is 2.8±1.2ms below 2km. The reflection line shown in Figure 5.2, which intersects this VSP, gives a fast direction close to the crossline direction and two way time delays of about 10ms [M.Mueller, personal communication; Li 1992] and these independent results agree with my results from this VSP.

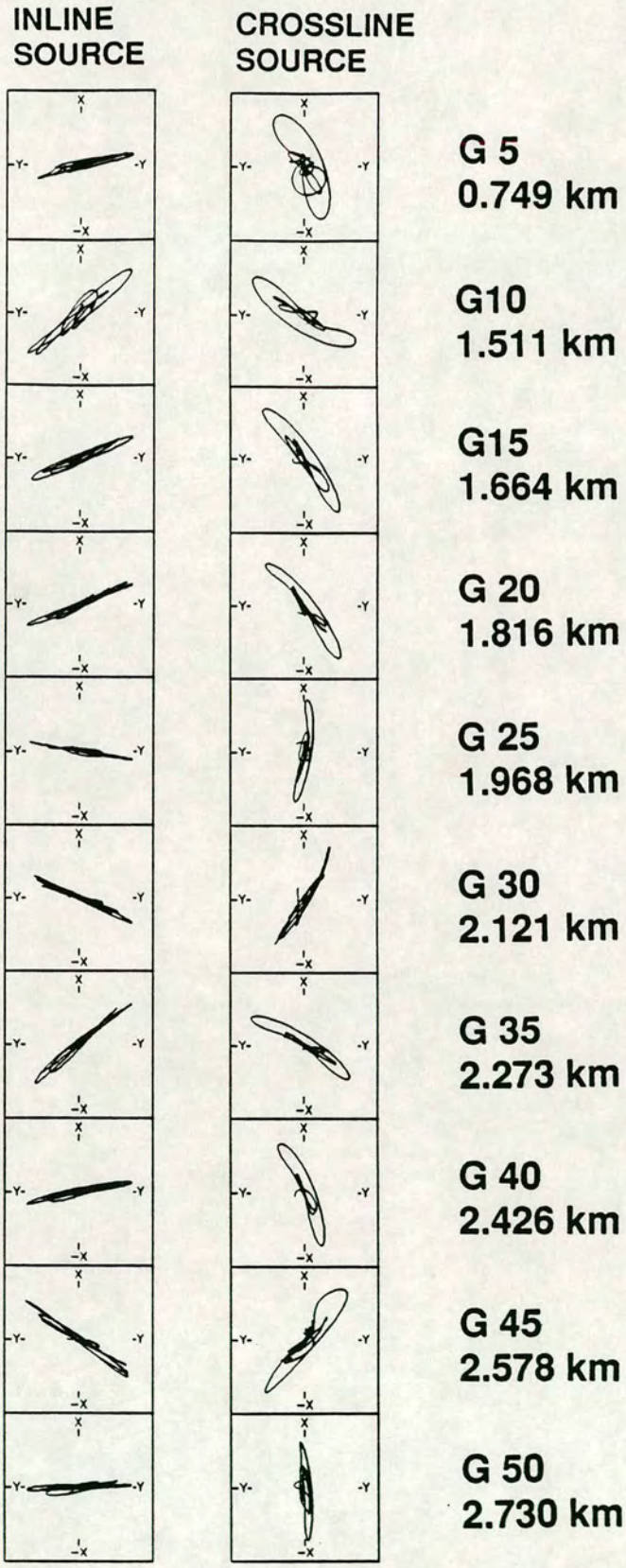

FIGURE 5.13: Unrotated horizontal plane polarization diagrams windowed around the downgoing shear-wave in the Dimmit County VSP. The motions are linearly polarized and orthogonal for the two source types.

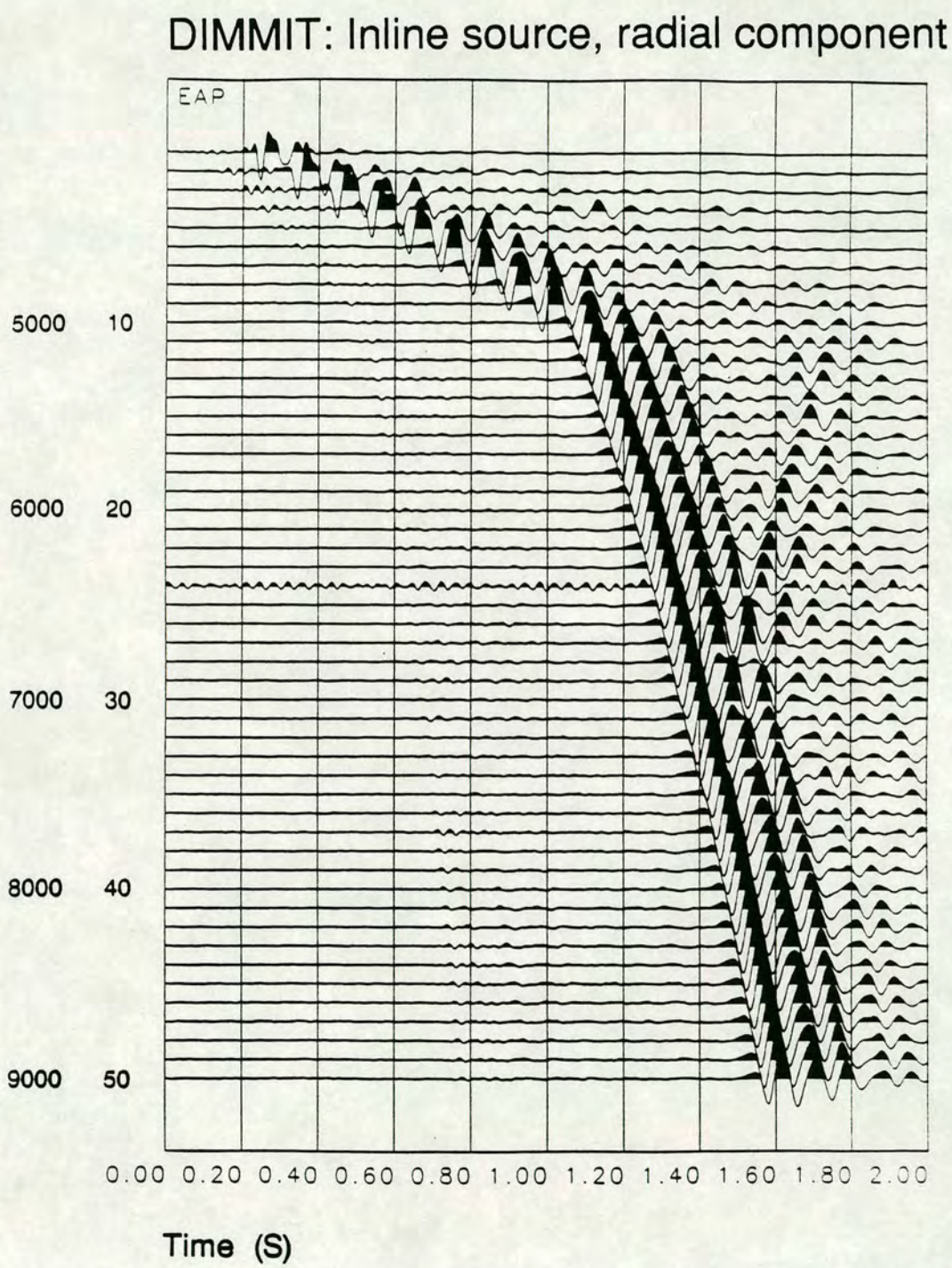

FIGURE 5.14: The radial component from the inline source in the Dimmit County VSP after the shear-wave energy has been rotated into the radial direction.

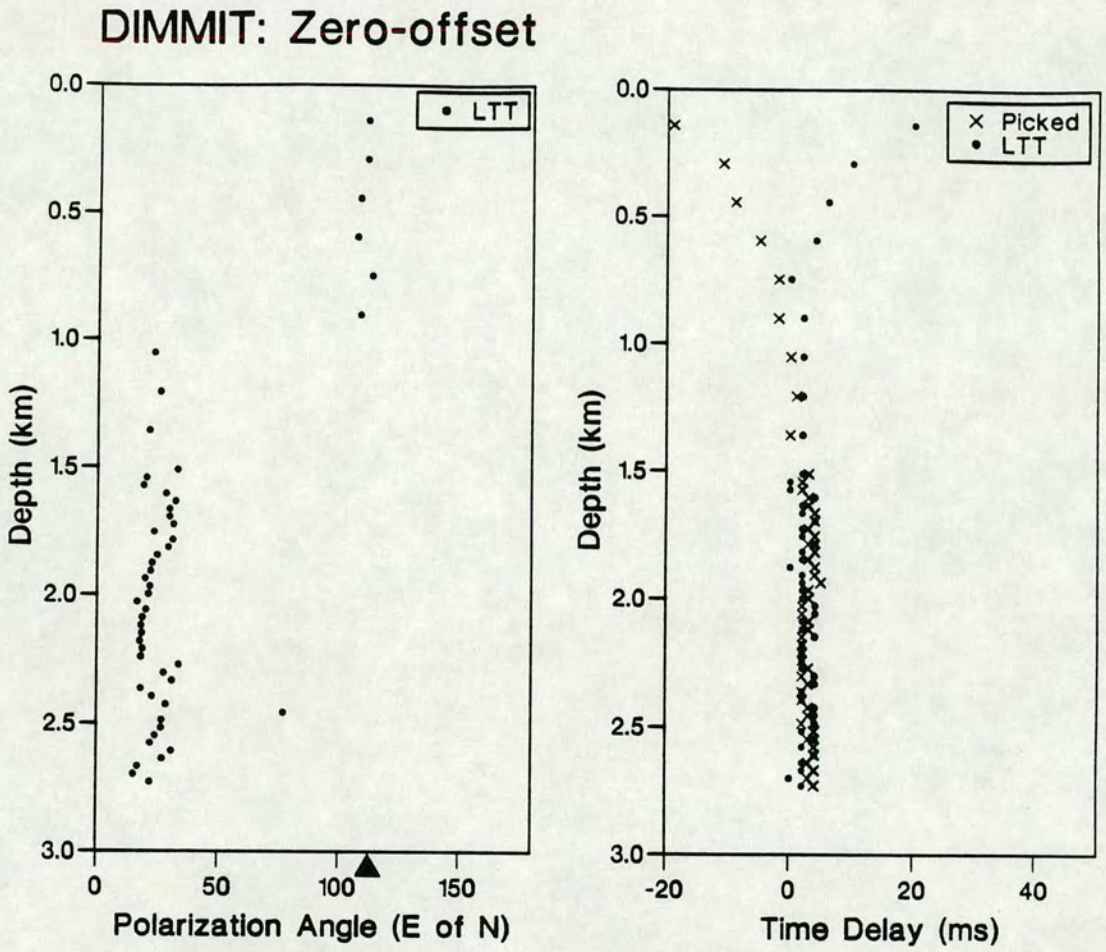

FIGURE 5.15: Polarization and time delay estimates for the Dimmit County VSP calculated using LTT. The time delay estimate is compared to the difference in picked arrival times from the inline and crossline sources (inline arrival time minus crossline arrival time). The difference near the surface is because LTT always records positive time delays. This gives a 90° change in polarity at 1km depth as the shear-wave from the crossline source becomes the first arrival below this. The radial direction is marked by a black triangle.

Cycle Skipping in the estimation techniques

In some cases, particularly with the zero-offset data from Burleson and Dimmit Counties, the estimation techniques produce time delays which are a half period out from the true answer. This occurs when the crosscorrelation picks the wrong peak. The shape of the PDs and the change in measured time delay with depth give an estimate of what order of magnitude of time delay to expect. Limits can be introduced into the crosscorrelation so that the time delay is picked from a specified range. In the case of Dimmit, where direct timing provides the limits, I used time delay limits from 0ms to 42ms (half a period) to prevent cycle skipping.

5.4.3 Devine Test Site: Anisotropy parameters

I applied LTT to the unrotated zero-offset data for a range of window lengths between 0.1s to 0.7s in 0.05s steps to see if the results of the estimation techniques were stable. The start of the window was picked interactively to be just before the first break. Example results are plotted in Figure 5.16. Results are insensitive to the window length as long as all the main arrival is included as this contains the dominant energy. From now on I pick all windows interactively to include all the main shear-wave arrival (about 350ms). LTT gives the *qS1* direction for the upper anisotropic layers in W2S2 as N62°±1.9°E, whereas in W9S4 the polarization angle is N50°±5°E. The time delay rises from zero to about 10ms in the top 250m and reaches 12.8±1.6ms at depth in W2S2. The difference in the W9S4 *qS1* direction could be due either to the effects of the high amplitude multiples from the anomalous surface layer below S4 or the effects of a different anisotropic structure between the wells. Dipmeter and televiewer data from this site show dipping fractures in W4 and W9 striking ENE (N67.5°E) and N40°E respectively [S.A.Raikes, personal communication]. Therefore the difference in polarization measured in W9S4 could be a genuine feature of the rock structure. Winterstein & Meadows [1991b] also determined local variations in crack direction between closely separated wells from dipmeter data and shear-wave analysis.

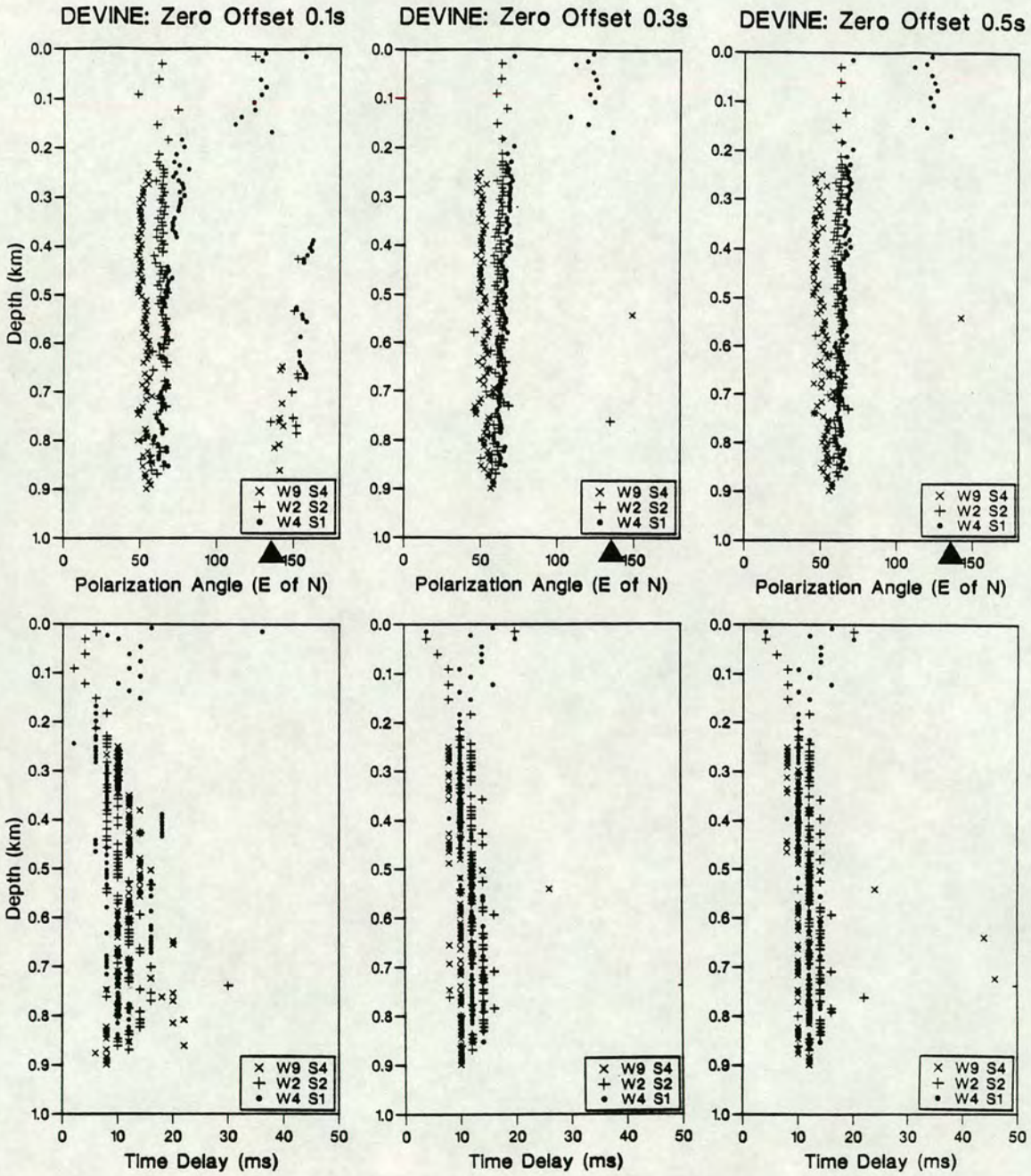

FIGURE 5.16: Polarization and time delays estimates for each of the zero-offset VSPs at Devine for a range of analysis window lengths. LTT is stable for window lengths that include all the main shear-wave arrival. The radial direction is marked by a black triangle.

Offset data and dynamic axes

The horizontal plane is generally used for the calculation and display of polarization directions as it provides a fixed reference frame. For offset data, most of the shear-wave energy may not be in the horizontal plane. The estimation techniques used here assume orthogonal split shear-waves. However, for shear-waves with wide incidence angles the projections of the split shear-waves onto the horizontal plane are not orthogonal. In order to get the most robust results I also ran the estimation techniques in the plane containing the shear-wave energy (the dynamic plane). The incidence angle of the incoming shear-wave was calculated as being 90° to the energy in the sagittal plane (over a 300ms window) from the inline source. [There is insufficient energy in the sagittal plane to do similar calculations for the crossline source.]

Measured incidence angles are shown in Figure 5.17. For the 115m and 185m offsets, incidence angles show no distinct depth related variation, although they vary with rock type. Average incidence angles are 6° for the 115m offset and 12° for the 185m offset. The shallow geophones in the 300m offset VSPs have wide incidence angles and are approximately 18° below 500m. Results from each source, in a given offset grouping, are consistent. The incidence angle calculated by this means is the group velocity incidence angle and is not necessarily the same as the phase velocity incidence angle (Section 2.4). [For the model developed in Chapter Six, the difference in phase and group velocity incidence angles is about 5°.]

In Figure 5.17, I also mark the straight line angle from source to receiver. For structures where the velocity increases with depth this should be an underestimate of incidence angle and not an overestimate as seen here. The sagittal plane PD of the shear-wave is not completely linear which will cause errors in the estimates of incidence angle. Errors in estimating incidence angles could arise from:

1) interference between the fast and slow shear-wave arrivals;
2) distortion by interface effects (as seen for the shallow levels in Figure 5.6);
3) mode converted arrivals following the *P*-wave arrival, as seen in the radial sections in Figure 5.6);
4) the vertical and horizontal geophones may have different sensitivities.

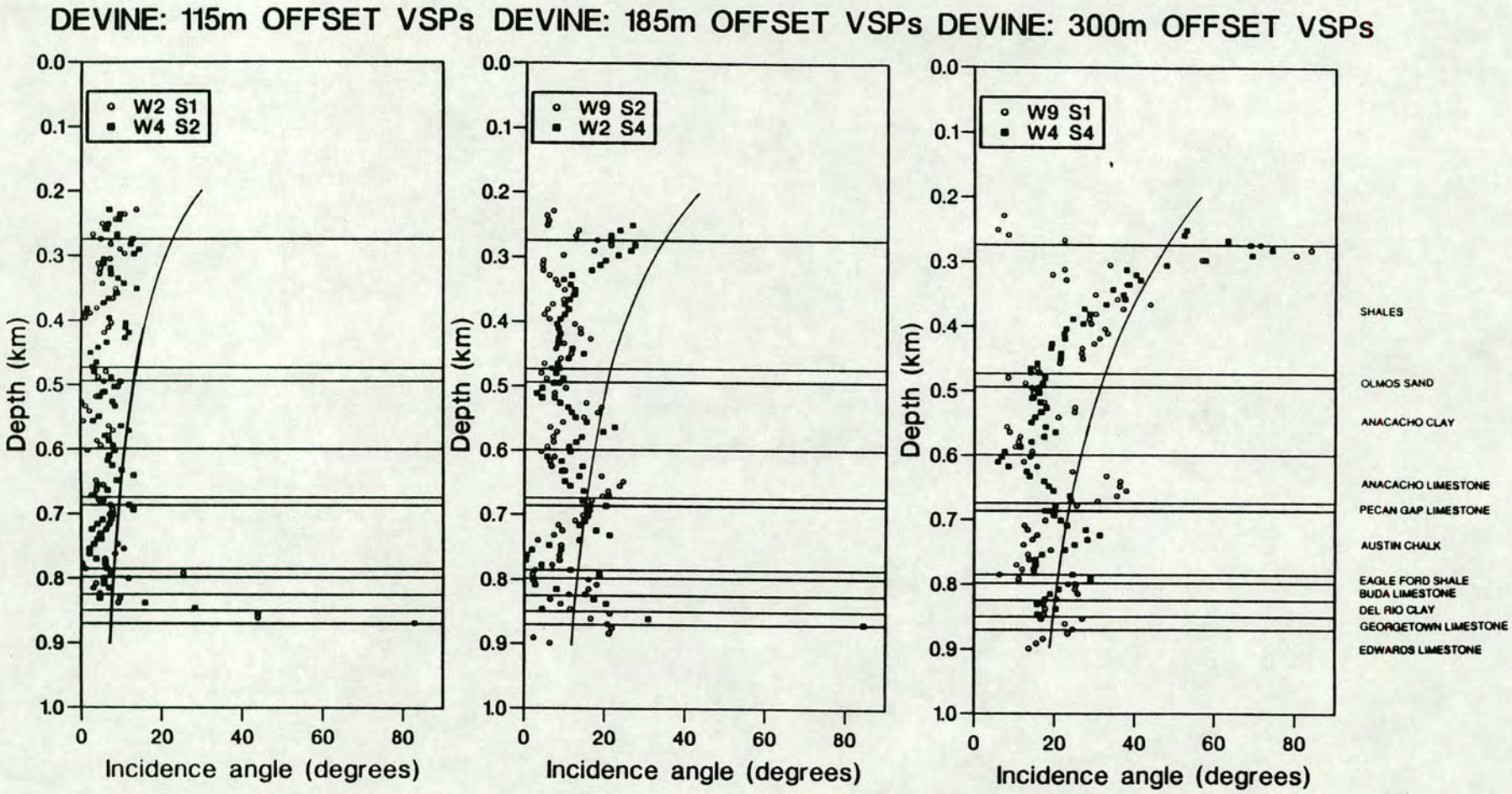

FIGURE 5.17: Shear-wave incidence angles for each VSP at Devine calculated from the inline source energy in the sagittal plane. The results are consistent for each offset grouping and there are changes in incidence angle at interfaces which are dependent on the velocity (sonic logs are shown in Chapter Six). The solid line is the angle of the straight line from source to receiver.

The plane found by this means contains more shear-wave energy than the horizontal plane, giving it a higher signal-to-noise ratio. These angles were used to rotate the data into dynamic axes and the estimation techniques were run in both the dynamic and the horizontal planes to evaluate how the results were affected (an example is shown for AIT and AST later in this section). Polarizations calculated in the dynamic plane were projected back onto a horizontal surface so that all polarization angles are plotted with respect to a fixed coordinate system.

A better estimate of the incidence angle could have been found by using incidence angles derived from the model structure developed in Chapter Six. Alternatively, Li, Crampin & MacBeth [1993] have now developed a method for finding the polarization directions of non-orthogonal shear-waves using four-component data without the need to use the vertical component data. This would be the best method to use if the vertical component has a different sensitivity.

Changes in source positions

The positions of sources at S1 and S4 change during the VSP run at two depths by 3m (but 5m for one change in source location at S4). The depths at which the source position changes are 549m and 419m for S1 and 709m and 495m for S4. These depths are marked on the relevant figures by open triangles. The changes in ray path for such small lateral changes in source position are small and are unlikely to have an effect. Figures 5.21 and 5.22 show that there are no breaks in the estimates at depths where the source position changes. There is a break in the polarization estimates at around 550m; however, this is also seen in W4S2 for which the source positions are constant.

Single source estimation technique (DTS)

DTS was applied to all the offset data in the dynamic axes (Figures 5.18 and 5.19). The results are scattered; however, both polarization angles and time delays for each source at a given offset are consistent. Polarization angles are generally between N50°E and N100°E for the near-offset data and over N100°E for the far-offset data. Time delays are around 10ms in all cases. Here, the source directions are close to

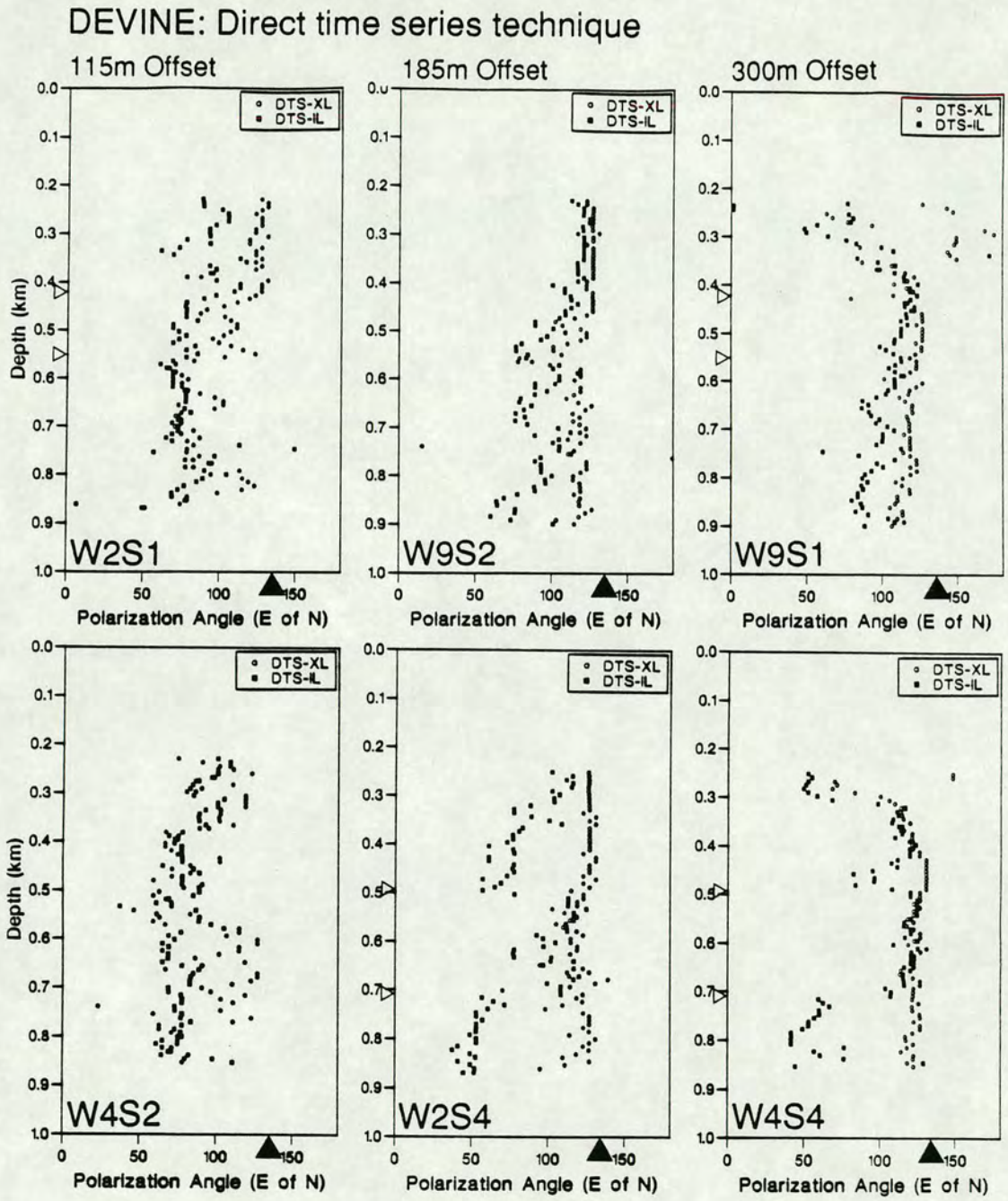

FIGURE 5.18: DTS estimates of polarization angle for both sources for all offset data at Devine. Results are consistent for each source at each offset. The solid triangles mark the radial direction. The open triangles mark depths at which the source position was moved.

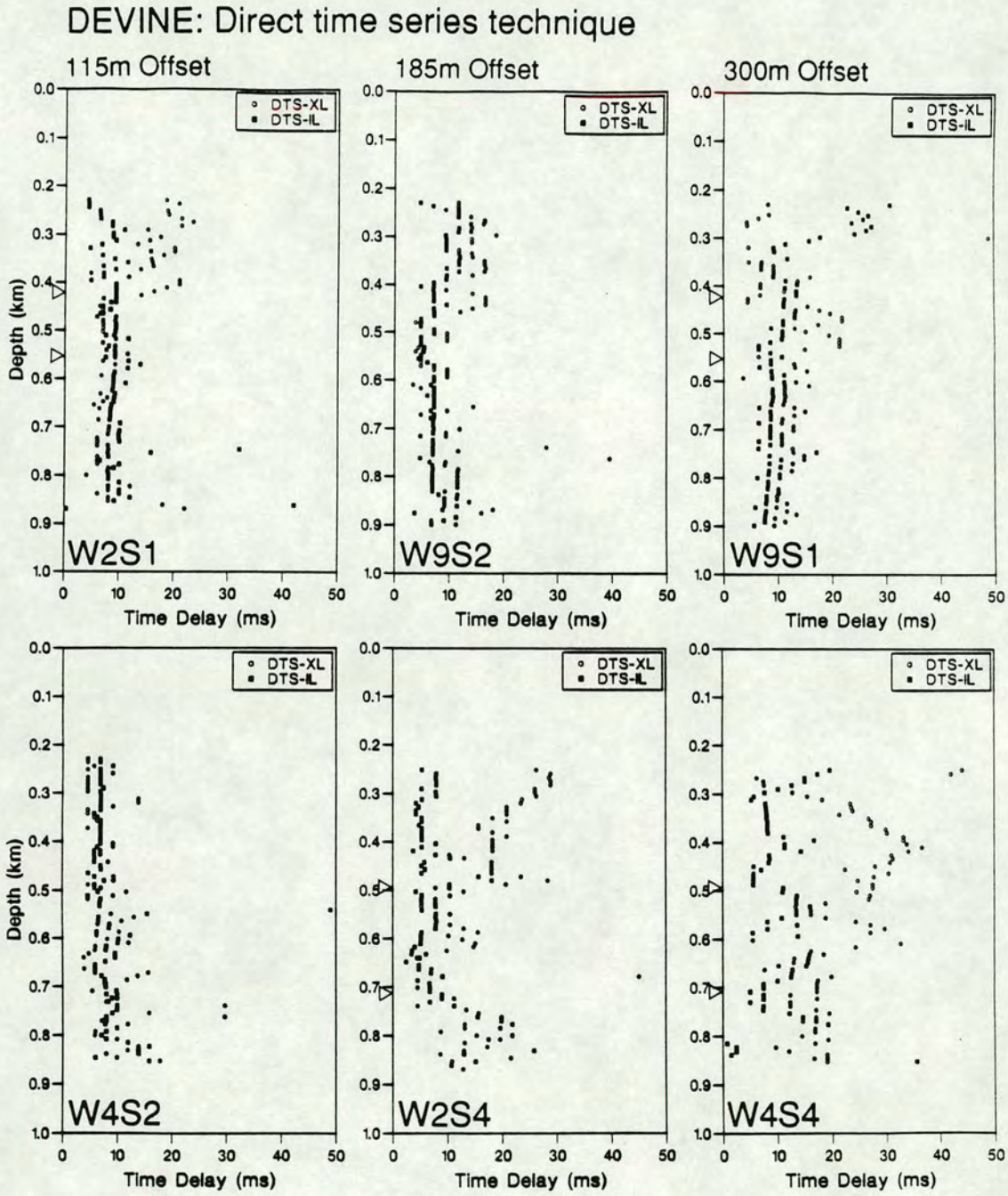

FIGURE 5.19: DTS estimates of time delay for both sources for all offset data at Devine. Results are consistent for each source at each offset. Open triangles mark depths at which the source position was moved.

anisotropic symmetry directions, in such cases single source techniques give poor results as the arrival is nearly linearly polarized.

Double source estimation techniques (AST and AIT)

Both AST and AIT were applied to all the offset data. *SV*- and *SH*-sources have different shear-wave radiation patterns [Edelmann & Schmoll 1983]. For offset data, the recorded signal from the inline and crossline sources have different energies and I used the source balancing versions of AST and AIT (Section 2.7). The effect of different inline and crossline radiation patterns is mitigated by the velocity structure (Figure 6.2) as most rays leave the source position at steep angles where there is little difference in radiation patterns. Also, Zeng & MacBeth [1993a] show that source strengths must differ by at least 50% before the estimated polarization angle changes by more than 5° from the true value.

The effects of source balancing and calculations in the dynamic plane are shown in Figure 5.20. The example shown is for a 300m offset VSP as this has the widest incidence angles and hence, the most severe source balancing problems. Most of the observed change in estimates is caused by performing the calculations in the dynamic axes. This shows that it is necessary to correct for non-orthogonal shear-waves. Polarization angles change more than time delays. In general, the crosscorrelation used to calculate time delays is stable in the presence of distortions [C.MacBeth, personal communication]. The source balancing correction does not produce large changes in the results. Therefore, differences in source radiation patterns are not significant for this data set, as expected by Zeng & MacBeth [1993a].

Both versions of AST and AIT were run on all the offset data in both dynamic and horizontal planes. Figures 5.21 and 5.22 show polarization angle and time delay estimates for all offset data using the source balanced forms of AST and AIT in the dynamic plane. Results from both techniques in each offset grouping are consistent. The 115m offset gives similar results to the zero-offset data as expected for such a short-offset. All offsets show similar results at depth as ray paths through the upper structure, where most of the time delay builds up, are similar (see Figure 6.2). The source and geophone estimates from AIT are close together indicating that there is

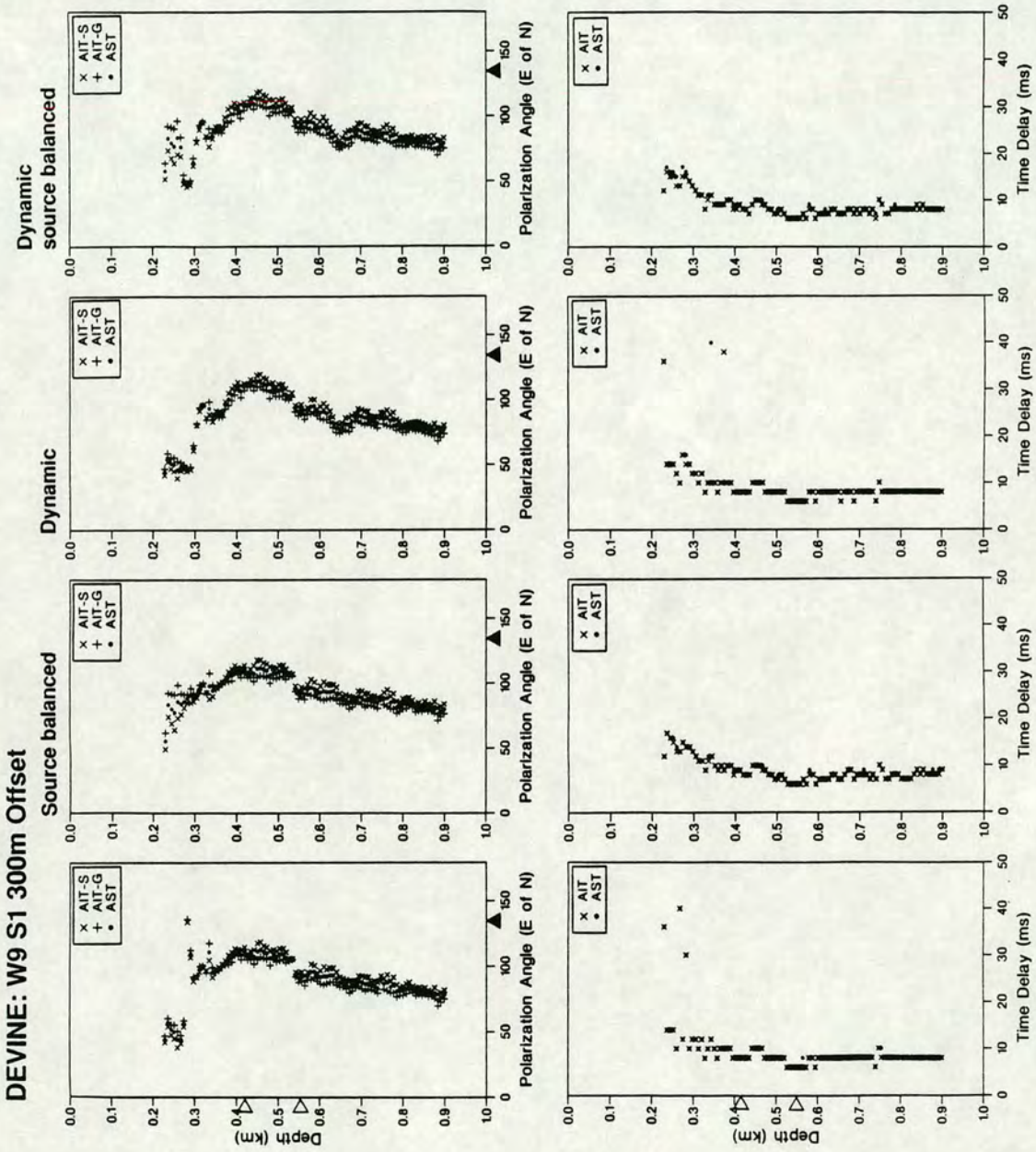

FIGURE 5.20: A comparison of different analysis methods on the 300m offset W9S1 VSP. Adaptations of AST and AIT are used which balance the energies of the sources and these are applied in both the horizontal plane and the dynamic plane containing the shear-wave energy. In each case, the radial direction is marked with a triangle.

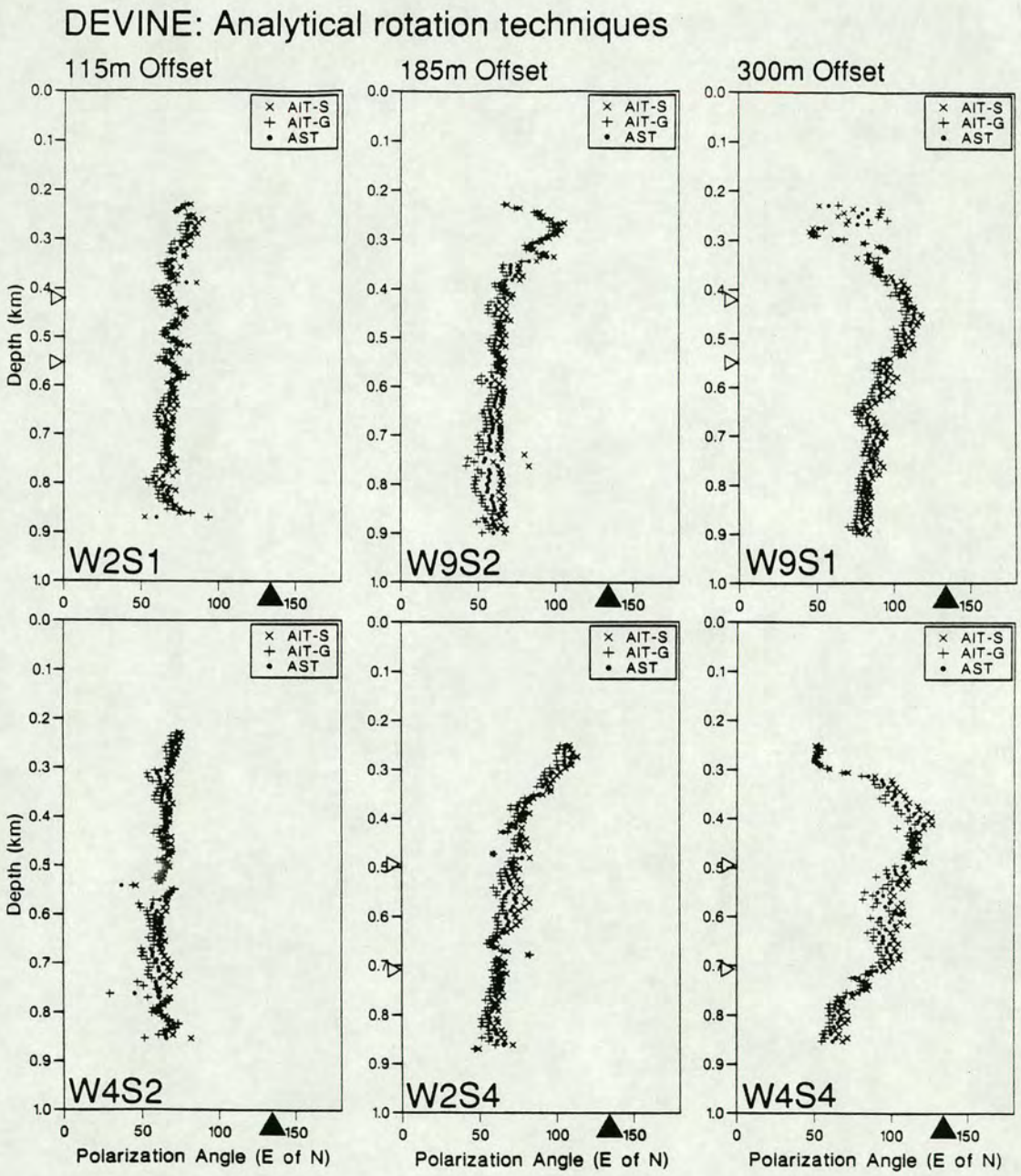

FIGURE 5.21: Polarization angle results of source balanced AST and AIT applied in the dynamic plane for all of the offset data at Devine. At depth all offsets show similar polarizations, around N55°E; however, the polarization angle varies with depth for the wider offsets. The solid triangles mark the radial direction. The open triangles mark depths at which the source position was moved.

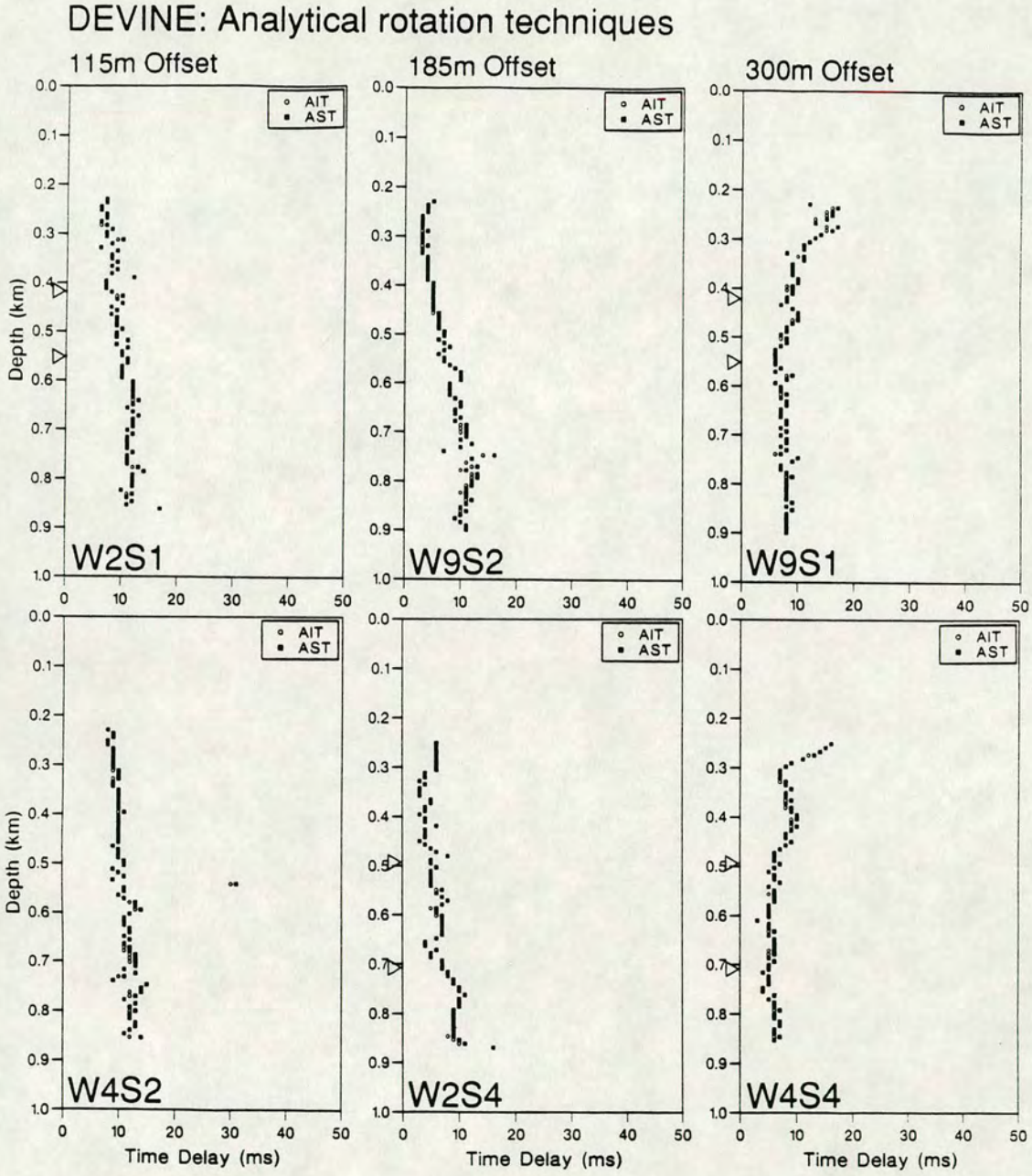

FIGURE 5.22: Time delay results of source balanced AST and AIT applied in the dynamic plane for all of the offset data at Devine. At depth all offsets show a similar time delay, around 12ms; however, the variation with depth of time delay is offset dependent.

neither multiple splitting or source misalignments. The time delay and polarization angle vary differently with depth for each offset grouping.

The polarization direction at shallow levels in W4S4 is about N45°E which is consistent with shallow incidence angles through horizontal thin layer anisotropy. However, these shallow incidence rays are distorted by mode conversions (Figure 5.6) and the near-surface estimates may not be meaningful. Also, for wide-offset data, all polarization estimates will tend to the transverse direction (N45°E) when projected onto the horizontal plane.

The similarity of the two DTS estimates and the AST estimate for each offset position shows that the inline and crossline sources had similar characteristics (phase, shape etc). Large differences in the inline and crossline source characteristics would mean that AST does not give the same results as DTS as it has to combine the information from both source directions.

Propagator matrix technique (DPM)

DPM was run in both the dynamic and horizontal plane for all offset (rotated) data. All but the 115m offset show very scattered results as DPM is only applicable for vertical propagation (Section 2.7). I used a variety of window lengths and calculation intervals. Figure 5.23 shows the results for a 500ms window over 10 geophone levels (72m) as this gave the least scatter. Results are N63.6°±13.5°E and N65.0°±17.5°E for W4S2 and W2S1 respectively which are consistent with results from the other techniques. The scatter is due to:

1) the small amount of anisotropy over the calculation interval;
2) errors in geophone rotation (this was based on *P*-wave arrivals rather than gyro-data).

The results shown are from the horizontal plane as estimates in the dynamic plane are more scattered. DPM is an interval technique (unlike the other techniques used) and, in this case, the separate rotation of each geophone into a local coordinate systems distorts the results.

As most of the anisotropy appears to be in the near-surface it is possible that the observed anisotropy is merely a product of interactions between the source and the

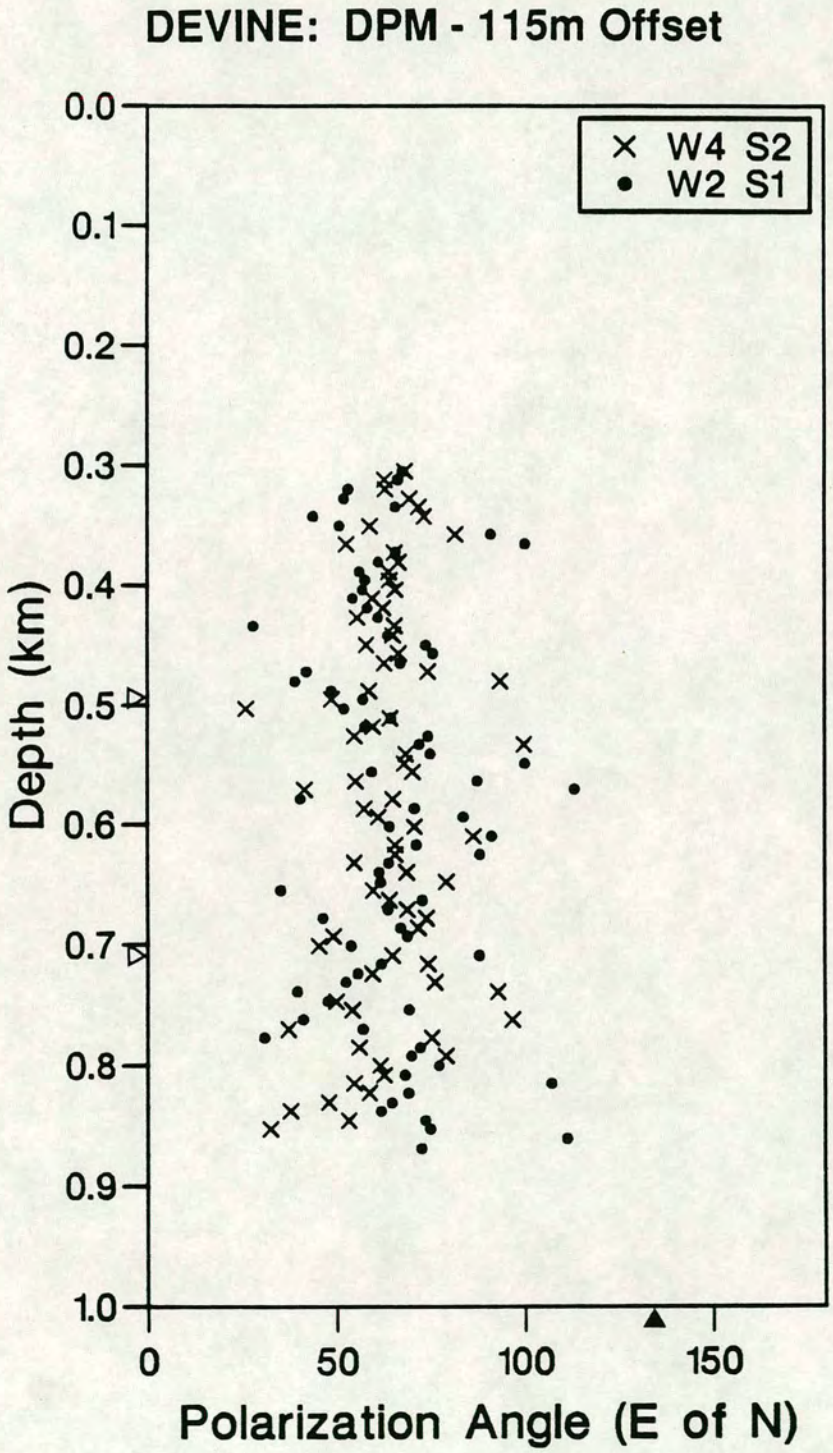

FIGURE 5.23: Polarization angle results of DPM for the 115m offset VSPs at Devine for a calculation over 10 geophone levels. Results are scattered around N63.6°±13.5°E and N65.0°±17.5°E for W4S2 and W2S1 respectively. The radial direction is marked.

surrounding rockmass (e.g. conversions). Campden *et al.* [1990] reinterpret a large apparent anisotropy at the Geysers, California, as a *P*-to-*S* mode conversion from the inline source caused by a thin low velocity layer at the surface. DPM is not affected by disturbances in the near-surface. The DPM results are important as their consistency with results from other estimation techniques indicate that the rockmass is anisotropic with a constant *qS1* direction with depth.

Layer stripping

It has been suggested [M.A.Meadows, personal communication] that layer stripping could be applied to this data. The above results and the regionally simple geological setting imply that the medium polarization is constant with depth. If layer stripping is applied incorrectly, or on inappropriate data sets it can introduce apparent anisotropy.

Anisotropic parameters determined by Raikes [1991]

Raikes [1991] extracted time delays from these data using a method similar to that used on the Dimmit data in Section 5.4.2. Here, the actual fast direction of the medium is 17° from the crossline direction. However, most of the crossline source energy excites the fast wave and most of the inline energy excites the slow wave and this method produces a good estimate of the time delay (12ms at depth). This method has the advantage that it is independent of source/receiver polarities. The similarity between the result determined here and those found by Raikes further confirms that I correctly determined the source/receiver polarities.

5.4.4 Devine Test Site: *P*-wave data

BP also provided the ARIS *P*-wave data (produced by adding the left, right, forward and backward shots together, Section 2.6). I analyzed this data set to see if the anisotropy parameters could be extracted from shear-waves created at a *P*-source or by deeper *P*-to-*SV* mode conversions. If satisfactory results can be obtained it might not be necessary to go to the expense of using separate shear-wave sources. This study also has implications in marine experiments where all shear-energy comes from mode

conversions as shear-waves do not propagate through fluids.

Analyzing shear-wave data from a *P*-wave source introduces problems not found in analyzing direct shear-wave data from a shear source. Firstly, the shear-wave arrival is preceded by the *P*-wave arrival which needs to be removed before anisotropy estimation techniques can be applied. Also, mode conversions only create *SV* energy (for a horizontal interface) and the robust double source estimation techniques cannot be used. Lefeuvre & Queen [1992] presented a method of using propagator matrix techniques on shear-wave data from *P*-wave VSPs if two, linearly independent, mode converted shear-waves are present. The mode conversions seen here are not linearly independent and as Lefeuvre & Queen's results were inconclusive I use DTS to extract the anisotropy parameters.

Unrotated P-wave data were supplied and I rotated the offset data in the horizontal plane by maximising the energy on the radial geophone component using a 70ms window around the *P*-wave arrival. The data are clean and the rotation gives good results with no *P*-wave energy on the transverse component. I applied an FK filter to pass the entire downgoing wavefield between 0 and 40Hz and enhance the shear-wave signal. An example rotated data set is shown in Figure 5.24. There is more shear-wave energy on the crossline component than expected from the level of anisotropy estimated from shear-wave sources at this site.

Source generated shear-waves

I examined the shear-wave arrival created at, or near, the source (Figure 5.24). This shear-wave arrival is seen at all offsets. It is well separated spatially from the *P*-wave energy and no steps were taken to remove the *P*-wave energy. I applied DTS in the horizontal plane, as previous work showed that the effect of using the dynamic axis is small. I picked time windows on the transverse component; this has less *P*-wave energy to confuse the picking. Results from the 185m and 300m offsets are shown in Figure 5.25. Both VSPs, at a given offset, give consistent polarization angles, which show a pattern similar to the direct shear-wave results, but are rotated clockwise (by at most 25° for the 185m offset and less than this for the 300m offset). It is possible that this is due to dipping structures in the near-surface leading to a

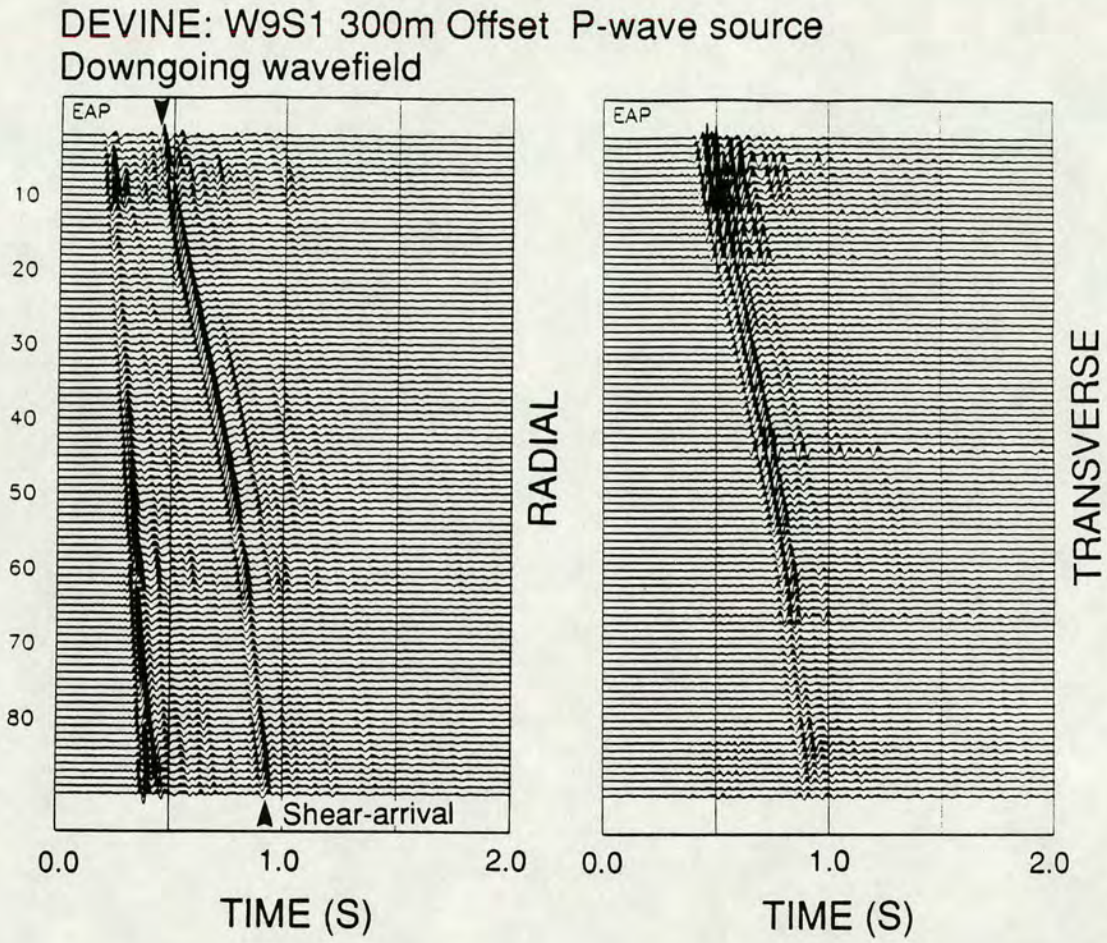

FIGURE 5.24: Radial and transverse components of the downgoing wavefield from a *P*-wave source for a 300m offset. A large shear-wave arrival is marked which is generated either at, or very close to the source.

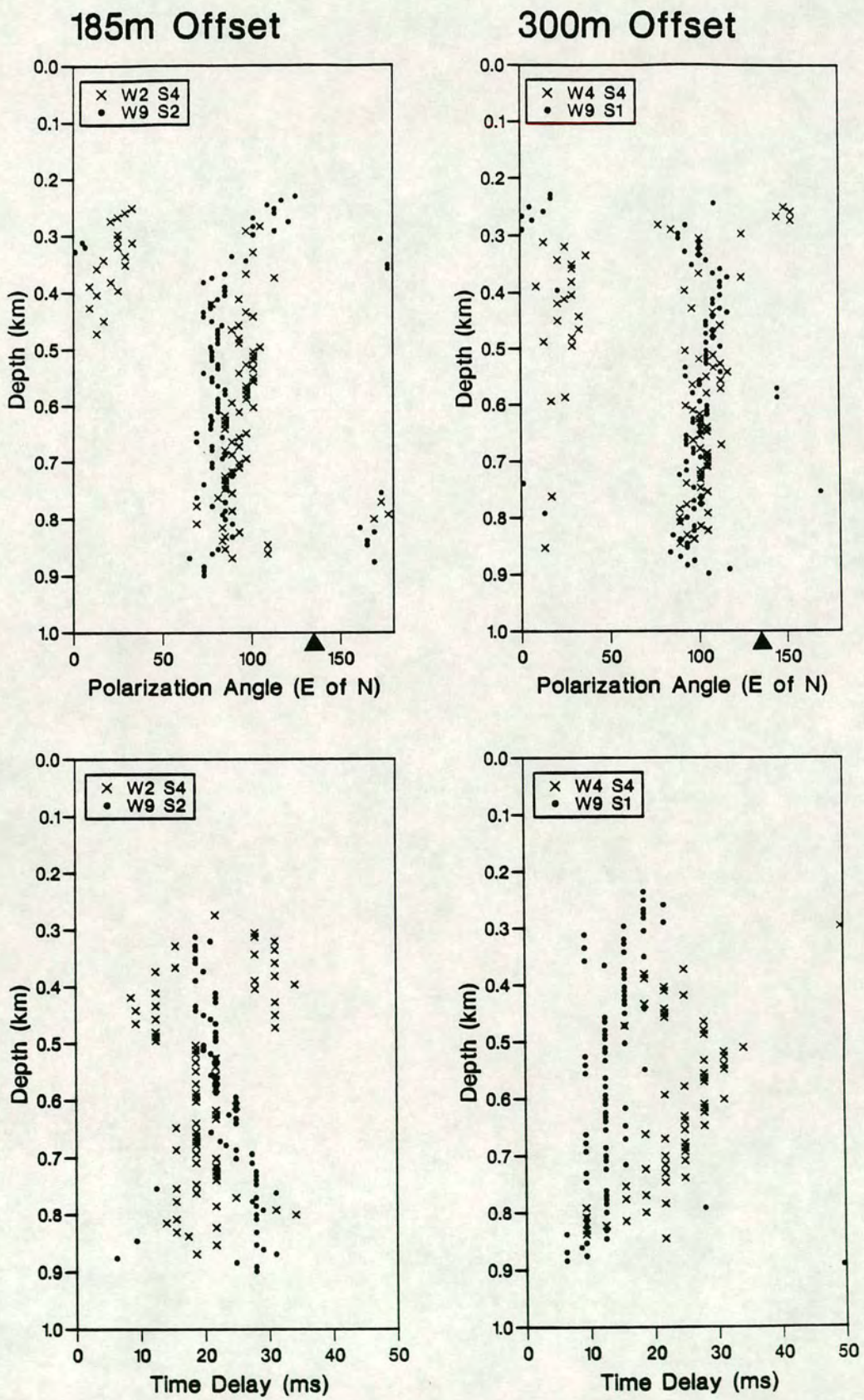

FIGURE 5.25: Results of DTS applied to the direct shear-wave arrival from the 185m and 300m offset *P*-wave sources. The radial direction is marked.

mode converted arrival that was not pure *SV*. DTS calculates the *qS1* polarization angle with respect to the source direction; therefore, knowledge of the source direction is required. A dipping mode converting interface would also account for the larger amounts of energy on the crossline component; however, there is no information about near-surface structures to support this. The time delays are more scattered and larger than found for the direct shear-wave (except for W9S1 which shows less scatter and matches previous results). It must be remembered that the time delays are small and that the fast direction is within 20° of the crossline direction, making it difficult for a single source technique to obtain satisfactory answers.

Mode converted shear-waves

I now try to extract the anisotropy parameters from deeper mode converted shear-waves (similar to those that would need to be examined in a marine environment). Figure 5.26 shows the two mode conversions in W9S1. Very little energy from the two arrivals can be seen on the transverse component implying little splitting. These arrivals are close to the *P*-wave arrival, which I removed by rotating the data set into the *P*-wave dynamic axis, zeroing the component containing the *P*-wave energy [Ahmed 1989] and rotating the data back into the horizontal plane. This works well for Arrival 1 which is well separated from the *P*-wave. Arrival 2 is very close to the *P*-wave and it is likely that some shear-energy was also present in the analysis window for the rotation which may bias the results. Also the *P*-wave energy and the shear-wave energy may not be normal to each other. However, this technique does remove the direct *P*-wave energy which is the cause of most of the noise in the shear-wave data. Some shear-wave energy will also be removed; the effect of this is similar to applying the estimation techniques in a plane at an angle to the shear-wave arrival. The analysis of the use of the estimation techniques in the dynamic, as opposed to the horizontal plane, showed that this has little effect. This level of processing is sufficient here, where visual inspection of the seismograms has already provided the main conclusion: that there is no splitting at depth. More detailed wavefield separation techniques would need to be used if more exact measurements of shear-wave anisotropy were to be made.

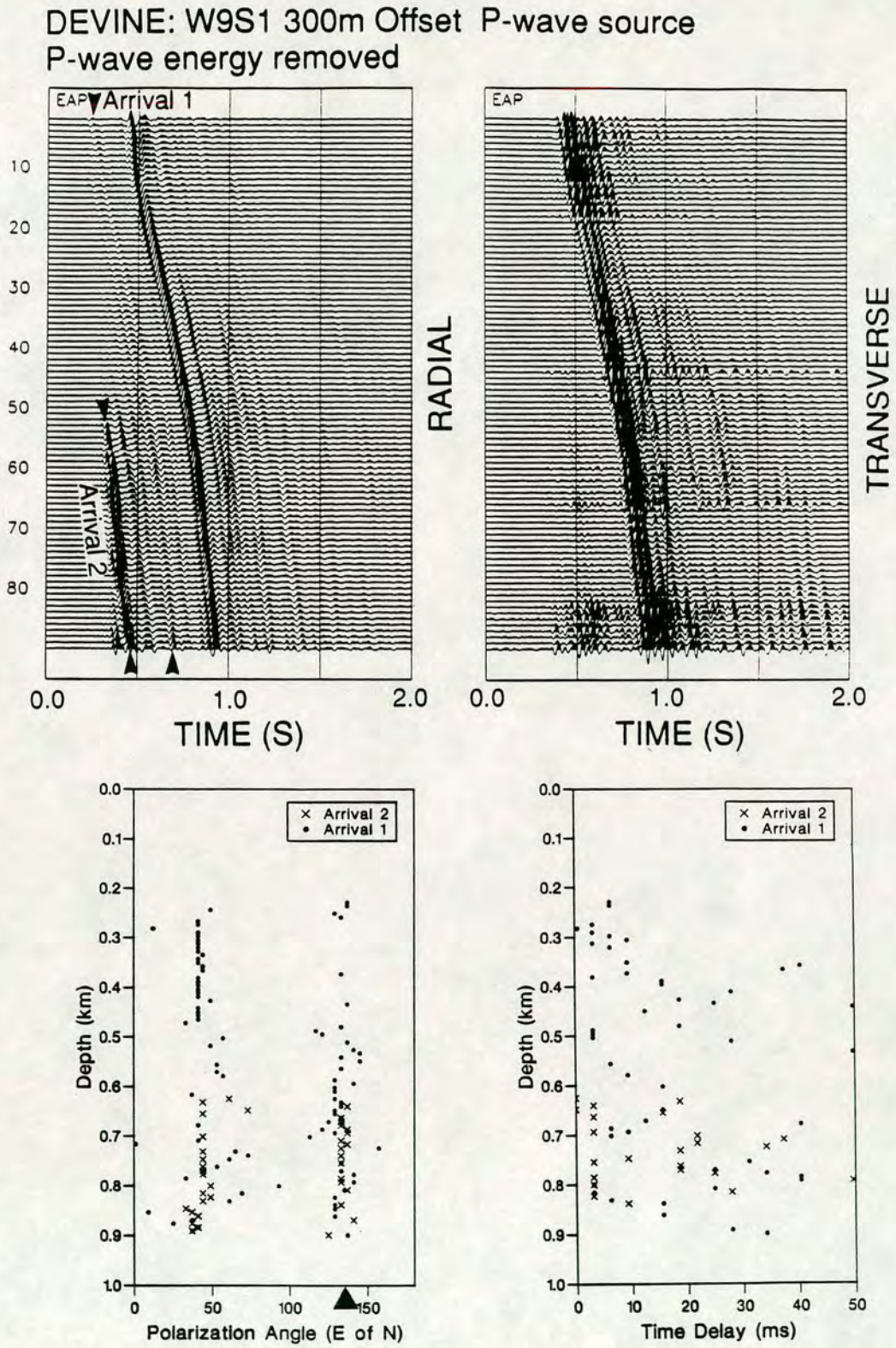

FIGURE 5.26: Radial and transverse components of the downgoing wavefield from a *P*-wave source after removal of the *P*-wave energy. Also polarization angle and time delay estimates calculated using DTS are shown for the two marked arrivals. The radial direction is marked.

The results of DTS on these arrivals are shown in Figure 5.26. The polarizations cluster around the inline and crossline directions and the time delays are scattered with no consistent values. This is expected because previous work by Raikes [1991] and this study, show that most of the anisotropy is in the top 250m and these arrivals were created below this level.

I have shown that the anisotropy parameters can be extracted from shear-wave energy created from a *P*-wave source. However, there is little control of the source and if dipping mode converting interfaces are present the initial shear-wave polarization may be unknown.

5.4.5 Burleson County: Anisotropy parameters

A similar suite of estimation techniques to those run on the Devine data were used here. DPM was not used as the offsets are large and the assumption that signals to different geophone levels follow the same ray path apart from the interval between the levels is not valid (Section 2.7). Results from obviously bad levels (see Figures 5.10 to 5.11) were omitted from all plots.

LTT was applied to the zero-offset data for a range of window lengths. Results are stable for window lengths that included most of the downgoing shear-wave energy. LTT, for a 300ms window, gives a polarization angle for the fast shear-wave of about N103.1°±2.8°E for the interval below 1.8km where the results are stable (Figure 5.27). This is close to the EW fracture orientation found by Amoco in this area from cores and shear-wave splitting [M.C.Mueller, personal communication]. This direction is also consistent with stress measurements at this location (Figure 5.1b). The time delay increases down to 1.5km, below which it is constant at 30.1±0.8ms.

Anisotropy estimation techniques on offset data

The estimation techniques were run in both horizontal and dynamic planes. As with the Devine data the difference between results from the two planes was not great and only results from the dynamic plane are shown here. Figure 5.28 shows shear-wave incidence angles for the three offset VSPs that I used to rotate the data into the dynamic plane. VSP2 and VSP3, with similar offsets, have incidence angles

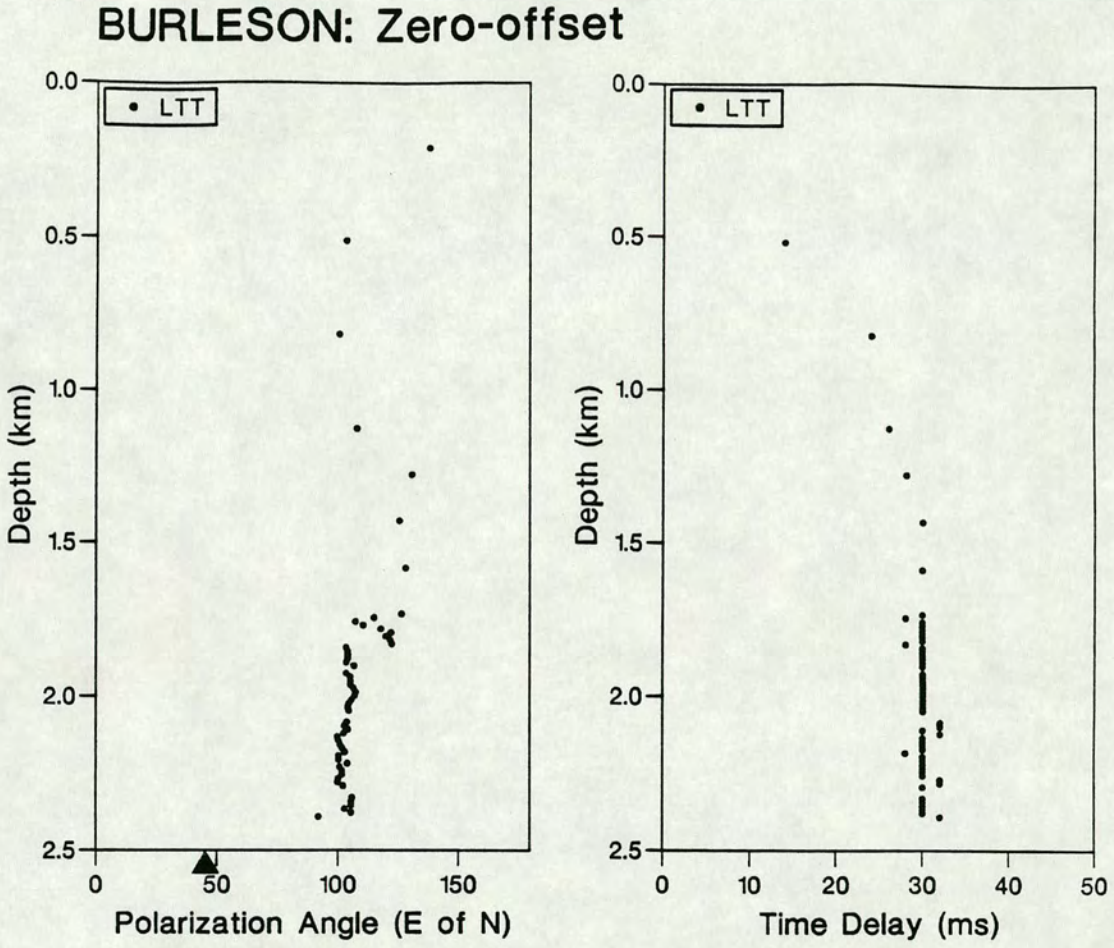

FIGURE 5.27: Polarization and time delay estimates using LTT on the zero-offset VSP at Burleson County calculated for a 300ms window. The radial direction is marked.

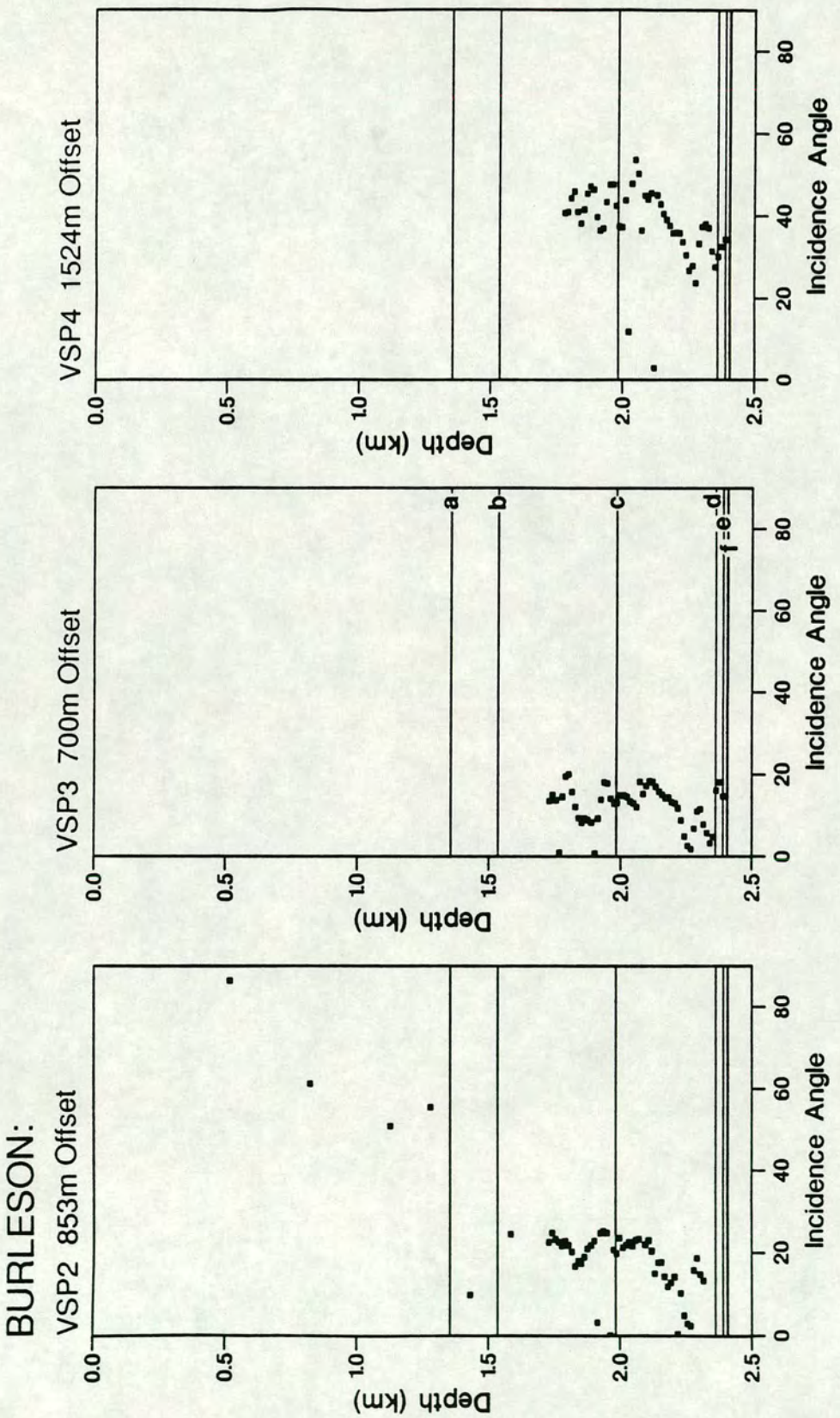

FIGURE 5.28: Angle of incidence of incoming shear-waves from inline source at the A.B.Childers #2 well. The marked interfaces are: a) Midway; b) Navarro; c) Pecan Gap; d) Austin Chalk; e) Base of Austin Chalk and f) Eagleford [M.Mueller, personal communication].

below 20° at depth. VSP4 (1524m offset) has incidence angles around 40°.

Results from DTS were scattered and I show only the more stable results from AST and AIT here. [The PDs for VSP3 (700m offset) and VSP4 (1524m offset) are nearly linear (Figure 5.12). In cases, such as this, where there is only significant energy from one split shear-wave single source techniques are highly sensitive to noise.] Results from AST and AIT on the offset data are shown in Figure 5.29. VSP2 shows a decrease in time delay and polarization direction. The source and geophone results of AIT are separated which can indicate multiple splitting [MacBeth & Yardley 1992], although apparent splitting can be caused by interface effects [Liu & Crampin 1990]. VSP3 shows tightly grouped polarization directions along the crossline direction and an increase in delay with depth. The arrivals for this offset are linearly polarized (Figure 5.12) and it was possible to check the results of AST and AIT by interactively picking the arrival times (on the maximum signal amplitude) for the arrivals from the inline and crossline sources. The delays calculated by this method are shown in Figure 5.30 and agree with AST and AIT results.

VSP4 gives more scattered polarization angle results with the AST estimates changing from about N115°E in the upper part of the section to about N10°E in the lower part. Time delays go through a minimum indicating a singularity at around 2.0km as expected from analysis of the polarization diagrams (Figure 5.12). A direct interpretation of the results of the estimation techniques is not possible if multiple splitting has occurred (Chapter Four). Source and geophone polarization estimates from AIT are about 20° either side of the AST results which may indicate a change in polarization direction of the medium along the source-receiver ray path.

Results from estimation techniques with the source balancing correction are not shown here as the source and geophone results of AIT are separated in VSP2 and VSP4 indicating multiple splitting. The source balancing correction assumes no multiple splitting and in this case does affect the estimates, particularly for VSP4.

5.5 CONCLUSIONS

In this chapter I have extracted the anisotropy parameters from VSP data at three sites. For the Devine and Burleson data polarization angles and time delay results

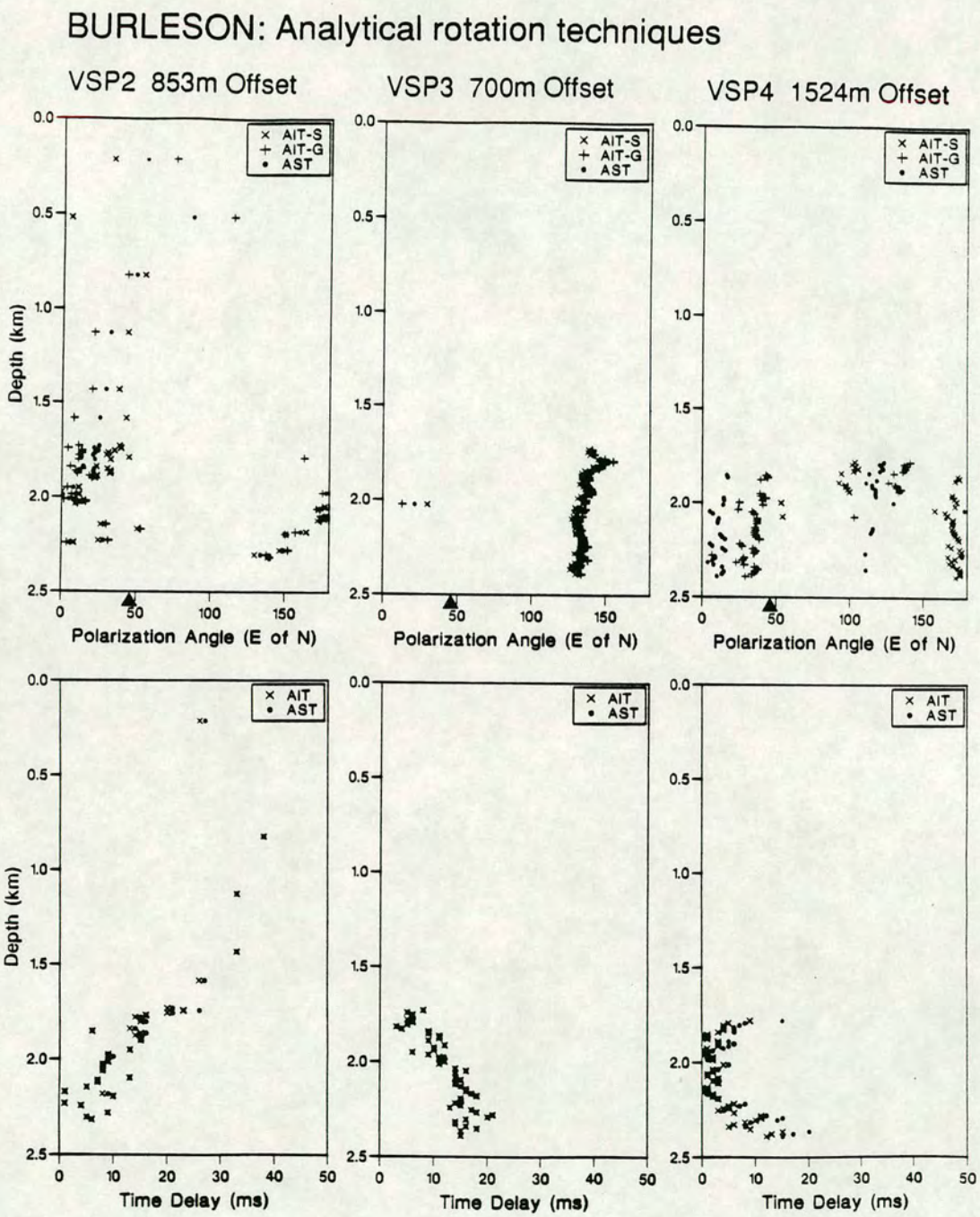

FIGURE 5.29: Results from AST and AIT applied to all offset data at the A.B.Childers #2 well. Two source estimation techniques give less scattered results than single source results; however, there is still a large amount of scatter for the furthest offset. The radial direction is marked.

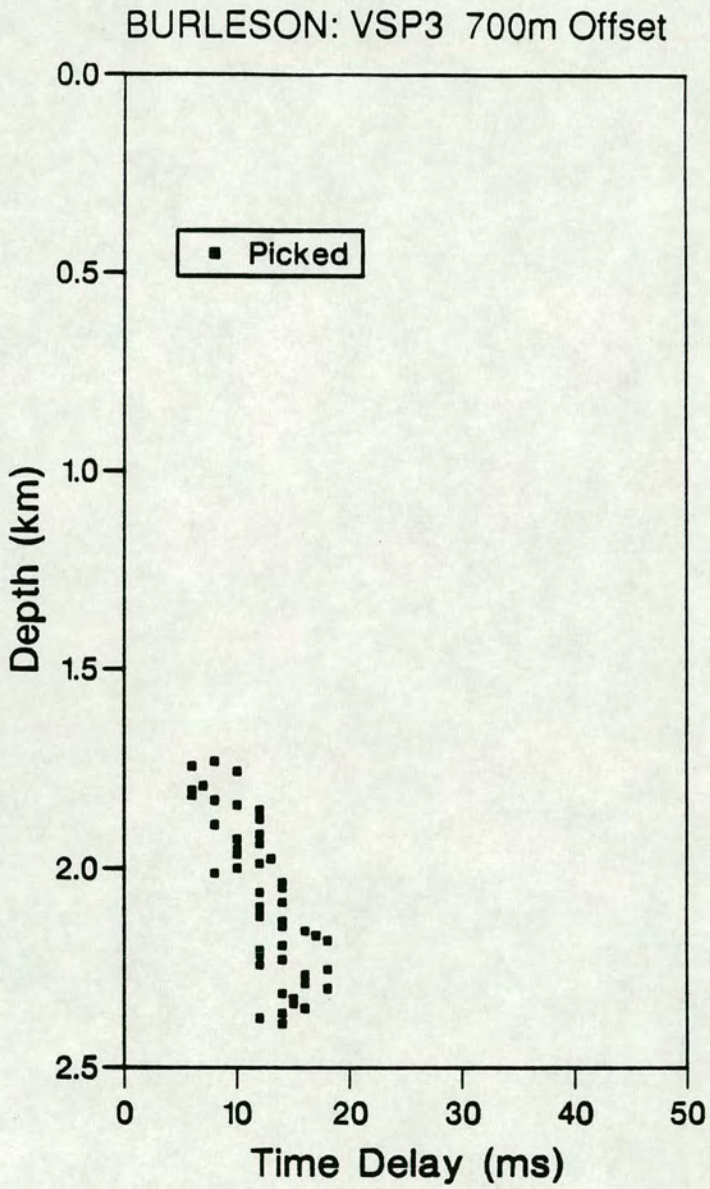

FIGURE 5.30: Time delay between the inline and crossline sources for VSP3 giving a fast direction along approximately N135°E, which is the crossline direction, this result is consistent with those from the estimation techniques (Figure 5.29).

change with offset. This is likely to be the effect of different ray paths through a homogeneous anisotropic medium, rather than changes in the anisotropic structure along the different ray paths. Modelling is required (Chapter Six) before *qS1* polarizations can be interpreted in terms of the anisotropic structure. However, in the zero-offset VSPs, most of the observed time delay is built up in the near-surface with little resolvable anisotropy at depth. The determined polarization angles are consistent with known stress and fracture directions. Shear-waves generated by *P*-wave sources, and at later mode conversions, also gave similar anisotropy parameters. More work needs to be done on wavefield separation in the presence of anisotropy.

This analysis has raised some points about the experiment design and the application of the estimation techniques:

1) Source and receiver polarities can be determined uniquely using the estimation techniques. Estimation techniques can still give plausible results if incorrect source and receiver polarities are used and it is only by using a suite of techniques that such errors can be detected.

2) Results of single source estimation techniques are degraded if the source orientation is close to the fast or slow directions. In planning acquisition geometries it would be useful for the radial direction to be at least 30° from the probable crack strike so that the shear-wave arrival from each source contains energy from both split shear-waves.

3) The difference in polarization estimates calculated in the horizontal and dynamic planes is not large for these data sets, even for the Devine 300m offset data which has incidence angles of 20°. Although, the incidence angle was determined from the incident shear-wave energy which gives an underestimate and it might be better to use calculate the incidence angle using a synthetic model structure.

4) For the Devine data set source balancing does not affect the polarization and time delay estimates. This is consistent with the conclusions of Zeng & Macbeth [1993a].

5) Inadequate knowledge of a mode converting interface can lead to errors in polarization angle estimates using DTS which calculates angles with respect to the source direction.

CHAPTER SIX

SHEAR-WAVE ANISOTROPY IN THE AUSTIN CHALK, TEXAS: MODELLING

6.1 INTRODUCTION

In this Chapter, I model the estimates of *qS1* polarization direction and time delay determined in Chapter Five. The Devine Test Site data have a total of nine VSPs, six of which are offset. This data coverage allows much better control on the nature of the anisotropy used in the models than was possible in Chapter Four with a single zero-offset VSP. I obtained a good match with the observed data using a combination of vertical, aligned, Hudson cracks and horizontal PTL-anisotropy. Most of the azimuthal anisotropy is in the near-surface and modelling shows that it is caused by vertical features, aligned with known stress and fracture directions. The most likely cause is that it is due to fractures which formed in the current stress field.

The anisotropic structure is similar at the other two sites; with most of the azimuthal anisotropy in the near-surface and *qS1* polarization directions that are parallel to known fracture and stress directions. Analysis of transmitted shear-waves shows no resolvable anisotropy in the Austin Chalk, even though the chalk is known to contain a fractured reservoir at Burleson. The Austin Chalk is thin at Burleson and may still be anisotropic. In Chapter Seven, I use reflected amplitudes to examine the anisotropy in the Austin Chalk.

6.2 MODELLING OF THE DEVINE TEST SITE

The Devine Test Site data provide the most complete data set to model. In this section, I develop an anisotropic model of the upper 900m at Devine which matches the estimates of polarization angle and time delay determined in Chapter Five. I do this by adding anisotropy to an isotropic velocity model. BP provided a suite of well logs from W9 (Figure 6.1) and a geological column to aid modelling. The region consists of subhorizontal layers (see Figure 5.2) and it is appropriate to use ANISEIS for the modelling.

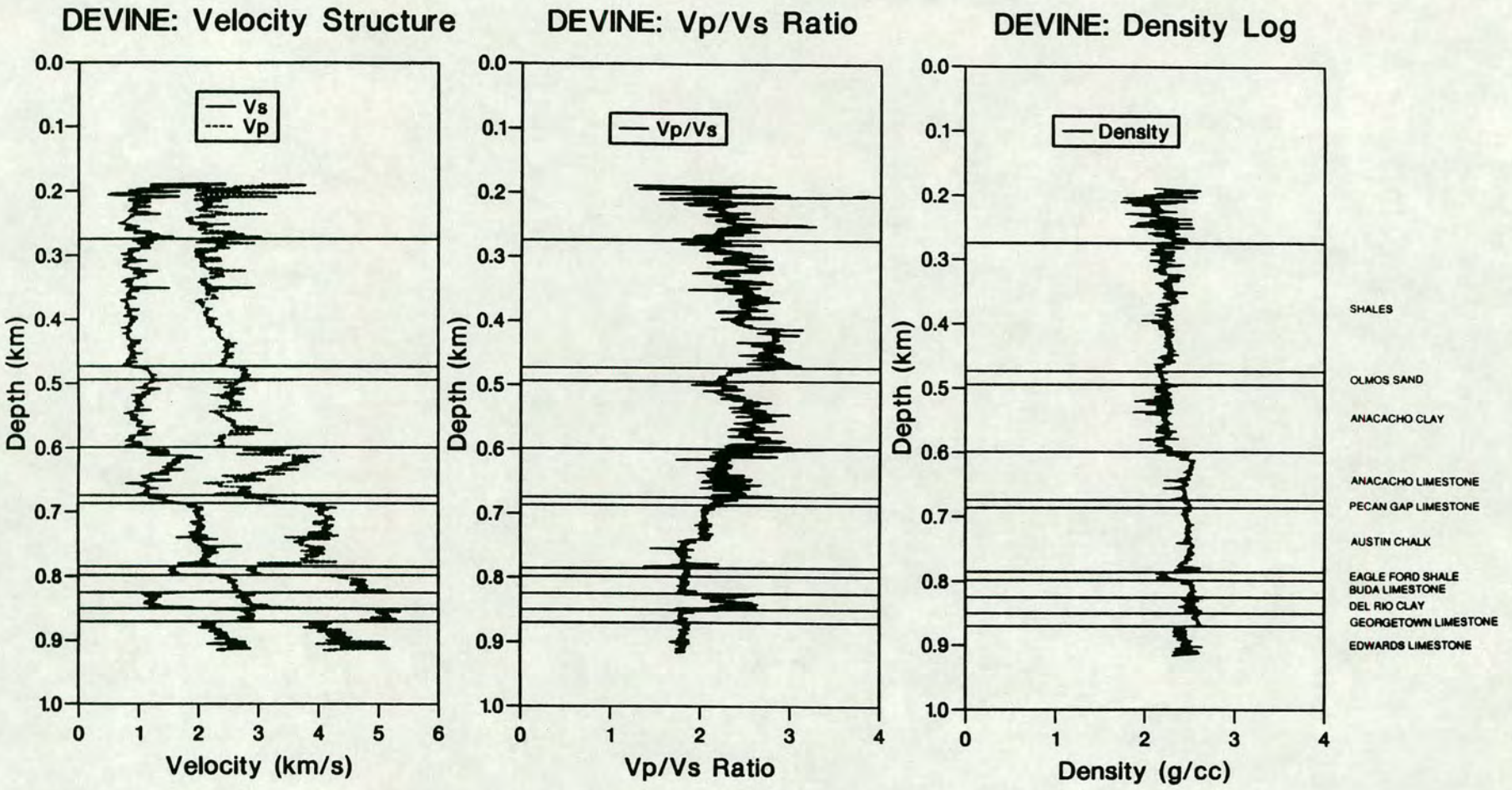

FIGURE 6.1: Corrected *P*-wave and shear-wave velocities and density well logs from W9 at the BP Devine test site with formations taken from geological logs. The Austin Chalk is characterised by an increase in velocity. The *Vp/Vs* ratio decreases from a maximum of about 2.8 at 0.45km to about 1.8 at 0.9km. Densities are stable except for a step from 2.2 to 2.5g/cm^3 at the top of the Anacacho Limestone.

6.2.1 Isotropic velocity model

The first step was to produce an isotropic velocity model. The shear-wave velocity structure was inverted using arrival times picked from the fast section from W2S2 (as determined by LTT). These velocities give the required isotropic matrix velocity as, for thin cracks, the velocity of the fast split shear-wave is the isotropic matrix velocity (Section 2.5). W2S2 was used as it has data coverage into the near-surface and gives the most consistent results for LTT (see Figure 6.9). Layer boundaries were taken from the geological logs and the top 272m, where there is no geological information, was split into three layers. I did not use a more complex model because:

1) the estimation techniques are insensitive to changes in anisotropic structure over short path lengths [Section 3.6.2; MacBeth & Yardley 1992].
2) I have little information about the near-surface structure, where the dominant azimuthal anisotropy is concentrated.
3) This model provides a good fit to the observed results.

The *P*-wave velocity for each model layer was taken from the Vp/Vs values calculated from the sonic logs. I took the density for each layer from the density logs. Synthetic seismograms were calculated and arrivals times compared with the observed data. The velocity of the upper layer (which is least well constrained) was adjusted until a match of arrival times with the observed data was achieved. The isotropic model velocity structure matches well with the sonic velocities (compare Figures 6.1 and 6.2). Model parameters are shown in Table 6.1.

6.2.2 What are the causes of the anisotropy?

Before anisotropic modelling, I must decide what types of anisotropy to add to the model. The geological section is made from a sequence of subhorizontal layers. In the upper structure, down to the Anacacho Limestone at 594m, these are predominantly shales with interbedded sands and limestones. Thin layer anisotropy is found in other horizontally layered sedimentary sequences [Bush & Crampin 1991]. Shales are also present in this structure. Lamination in shales causes them to be anisotropic [Kaarsberg 1968; Miller, Costa & Schoenberg 1992]. Therefore, it is likely that thin layer anisotropy is present. The results from Chapter Five show that shear-wave

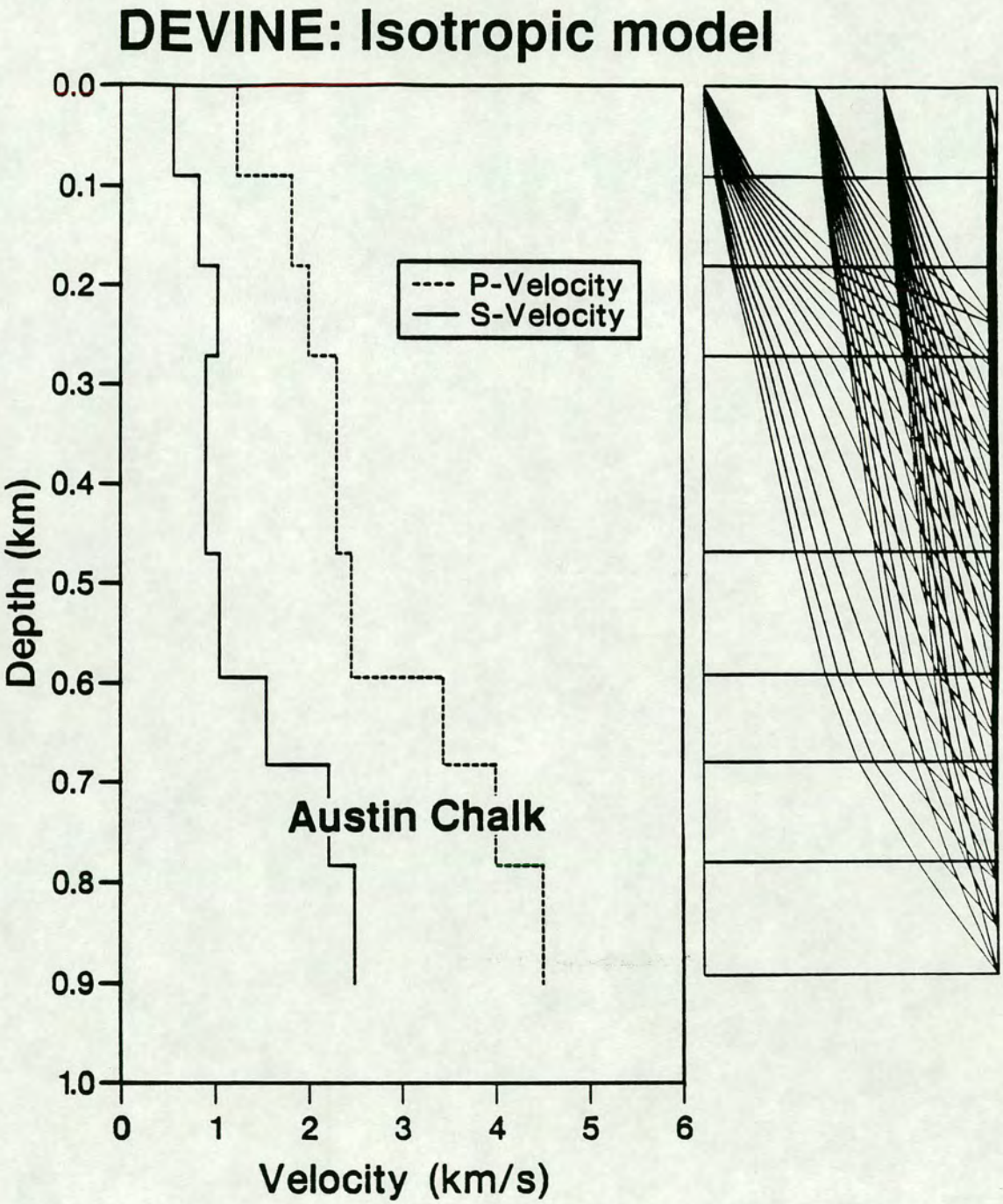

FIGURE 6.2: Isotropic model for BP's Devine test site together with ray tracing through the structure. The modelling assumes that the structure at the site is laterally invariant, therefore each of the real offset VSP groupings (containing either two or three VSPs) are modelled as a single VSP. These have offsets of zero (10m), 115m, 185m and 300m.

TABLE 6.1: Parameters for models of the BP Devine test site.

ISOTROPIC MODEL PARAMETERS

Layer	Thickness (km)	Density (g/cm^3)	*Vp* (km/s)	*Vs* (km/s)
1	0.092	2.20	1.236	0.562
2	0.090	2.20	1.822	0.828
3	0.090	2.20	2.000	1.031
4	0.198	2.25	2.300	0.905
5	0.124	2.20	2.460	1.050
6	0.088	2.50	3.440	1.550
7-Austin Chalk	0.101	2.50	4.000	2.217
8	Halfspace	2.50	4.500	2.488

ANISOTROPIC MODEL PARAMETERS

	Crack strike (N°E)	Crack density ε	% PTL anisotropy
Model 1			
Layer 1	62°	0.038	-
Layer 2	62°	0.026	-
Layer 3	62°	0.013	-
Layer 4	62°	0.007	-
Model 2			
Layer 1	62°	0.038	4.0
Layer 2	62°	0.026	4.0
Layer 3	62°	0.013	4.0
Layer 4	62°	0.007	4.0

DIPPING CRACK MODEL PARAMETERS

	Crack strike (N°E)	Dip	Crack density ε
Layer 7 (W4S4)	67.5°	34°	0.10
Layer 7 (W9S1)	40.0°	34°	0.10

Cracks have a radius of 0.001m, an aspect ratio of 0.01 and are water-filled.

splitting is present even for vertical incidence. This cannot be due to horizontal layering (Section 2.4), so another mechanism must be present to produce splitting for vertically propagating shear-waves.

Azimuthal anisotropy

The Austin Chalk is often fractured [Corbett, Friedman & Spang 1987] and such fractures can cause the chalk to be anisotropic [Mueller 1992]. Fractures in this region are usually subvertical; However, a dipping fracture was seen in W4 and another in W9 [Raikes, personal communication]. Table 6.1 lists the dip and strike of these fractures. It is possible that some azimuthal anisotropy is due to fracturing.

Most of the observed time delay builds up in the top 250m. In the near-surface the lower overburden stress means that rocks are less well consolidated than at depth. The stress may not be sufficient to close up intergranular pores and micro-cracks in the rockmass. Anisotropy due to aligned pore space and micro-cracks has been proposed [Crampin, Evans & Atkinson 1984; Crampin 1985b, 1987a] as the cause of azimuthal anisotropy.

As dipping fractures are present at depth at this site [S.A.Raikes, personal communication] it is possible that the near-surface azimuthal anisotropy is also due to dipping features. However, the consistency between results from the two offset VSPs in each offset grouping, with opposite radial directions, implies that the structure has a horizontal plane of symmetry. A structure with dipping fractures, micro-cracks or pores cannot have a horizontal symmetry plane unless they dip in a direction 90° from the acquisition line and the fractures found at depth do not.

So contributions to the observed splitting may come from a mixture of horizontal thin layers and vertical fractures, cracks, or aligned pores. The exact nature of the azimuthal anisotropy does not affect the modelling. This is because an equivalent medium, to model the effects of aligned cracks, fractures or pores, can be created using Hudson cracks as long as their size is much less that the seismic wavelength (Section 2.3). Fractures can cross chalk units [Corbett, Friedman & Spang 1987]; however, it is unlikely that they are open for all of their length, meaning that their effective length is shorter. Synthetic studies show that Hudson's model still gives good

approximations to velocities where the open fracture length is close to the wavelength [Rathore *et al.* 1991]. I will therefore use Hudson cracks to model the azimuthal anisotropy. [In any case, this analysis shows that the large chalk intervals at Devine and Dimmit are isotropic.]

6.2.3 Cracked anisotropic model for Devine

I now try to create an anisotropic model to match the observed results. Although, the polarization estimates and the observed fracture strikes in W4 and W9 are different, I will try a single laterally invariant structure to model all offsets because:

1) the symmetry of the results for the offset data imply lateral invariance;
2) the observed fractures, which indicate lateral changes in fracture strike, are below the observed azimuthal anisotropy and do not contribute to the model;
3) the W9S4 polarization estimates may have been distorted by the near-surface anomalous velocity layer under source position S4;
4) the structure is simple and evidence (including well logs), in general, points to only regional changes in fracture and stress directions.

[In Section 6.2.6, I model changes in dipping fractures in the Austin Chalk to see if the observed fractures can be detected.]

Inserting Hudson cracks into the isotropic model

Horizontal thin layer anisotropy has no affect on the zero-offset estimates (Section 2.4) and the first step in producing an anisotropic model is to add crack induced anisotropy to the isotropic model to match the results of the zero-offset VSP.

I inserted vertical parallel Hudson cracks until the results of AST on the model data matched the field results. 3.8% anisotropy had to be added to the top layer, but the amount of anisotropy required decreased with depth. Only 0.7% anisotropy was required in the shale layer between 272m and 470m and it was not necessary to add any azimuthal anisotropy to the layers below this (including the Austin Chalk). Table 6.1 lists the anisotropic model parameters used and Figure 6.1 shows the geological sequence. I use a constant crack direction with depth because:

1) the results of DPM and AST are the same (Figures 5.23 and 5.21); the source and

geophone estimates for AIT are close to each other. Both these indicate no changes in crack strike;

2) known fracture strikes at depth in W4and W9 match the *qS1* polarization direction found in the near-surface by the estimation techniques;
3) observed fracture and stress directions in this region are constant with depth and vary only regionally [Corbett, Friedman & Spang 1987; Zoback & Zoback 1992].

In Chapter Four, I compared synthetic and observed PDs (by extracting a pulse shape from the field data and using it to produce synthetic seismograms in ANISEIS) to assess the fit of some models. Matching synthetic and observed polarization diagrams is only useful if there is a large amount of splitting which gives rise to characteristic shapes in the PDs which can be matched. Here, the time delays are small and the acquisition geometry is close to the polarization direction of the medium. This means that the PDs are elongated ellipses without characteristic features. Therefore, in this chapter, I assess the fit of the models by comparing the results of estimation techniques on the real and synthetic data. This means that the exact pulse shape used in the models is not critical and I used the standard ANISEIS pulse closest in shape to the observed pulse (Pulse 2, 18Hz, damping factor 5). [In order to extract a pulse from the field data the fast direction must be known. If there are errors in the rotation used to extract the pulse shape then the extracted pulse shape will be different from the source pulse as it will contain energy from both fast and slow arrivals. This will lead to problems in matching model and observed data.]

Once a match of time delays and polarization direction estimates had been found for the zero-offset data, seismograms for the offset source positions were calculated through the same model. Results from the estimation techniques on the synthetic seismograms (Model 1), together with observed results for each offset grouping, are shown in Figures 6.3 and 6.4. All results were calculated in the dynamic plane using AST with the source balancing correction. Model 1 gives a good match to the zero-offset results; however, the match decreases with offset, especially in the near-surface. The Model 1 time delay goes to zero at 340m in the 300m offset data. This occurs as the ray paths span the line singularity found in hexagonal materials (Section 2.4).

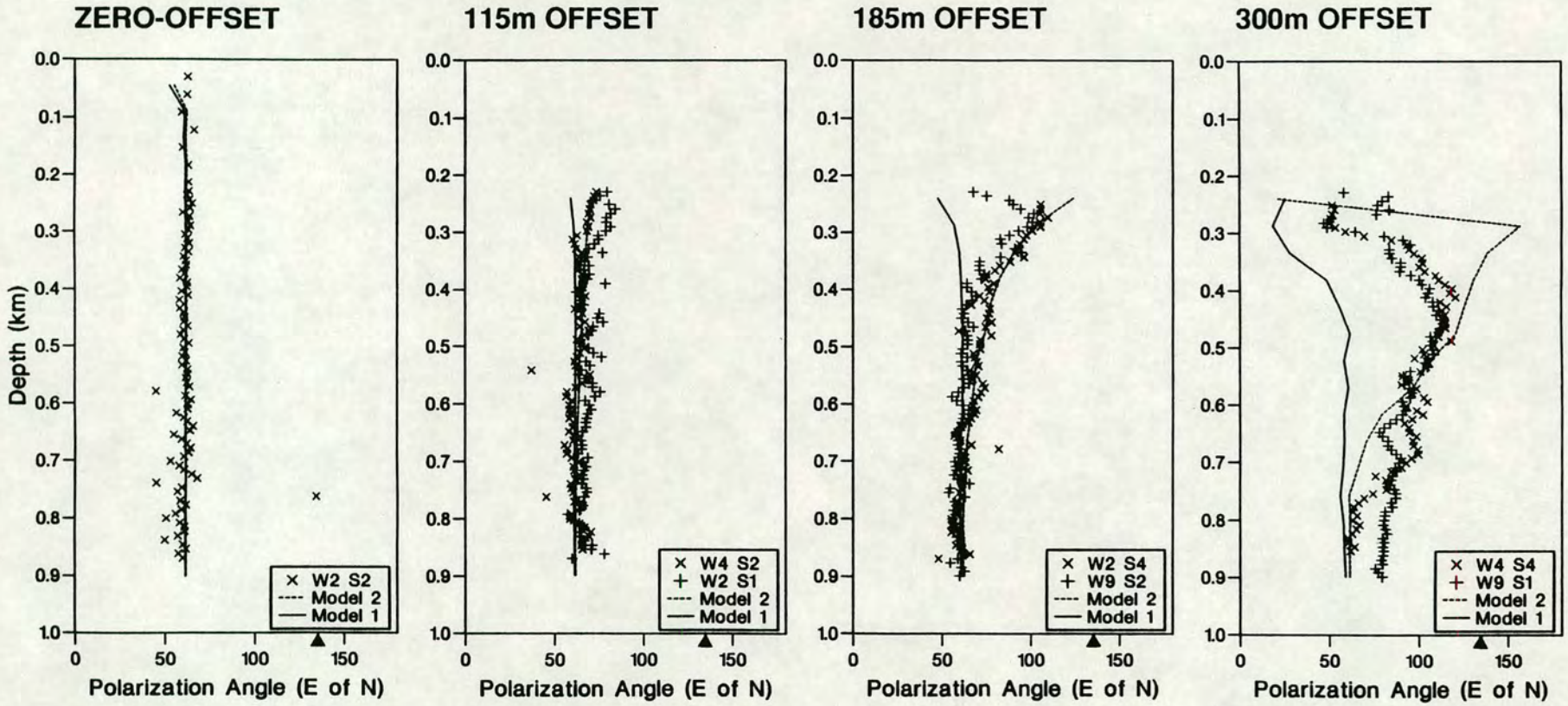

FIGURE 6.3: A comparison of modelled and observed polarization angles at each offset. Estimates were calculated using LTT on the zero-offset field data and AST on all other data. Model 1 contains just cracks, whereas Model 2 includes PTL-anisotropy (see Table 6.1). The addition of PTL-anisotropy (Model 2) gives a better match.

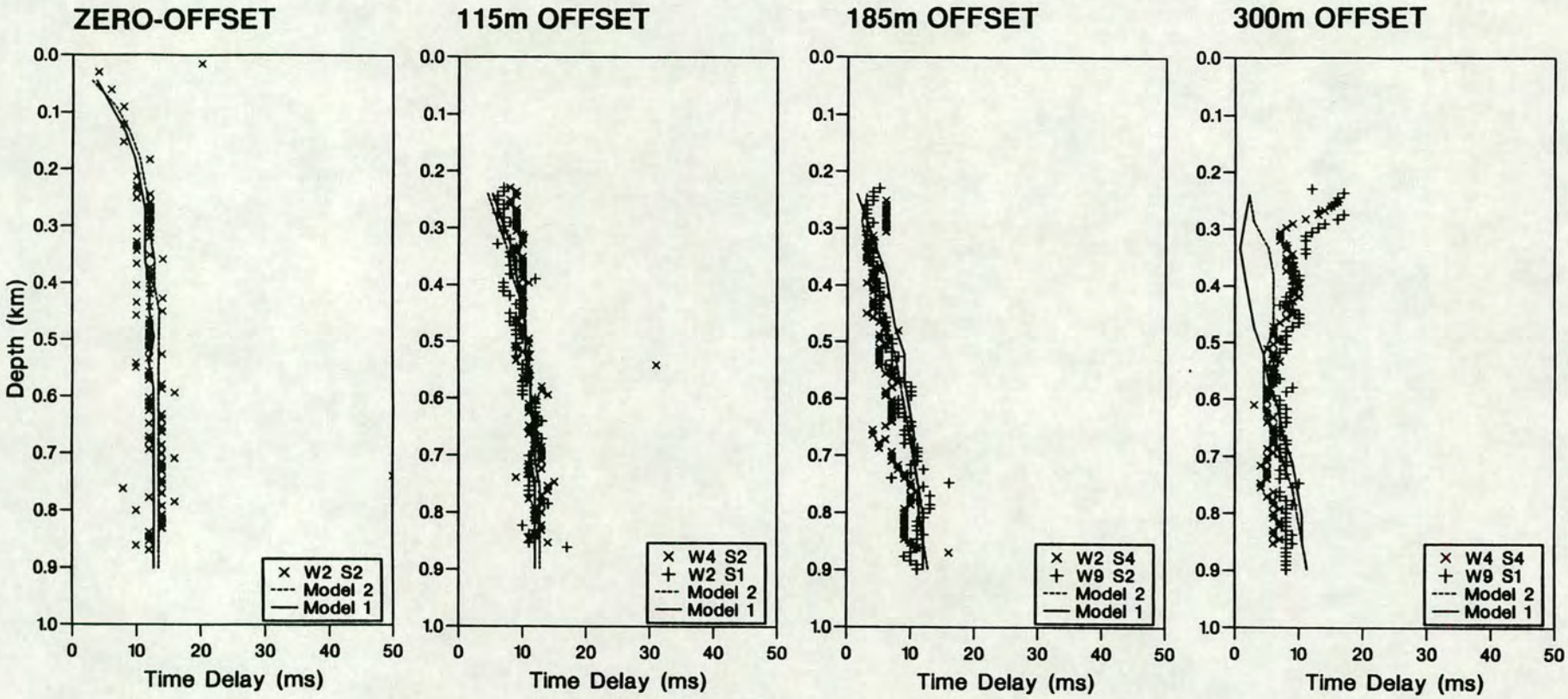

FIGURE 6.4: A comparison of modelled and observed time delays at each offset for the same models and estimation techniques as in Figure 6.3. Both models match well out to the 300m offset. Where Model 1 shows a zero point in the time delay which is not present in the observed data. The addition of PTL-anisotropy improves the fit.

6.2.4 Orthorhombic anisotropic model for Devine

I now add PTL-anisotropy to see if a better fit can be achieved. A range of PTL-anisotropies was tested. The shales in the geological column extend down to the Anacacho Limestone at 0.594km. However, I found that the addition of 4% PTL-anisotropy (Table 6.1) to the top four layers of Model 1 gives a good fit to the observed data (Figures 6.3 and 6.4). Anisotropic shales were found at depth in crosshole work at this site [Miller, Costa & Schoenberg 1992]. My main interest is in the Austin Chalk layer, and the anisotropic structure above it, which may affect measurements of the anisotropy in the chalk. I have not included these deeper shales in my model as they are below the Austin Chalk.

The addition of PTL-anisotropy changes the estimated polarization angles in the near-surface for the 115m and 185m offsets to match the observed results. The match is improved for the 300m offset with the polarization angle following the depth dependent changes in observed results, except in the near-surface where mode conversions mean that the field data are noisy. The time delay match has improved; the line singularity seen for the 300m offset in the cracked model is no longer present.

Observed and modelled polarization diagrams

In Figures 6.5 to 6.7, I compare observed and modelled PDs from the orthorhombic model. Whilst the match will not be exact, as an approximate pulse shape was used, the same features should be apparent in both.

For the 115m offset (Figure 6.5) the general character of the observed polarization diagrams has been matched with the major axis of the ellipse rotated slightly clockwise from the source direction. The direction of motion is clockwise for the inline data and anticlockwise for the crossline data. The match is good for the 185m offset data (Figure 6.6) with the major axis of the ellipse changing, with depth, from a few degrees anticlockwise to a few degrees clockwise of the source direction as seen in the field data.

In the 300m offset modelled data (Figure 6.7) there is a singularity, with a reversal in direction of motion, at 0.350km. This is not seen in the observed data. However, the field data are distorted down to around 0.330km due to mode

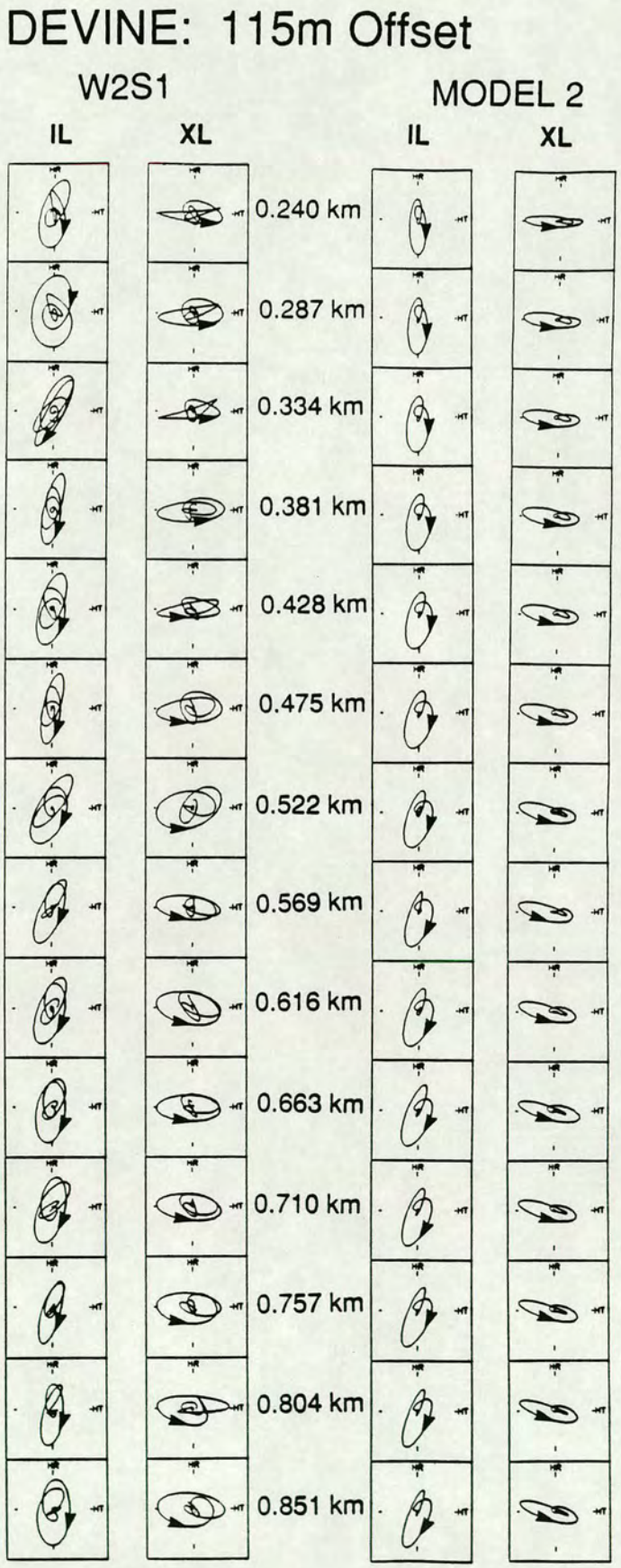

FIGURE 6.5: Selected observed and modelled horizontal plane shear-wave polarization diagrams from the 115m offset VSP for Model 2. The direction of motion is marked by an arrow.

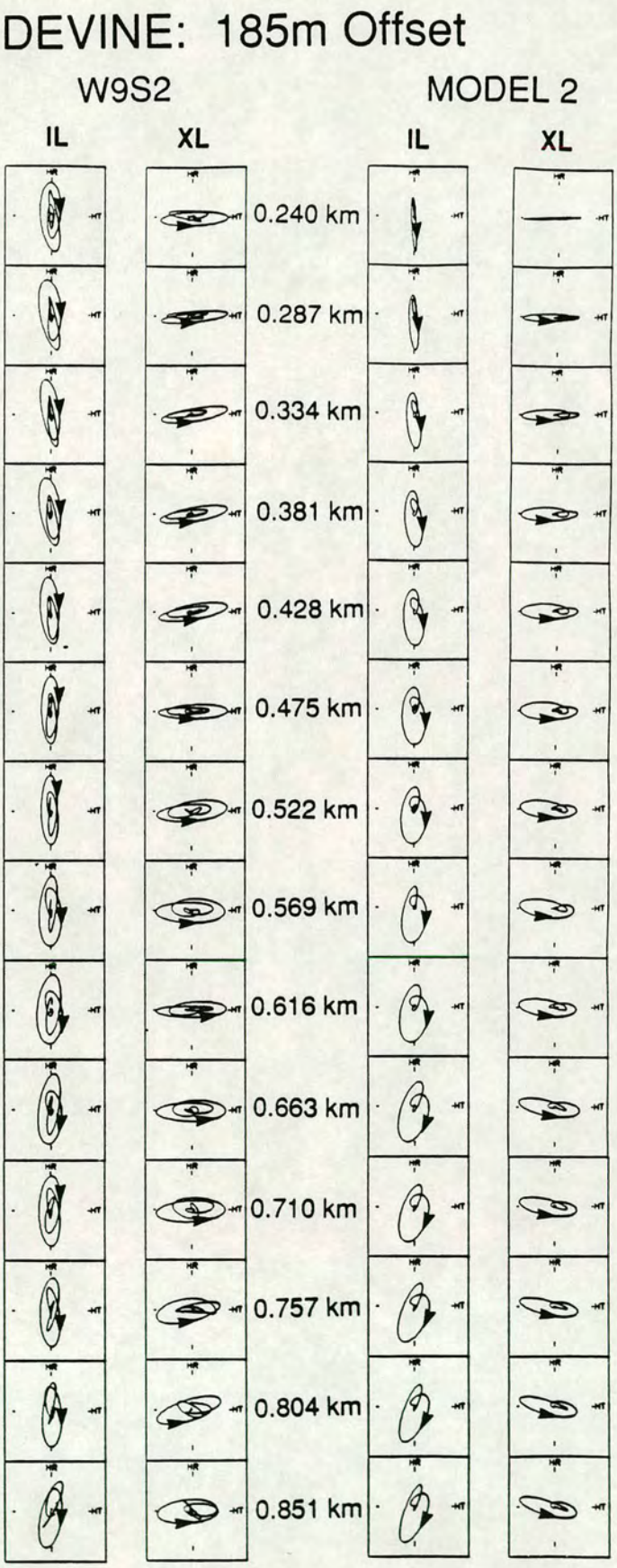

FIGURE 6.6: Selected observed and modelled horizontal plane shear-wave polarization diagrams from the 185m offset VSP for Model 2. The direction of motion is marked by an arrow.

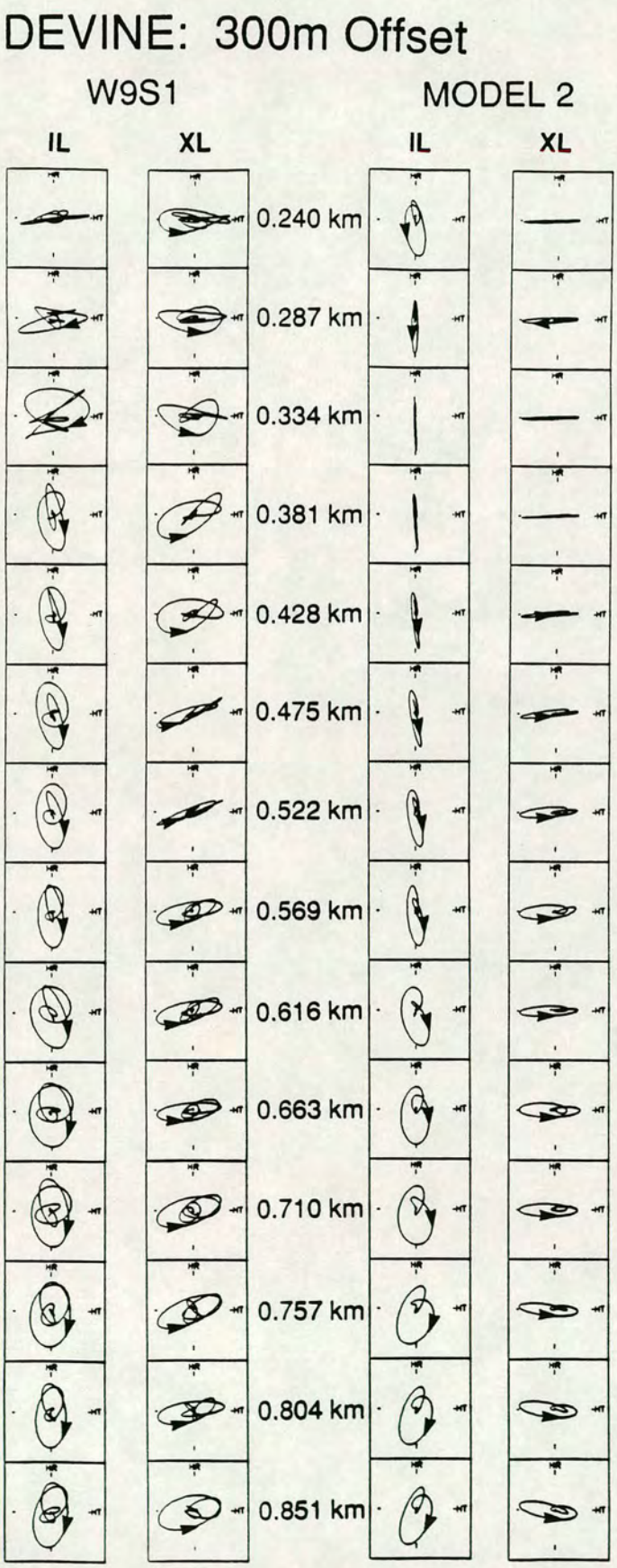

FIGURE 6.7: Selected observed and modelled horizontal plane shear-wave polarization diagrams from the 300m offset VSP for Model 2. The inline field data are distorted down to around 0.330km due to mode conversions (Figure 5.6). The direction of motion is marked by an arrow.

conversions (Figure 5.6) and the singularity may be obscured. Also, for the 300m offset the major axis of the ellipse rotates more in the model data than in the field data. In Section 5.4.3, I showed that the incidence angles used to calculate the dynamic plane were underestimates and this may lead to errors in the estimated anisotropy parameters for this wide offset data. Hence, errors may occur in the modelling as I am trying to match estimated anisotropy parameters between model and field data. This only affects the amount of PTL-anisotropy that needs to be added to the model; the crack parameters (industrially the most important parameters) were determined independently of the offset data.

Modelled and observed incidence angles

In Figure 6.8, I compare the observed and modelled incidence angles. As discussed in Section 5.4.3 the observed incidence angles are underestimates. The incidence angles from the model are as expected for this geometry (compare these estimates to the straight line incidence angle shown in Figure 5.17). Figure 6.8 shows model incidence angles calculated by: isotropic ray tracing through the model (the phase velocity incidence angle); and from the shear-wave energy (Section 5.4.3) in the sagittal plane (the group velocity incidence angle). In anisotropic media, the group velocity direction is not necessarily the same as the phase velocity direction (Section 2.4). In this case the phase and group velocity incidence angles are about 5° apart.

Conclusions to the modelling

Calculation of synthetic seismograms for offset VSPs in orthorhombic media is computer intensive. This limits the amount of model space that can be examined by forward modelling. The density and strike of cracks in the model (industrially the most important parameters) are stable as they can be determined independently of the PTL-structure and offset incidence angles.

I have obtained a good match between observed and modelled data and the decision to match all data using a single model proved to be valid. The model used a combination of vertical Hudson cracks and horizontal PTL-anisotropy. This shows that vertical features, which are aligned parallel to the stress direction, are present in

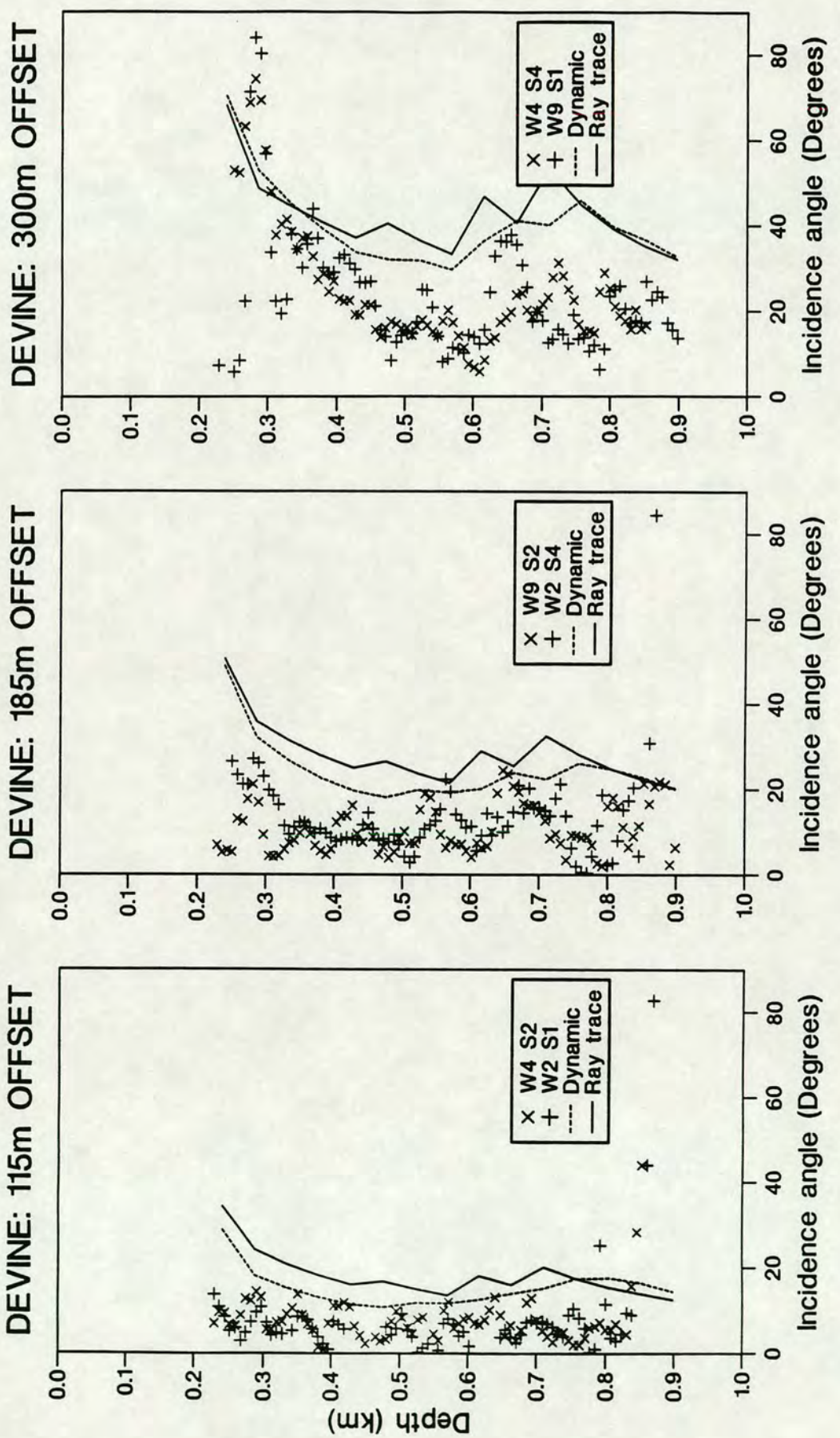

FIGURE 6.8: Observed and modelled incidence angles for the devine test site. The observed incidence angles and the dynamic incidence angles were calculated as being normal to the maximum shear-wave energy direction in the sagittal plane. This gives the group velocity direction. The remaining line was calculated by ray tracing through the isotropic model for Devine.

the near-surface layers. It is not possible determine the exact nature of these features without detailed cores from the top 250m. It was not necessary to introduce any anisotropy into the Austin Chalk layer. In the following two sections and in Chapter Seven I examine the limits this puts on the anisotropy in this layer and look at other ways of examining the anisotropy in the chalk layer.

MacBeth [1991a, 1991b] proposed an inversion scheme, in which observed estimates are compared with a precalculated data base of polarization angles and time delays for a wide range of media. I did not use this inversion scheme as most of the anisotropy is in a near-surface layer where there are no geophones to record the offset data. The inversion routines require the polarization direction, incidence angle and azimuth of the fast shear-wave and time delay in each layer. Here, polarization directions and time delays for the top layers are not known as the signal was not recorded until it has passed through subsequent layers.

6.2.5 Anisotropy in the Austin Chalk?

In order to match modelled and observed data it has not been necessary to introduce an anisotropic Austin Chalk layer. As the Austin Chalk is the target of this investigation, I now examine more closely what limits this puts on the anisotropy in the Austin Chalk. The time delay and polarization estimates for the zero-offset VSPs are shown in Figure 6.9. An estimate of the maximum time delay built up in the chalk can be found by comparing time delays in intervals above and below the chalk. The average time delays in 60m intervals above and below the chalk for W2S2 are 13.0±1.0ms and 13.5±1.8ms. Similarly for W4S1 the delays are 12.5±0.9ms and 13.0±1.0ms. [I used 60m intervals as this give a robust estimate of time delay. A wider range could not be used as there are only a few geophone levels below the Austin Chalk.] This puts a limit on the time delay developed in the chalk of 0.5±1.3ms and 0.5±2.1ms in W2S2 and W4S1 respectively. [W9S4 has not been used as this gives anomalous results for time delays and polarization angles.] The shear-wave velocity in the Austin Chalk is 2.217km/s (Table 6.1). Using the maximum standard deviation in the time delay this gives an upper limit on shear-wave anisotropy in the chalk of about 5%. Whilst it is likely that the anisotropy in the chalk is much

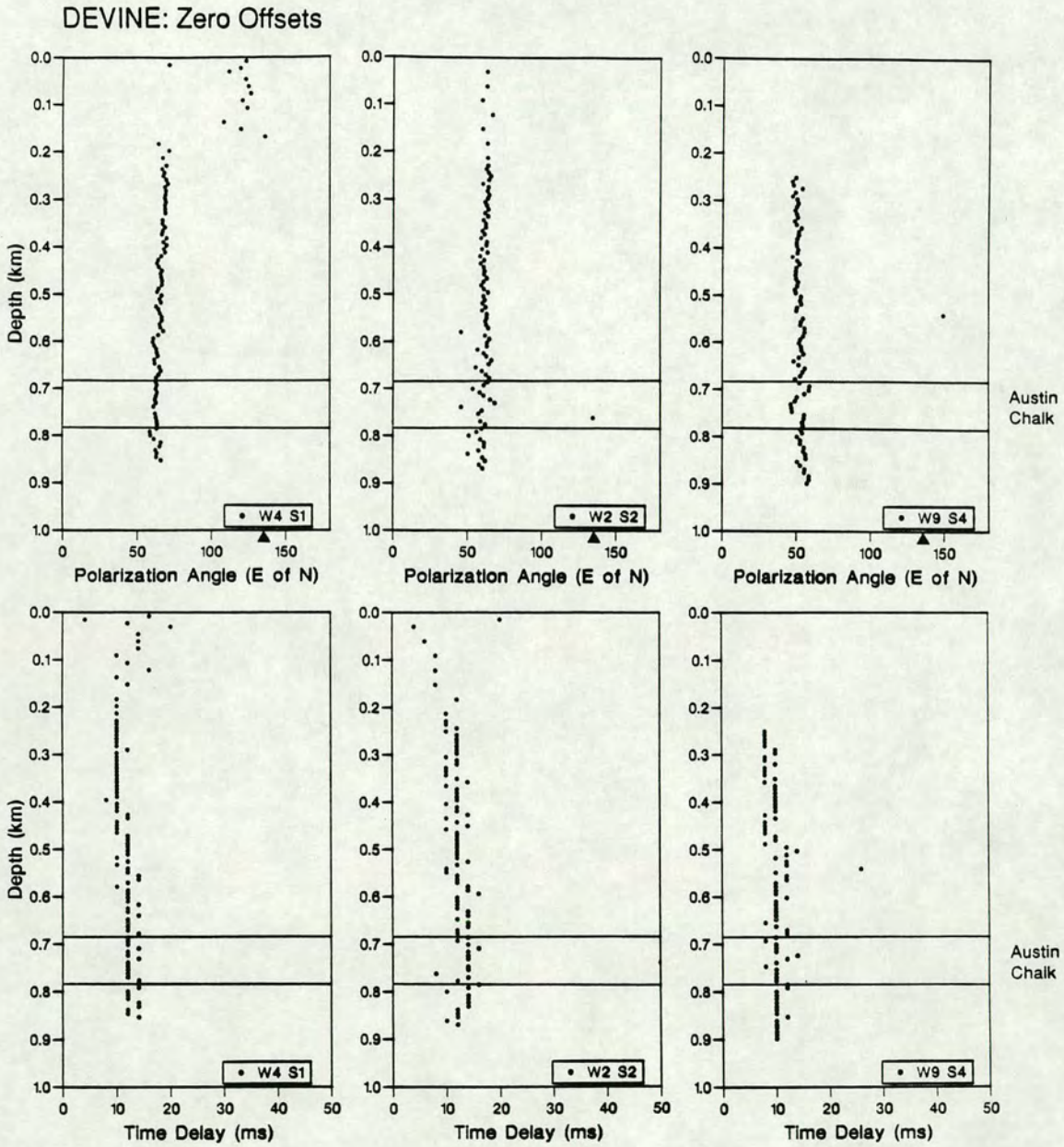

FIGURE 6.9: Zero-offset polarization angle and time delay results from Devine. The radial directions of the acquisition systems are marked with black triangles. The Austin Chalk interval is marked and it can be seen that there are no noticeable changes in either polarization direction or time delay in this interval.

less than this, it may still be anisotropic even though transmitted waves did not detect a time delay. Miller, Costa & Schoenberg [1992] used *P*-wave crosshole tomography to examine the anisotropy below the Austin Chalk. They had little data coverage in the Austin Chalk but their diagrams showed that there may be some differences between vertical and horizontal *P*-wave velocities in the chalk.

6.2.6 Detection of dipping fractures

The above analysis shows that the chalk layer has little or no anisotropy. A dipping fracture was observed both in W4 and W9 [S.A.Raikes, personal communication; Section 6.2.2] and it is possible that the anisotropy in this layer does not have a horizontal axis of symmetry making it hard to resolve for near-vertical propagation. I now do further modelling to see if the 300m offset VSPs could be used to identify anisotropy in the chalk caused by dipping fractures.

The 300m offset VSPs have opposite radial directions and will develop different time delays and polarizations angles if the chalk is anisotropic due to dipping fractures, as the rays propagate with different angles relative to the fractures (Figure 6.10). The differential effect on the estimates is largest for the two 300m offset VSPs as for nearer offset data, with near vertical ray paths, the time delay behaviour and polarization directions are symmetrical about vertical propagation (Figure 6.10).

Figure 6.3 shows that the polarization estimates (for W4S4 and W9S1) diverge for the deepest levels. This may be due to the two offsets having different ray paths with respect to the dipping fractures in the chalk layer. However, the deeper levels in W4S4 are contaminated by multiple energy (see Figure 5.7) which may cause this divergence.

Dipping fractures in the chalk layer

The observed fractures are water-filled [S.A.Raikes, personal communication] and I recalculated Model 2 for the 300m offset data with water filled Hudson cracks dipping at 34° to the NW in the Austin Chalk (Layer 7, Table 6.1). I had to calculate this model twice: once for each of the 300m offset VSPs, as these have opposite radial directions with respect to the dipping structure. In the Austin Chalk layer, the

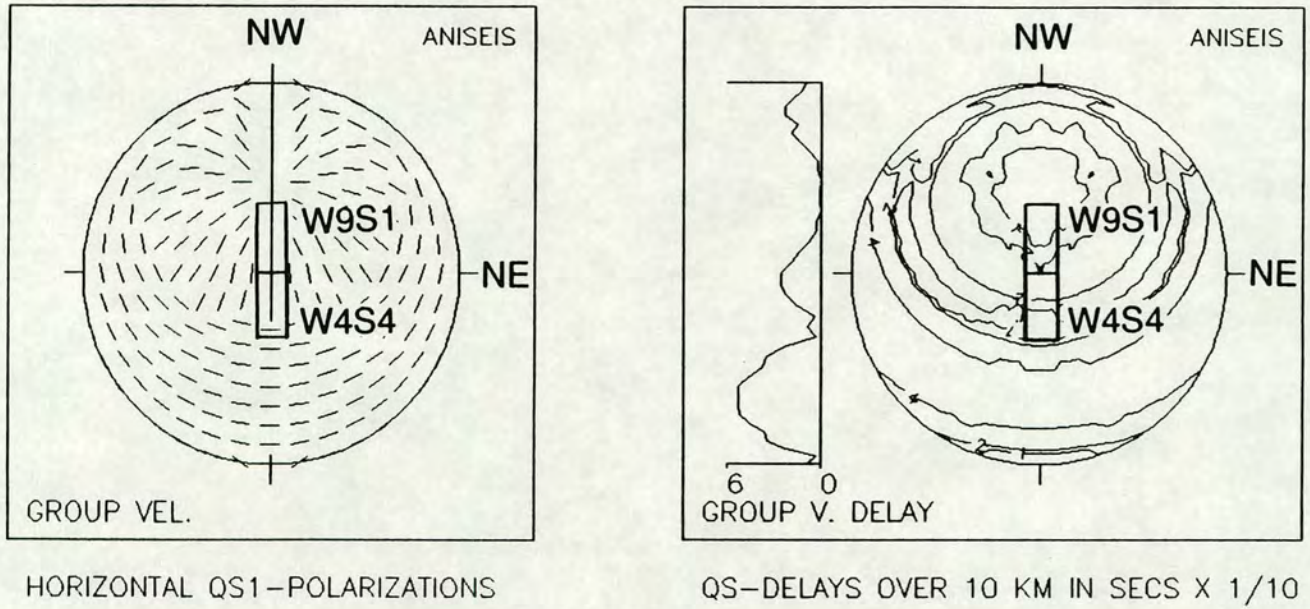

FIGURE 6.10: Equal area plots of polarization directions of the leading split shear-wave and time delays for the material used to model the Austin Chalk layer at Devine (Table 6.1). Water-filled cracks giving rise to 10% anisotropy have been added and here these dip at 34° towards the NW (in the models the crack strike is set to match borehole data). The approximate limit of the range of incidence angles through this layer for the two 300m offset VSPs has been marked.

estimates of the polarization angle and time delay for the two modelled offsets pulled apart (not shown). The polarization estimates in the chalk layer for the W9S1 model are clockwise of those for W4S4 (as in the observed data).

Figure 6.11 shows a further extension of this modelling with the two offset VSPs now at their true offsets (see Table 5.2). First, I ran the model with an isotropic chalk layer to provide a control; the estimates for W4S4 and W9S1 are slightly different due to the difference in ray paths. In the chalk layer the polarization angle curves come together, for this control model, as ray paths become similar for deeper geophone levels. Second, I added dipping fractures to the chalk layer. Crack orientations are given in Table 6.1 and are consistent with borehole information from W4 and W9. I used dipping cracks which produced 10% shear-wave anisotropy as this gives a vertical shear-wave anisotropy of about 5%: the maximum allowable limit from the analysis in Section 6.2.5. The presence of dipping cracks in the chalk layer causes the estimates of polarization angle and time delay to pull apart with the polarization estimate for the W9S1 model being to the east of that for the W4S4 model (as in the field data, Figure 6.3).

I have shown that the presence of dipping fractures can be detected using offset VSPs with opposite radial offsets. As the deeper levels in W4S4 are contaminated by high amplitude multiples (Figure 5.7) it is not possible to say whether the difference in the polarization estimates (Figure 6.3), at depth, for the two 300m offset VSPs is due to the dipping fractures observed in the wells.

6.3 MODELLING THE BURLESON COUNTY VSP

A modelling sequence similar to that applied to the Devine data was used on the Burleson data. However, no well logs were available and there are only six geophone levels in the upper 1.7km of the structure. These six levels are noisy and as the remaining data coverage is only between 1.7km and 2.4km it was not possible to create a complete model. I decided to try to match the bulk features of the observed data using a simple model. The position of some interfaces were supplied by M.C.Mueller (Amoco):

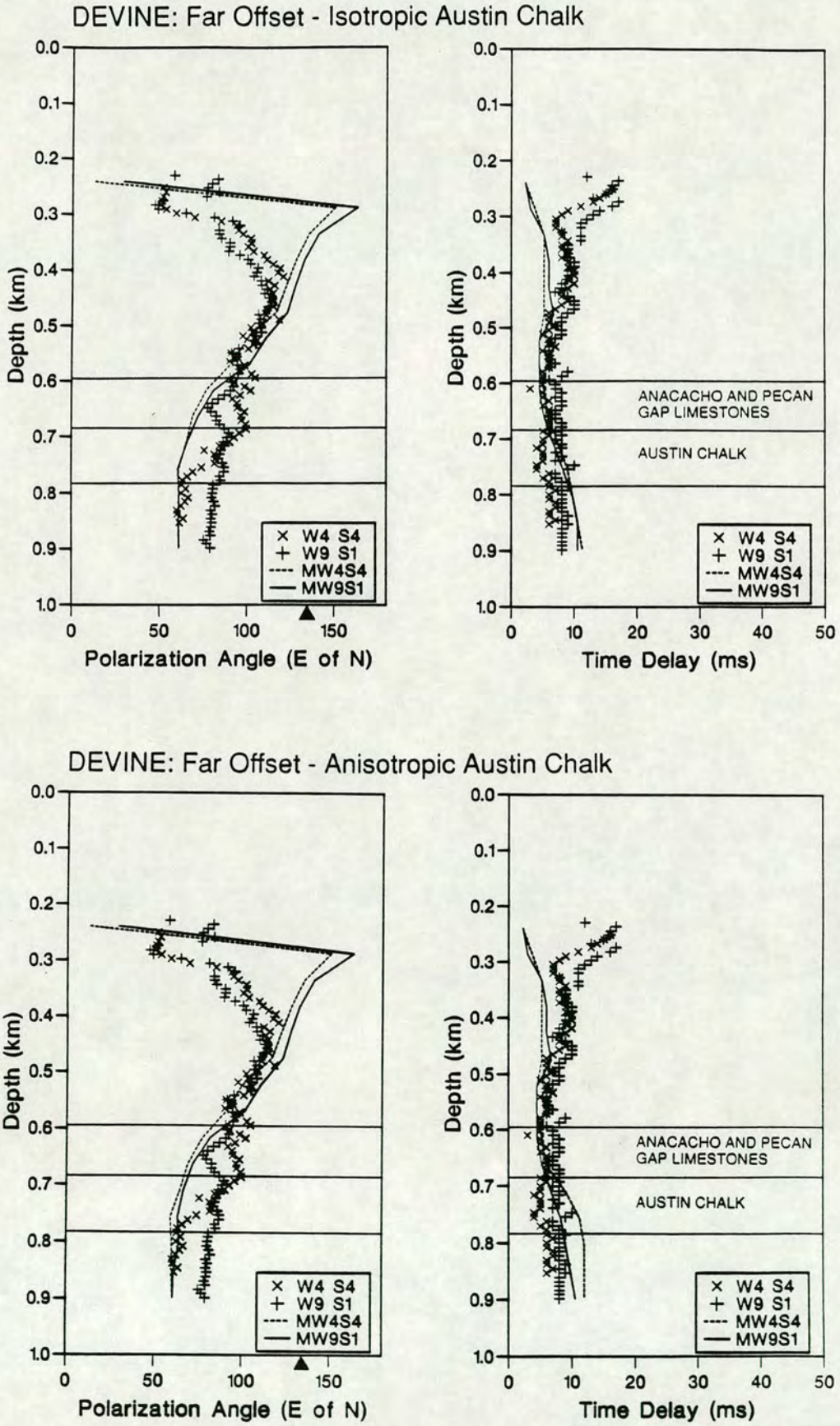

FIGURE 6.11: The models for the 300m offset VSPs have been recalculated using the true offsets (284m for W4S4 and 312m for W9S1) for two cases: the first has no cracks in the Austin Chalk layer; in the second case the Austin Chalk contains dipping cracks.

Layer	Depth (km)
Midway (Shales)	1.354
Navarro (Shales)	1.536
Pecan Gap Limestone	1.984
Austin Chalk	2.362
Base Austin Chalk	2.390
Eagleford Shale	2.408

I created a five layer isotropic velocity model, with interfaces at the zero-offset geophone positions, in the upper structure, and at the geological boundaries in the deeper structure. The shear-wave velocity structure was created by inverting the arrival times for the fast arrival determined using LTT on the zero-offset data. The *P*-wave velocity structure was found by inverting the *P*-wave arrival times for the vertical geophone component. I calculated densities from *P*-wave velocities using the formula of Gardner, Gardner & Gregory [1974]. This is known to be only a rough guide to densities; however, in view of the simple model structure, inaccuracies in the density are insignificant. The isotropic model parameters are shown in Table 6.2. Figure 6.12 shows the calculated isotropic velocity structure together with ray tracing for all offset locations.

Source positions S2 and S4 are 2.4km apart (Figure 5.9) and I have to assume that both the isotropic and anisotropic structures are invariant over this distance. I have no information about whether the medium polarization changes with depth. As the geology and regional setting are similar to those at Devine, I assume that the nature and causes of the anisotropy are the same as at Devine:

1) with a constant polarization direction of the medium with depth.
2) Azimuthal anisotropy is due to vertical aligned features.
3) Thin layer anisotropy is also present (shales are present at this site).

Therefore, I model the anisotropy using a combination of vertical Hudson cracks and horizontal PTL-anisotropy.

TABLE 6.2: Parameters for models of the Burleson VSP suite.

ISOTROPIC MODEL PARAMETERS

Layer	Thickness (km)	Density (g/cm^3)	*Vp* (km/s)	*Vs* (km/s)
1	0.518	2.07	2.010	1.005
2	0.762	2.24	2.745	1.415
3	0.451	2.22	2.632	1.258
4	0.661	2.35	3.277	1.562
5	Halfspace	2.35	3.277	1.562

ANISOTROPIC MODEL PARAMETERS

	Crack strike (N°E)	Crack density ε	%PTL-anisotropy
Model 1			
Layer 1	105°	0.030	-
Layer 2	105°	0.020	-
Layer 3	105°	0.0055	-

Cracks have a radius of 0.001m, an aspect ratio of 0.01 and are water-filled.

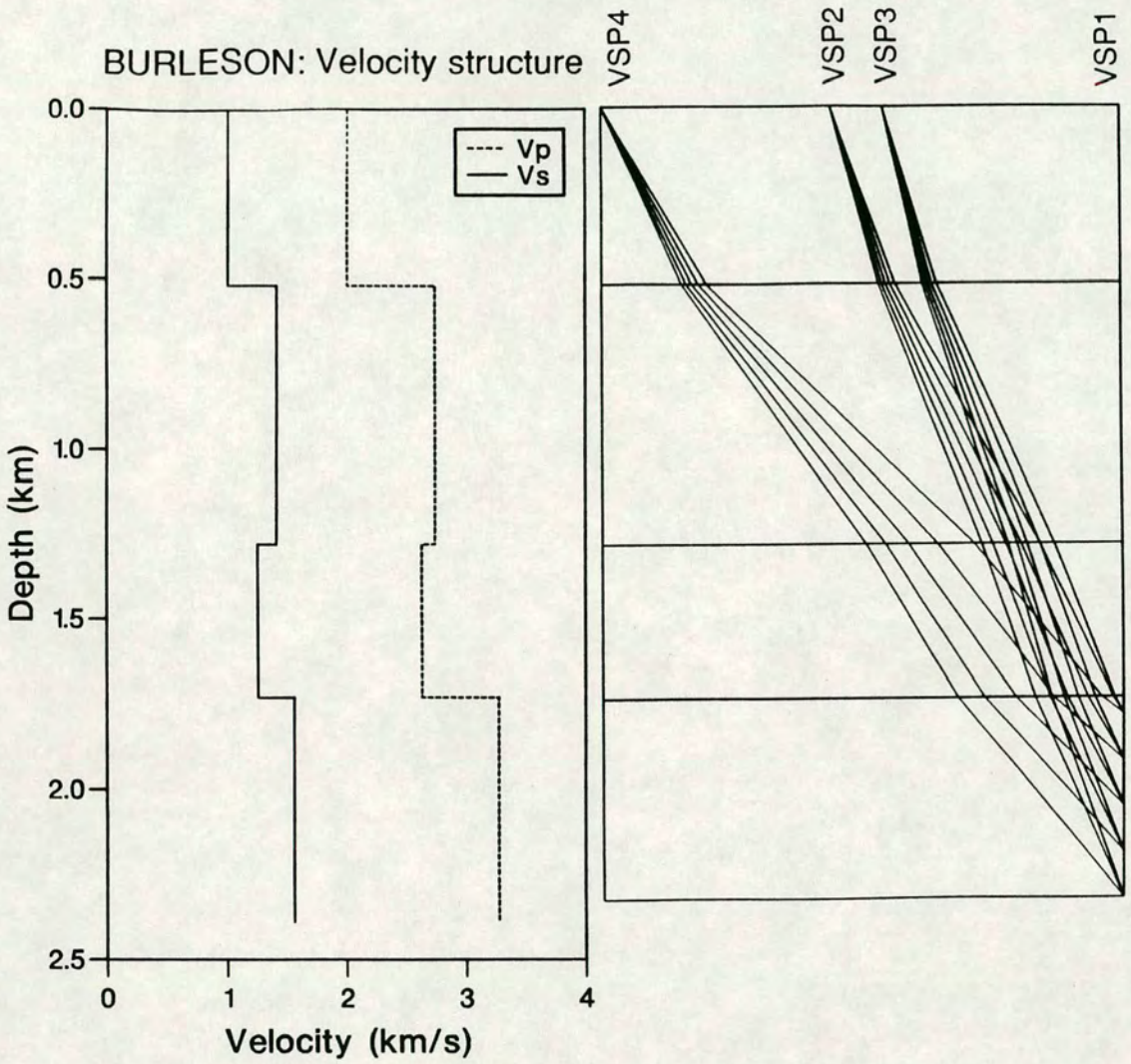

FIGURE 6.12: The isotropic velocity structure used in modelling the Burleson VSPs inverted from *P*-wave and shear-wave arrival times together with ray tracing from each offset through this structure. Lateral invariance of the structure is assumed and this diagram shows all offsets on the same side of the well.

6.3.1 Cracked anisotropic model for Burleson

I inserted cracks into the model to match polarization angles and time delays for the zero-offset data (the anisotropic model parameters are shown in Table 6.2). Seismograms were then calculated for all offsets through this model. Both AST and AIT were applied to the offset data in the dynamic plane. Model results are compared with the observed data in Figure 6.13. Section 5.4.5 showed that the source and geophone estimates of AIT are not coincident for the offset field data. This may mean that multiple splitting has occurred [MacBeth & Yardley 1992] in the field data and I applied both AST and AIT (AIT is sensitive to changes in medium polarization).

The source balancing correction was not applied as multiple shear-wave splitting is suspected (Section 2.7). There is a good agreement for the zero-offset case between observed and modelled polarizations and time delays. The fit at offset is poor, indicating that a more complex anisotropic model is needed. The AIT source and geophone estimates are coincident for the modelled data indicating no multiple splitting in the model.

Internal shear-wave windows (see Section 3.3)

The shear-wave signal may be distorted by mode conversions for wide angle incidence [Liu & Crampin 1990] leading to apparent splitting. The offset for which these become apparent is where the transmission coefficients for *SV*- and *SH*-waves diverge. In my model this occurs at 45° for the first interface (and at greater offsets for the deeper ones) and does not distort the shear-waves. This is confirmed by the AIT source and geophone estimates being coincident for Model 1 (Figure 6.13). However, the real incidence angles may be wider for some interfaces leading to distortion of the shear-wave signal.

6.3.2 Orthorhombic anisotropic model for Burleson

I ran further models with combinations of Hudson cracks and PTL-anisotropy; however, I was not able to get a good fit between the model and observed results. Poor data coverage means that I could not adequately define the model and I now discuss the problems encountered in modelling these data.

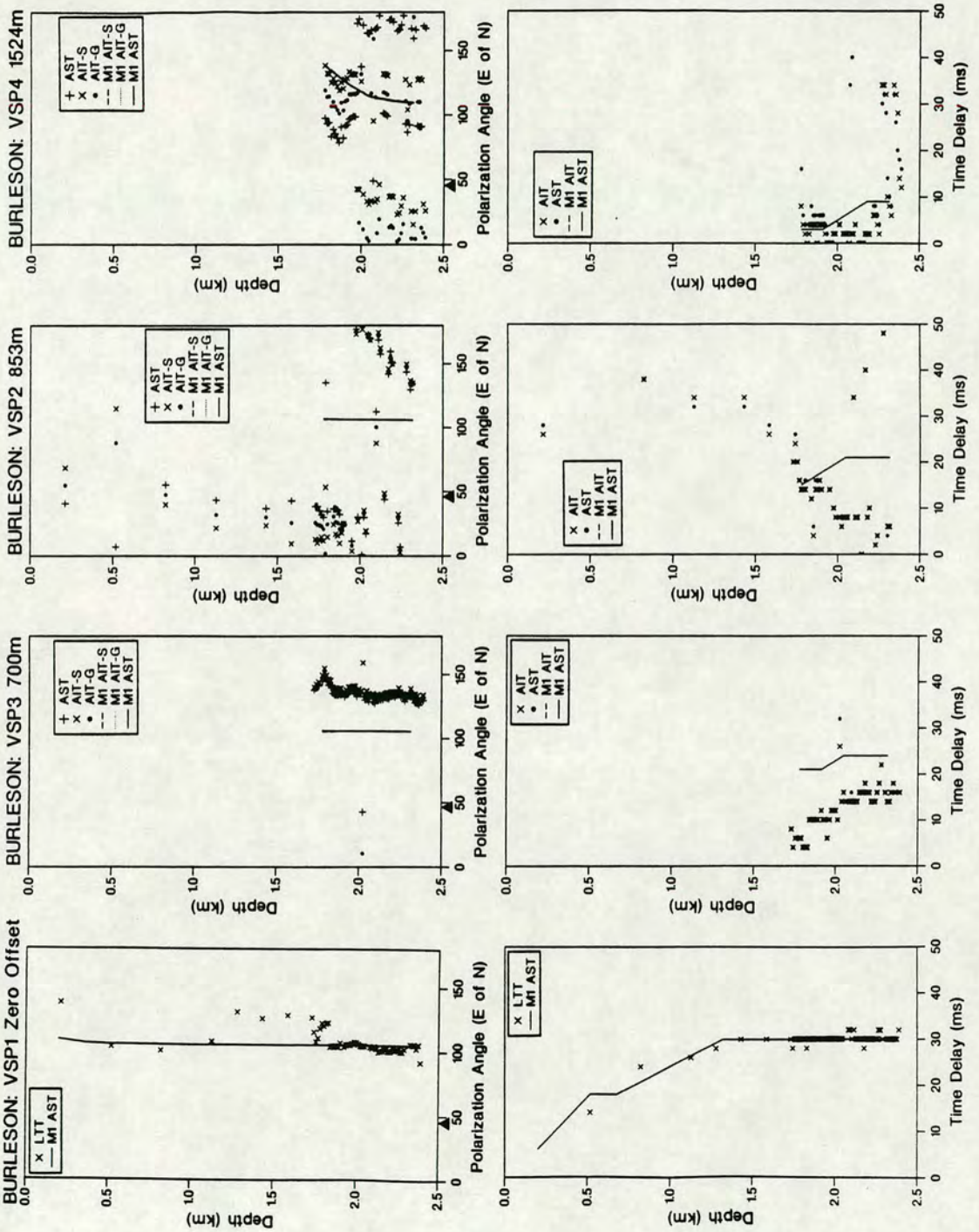

FIGURE 6.13: Comparison of estimations of polarization angle and time delay from observed and modelled VSPs for increasing offset at the Burleson VSP. Estimates were calculated using both AST and AIT in the dynamic plane.

Multiple splitting with a constant crack strike

In orthorhombic models that I attempted, the source and geophone estimates of AIT pulled apart; however, the polarization angles and time delays did not fit. The pull apart in AIT estimates is due to multiple splitting caused by the change in incidence angle at an interface. In Figure 6.14, I demonstrate that this can occur even with a constant crack strike. [The case shown has 4% PTL-anisotropy added to each layer in the anisotropic structure in Table 6.2.] Equal area plots for the top two layers of the model are shown. I have marked the direction, through these layers, of the ray to the bottom (open circle) and top (closed circle) geophone levels in the model from VSP4 (see Figure 6.12). For a given source-receiver ray path, the *qS1* polarization direction changes at the interface between Layer 1 and Layer 2, even though the crack strike is constant. This means that the results of the estimation techniques will not reflect the true polarization direction of the medium for the offset VSPs as multiple splitting has occurred (see Section 4.7.2). As the data are offset, DPM cannot be used to estimate the *qS1* polarization direction at depth (Section 2.7).

The position of singularities

Further problems were experienced modelling the transverse *qS1* polarization found for VSP3 (700m offset, see Figure 6.13). This VSP has ray paths with incidence angles around 15° in the top layer (Figure 6.12) where most of the anisotropy is thought to be present. For orthorhombic media it is rare to get a N135°E polarization in the presence of cracks striking N103°E [Wild & Crampin 1991] and it is likely that it is caused by ray paths close to a singularity. Wild & Crampin show equal area plots for a range of orthorhombic media. They show that *qS1* polarizations are usually closer to the radial direction for the propagation direction in VSP3, although singularities can occur this close to the vertical. The exact position of singularities is critically dependent on the elastic constants [Brown, Crampin & Gallant 1992]. As I had to make gross approximations to the properties of each layer to get this simple model, the singularities in the model will not reflect the properties of the real earth.

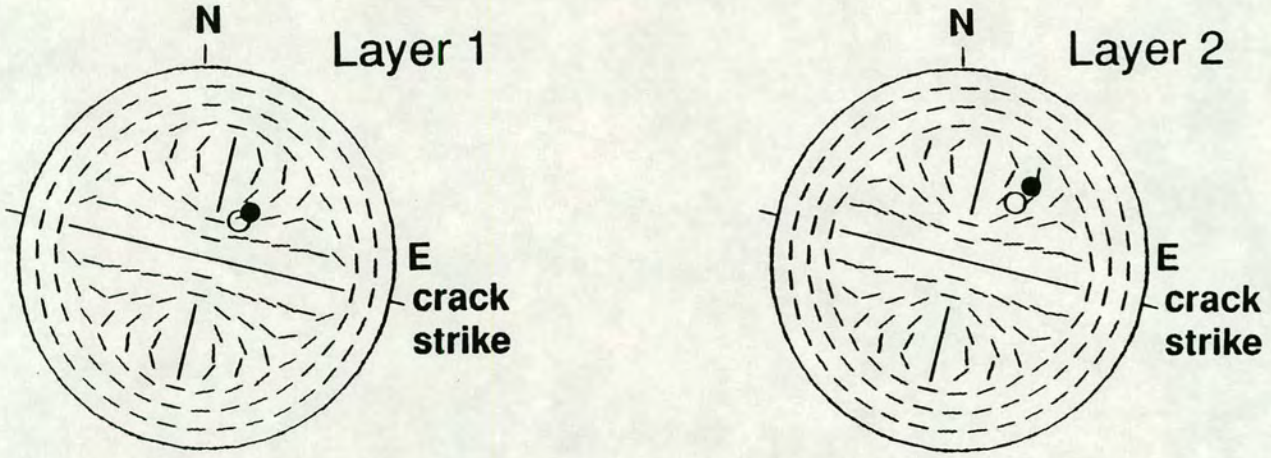

FIGURE 6.14: Equal areas plots of the *qS1* polarization in the top two layers of the Burleson model with 4% PTL-anisotropy added to the crack structure in Table 6.2. The open and closed circles show the path of the rays from VSP4 (1524m offset) to the bottom and top geophone levels, respectively, in the model. Although the crack strike is the same in each layer the change in incidence angle means that the *qS1* polarization for each ray is different in each layer. Source and receivers lie in the vertical, NE-SW plane.

Conclusions to the modelling

It has not been possible to generate an anisotropic model for this data set. This is mostly due to the inadequate data coverage with depth and offset. This has meant that an accurate model structure could not be defined. Whilst wide angle data are useful to build up a picture of the full anisotropic structure, it may not be practical to collect it in many cases as:

1) multiple splitting, caused by the change in incidence angle at interfaces, means that the results of the estimation techniques are invalid;
2) wide angle shear-waves can be distorted by mode conversions at interfaces;
3) the anisotropic structure may change over the large distances spanned in such experiments. Therefore, the shear-waves from different offsets may travel through different structures.

If the structure is subhorizontal with vertical fractures, then only zero-offset data need to be used. If offset data are included in the analysis the effects of layering also need to be considered. Where offset data are required, smaller increments between offsets than those used at Burleson would allow changes in the shear-wave behaviour to be followed with offsets.

6.3.3 Anisotropy in the Austin Chalk?

The polarization and time delay estimates for the zero-offset Burleson VSP are shown in Figure 6.15. Again, most of the anisotropy is in the near-surface and at the depth of the Austin Chalk both polarization and time delay are stable. The chalk here is thin (28m) and the geophone levels in the chalk yield a constant time delay (30ms). There is one geophone level below the chalk, which shows a 2ms increase in delay. Inspection of the seismograms for this level shows that the data are noisy. This imposes a limit on the time delay build up to 2ms (one sample interval) over the Austin Chalk and a maximum anisotropy of 15%[1]. The chalk layer is too thin for an

[1]This was calculated using a velocity of 2.35km/s. This is the velocity for the 0.661km thick layer at the depth of the chalk and was inverted from shear-wave arrival times for the modelling (see Table 6.2). Data coverage and layer thickness mean that an interval velocity for just the chalk layer cannot be found, although this velocity (2.35km/s) is similar to the Austin Chalk velocities at the other two sites.

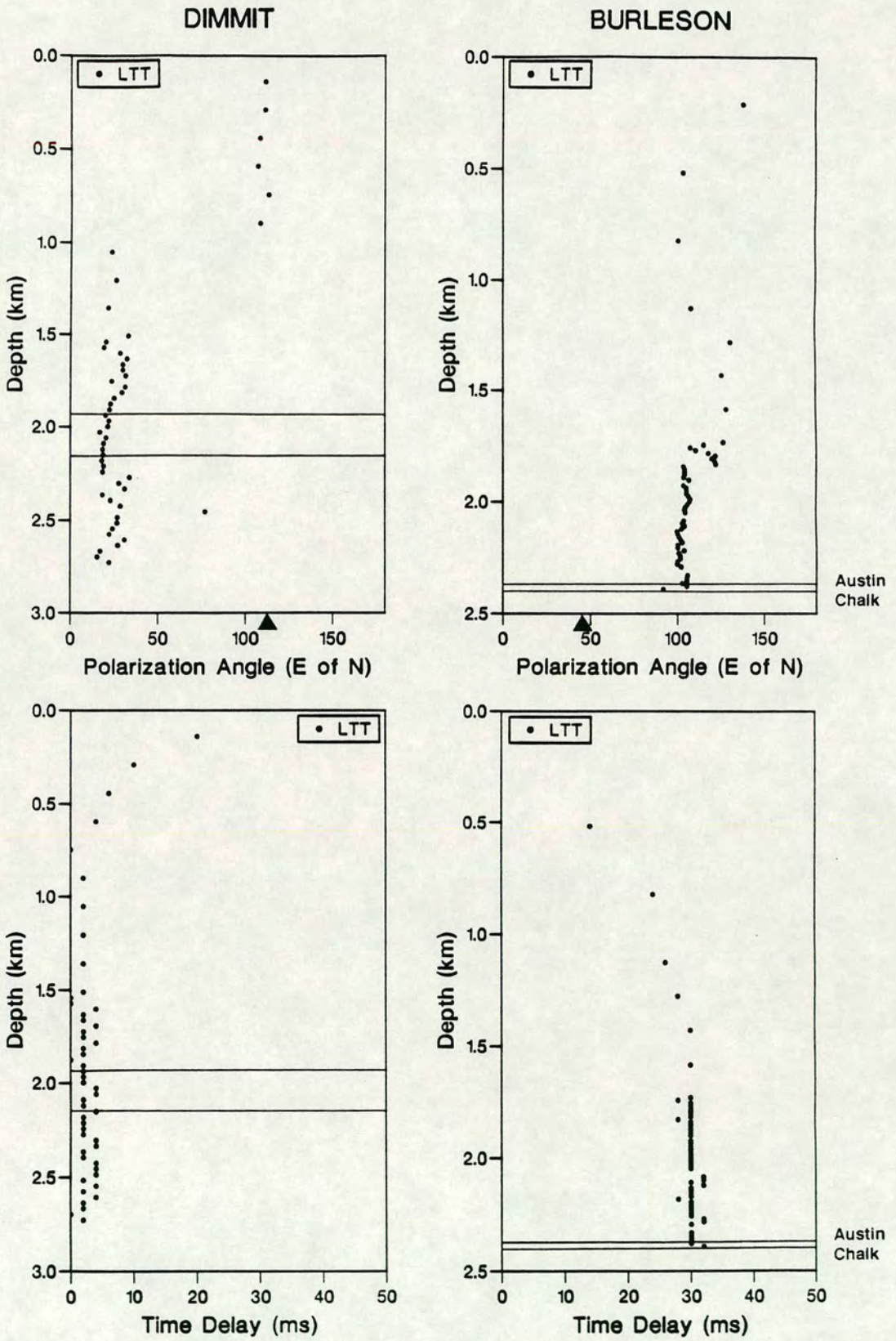

FIGURE 6.15: Zero-offset polarization angle and time delay results from Dimmit and Burleson. The radial directions of the acquisition systems are marked with black triangles. The Austin Chalk interval is marked and it can be seen that there are no noticeable changes in either polarization direction or time delay in this interval.

accurate estimate of shear-wave anisotropy to be made and it is possible that this layer is anisotropic. Field observations show that thin layers are more likely to have a high fracture density than thick layers [Barthelemy, Tremolieres & Andrieux 1992].

This well is a producing well, and together with the A.B.Childers #1 well, had a cumulative production of 5.7×10^6 litres of oil in 1990 from a fractured Austin Chalk reservoir [M.C.Mueller, personal communication]. Although, the above analysis gives a large upper limit for the amount of anisotropy present, further analysis is necessary to determine if there is a link between productivity and anisotropy (Chapter Seven).

6.4 THE DIMMIT COUNTY VSP

I do not present an anisotropic model for the Dimmit data as there is only a single zero-offset VSP and the time delay is small. If it is assumed that the azimuthal anisotropy is caused by vertical aligned features, as at Devine, then these are parallel to region stress and fracture directions. [This assumption is reasonable as the tectonic setting and geology are similar to those at Devine.] This confirms the results of Li, Crampin & Mueller [1992] who worked on the reflection profile shown in Figure 5.2. The depth range over which the time delay develops is hard to determine due to the difference in inline and crossline source positions. However, it develops by 1.6km implying a shear-wave anisotropy of less than 0.5% for the upper structure. [At 1.6km the difference in the shear-wave source positions causes negligible differences in travel time for isotropic models.]

The polarization direction and time delays determined for the Dimmit well are shown in Figure 6.15. The time delay built up in the reservoir can be estimated by finding the average time delay in 300m intervals above and below the reservoir and finding the increase in time delay between these two regions. This give time delays of 2.3±1.2ms above the reservoir and 2.9±1.1ms below the reservoir, meaning that at most 0.6±1.6ms delay builds up in the Austin Chalk. This means that the chalk is isotropic. [Although, the maximum allowable anisotropy for the 229m thick chalk layer about 2%.]

6.5 INTERPRETATION OF REGIONAL TRENDS

Figure 6.16 shows the polarization directions of the leading split shear-waves determined in this study (from zero-offset VSPs) together with recently published values. These should be compared with stress directions given in Figure 5.1. Results from the multi-offset VSPs at Devine indicate that the media has a horizontal plane of symmetry. Therefore the polarization direction of the leading split shear-wave can be interpreted in terms of the strike of vertical features. The *qS1* polarization directions are in agreement with known fracture dips and strikes [Corbett, Friedman & Spang 1987; Kuich 1989]. Fracturing occurred as a result of the regional stress field (extension directed towards the coast) and it is reasonable to link the vertical aligned features from the models with the observed fractures. The regional stress appears to be the governing influence on the fracture alignment and observed anisotropy. The anisotropy may be caused by any structure in the rock matrix and may be due to cracks, micro-cracks or pores as suggested by Crampin [1992b]. A detailed analysis of core data would be required to prove this.

The polarization direction in the Burleson VSP (N103°E) appears to be anomalous. However, the result is consistent with the E-W fracture orientation determined by Mueller [1991, 1992], from shear-wave analysis and cores, in the northern part of the Giddings field. Also Figure 5.1 shows anomalous stress directions in this area.

Most of the anisotropy seen in the field data is in the near-surface layers; this is a common observation [e.g. Becker *et al.* 1990; Bush 1990; Mueller 1991]. 3% appears to be a typical value for crack anisotropy in the near-surface [e.g. Alford 1986; Winterstein & Meadows 1991b].

6.6 CONCLUSIONS

In this chapter I have shown that the anisotropy parameters determined for the Devine data can be matched using a model which combines vertical aligned Hudson cracks and horizontal PTL-anisotropy. The crack parameters in the model are stable as they can be determined independently of the horizontal PTL anisotropy and the offset data.

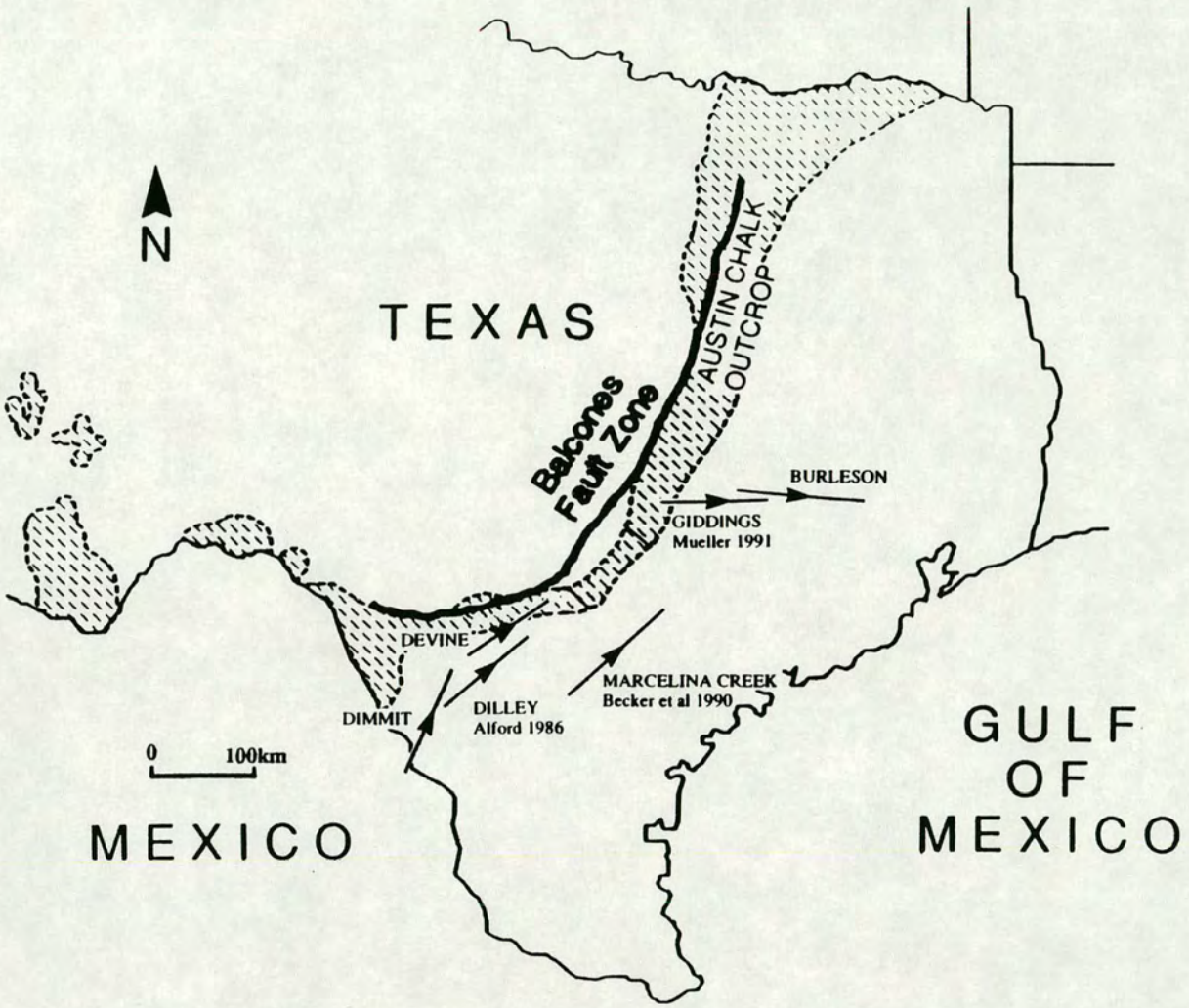

FIGURE 6.16: Map of Texas (adapted from Corbett, Friedman & Spang [1987] and Kuich [1989]) showing the polarizations of the leading split shear-waves at the sites studied here, together with other published results.

In the model, the Hudson cracks are aligned parallel to the regional stress direction and are vertical. It is possible that aligned pores, cracks (EDA) proposed by Crampin [1992b] cause the anisotropy. Fractures are known to be present at depth. A detailed analysis of core data from the uppermost 250m is required to determine whether the near-surface anisotropy is caused by fractures or EDA.

Analysis of transmitted waves has shown that the Austin Chalk at Dimmit and Devine has little or no anisotropy. The fractures seen in W9 and W4 at Devine do not have a high enough density to give resolvable anisotropy for vertically travelling waves. The Austin Chalk reservoir at Burleson is thin and the analysis of transmitted waves was not sensitive enough to resolve any anisotropy in this layer. In Chapter Seven, I use reflected amplitudes to quantify the anisotropy in reservoir layers.

Along the Austin Chalk trend, changes in stress and fracture directions occur regionally. In cases with such a simple structure, zero-offset VSPs provide all the required data about fracture strike and density. [This is not true where dipping cracks or layers are expected. In such cases offset data are needed to identify the anisotropic structure and can be used to identify dipping cracks in the reservoir layer.] Interpretation of offset data is difficult as multiple splitting can occur as a result of the change in incidence angle at an interface, even when crack strike is constant.

CHAPTER SEVEN

SHEAR-WAVE ANISOTROPY IN THE AUSTIN CHALK, TEXAS: NORMAL INCIDENCE REFLECTIONS

7.1 INTRODUCTION

In the previous two chapters I was not able to quantify the amount of anisotropy in the Austin Chalk layers by analysis of transmitted shear-waves. Thomsen [1988] suggested that the amplitudes of reflected shear-waves can be used to determine the anisotropic nature of a reflector. This approach is based on the fact that the velocity contrast, and reflection coefficient, parallel and perpendicular to the fractures in a reflector are different.

Hydrocarbon productivity is often governed by fracturing. Methods which can locate fractures and quantify fracture density are of direct importance to the hydrocarbon industry. Two methods of using reflected shear-waves to locate regions of high fracture density in reflection lines have recently been proposed. I review these and extend the analysis for use in VSP data. I compare reflected amplitudes, normalized with respect to the downgoing arrival, of shear-waves polarized parallel and perpendicular to fractures in the reflector. This method allows reservoir anisotropy to be quantified.

I apply this analysis to the zero-offset data from the three VSP sites in Texas. I find that the Austin Chalk at Dimmit and Devine is isotropic. The Austin Chalk at Burleson, which is a producing fractured reservoir, is anisotropic. In this case, it is not possible to quantify the anisotropy as the reservoir is too thin. I conclude that reflected amplitudes, in field data, are sensitive to anisotropy in the Austin Chalk. The likely cause of anisotropy is the fracturing, which controls reservoir productivity. Therefore, this is an important result, as it shows that shear-waves can be used in exploration for fractured reservoirs.

7.2 REVIEW OF REFLECTION METHODS

For vertical propagation, the velocity of the shear-wave polarized parallel to the fractures in a layer is greater than that of the shear-waves polarized perpendicular to the fractures (see Figure 2.1). So, for reflections from the top of a fractured reservoir, the reflection coefficients parallel, and perpendicular, to the fractures are different. This approach for locating fractured reservoirs forms the basis of theoretical work by Spencer & Chi [1990, 1991] and analysis of field data by Mueller [1991]. I now examine these two methods to see if they can be used to quantify the anisotropy in the Austin Chalk at Burleson. [These methods were originally suggested for reflection data where changes in the reflected shear-wave signal along a profile could be used to identify regions with high fracture densities.]

As I am specifically interested in using these techniques on the Austin Chalk data, I evaluate them for normal incidence in cases where the azimuthal anisotropy is caused by vertical fractures in a horizontally layered medium. In such cases horizontal thin layer anisotropy has no effect (see Section 2.4).

7.2.1 Normal reflections: Spencer & Chi [1990, 1991]

A linearly polarized shear-wave changes polarization upon reflection at an isotropic/anisotropic interface if the fractures in the reflector are not aligned parallel or perpendicular to the polarization of the wave. [This can be seen for the first geophone (G1) in Figure A1.9.] Spencer & Chi [1990, 1991] extended this principle to look at very thin reservoir layers where the reflections from the top and bottom of a reservoir interfere. The PD for the resulting reflected shear-wave arrival shows elliptical motion. As reservoir anisotropy increases, the orientation of the major axis of the ellipse increasingly deviates from the original source direction (for cases where the source is not polarized parallel or perpendicular to the crack strike). I demonstrate this approach using the model shown in Figure 7.1. The source is along the Y-direction and all cracks strike at X45°Y. The 20m thick anisotropic reservoir layer is sandwiched between a 1km thick isotropic layer and a halfspace. Figures 7.2 shows horizontal plane polarization diagrams recorded at the surface for a zero-offset reflection. The PDs are windowed about the reflected shear-wave arrival.

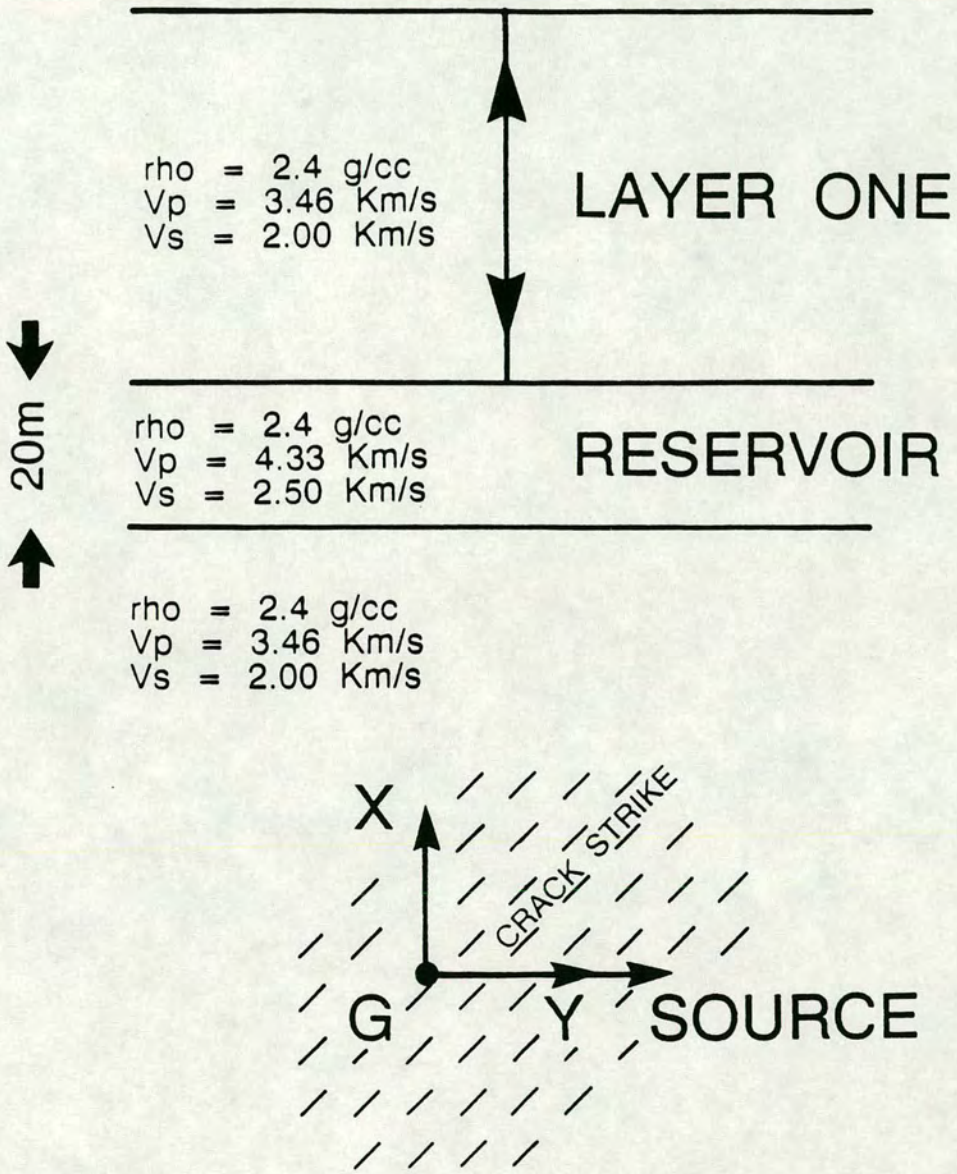

FIGURE 7.1: Schematic illustration of model for investigating reflections from a thin reservoir layer. The source is polarized along the Y-direction. Matrix constants are shown. Thin cracks strike at X45°Y in the reservoir layer.

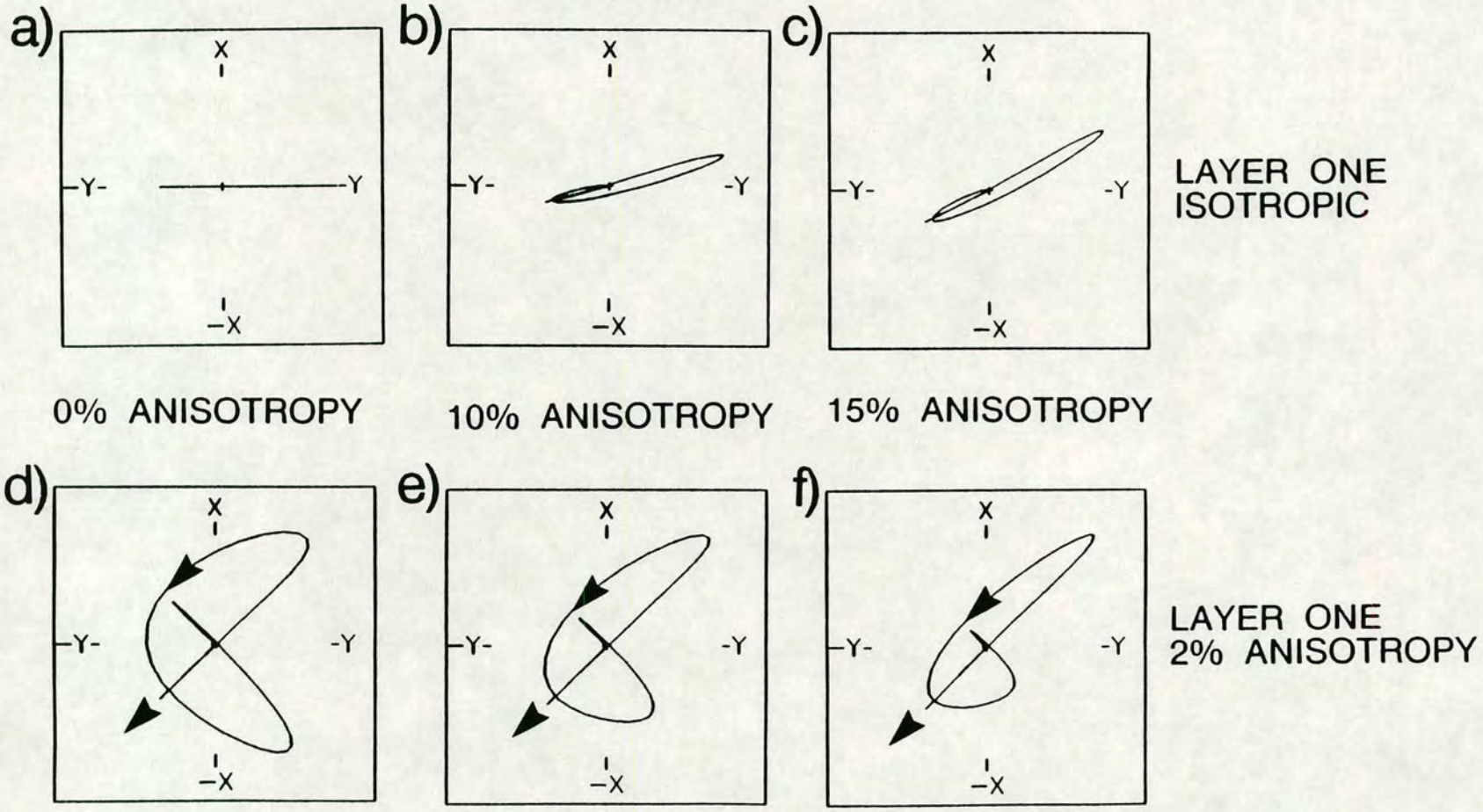

FIGURE 7.2: Horizontal polarization diagrams of the reflected shear-wave signals for the model in Figure 7.1. Two cases are shown: (a), (b), (c) upper layer is isotropic, and the direction of the major axis of the shear-wave ellipse progressively rotates away from the source orientation and towards the crack strike as the reservoir anisotropy is increased; and (d), (e), (f) upper layer is anisotropic, and the first motions (marked by arrow) of the shear-waves are now determined by the fracture strike direction in the upper layer. The source is polarized in the Y-direction and has a dominant frequency of 25Hz. All cracks strike X45°Y.

Figures 7.2a to 7.2c show that the direction of the major axis of the elliptical motion deviates progressively from the source polarization as the percentage anisotropy in the reservoir layer is increased. The shape of the PDs is critically dependent on the velocity contrasts at the top and bottom of the layer. Effects can vary widely with different matrix parameters in the three layers, and also with the thickness of the reservoir layer with respect to the seismic wavelength.

Analysis of field data shows that most observed azimuthal anisotropy is in the near-surface [e.g. Chapter Six; Bush & Crampin 1991]. The technique of Spencer & Chi [1991], along with all techniques which look for rotation of the shear-wave signal upon reflection, will be unusable when applied to field data because the overburden is generally anisotropic. In Figures 7.2d to 7.2f, I show what happens if 2% crack anisotropy is added to Layer 1 in the previous model. The cracks in Layer 1 strike in the same direction as in the reservoir layer. The direction of the first arrivals at the surface is now fixed by the anisotropy in the upper layer. Variations in anisotropy in the reservoir layer changes the relative energy in the interference lobes between the split shear-waves. Such a difference is hard to interpret quantitatively in terms of anisotropy in the reservoir layer and may be hidden by noise in the field data or lateral inhomogeneities.

If the fracture strike changes above the reservoir, then the reflected signal will be a complex superposition of several arrivals. This means that changes in the shape of the PD due to reservoir anisotropy will be even harder to interpret than those in Figures 7.2d to 7.2f, where there is a constant crack strike.

It may be possible to employ a layer stripping technique (similar to that described in Section 3.6.1) to remove the effects of shallower anisotropic layers. However, such techniques are likely to increase errors in the determination of the anisotropy parameters. Below, I review an alternative method of using reflected amplitudes, which does not require a layer stripping approach.

7.2.2 Normal reflections: Mueller [1991, 1992]

Mueller [1991, 1992] presented a simple way of comparing the fast and slow reflection coefficients, parallel and perpendicular to the fractures, for entire shear-wave

reflection sections from the Austin Chalk, Texas. The field data were processed and rotated into fast (polarized parallel to fractures) and slow (polarized perpendicular to fractures) sections using Alford's rotation [1986]. For thin fractures (Section 2.5), an increase in fracture density reduces the velocity perpendicular to the fractures. For cases where the reservoir layer has a velocity a few per cent higher than the overlying rock, this leads to a reduction in the reflection coefficient perpendicular to the fractures. So the reflection on the slow shear-wave section has a lower amplitude.

Results from the work of Mueller [1990] are shown in Figure 7.3, which shows data from a field in Texas with a visible amplitude anomaly in the centre of the slow section. Mueller [1991, 1992] attributed such anomalous reflector discontinuities on slow sections to high fracture densities in the Austin Chalk. Some of these reflector discontinuities were horizontally drilled and found to be associated with producing fractured oil reservoirs. This method was an important advance in the study of shear-wave anisotropy in the hydrocarbon industry as it showed that fracture swarms, where hydrocarbons accumulate, are anisotropic. It also represents an important use of shear-wave anisotropy as an exploration tool, as it shows that reflection sections can be used to locate fractured units.

I use the multi-layered model in Figure 7.4 to demonstrate the principles behind this method. Figure 7.5 shows synthetic seismograms for source and geophone polarizations parallel and perpendicular to the aligned fractures. The shear-wave velocities I use in the model are consistent with a simplified structure from the Austin Chalk trend. The fractured reservoir is seen as the region in which the reflected amplitudes from the top of Layers 3 and 4 are reduced in the section perpendicular to the fractures. In Figures 7.4 and 7.5, Layer 3 is shown with a central reservoir section in which there is a 15% a differential shear-wave velocity anisotropy. This was achieved by combining data from two models with different shear-wave velocities in Layer 3. Mueller [1992] uses these diagrams to explain the amplitude anomalies on the slow shear-wave sections in his reflection data.

In Figure 7.5 I use a simple single sided 25Hz pulse and do not include internal multiples, also the reservoir layer is 100m thick and the reflections from the top and bottom of the reservoir do not interfere. I use such a simple model to show how the

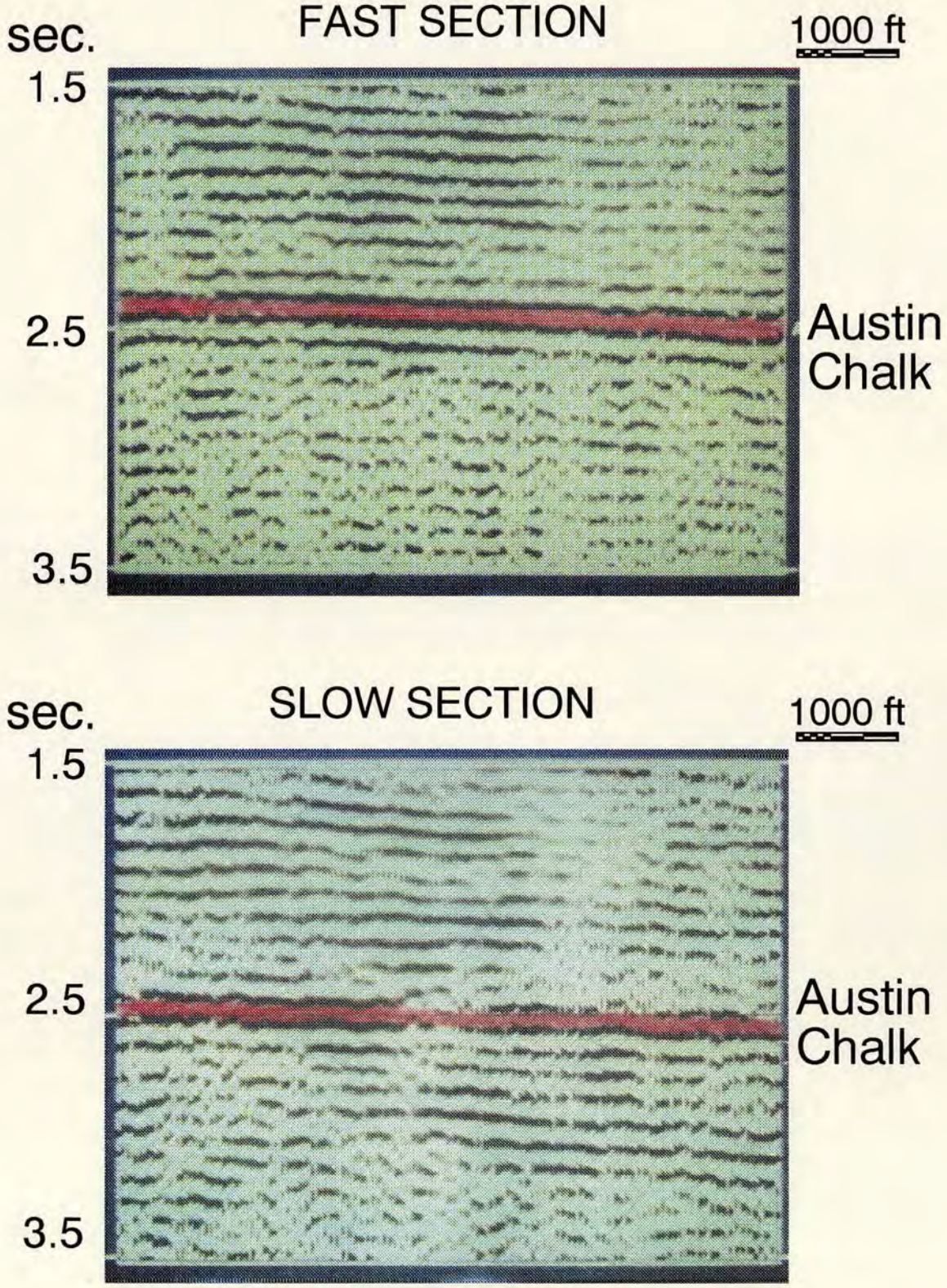

Figure 7.3: Results from the work of Mueller [1990] showing continuous Austin Chalk reflectors on the fast section and an amplitude anomaly on the slow section.

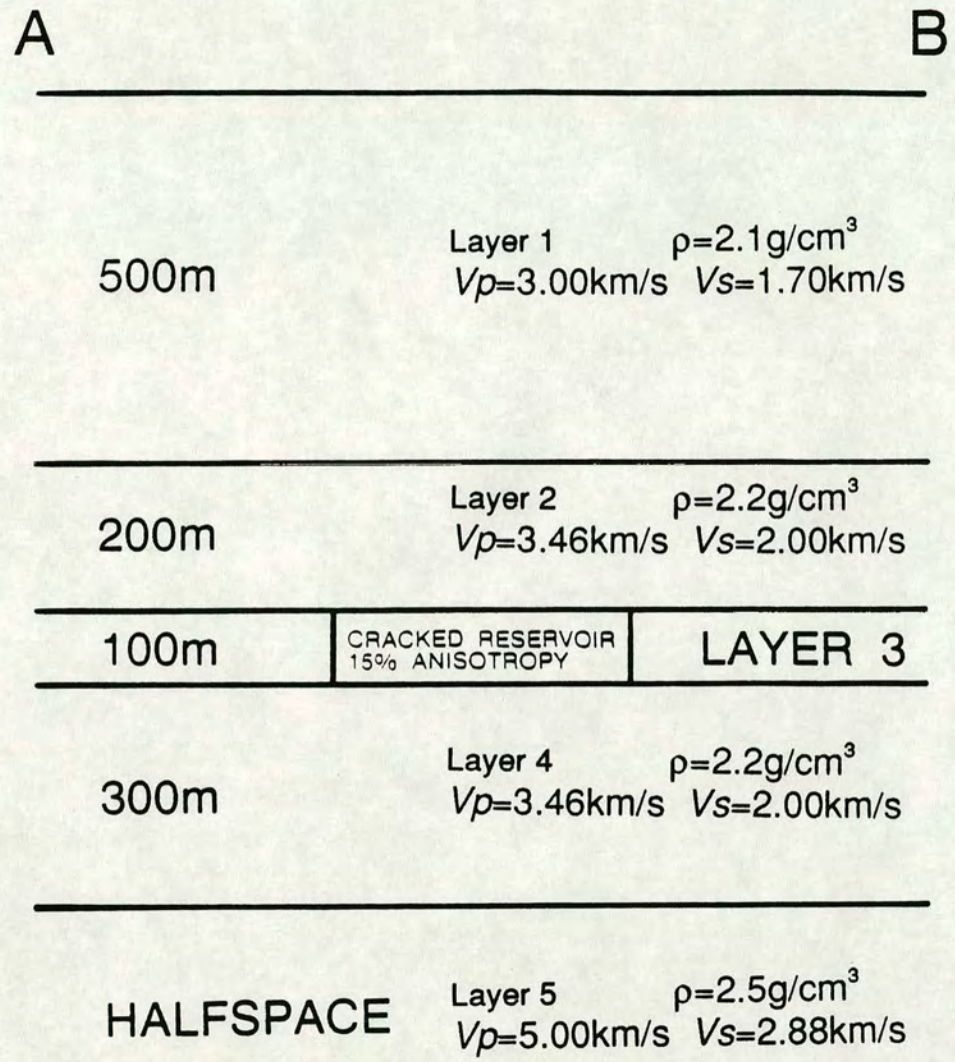

FIGURE 7.4: Schematic model of a multilayered earth containing a region with 15% shear-wave velocity anisotropy in Layer 3 simulating a fractured reservoir. Layer 3 has a density of 2.2g/cm^3; *Vp* and *Vs* are 4.33km/s and 2.50km/s respectively. The reservoir region has the same parameters as the rest of Layer 3, but has *qS1* and *qS2* velocities of 2.50km/s and 2.125km/s respectively.

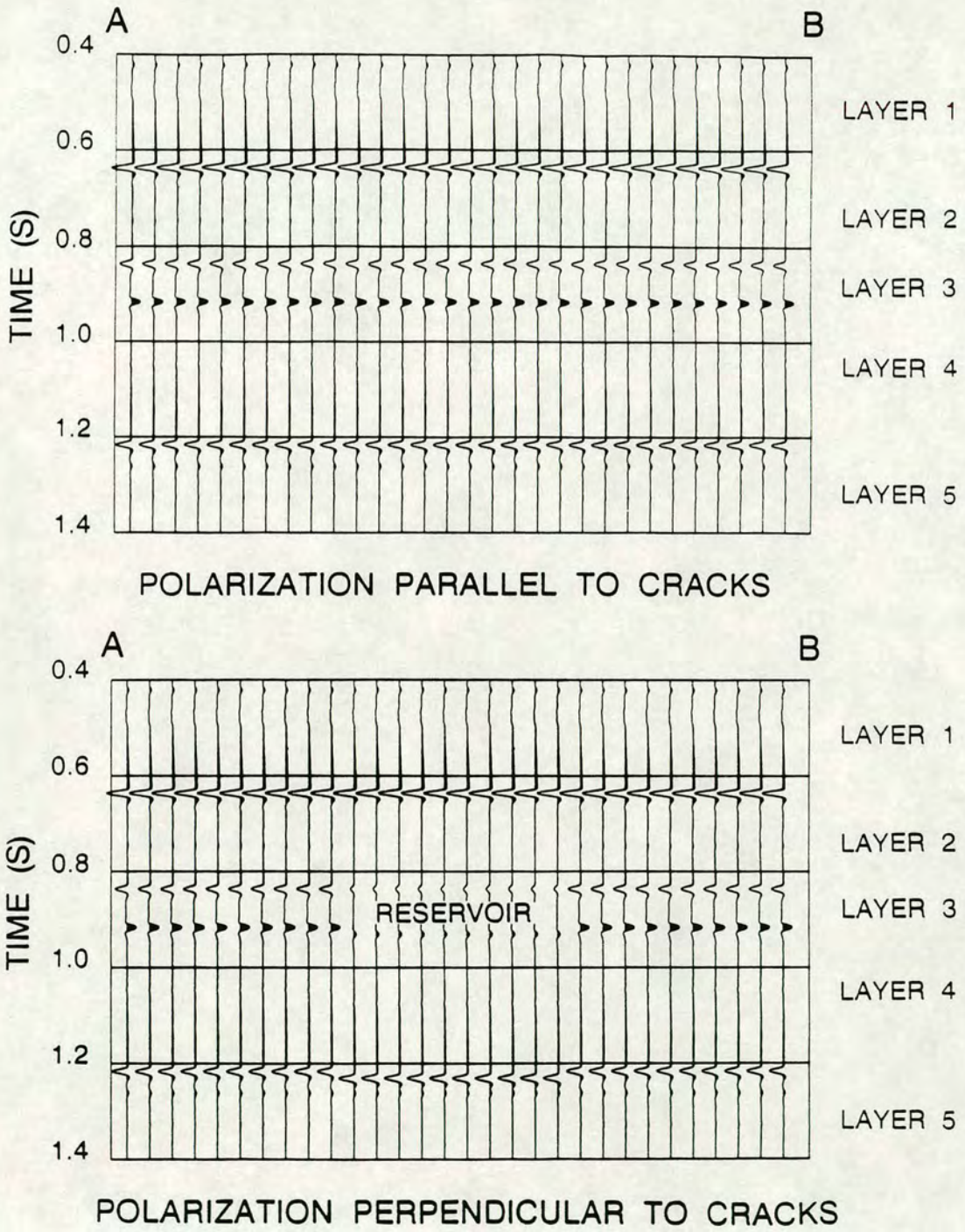

FIGURE 7.5: Synthetic shear-wave normal incidence sections for the model shown in Figure 7.4 for source polarizations parallel and perpendicular to the fracture direction. The reflections from the top of Layer 3 and the top of Layer 4 are continuous for the fast shear-wave section (source polarization parallel to the cracks) but discontinuous for the reservoir region for the slow section (source polarization perpendicular to the cracks). The reflection from the top of Layer 5 has undergone a velocity pull-down in the slow section; the size of the pull-down is dependent on the thickness and anisotropy of the reservoir layer. The dominant frequency of the source pulse is 25Hz.

technique of Mueller works. If the thickness of the reservoir is decreased and the dominant frequency of the pulse is reduced so that the reflections from the top and bottom of the reflector interfere, then amplitude anomalies will still be present if the reservoir is anisotropic; however, such they may be harder to detect. [In Section 7.3.1 and Figure 7.8, I discuss and model such cases.]

This method is also invalid in cases where fracture strike changes with depth as it is not possible to separate the shear-wave energy onto fast and slow sections (see Section 3.6). However, reflector discontinuities may still be seen if the *qS1* polarization direction is constant with depth, even if the overburden is anisotropic.

7.2.3 When can reflected amplitudes be used?

For this technique to work successfully two conditions must be met:

1) the reservoir anisotropy, the velocity contrast and the density contrast must be such that the reflection coefficients parallel, and perpendicular, to the fractures are measurably different;
2) one of the reflection coefficients (either perpendicular or parallel to the fractures) at the top of the reservoir must give a reflected arrival with an amplitude above the noise level. If both reflection coefficients are small then any difference in amplitude between the reflected arrivals, parallel and perpendicular to the fractures, is hidden by noise.

Here, I examine the range of circumstances over which such investigations of the vertical incidence reflection coefficient can provide useful results. Figure 7.6 shows the vertical incidence reflection coefficients at an isotropic/anisotropic interface for the shear-wave polarized perpendicular to the fractures. In Figure 7.6, I vary the velocity contrast and the percentage anisotropy in the reflector. The matrix shear-wave velocity in Layer 2 is 2.5km/s. The curves were calculated using the standard reflection coefficient formula for an isotropic/isotropic interface:

$$\text{reflection coefficient} = (\rho_1.Vs_1 - \rho_2.Vs_2)/(\rho_1.Vs_1 + \rho_2.Vs_2); \qquad (7\text{-}1)$$

where ρ_1, ρ_2, and Vs_1 and Vs_2 are the densities and shear-wave velocities in Layer 1

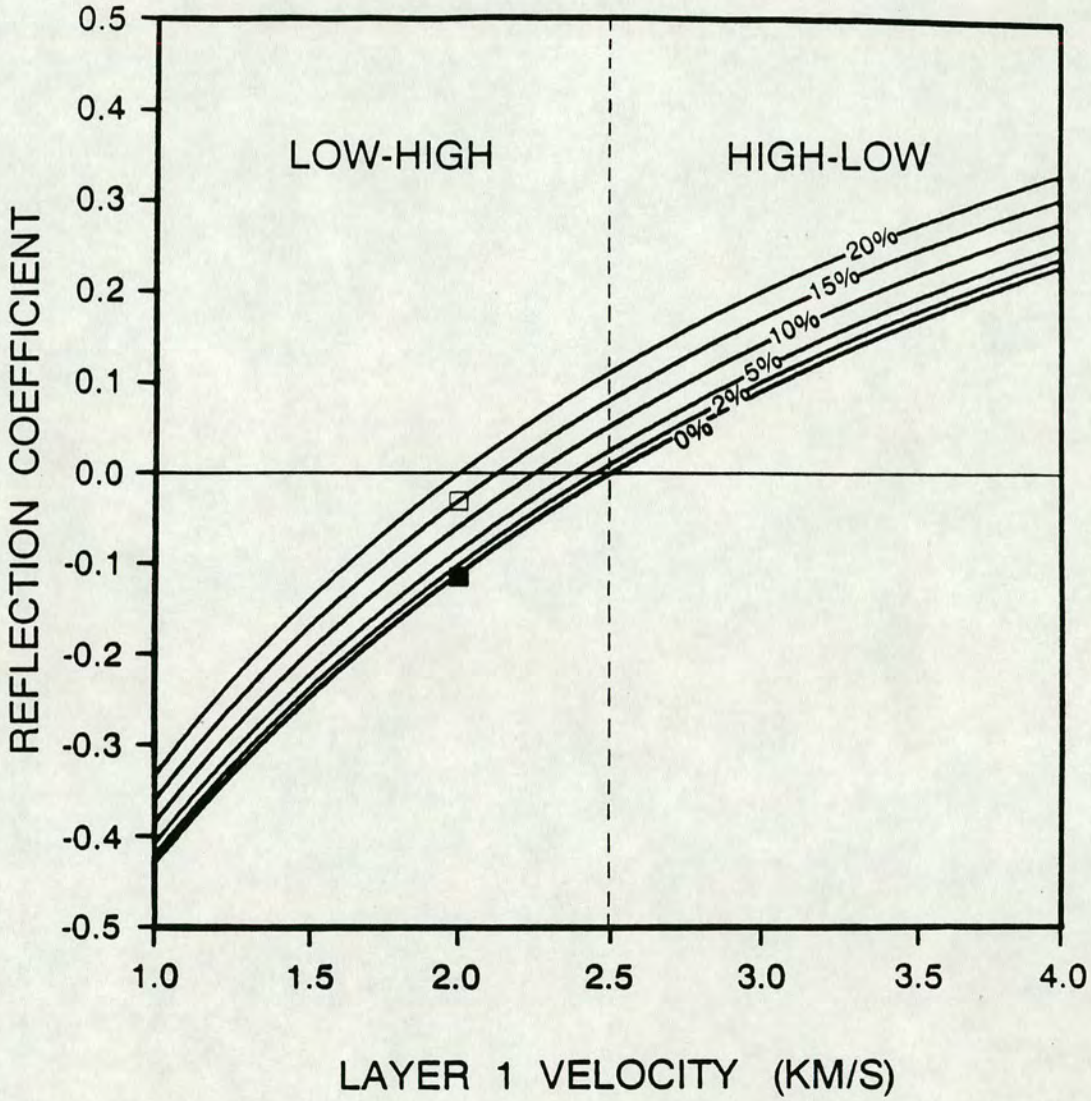

FIGURE 7.6: Vertical incidence reflection coefficients for reflection at a simple isotropic/anisotropic interface for the source polarized perpendicular to the cracks (slow shear-wave) for a range of anisotropies and a range of shear-wave velocity contrasts. The shear-wave velocity of Layer 1 varies from 1 to 4km/s whilst the anisotropy in Layer 2 varies from 0% up to 20%. The open and closed squares mark the reflection coefficients for the shear-waves polarized perpendicular and parallel to the cracks respectively at the top of the reservoir region in Figure 7.5.

and 2, respectively. To create the change in percentage anisotropy the velocity in Layer 2, Vs_2, was varied. The 0% anisotropy curve also represents the curve for the shear-wave polarized parallel to the fractures. [This assumes that the anisotropy is caused by thin fractures and that increasing the anisotropy does not greatly affect the velocities in the fast direction (Section 2.5).] If the upper layer is also anisotropic (e.g. with a constant background level of anisotropy) a similar approach could still be used. However; different velocities parallel and perpendicular to the cracks in Layer 1 would have to be used in Equation (7-1). I used a constant density of 2.2g/cm^3 in each layer. Using a different density contrast affects the position of the curves shown in Figure 7.6 but not their shape. A high-to-low density contrast moves the curves to the left, and a low-to-high density contrast moves the curves to the right. In general, density varies with velocity (although, there is no fixed relationship between them) and a more complicated curve would be needed. This would need to be calculated at each field site, as the relationship between density and velocity is dependent on the local geology.

These curves can be used in experiment design to verify whether reflection amplitude methods are appropriate. Curves, similar to those in Figure 7.6, should be calculated using available well log data from a site. This will show if the necessary difference in reflection coefficients parallel and perpendicular to the fractures is present.

It can be seen from Figure 7.6 that the absolute difference between reflection coefficient curves for different percentage anisotropies does not vary significantly with velocity contrast. However, as velocity contrast becomes small (near the centre of the graph) the values of the reflection coefficients decrease. So for a small velocity contrast, changes in anisotropy in the reflecting layer lead to large percentage differences between the amplitudes of the shear-waves polarized parallel and perpendicular to the strike of the cracks. Conversely, for large velocity contrasts, changes in anisotropy lead to small percentage differences in the amplitudes of the shear-waves polarized parallel and perpendicular to the cracks. To use Mueller's approach, in cases where the reservoir is only slightly more anisotropic than the surrounding rockmass, the velocity contrast between the reservoir layer and the layer

above must be small. If the reservoir is highly anisotropic (heavily fractured) the anomalies should be visible even for large velocity contrasts. The exact details depend on the particular velocity and density contrasts at the site under investigation.

As an example, the reflection coefficients for the reflection from the top of Layer 3 in Figure 7.5 are marked in Figure 7.6. The solid square marks the reflection coefficient for the shear-wave polarized parallel to the fractures. The open square marks the reflection coefficient for the shear-wave polarized perpendicular to the fractures. Figure 7.6 shows that there is a large difference between the reflection coefficient parallel and perpendicular to the fractures in the reservoir layer. Therefore, the reservoir is visible as a reflector discontinuity on the slow section (as is seen in Figure 7.5). The use of graphs, as in Figure 7.6, provides a simple method for seeing if shear-wave reflection amplitude methods are viable at a particular site.

7.3 REFLECTED ARRIVALS IN VSPs

The approach used by Mueller [1991, 1992], described above, has been successful in locating fractured reservoirs. However, in its present form it does not allow reservoir anisotropy to be quantified. I now adapt this technique so that it can be used to quantify reflector anisotropy in VSP data. Modelling has shown that the polarization direction of the medium is constant with depth in the Austin Chalk data and I will only consider such cases in this analysis.

7.3.1 Synthetic examples

In order to quantify reflector anisotropy it is necessary to compare the amplitudes of the reflected shear-waves polarized parallel and perpendicular to the fractures in the reflector. The basic principle of the method I use to do this is shown in Figure 7.7. This shows fast and slow VSP sections with a reflected event from a reservoir. Before comparing the upgoing amplitudes from each section, I normalize their amplitudes with respect to the downgoing wavefield on the same trace. This eliminates problems due to changes in source strength and spherical divergence. This procedure is repeated for every trace on which the reflected event is seen. For each geophone level the amplitude ratio of the two normalized upgoing amplitudes is then calculated. If the

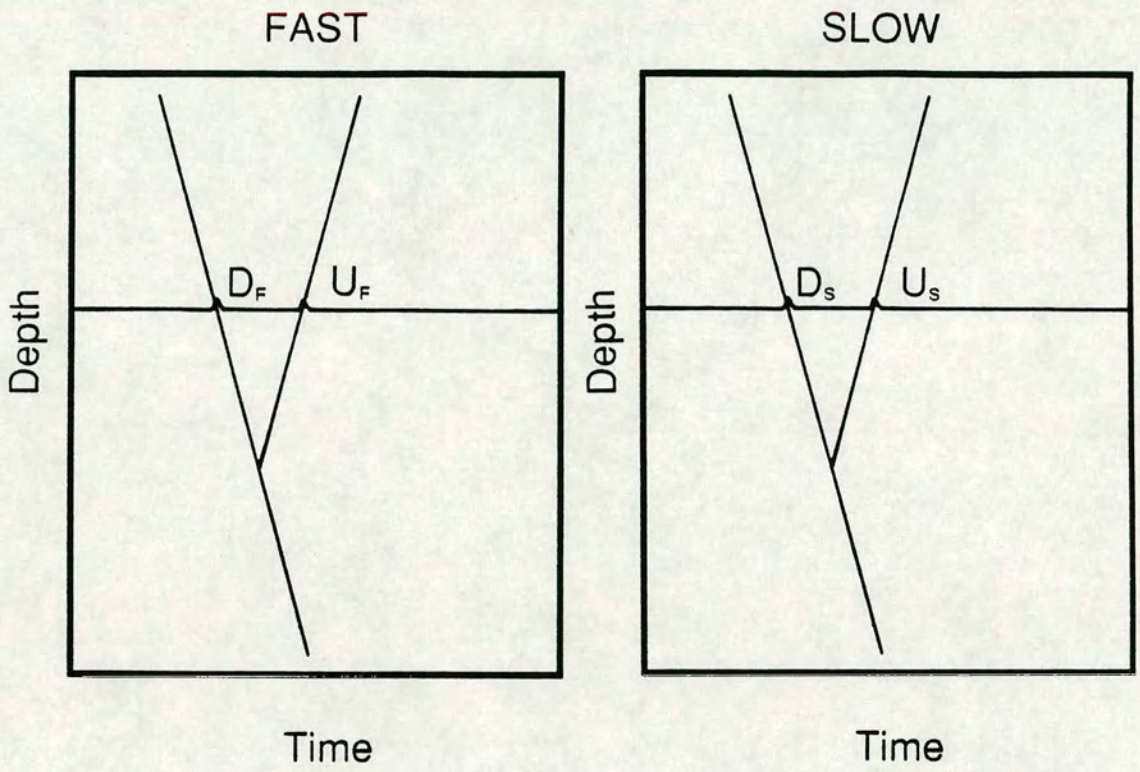

Normalize $\frac{U_F}{D_F} = A_F$ $\frac{U_S}{D_S} = A_S$

Amplitude ratio = $\frac{A_S}{A_F}$

FIGURE 7.7: Schematic diagram of fast and slow VSP sections. In order to analyze amplitudes the upgoing amplitude at a given level is normalized against the downgoing amplitude (U/D) to get rid of source imbalance and divergence problems. The amplitude ratio between the reflected slow and fast events is then calculated.

velocities and densities are known from well logs the amplitude ratio can be used to calculate reservoir anisotropy.

In Figure 7.8, I show the results of this technique applied to a synthetic structure. The model is a simple two layer structure with shear-wave velocities and densities of 2.0km/s and 2.2g/cm^3 in layer one and 2.5km/s and 2.2g/cm^3 in the reflecting layer. The pulse is the same as used for modelling the Devine data set (Section 6.2.3) and has a dominant frequency of 18Hz. The amplitude ratio at each geophone level was first determined for an isotropic reflector and then with 5% crack anisotropy in the reflecting layer. [This model has the same structure as that used in Figure 7.6 which may be consulted to see how changes in reflector anisotropy affect the reflection coefficient.] For normal incidence at an isotropic reflector, the reflection coefficient is independent of shear-wave polarization and the amplitude ratio is 1.0 (Figure 7.8). For the anisotropic reflector (Refl.1, Figure 7.8), the amplitude ratio is 0.77 as expected for 5% anisotropy in the reflector. For this simple case, the greater the deviation in amplitude ratio from unity, the greater the reflector anisotropy. Also, reservoir anisotropy can be calculated from the amplitude ratio. In this synthetic example, amplitude ratios are shown for each level. In field data, where the results are noisy, the results from each geophone level are averaged to give the amplitude ratio for the interface.

Reflection from a thin reservoir layer

At Burleson the Austin Chalk is only 28m thick and I now reduce the thickness of the reflecting layer to 30m to see if this method can still be used to determine reservoir anisotropy. A halfspace with a density of 2.2g/cm^3 and shear-wave velocity of 2.7km/s was introduced below the original reflecting layer. All internal multiples are included in this model and the upgoing event is a superposition of reflections from the top and bottom of the layer of interest. I recalculated the amplitude ratio for this case (Refl.2, Figure 7.8). The amplitude is less than unity and shows that the reservoir layer is anisotropic. In the general case, it is not possible to quantify the anisotropy in the reflector. This is because the amplitude of the recorded arrivals are dependent on the velocity, density and anisotropy in all three layers as well as the pulse shape

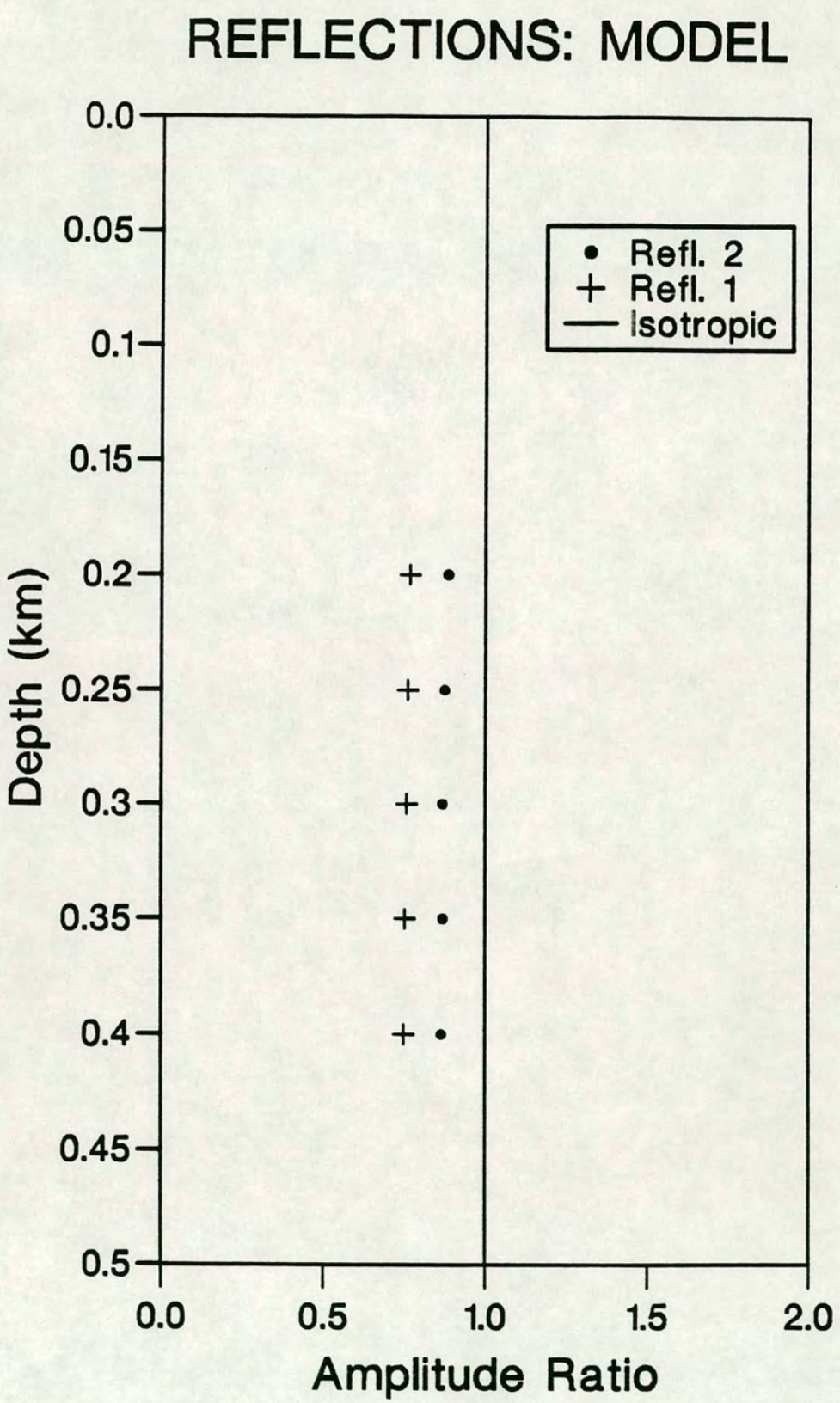

FIGURE 7.8: Amplitude ratios of the normalized upgoing shear-wave polarized parallel and perpendicular to the cracks for: an isotropic interface; a reflecting layer (Refl.1) with 5% anisotropy and the same reflecting layer (Refl.2) reduced to 30m thickness. The model parameters are given in the text. The reflector is at a depth of 500m.

and frequency. However, even for complicated multiple arrivals the amplitude of the reflected waves is different, parallel and perpendicular to the fractures in the reflector. Any deviation from an amplitude ratio of unity indicates anisotropy; although, the size of the deviation does not indicate the amount of anisotropy.

7.3.2 Field data examples

I have shown how reflected amplitudes can be normalized with respect to the downgoing wavefield and used to determine whether reflectors are anisotropic, even for thin reflecting layers. Absolute amplitudes are notoriously difficult to measure in field data and this method has the advantage that only normalized amplitudes are compared between traces. I now apply this technique to field data from Dimmit, Devine and Burleson to see if the reflected arrivals give more information than transmitted arrivals on anisotropy in the Austin Chalk.

I apply this technique only to zero-offset data from the three sites. Application of this technique to offset data could allow the area around a well to be imaged for fracture swarms as different offsets would give different reflection points. However, this is likely to be impractical in field data, particularly in cases where the upper layers are anisotropic as the *SV* and *SH* reflection coefficients are different for non-normal incidence (even at isotropic reflectors [Achenbach 1973]). This causes a generally polarized shear-wave to split on reflection making any determination of the reflected amplitude difficult. [I discuss such problems in Appendix 1. In Figure A1.8, I show that *SV* and *SH* reflection coefficients can diverge for incidence angles under 5°.]

Preparing the fast and slow shear-wave sections for field data

I applied LTT to the Devine and Burleson data sets to find the *qS1* polarization direction with respect to the geophone axis. I then used these angles to rotate the signal from each source direction into the fast and slow directions. LTT has the facility to do a four-component matrix rotation to yield a data matrix as shown in Figure 2.4b. However, this was not used as it combines the energy from the two sources and any difference in source strength may give errors in the amplitudes on the

fast and slow sections. [Source strength imbalances cause minimal errors in *qS1* estimates [Zeng & MacBeth 1993a].] The shape of the PDs varies smoothly with depth and I checked PDs and seismograms for incorrect rotations which, when found, were manually corrected.

The *SV* arrival at Dimmit is linearly polarized implying that it is very close to the anisotropic axes (results of LTT in Chapter Five confirm this). So I created the fast and slow sections, for the Dimmit VSP, by treating the arrival from the crossline source as the fast section and the inline source as the slow section. As the arrivals at Dimmit and Devine are nearly linearly polarized, with the inline direction close to the slow direction, the fast section was taken from the crossline source and the slow section from the inline source. This increases the signal to noise ratio. At Burleson there is more splitting and I calculated fast and slow sections for each source polarization.

I applied FK filters to separate the up and downgoing wavefields. This prevents the coda of the downgoing arrival from distorting the amplitude measurement on the upgoing arrival at a given level. This requires equally spaced geophone levels. The zero-offset VSP sections have several widely spaced levels in the near-surface and I removed these to give a constant geophone spacing. The Burleson data set contained four bad levels and I inserted new traces in their place by interpolation using the GEOWELL package. Whilst not giving a perfect waveform, the interpolation of new traces means that FK filtering may be used on the data. I normalized all traces based on a window around the main downgoing event and applied an FK filter to give the up and downgoing sections. To give the upgoing wave field I used an FK filter which passed the entire upgoing arrival between 3 and 40Hz. Similarly, a filter which passed the entire downgoing arrival between 3 and 40Hz was used to give the downgoing arrival. [Rescaling of amplitudes after filtering is not necessary as only the ratio of up and downgoing amplitudes is compared between traces.] I picked windows interactively around the required events then found the maximum amplitude within the window.

Field results

I tested this method of analysis on the largest reflector at each site (Figure 7.9). At Dimmit the largest reflector is the Georgetown Limestone (see Figure 5.2), and results for this reflector are very close to the isotropic value. At Devine the largest reflector is the Eagleford Shale. [The layers below the Austin Chalk are thin (Figure 6.1) and this arrival is probably a superposition from several reflectors.] Miller, Costa & Schoenberg [1992] used crosshole data to study the anisotropy at this depth and found only transverse isotropy with a vertical axis of symmetry. The lack of azimuthal anisotropy in the Eagleford shale is confirmed here: the amplitude ratios from both VSPs are not significantly different from the isotropic value. At Burleson the amplitude ratio from both source polarizations is around 0.84±0.15 indicating that this reflector is anisotropic. The chalk is thin and this arrival is a superposition of several reflected events. However, as seen in the synthetic examples, this still implies anisotropy in the reflecting layer. This is a direct measurement of anisotropy and is independent of modelling theory.

To try and resolve the reflected events from the Austin Chalk, deconvolution operators were designed, based on the total wavefield each section and these were applied to the fast and slow sections prior to separation of the up and downgoing wavefields. This approach is described by Smidt [1989]. As the fast and slow sections are separated before the deconvolution operator is applied there is no need for three-dimensional operators to preserve the effects of splitting as used by Kramer [1991]. Also, as the upgoing wavefield is normalized with respect to the downgoing signal on the same trace the actual deconvolution operator used is unimportant, as long as it reduces the pulse length. The processing was done using the GEOWELL package and the output was a zero phase wavelet. The shear-wave sections were then FK filtered, as before, to give the up and downgoing wavefields. I then calculated the amplitude ratios for the Austin Chalk reflector at each site.

The results are shown in Figure 7.10. Wavelet compression has enabled the reflected events from the Austin Chalk at Burleson and Dimmit to be picked. In both cases the average results are close to unity. However, there is some scatter as the reflector is weak. The result from W4S1 (1.00±0.03) at Devine shows clearly that the

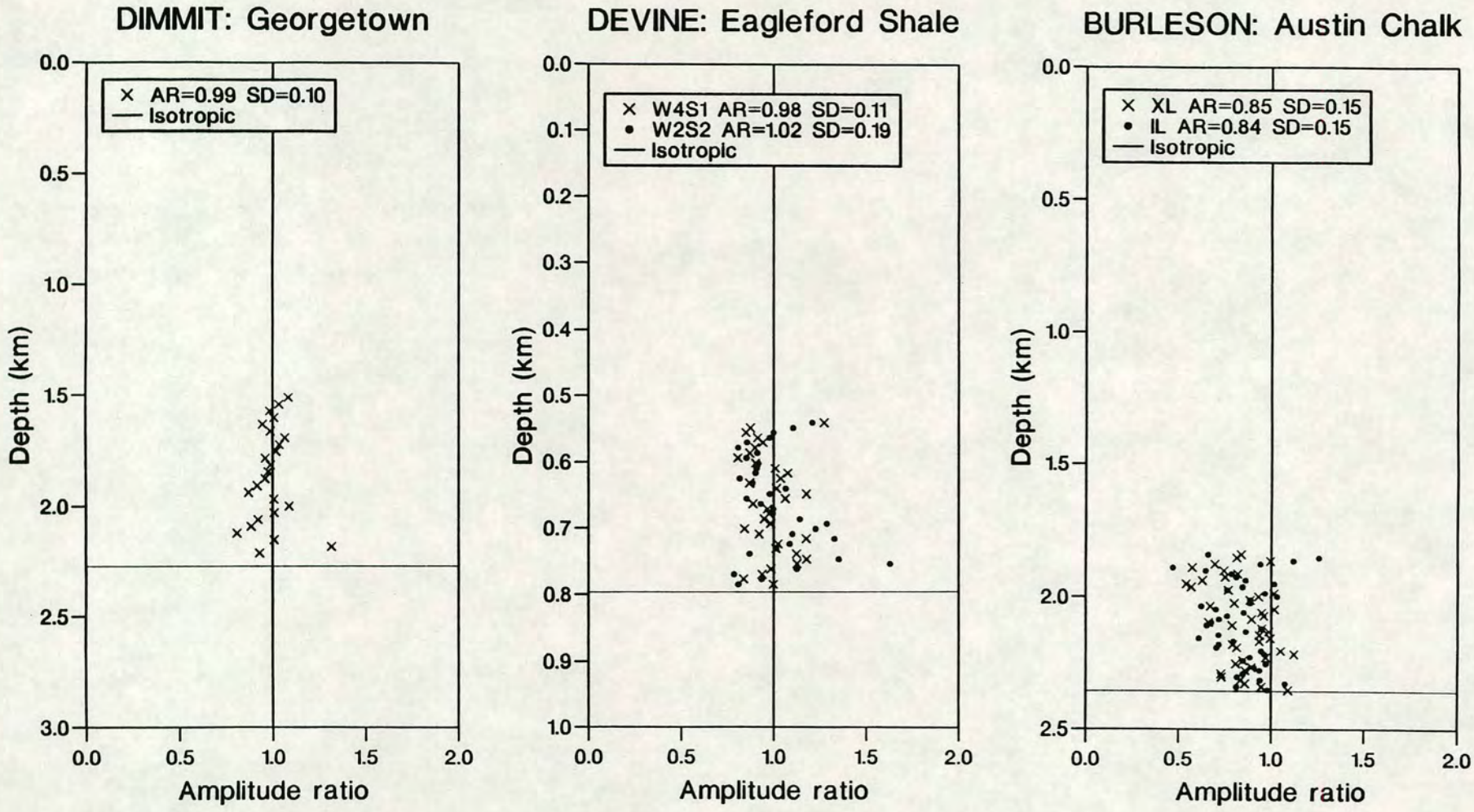

FIGURE 7.9: Amplitude ratio results from zero-offset VSP data for the largest reflector at the three study sites. The amplitude ratio (AR) and standard deviation (SD) are given in the legend. The reflectors at Dimmit and Devine are isotropic with amplitude ratios around 1.0 as expected from analysis of transmitted waves (see Chapters Five and Six). At Burleson the amplitude ratio is less that 1.0 indicating an anisotropic reflector.

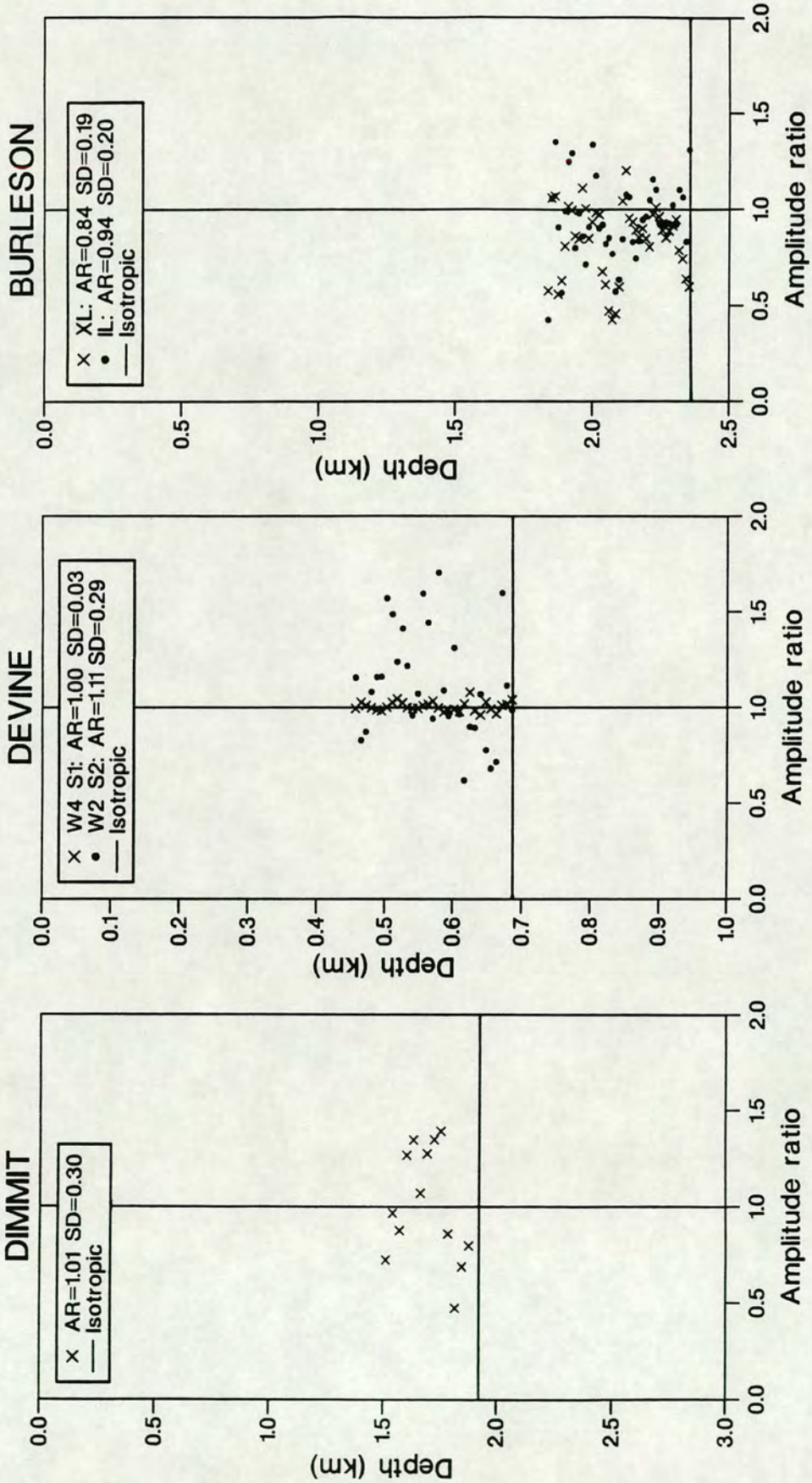

FIGURE 7.10: Amplitude ratios calculated for the Austin Chalk reflectors after waveshaping to make picking of arrivals easier. The amplitude ratio (AR) and standard deviation (SD) are given in the legend. The results, although scattered, cluster around unity as expected for isotropic reflectors, except at Burleson where the reflector is anisotropic.

chalk is isotropic for vertical incidence. Using the densities and velocities for Layers 6 and 7 (Austin Chalk) given in Table 6.1, this gives a maximum anisotropy in the Austin Chalk at Devine of 1%. So the fractures observed at Devine in well data do not make the chalk significantly anisotropic for vertically propagating waves. The data at Burleson still show amplitude ratios of less than unity; however, results are more scattered than in Figure 7.9. The application of the deconvolution operator has not improved the results. I cannot calculate the limits on the anisotropy in the Austin Chalk at Burleson as the reflected arrival is a superposition of arrivals from the top and bottom of the layer. Also the structure, and pulse shape are not known sufficiently well.

I also calculated amplitude ratios for two other major limestone sequences; these were the Georgetown Limestone at Dimmit and the Anacacho Limestone at Devine (Figure 7.11). Again, the amplitude ratio is clustered around 1.0 showing that these layers are isotropic as expected from the analysis of transmitted waves in the previous two chapters. Using the densities and velocities for Layers 5 and 6 (Table 6.1) and the amplitude ratio from W4S1 this gives an azimuthal anisotropy in the Anacacho Limestone of 0.0±3.5%. The means that leaving this layer isotropic in the Devine model was valid.

7.4 CONCLUSIONS

In this chapter I examined current methods of using vertical incidence reflections to find anisotropy in a reflector. I conclude that methods that look for rotations of the wavefield will be impractical in the general case, as the near-surface is anisotropic. The most effective methods are those which compare the reflected amplitudes for shear-waves polarized parallel and perpendicular to fractures in the reflector. Such methods can be used only where the velocity contrast is small or the percentage anisotropy in the reflector is large.

I adapted the work of Mueller [1991, 1992] for use with VSP data. I overcame problems associated with spherical divergence and source imbalance by normalizing the upgoing event with respect to the downgoing event on each trace.

Using this technique, I showed that the Austin Chalk at Burleson is anisotropic.

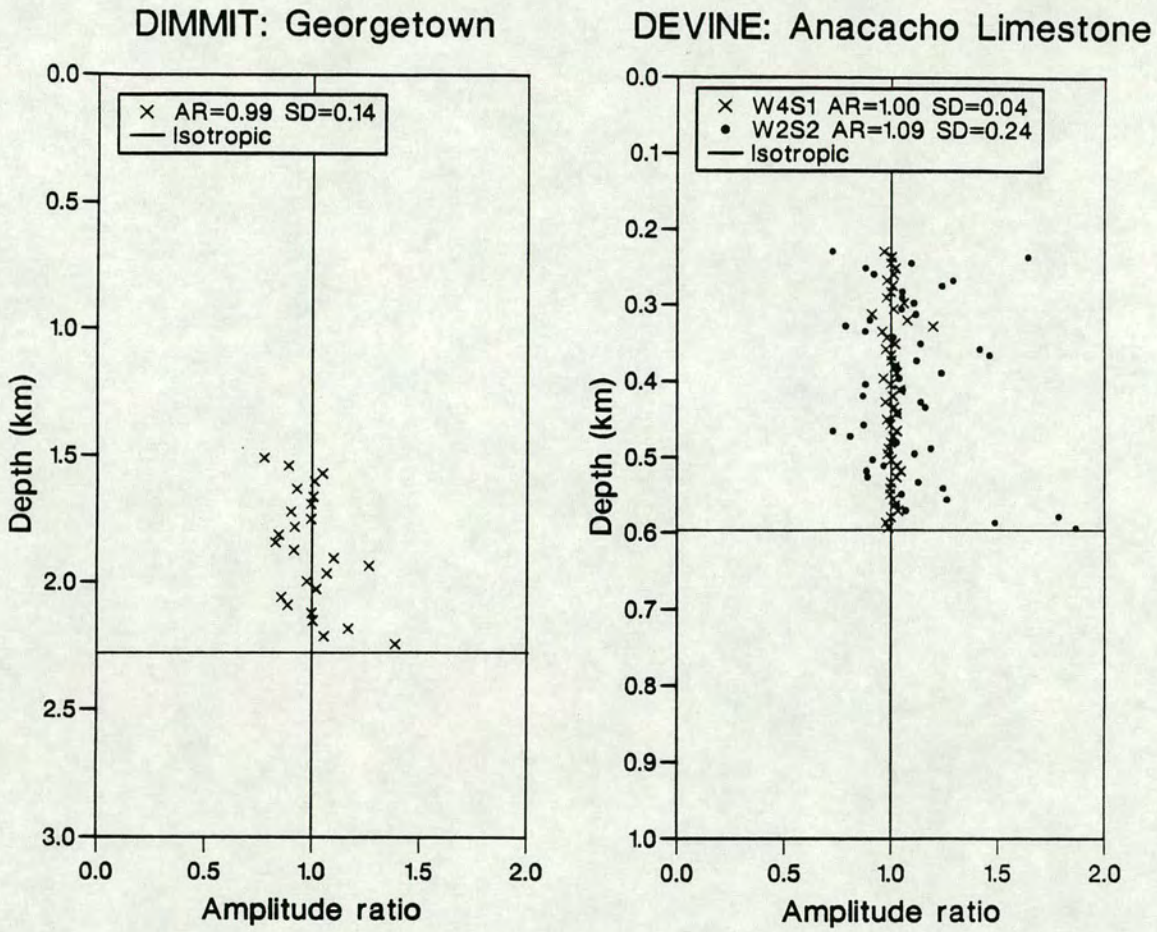

FIGURE 7.11: Further amplitude ratios for other major limestone units at Dimmit and Devine. The amplitude ratio (AR) and standard deviation (SD) are given in the legend. As expected from analysis of the transmitted shear-waves the amplitude ratios are close to unity.

This chalk is known to contain a producing fractured reservoir [M.C.Mueller, personal communication]. The Austin Chalk at the other two sites (and other limestone units) were found to be isotropic confirming the results of the estimation techniques on transmitted waves and the modelling. For the three VSPs there is a positive correlation between anisotropy and fractured hydrocarbon reservoirs.

This has shown that reflected amplitudes can be used to establish the anisotropic nature of layers in cases where the anisotropy is too weak, or the layer too thin, for time delays to build up in transmitted waves. Although it may not be possible to quantify anisotropy in thin reservoirs, I have shown that reflected shear-waves can be used to identify fractured reservoirs. This work confirms the results of Mueller's analysis of field data: shear-wave reflections can be used as an exploration tool in plane layer structures.

CHAPTER EIGHT

CONCLUSIONS

8.1 INTRODUCTION

My aim in this thesis was to extract useful information about fracture density and orientation in regions where reservoir productivity is known to be governed by fracturing. I have determined the *qS1* polarization direction and time delays at VSP sites in California and Texas and I have used these to produce anisotropic models for the structure in the Lost Hills field, California, and the BP Devine Test Site, Texas. I have also developed a technique that can be used to identify anisotropy in thin reservoirs. Here, I summarize my conclusions and discuss their implications for the use of shear-wave anisotropy in the hydrocarbon industry. I also make suggestions for future work.

8.2 ACQUISITION AND PROCESSING

In this thesis I have shown that there are two cases when estimation techniques can give consistent, but incorrect, results with depth:

1) when multiple splitting has occurred (Section 3.6.2);
2) in cases where source and receiver polarities are unknown (Section 5.4.1). This is a common problem and was encountered in all data sets analyzed in this thesis.

I have shown that application of a range of estimation techniques can be used to determine uniquely instrument polarities. Also, MacBeth & Yardley [1992] have shown that AIT can be used to locate depth levels at which multiple splitting occurs. Therefore, it is necessary to apply a range of estimation techniques (DTS, AST and AIT) before interpreting the results of estimation techniques.

Window lengths for applying estimation techniques

I tested the effect of varying the window length over which the estimation techniques (DTS, LTT, AST and AIT) are applied. Results are stable once the window contains the main shear-wave arrival and are not affected by the presence of low

amplitude multiple events following the main arrival.

Estimation techniques on offset data

The estimation techniques described in Section 2.7 require that the two split shear-waves are orthogonal. For offset arrivals, the projections of the split shear-waves on the horizontal plane are not orthogonal. To overcome this, I applied the estimation techniques in the dynamic plane and projected the polarization results back onto the fixed horizontal plane. I calculated the incidence angle of the incoming shear-waves from the energy in the sagittal plane. For the Devine data this gave an underestimate of the incidence angle and it would be better to rotate the shear-waves into the dynamic plane using incidence angles determined using the model structure.

Shear-waves from P-wave sources

Using *P*-wave data from the Devine Test Site, I was able to get reasonable estimates of time delay. Polarization estimates were rotated with respect to those determined using a shear-wave source. This may be due to a dipping *P-S* mode converting interface giving rise to an unknown initial source polarization. Therefore, estimates from mode converted data should be treated with caution.

Results from the single source estimation techniques on mode converted and direct shear-wave data were generally noisy. This is because the acquisition geometry is often arranged such that the suspected fracture direction is either perpendicular of parallel to the inline direction. This gives little observed splitting for single source data. I conclude that acquisition geometries should be at least 30° to the suspected fracture strike so that the arrivals from the inline and crossline sources contain enough energy for single source techniques to be used. This is important as single source data must be used to confirm the source and geophone polarities.

Data coverage

If it is necessary to model the entire anisotropic structure, or changes in medium polarization direction with depth are suspected, then VSP data should be recorded at all levels, including in the near-surface. In Chapter Four, I was unable to determine

the deeper structure by layer stripping as the change in medium polarization took place above the shallowest geophone level.

In cases such as along the Austin Chalk trend in Texas, the structure is simple, fractures are subvertical, and the medium polarization direction is constant with depth. Therefore, it is unnecessary to go to the expense of collecting offset data as it does not yield further information about fracture strike and density. If the anisotropic structure dips, then offset data also need to be recorded; however, the presence of internal shear-wave windows can lead to multiple splitting. This can make some of the recorded data harder to interpret (Section 6.3.2).

8.3 LOST HILLS

The data coverage at the Lost Hills field was poor and more data would be required to determine the full anisotropic structure. Results of the estimation techniques and modelling indicate that the medium polarization changes with depth and is N58°E at depth. I showed that application of AST on data containing multiply split shear-waves can give invalid results and that this has lead to incorrect interpretations based on this data set.

Whilst I have insufficient well data to determine the cause of the anisotropy, it is probable that it is caused by fracturing parallel to the stress field. Fractures, formed during recrystallization, are known to exist in the field. These have strikes parallel to the determined medium polarization direction and the regional maximum compressive stress.

8.4 AUSTIN CHALK

I extracted time delays and polarization angles from VSP data at three sites along the Austin Chalk trend in Texas. Modelling of the Devine Test Site multi-offset data indicated that azimuthal anisotropy (which cannot be attributed to thin layering) is present and that this is caused by aligned vertical features. Again, it is not possible to determine the cause of the anisotropy. However, extensional fractures, which are predominantly subvertical are known to be present throughout the region. These fractures are parallel to the maximum compressive stress. The determined *qS1*

polarization directions are also parallel to the fracture directions and it seems likely that the anisotropy is caused by fractures which formed in the current stress field.

At all sites, most of the observed time delay builds up in the near-surface and I was not able to resolve additional splitting in the Austin Chalk Layer. I examined the Austin Chalk layers for anisotropy by comparing the amplitudes of the upgoing waves on the fast and slow sections after normalization with respect to the downgoing arrival. This analysis showed that the thin, fractured, producing chalk layer in the Burleson County well is anisotropic, whereas the Austin Chalk at the other two sites is isotropic.

8.5 CAUSES OF AZIMUTHAL ANISOTROPY

At all sites, azimuthal anisotropy is present which cannot be attributed to horizontal layering. It is known that fractures are present, at least at some depths, at all sites and it is reasonable to assume that the fracturing is the cause of this anisotropy. Crampin [1992b] has suggested that azimuthal anisotropy is due to compliant pore space and micro-cracks, aligned by the current stress field (known as EDA). Although the *qS1* polarizations are parallel to the maximum compressive stress, fracture strikes are also parallel to the stress direction. Therefore, whilst it is possible that stress aligned pore space and micro-cracks cause the anisotropy, I have insufficient data to support this. Detailed analysis of cores is needed to determine the exact cause of this azimuthal anisotropy.

Even if fracturing is not the direct cause of the anisotropy, fracturing and anisotropy are related: independent evidence (e.g. core, televiewer and dipmeter data) shows that fractures are aligned parallel to the *qS1* direction. Therefore, fracture orientation can be determined from shear-wave VSPs.

8.6 IS SHEAR-WAVE ANISOTROPY USEFUL?

Shear-wave anisotropy can potentially be used to determine fracture orientation and to locate zones with high fracture densities. I now discuss how well shear-wave anisotropy can determine these parameters. I conclude that shear-waves can be used as an important tool in locating fractured reservoirs; however, fracture orientation

appears to be dependent on the regional stress pattern and could be found by other methods.

Fracture orientation

Although, the *qS1* polarization is parallel to the fracture strike at all study sites, the fractures are also parallel to the regional maximum compressive stress direction. Fracture directions, at these sites, can therefore be inferred from the World Stress Map [Zoback 1992].

Also, most anisotropy is seen in the near-surface [e.g. Bush 1990; Chapter Six], with little additional anisotropy at depth. Therefore, determinations of the deeper fracture orientations are extrapolations of the *qS1* polarization determined in the near-surface. This is reasonable for the Texas data, where the structure is simple and fracture orientations are constant with depth. However, it is dangerous in more complex structures, such as at the Lost Hills, where the *qS1* polarization direction changes with depth. In cases where the medium polarization changes with depth there needs to be sufficient anisotropy in the layer of interest to determine the *qS1* polarization direction in that layer.

Fracture density

For the sites examined here, fracture orientation appears to controlled by the regional stress pattern. However, it is also important to be able to determine fracture density as this can vary locally.

I was not able to identify reservoir anisotropy in any of my case studies using transmitted shear-waves, even though the Burleson well intersected a known fractured reservoir. I showed how reflected amplitudes in VSP data can be used to identify regions of high fracture density and that the chalk in the Burleson well was anisotropic. I believe, that this forms the most important potential application of shear-wave anisotropy: the ability to locate fractured reservoirs. This approach can be used in exploration for hydrocarbon reservoirs where the hydrocarbons are held in fractures or where fractures provide the dominant pathway for fluid flow within the reservoir. This technique is limited to plane layered structures as dipping (or offset) reflectors

can distort the reflected amplitudes.

8.7 THE FUTURE

Using the Austin Chalk data, I have shown that fractured hydrocarbon reservoirs in the Austin Chalk are associated with shear-wave anisotropy and that shear-waves can be used to detect fractured reservoirs. However, the scope of my study was limited by the data sets made available by the oil companies:

- I examined only three sites;
- I had very little information about fracture densities and production results in the wells; and
- the producing interval at Burleson, on which this result is based, is thin.

Before making any firm conclusions about the link between reservoir properties and anisotropy it is necessary to do a far more complete study. This should incorporate: more sites; large producing intervals; full well logs and information about observed fracture density and orientation (from televiewers or formation microscanners).

At present, I believe that we do not know enough about the anisotropic structure of the earth to study anisotropy in a complex geological setting where interface effects also distort the shear-wave signal. Therefore, it would be best to restrict (initially) such an experiment to VSP data from simple structures. VSPs allow recordings to be made at all depths allowing the changes in the waveform to be followed with depth. Texas is the obvious location in which to perform such an experiment as the structure is subhorizontal and fractures are predominantly subvertical. This allows the effects of anisotropy due to fracturing to be examined independently of layering affects.

APPENDIX 1: WHAT CAN OFFSET REFLECTIONS TELL US ABOUT THE ANISOTROPIC STRUCTURE OF RESERVOIRS?

A1.1 INTRODUCTION

Ostrander [1984] showed that reflected *P*-wave amplitude variations with offset (AVO) contains characteristic information about the fluid content of sandstone reservoirs. In Chapter Seven, I showed that vertical incidence reflected shear-wave amplitudes contain information on fracture density. Here, I examine what characteristic information offset shear-wave reflections contain about the crack structure of reservoirs. I conclude that, although offset reflected amplitudes contain information about the crack structure, they are difficult to measure in practice.

The aim of studying shear-wave AVOs is to look for characteristic differences in the shape of the reflection coefficients against angle of incidence curves for varying properties of the reservoir. A cracked, or fractured, reservoir might be identified by comparing the variation of the AVO curves along a shear-wave reflection line and locating the reservoir characteristics from their AVO signature. In this appendix, I examine the effect of reservoir anisotropy and crack-fluid content on the shear-wave AVO.

All modelled anisotropic media are hexagonally symmetric with a horizontal axis of symmetry, consistent with the presence of vertical aligned cracks or fractures. The velocity structures are typical (but non-specific) of rocks in sedimentary basins. A Poisson's ratio of 0.25 is used throughout which gives a *Vp/Vs* ratio of 1.73.

A1.2 AVO SENSITIVITY TO ANISOTROPY AND FLUID CONTENT

In anisotropic media, the shear-wave velocities generally vary with angle of incidence and azimuth. It is therefore expected that the shape of the AVO curve changes with azimuth and with percentage anisotropy in the reflecting layer. The shape of the shear-wave AVO curve can therefore yield information about the

anisotropic structure of the reflecting (reservoir) layer.[1]

Fluids cannot support shear stresses and it might be supposed that changing the fluid content in cracks would have no effect on the shear-wave reflectivity. However, if the fluid is contained in thin cracks then shear-waves propagating at an angle to the crack surface exerts some compressional force on the fluid in the cracks. For vertical propagation, the shear-wave velocity is principally dependent on the rock matrix properties, but for ray paths at an angle to the face of the cracks, the behaviour of shear-waves is modified by vertical cracks. In addition, because the two split shear-waves behave differently at the surface of the inclusions, even small differences between the shear-waves are likely to lead to identifiable changes in the highly sensitive polarization diagrams of the particle displacements.

Body wave behaviour in anisotropic media

Before looking at how variations in crack content and percentage anisotropy affect shear-wave AVO curves it is necessary to check the extent to which changes in these parameters affect the body wave velocities in anisotropic media. Without changes in the body wave curves there will be no change in the reflected amplitudes. Figures A1.1 and A1.2 show the behaviour of body waves, shear-wave polarizations and time delays for both water-filled and dry cracks for shear-wave anisotropies of 5% and 20%. Water-filled and dry (gas-filled) cracks were chosen to illustrate the range of possible variations in rock properties due to the fluid content of cracks.

---

[1]**P-wave AVO:** It must be noted that the situation for *P*-wave AVO [Ostrander 1984] is more dramatic. Liquids and gases have greatly different compressibilities and therefore different *P*-wave velocities: at 40°C, heavy crude has a *P*-wave velocity of about 1.4km/s [Wang & Nur 1988]; whereas methane has a *P*-wave velocity of 0.47km/s at this temperature (at one atmosphere) [Kaye & Laby 1986]. With increasing incidence angle at a water-saturated sand reflector more energy is mode converted to refracted and reflected shear-waves giving rise to a decrease in reflected *P*-wave energy with offset. As the sediment becomes partially gas saturated the *P*-wave velocity decreases quickly due to the change in compressibility caused by the presence of gas in the pores (the greatest decrease in *P*-wave velocity occurs over the first 3% to 8% of gas saturation). This reduction in the *P*-wave velocity can cause an increase in *P*-wave reflectivity (at, for example, a gas-sand to shale interface), without substantially affecting the shear-wave reflectivity (for angles of incidence out to about 40°, as will be shown later in this appendix). This means that a large proportion of the incident *P*-wave energy goes into reflected compressional waves and can lead to an increase in reflected *P*-wave amplitude with offset.

Figure A1.1 shows that there is little change in the pattern of *qS1* polarizations and time delays with increasing anisotropy. [The matrix material examined here is the same as used in later AVO calculations where it represents the reservoir layer.] The central band of polarizations (bounded by line singularities, Section 2.4) aligned parallel to the cracks is wider for dry cracks than for water-filled cracks. For 5% anisotropy this band of polarizations extends throughout the equal area plot. [For surface recordings the polarizations are distorted if recorded outside the shear-wave window [Section 3.3, Booth & Crampin 1985] and the extent of such aligned polarizations may not be seen. Ray bending, due to velocity increase with depth, means that a wider range of incidence angles at a reflector can be studied inside the shear-wave window at the surface.] Time delays are much larger for the case of 20% anisotropy than for 5% anisotropy.

Figure A1.2 shows body wave velocities for the same range of models as above. Figures A1.1 and A1.2 show that changes in the percentage anisotropy cause an increase in time delay, most noticeably for vertical propagation. The change in crack content, from water-filled to dry cracks, causes the line singularity to move away from the vertical (for vertical cracks) and causes the largest change for propagation at wide angles of incidence. These diagrams have confirmed that shear-wave velocities vary, for both azimuth and incidence angle, with changes in percentage anisotropy and crack content.

Calculation of reflection coefficients

The graphs of reflection coefficients against angle of incidence at an isotropic/anisotropic interface were calculated using a program adapted from the work of Booth & Crampin [1983]. Graphs of reflection coefficient against incidence angle at an isotropic/isotropic interface were calculated using modified Zoeppritz's equations [McCamy, Meyer & Smith 1962; Aki & Richards 1980]. The computer programs to calculate reflection coefficients in anisotropic and isotropic models were written, and required models, were run by Gerhard Graham.

[Note: the reflectivity technique of Booth & Crampin [1983] does not take account of azimuthal variations. The results from it are only strictly correct for propagation in

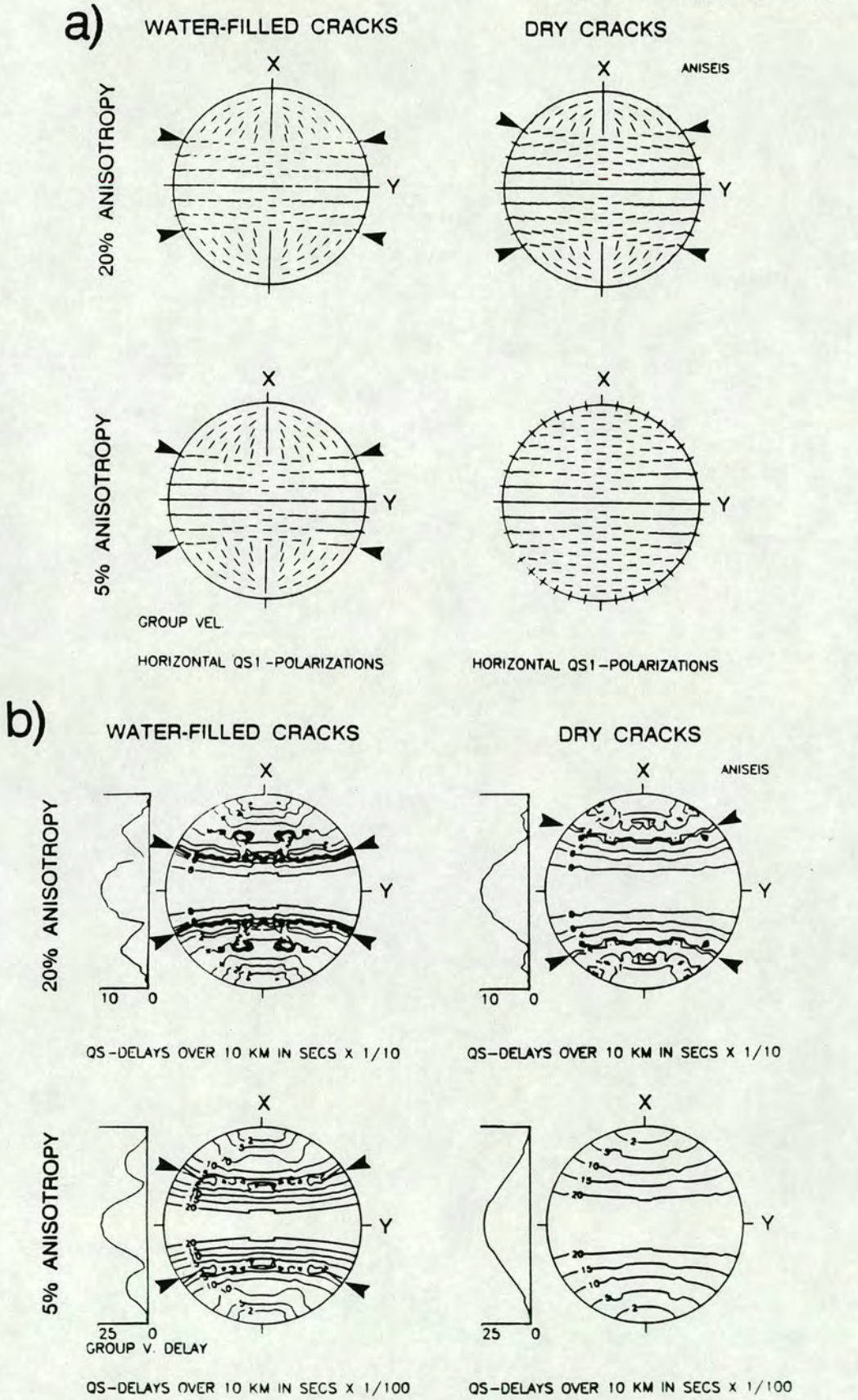

FIGURE A1.1: Equal area plots of (a) polarization of the leading split shear-wave and (b) time delays between the two group velocity sheets for both water-filled and dry cracks for 5% and 20% anisotropy. Matrix density, *Vp* and *Vs* are 2.2g/cm^3, 4.33 and 2.5km/s respectively. Cracks are aligned in the Y-Z plane. The line singularities are marked by arrows.

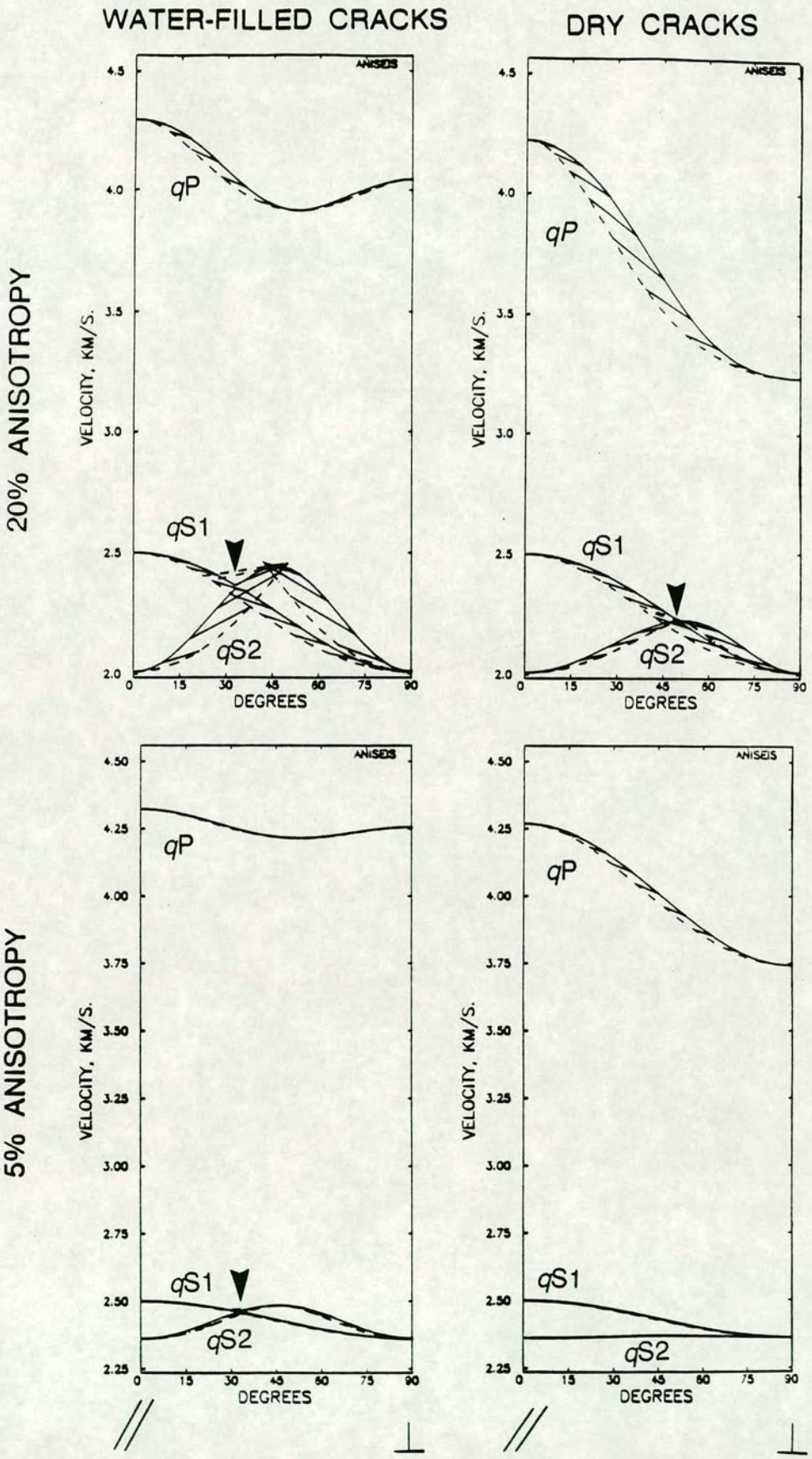

FIGURE A1.2: Group (dashed line) and phase (solid line) body wave velocities for the same range of models shown in Figure A1.1. [See Chapter Two for a more detailed explanation of the displays used in Figures A1.1 and A1.2.] The line singularities are marked by arrows.

planes of sagittal symmetry, although for non-sagittal symmetry the differences are likely to be negligible for weak anisotropy. The reflection coefficients presented in this appendix are calculated in planes of sagittal symmetry.]

Shear-wave AVO curves for crossline cracks

Figure A1.3 shows the variation of reflection coefficient with angles of incidence for *SV*-waves at an isotropic/anisotropic reflector. The second layer represents a possible reservoir in which the differential shear-wave velocity anisotropy varies from 0% to 20% and is caused by parallel vertical cracks aligned normal to the plane of incidence. The upper layer is isotropic for simplicity. In many cases cracks or fractures are likely to be thin: Corbett, Friedman & Spang [1987] show evidence of thin fractures in the Austin Chalk, Texas. I use thin cracks, with an aspect ratio of 0.01. Similar graphs were calculated for a range of velocity contrasts from a velocity increase of 15%, to a velocity decrease of 15% across the interface; however, the general results are the same as described here.

Figure A1.3 also shows that for both water-filled and dry cracks the amplitude of the near vertical reflected wave increases with percentage anisotropy in the reservoir layer. In this case, with cracks striking in the crossline direction, the *SV*-wave is polarized parallel to the slow direction (for vertical propagation) in the lower layer. For thin cracks the velocity parallel to the cracks does not change appreciably with anisotropy [Hudson 1980, 1981]. However, the velocity perpendicular to the cracks decreases with increasing anisotropy giving rise to a larger velocity contrast (for this high-to-low velocity interface) for a wave polarized perpendicular to the cracks and an increase in the near vertical reflection coefficient with increasing anisotropy for the *SV*-wave. Also the critical angle increases by about 6° as anisotropy increases from 0% to 20%.

There is a large difference in the shape of the AVO curves for wide offsets between the water-filled and dry cracks (as expected from the analysis above), but little change in the critical angle. This is because, for thin cracks, the shear-wave line singularity moves away from the vertical as the content of the cracks changes from water-filled to dry. The results here show that analysis of shear-wave AVOs may have

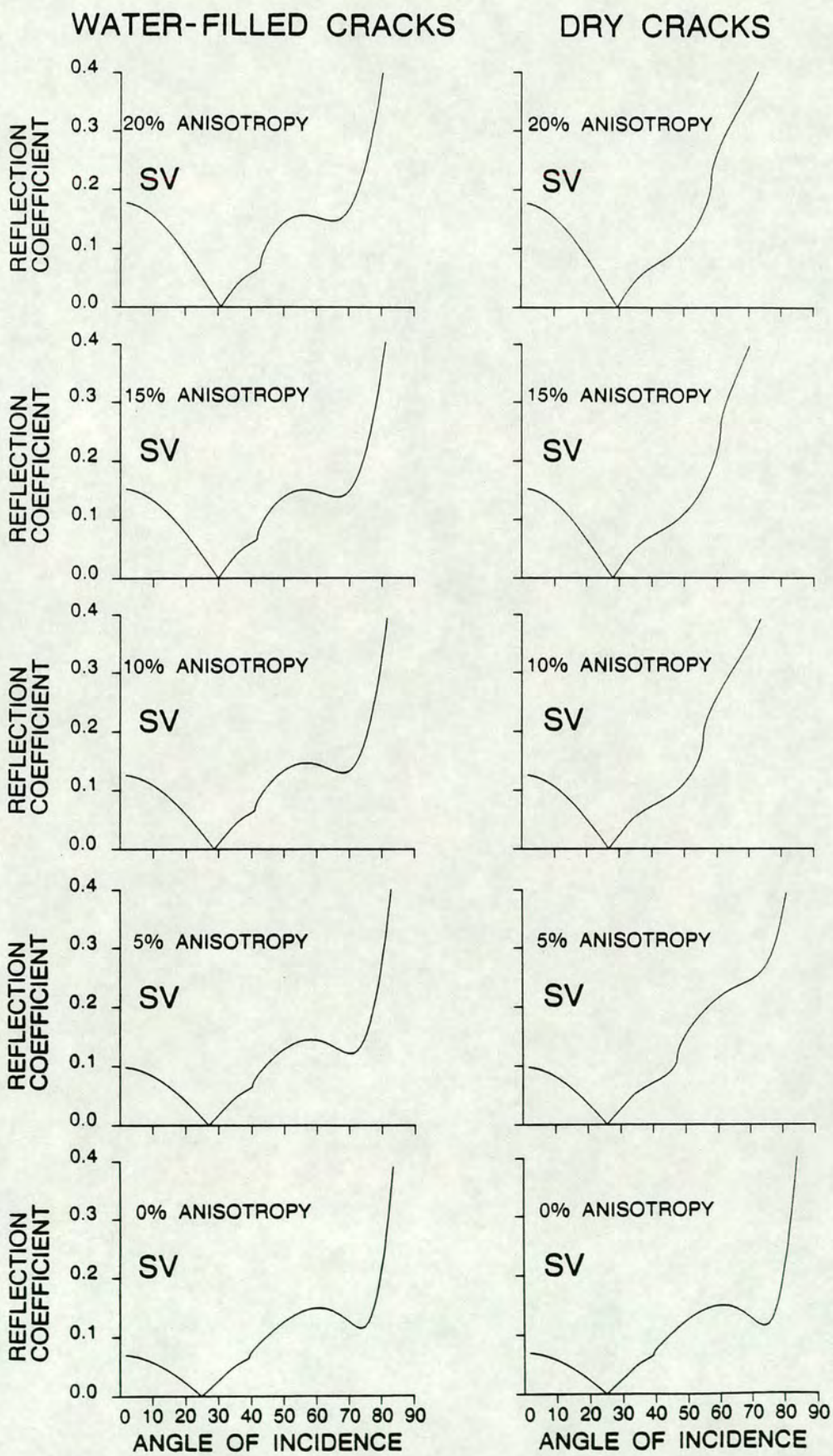

FIGURE A1.3: Plots of reflection coefficients against angle of incidence for *SV*-waves for a range of differential shear-wave anisotropies at a high-to-low velocity interface (matrix density, *Vp* and *Vs* are 2.3g/cm^3, 4.76 and 2.75km/s in Layer 1, and 2.2g/cm^3, 4.33 and 2.5km/s in Layer 2 respectively). The anisotropy is modelled by parallel vertical cracks aligned normal to the plane of incidence. Graphs are shown for both water-filled and dry (gas-filled) cracks.

potential uses in the monitoring of EOR. In EOR processes the fluid content of the reservoir is changed either by heating or injecting further fluids and these might be detected using shear-waves. The changes in rock matrix velocities due to heating are small [Wang & Nur 1988] and do not greatly affect the shear-wave reflectivity. Shear-wave reflectivity may be affected by the viscosity of the liquid in the cracks; however, the difference in shear-wave velocity between sandstones saturated with water (low viscosity) and heavy crude (high viscosity) is small [Wang & Nur 1990]. The probably more significant differences in shear-wave attenuation between low and high viscosity fluids have not yet been fully investigated, and could lead to considerable differences in the differential amplitudes of split shear-waves in cracked structures.

There are large changes in the shape of the shear-wave AVO curves at isotropic/anisotropic reflectors for angles of incidence greater than about 40°. There are more subtle changes in behaviour for angles of incidence greater than about 20°, but these angles may be too wide to be observed in most reflection profiles, unless the reflector is shallow. However, changes in the amplitude of the reflected shear-wave signal with crack content should be visible in shear-wave monitoring of EOR in a crosshole survey. For the range of ray paths encountered in crosshole work it should also be possible to see changes in crack content using reflected shear-waves.

In Figure A1.4 similar reflection coefficient against angle of incidence graphs are plotted for the *SH*-wave. There is no change in the vertical incidence reflection coefficient, as the wave is polarized parallel to the cracks and, for thin cracks, it is not affected by changing anisotropy. The position of the zero point changes by about 15° as the percentage anisotropy is increased from 0% to 20%. This is caused by the change in shear-wave velocity with incidence angle in an anisotropic medium. There is no difference in the reflection coefficients for water-filled and dry cracks as the *SH*-wave does not generate any compressional forces in the thin cracks. Note that the difference in the behaviour of the *SV*- and *SH*-waves on reflection would lead to very significant differences in the polarization diagrams of the reflected waves from incident shear-waves with polarizations intermediate between *SV* and *SH*.

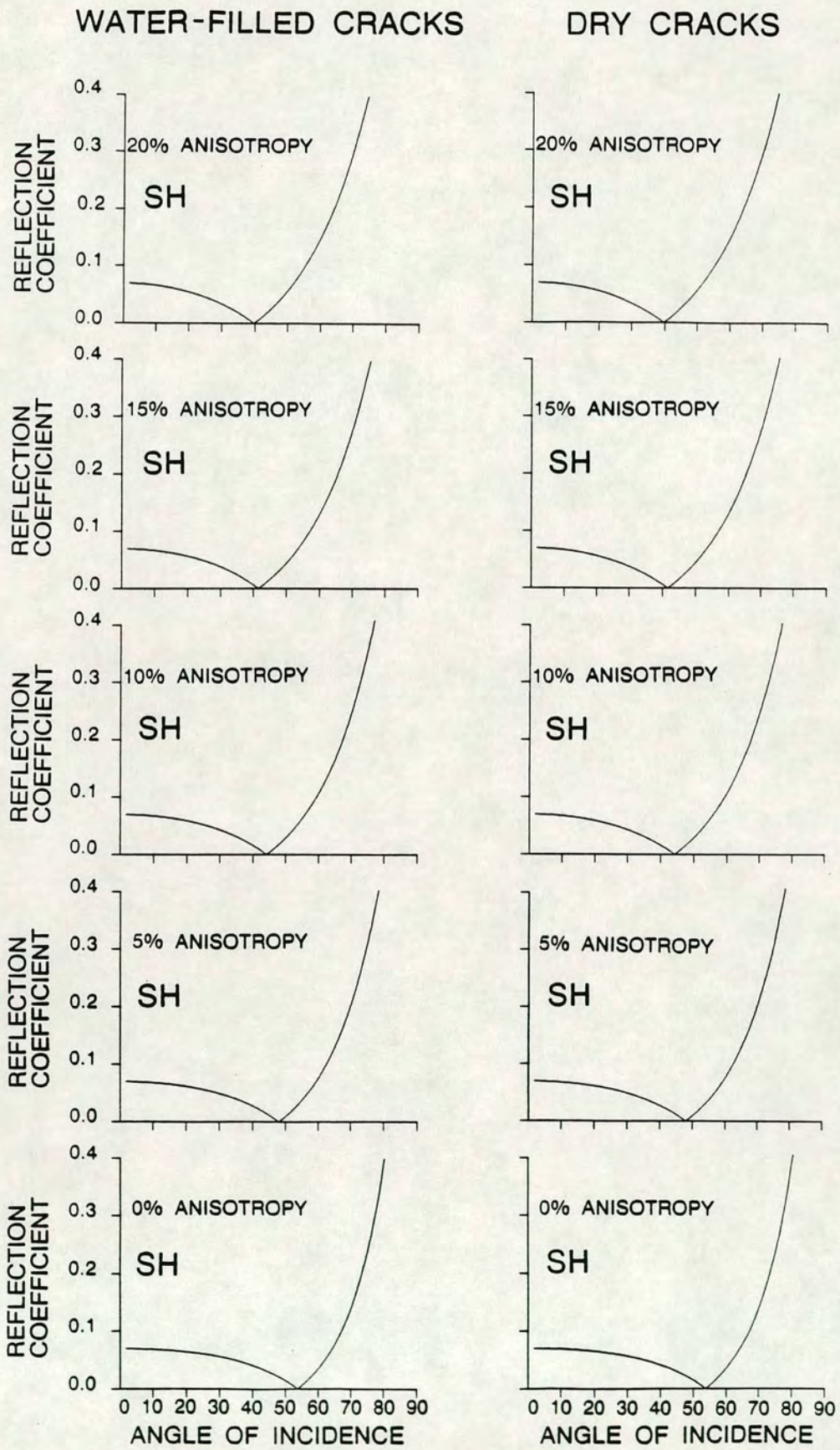

FIGURE A1.4: Plots of reflection coefficients against angle of incidence at an isotropic/anisotropic interface for *SH*-waves for the same range of models used in Figure A1.3.

Shear-wave AVO curves for inline cracks

In the above discussion, the cracks were aligned in the crossline direction. For cracks orientated in the inline direction (not shown here) the shear-wave velocities in the anisotropic layer do not vary with offset and so the position of the zero points do not change with anisotropy. Also, for inline thin cracks, there is no difference between the shear-wave AVO curves for water-filled and dry cracks. However, there is a change in the near normal reflection coefficient for the *SH*-wave, which would be polarized perpendicular to the cracks.

Discussion on Shear-wave AVO

For a general orientation of the cracks with respect to the acquisition plane there are variations in the shear-wave AVO for both percentage anisotropy and crack content for thin cracks. As cracks are made wider the observed change in the shear-wave AVO with crack content decreases until there is no change for spherical cracks. As the number of cracks is increased, there is a change in the near vertical reflection coefficients as the shear-wave velocity of the medium decreases due to the reduction in matrix material. This is most apparent for high porosity media where the fluid might be contained in spheroidal cracks and may also provide a means of distinguishing between areas of low and high crack densities within a reflector.

Thus, it can be seen that the largest change in the shear-wave AVO curves is in the near normal reflection coefficients. A comparison of the near-normal incidence reflected amplitudes for the shear-waves polarized parallel and perpendicular to the fractures yields information about the percentage anisotropy caused by parallel, vertical cracks in the reflecting layer [see Chapter Seven].

The reflected amplitudes of shear-waves are more difficult to interpret if the cracks in the reflecting layer are not aligned parallel to the inline or crossline directions as the shear-wave polarizations are rotated upon reflection. This, and other problems associated with the field measurement of shear-wave AVOs are discussed in the next section.

In the above section I showed that changes in anisotropy and fluid content in the reflecting layer lead to changes in the shear-wave AVO curves. Crack aspect ratio and

also different combinations of thin layer anisotropy and crack induced anisotropy cause changes in the position and nature of shear-wave singularities and it may be possible to use reflected amplitudes to study these parameters as well, although the information contained in the shear-wave AVO curves may not be sufficient to arrive at a unique model when so many variables are concerned. The shear-wave AVO curves may be of most use in monitoring EOR processes where only one parameter, the crack content, is changed.

A1.3 MODELLING SHEAR-WAVE AVO FIELD MEASUREMENTS

To study shear-wave AVOs with field data, it is desirable to have near noise and distortion free data. However, I now show that the orientation of the acquisition plane with respect to the crack strike can cause problems which distort the shear-wave signal.

Liu, Crampin & Yardley [1990] described the distorting effects on the shear-wave signal of offset reflections from an isotropic/isotropic interface if the source polarization was not strictly *SV* or *SH*. The distortions are caused by the difference in behaviour of the reflection coefficients with offset for the *SV*- and *SH*-waves leading to an effective rotation of the shear-wave signal. Such distorting effects would also be seen for vertical incidence at a dipping reflector. In general, shear-wave reflection surveys in the field use inline and crossline source orientations. In such cases, it might be thought that the effects described by Liu, Crampin & Yardley [1990] would be of no concern as shear-waves with polarizations parallel and perpendicular to the inline direction are generated at the source. However, if the strike of the cracks in the upper layer is not in the acquisition plane, the shear-waves split on their way to the reflector. The shear-waves generated at the source split into two components which are polarized parallel and perpendicular to the crack strike, and are distorted at the reflector for non-normal incidence. This leads to distortions in the measured shear-wave amplitudes. Both of the downgoing shear-waves then undergo an effective rotation upon reflection at the interface are split again on their upward path. This means that for a non-normal reflection, no matter what the source orientation, both the fast and slow shear-wave polarizations would be excited. A source-geophone rotation

[Alford 1986] would not calculate the correct polarization angle (as seen in Chapter Three) and it would not be possible to recover the required shear-wave amplitudes. In Figures A1.5 to A1.9, below, these distortions are examined in more detail.

Distortions at an anisotropic/isotropic interface

In the preceding section, shear-wave AVOs were examined for a model with an upper layer which, for simplicity, was isotropic. Now the distorting effects caused by an anisotropic upper layer are discussed. Field observations show that there is probably more anisotropy in the near-surface than at deeper levels [e.g. Becker *et al.* 1990; Bush 1990; Gaiser & Corrigan 1990]. Large amounts of near-surface anisotropy (compared to the entire depth interval) are also seen in data from the Austin Chalk in Texas (Chapters Five to Seven). Here, the second layer has been kept isotropic (Figure A1.5) so that only the distortions due to the presence of the upper anisotropic layer are seen. Cracks have been inserted in the upper layer with an aspect ratio of 0.01 and a crack density of 0.05 to give a differential shear-wave velocity anisotropy of approximately 5%.

Figure A1.5 shows the acquisition geometry for two reflection lines in the same model structure. In Figure A1.5a, the cracks are parallel to the inline direction, whereas in Figure A1.5b, the cracks strike is 30° from the inline direction. Figure A1.5c shows a side view of the acquisition geometry. Incidence angles range from 0° to 28° and are within the shear-wave window [Booth & Crampin 1985]. In Figure A1.6, the horizontal plane polarization diagrams are plotted, windowed around the reflected shear-wave arrival for both models. Figure A1.6a shows that shear-wave arrivals are linearly polarized if the source is polarized either parallel or perpendicular to the crack strike. It would be possible to measure the amplitudes of such arrivals after the usual AVO corrections for spherical divergence, NMO, etc. [Ostrander 1984]. Figure A1.6b shows that the arrivals from the model in which the cracks are 30° to the inline direction have been distorted and without detailed knowledge of the anisotropic structure and the initial pulse shape it would not be possible to estimate the undistorted shear-wave amplitude. The polarization diagrams shown in Figures A1.6a and A1.6b are fundamentally different from each other, and the information

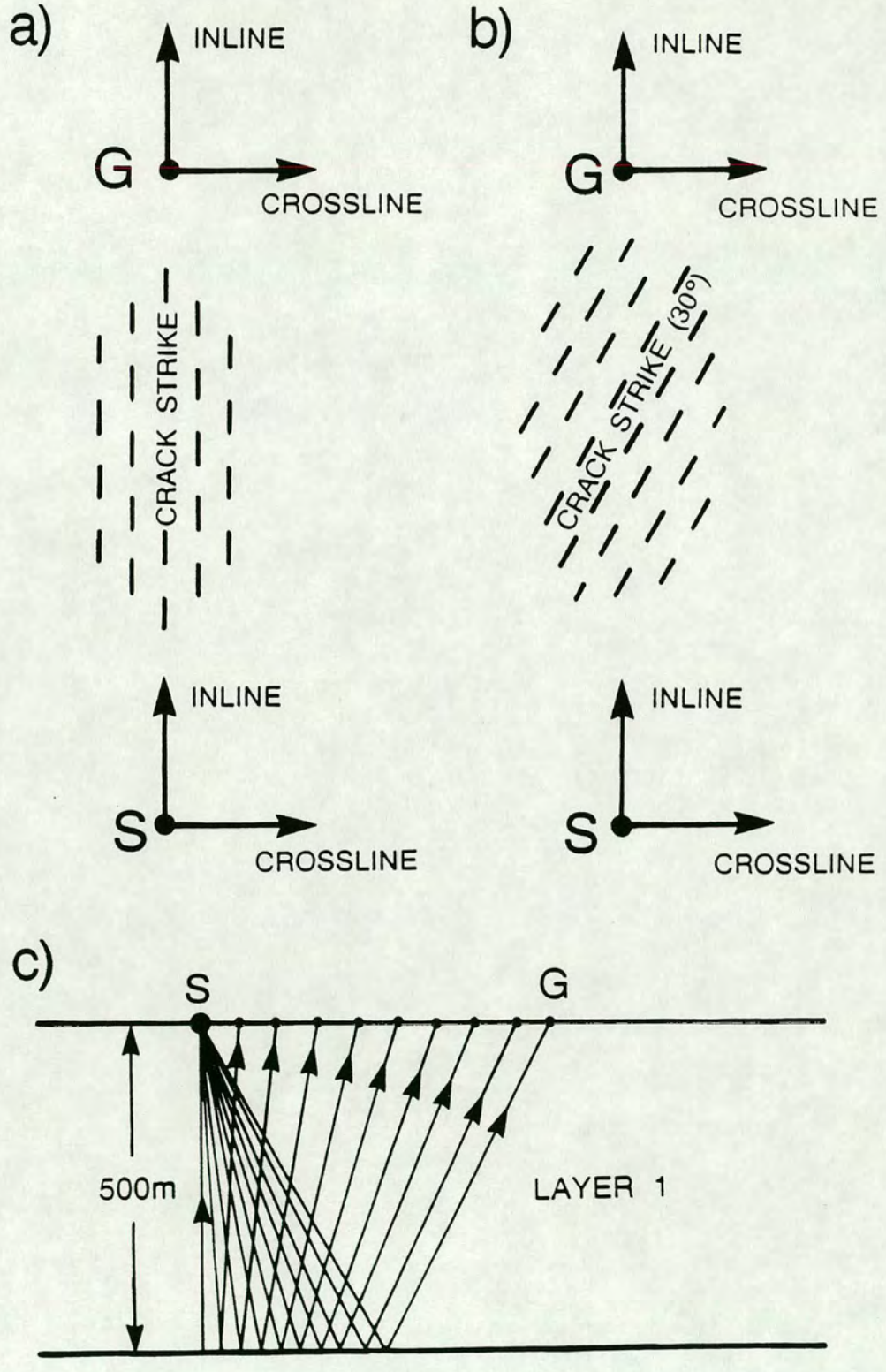

FIGURE A1.5: Schematic diagrams showing the plan view of acquisition geometry for a simple reflection line for two cases: (a) crack strike parallel to the acquisition plane; and (b) crack strike 30° from the acquisition plane. In these models the upper layer is anisotropic and the lower reflecting layer is isotropic. (c) Section of acquisition geometry. S marks the source location and there are 10 geophones 60m apart. Incidence angles range from 0° to 28° and are within the shear-wave window. Matrix density, *Vs* and *Vs* are 2.3g/cm^3, 4.33 and 2.5km/s, and 2.2g/cm^3, 4.07 and 2.38km/s in Layers 1 and 2 respectively.

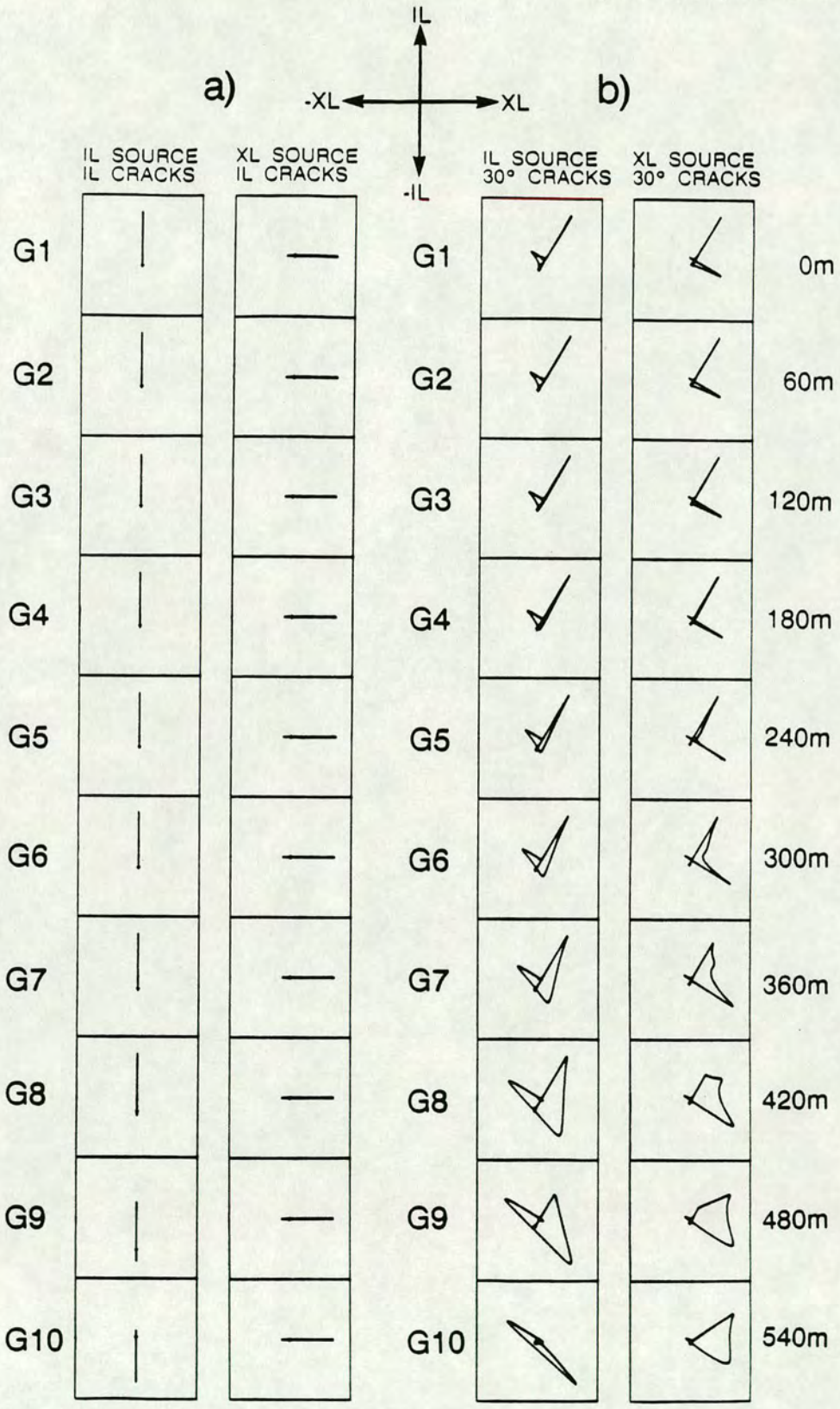

FIGURE A1.6: Horizontal plane polarization diagrams around the reflected shear-wave arrival normalized within each box for the model shown in Figure A1.5 Inline (IL) and crossline (XL) directions indicated. The polarization diagrams in (a) with crack strike parallel to the acquisition plane show linear motion. The polarization diagrams in (b) are non-linear due to the source wavelet being split by the anisotropic medium. In this case, direct amplitude information may be severely disturbed.

shown in Figure A1.6a cannot be recovered from Figure A1.6b by a simple source-geophone rotation. This is because the arrival seen the offset polarization diagrams is now the superposition of four shear-waves.

To illustrate this point the model was recalculated with the source and geophone axes parallel and perpendicular to the crack direction so that each source only excites one downgoing shear-wave (Figure A1.7). The incident shear-waves do not arrive at the reflector with polarizations either parallel or perpendicular to the inline direction, and for non-normal angles of incidence the reflected shear-waves are distorted. Such distortions are seen in Figure A1.7b, where the polarization diagrams change from linear for near vertical incidence reflections (geophones 1 to 3, incidence angles of 0° to 7°) to progressively more distorted shapes (geophones 4 to 10, incidence angles of 10° to 28°). This shows that to preserve the shape of the shear-wave AVO curves in the presence of near-surface anisotropy it is necessary for the acquisition plane to be parallel or perpendicular to the crack strike, that is the acquisition plane must be in a symmetry plane. I commented earlier that if the acquisition plane is parallel to the crack strike it does not yield any shear-wave AVO information as the shear-wave velocities do not change with angle of incidence for this azimuth. This means that the acquisition plane must be perpendicular to the cracks to be able to record any changes in the shear-wave AVO with increasing crack induced anisotropy or changes in fluid content without encountering such distortions in the shear-wave amplitudes.

It may be possible, with accurate information about the source pulse and velocity structure of the overlying layers to strip off the effects of these distortions. This may be desirable as then information about the shear-wave AVOs both perpendicular and parallel to the cracks would come from a single source. Where two sources are used to investigate reflected amplitudes the relative energy generated by each source must be known. However, at present our knowledge of source pulse shapes may not be adequate [Ziolkowski 1991].

At what offsets do distortions become apparent?

Such distortions as described by Liu, Crampin & Yardley [1990] occur at angles of incidence where *SV* and *SH* reflection coefficients become different. In Figure A1.8

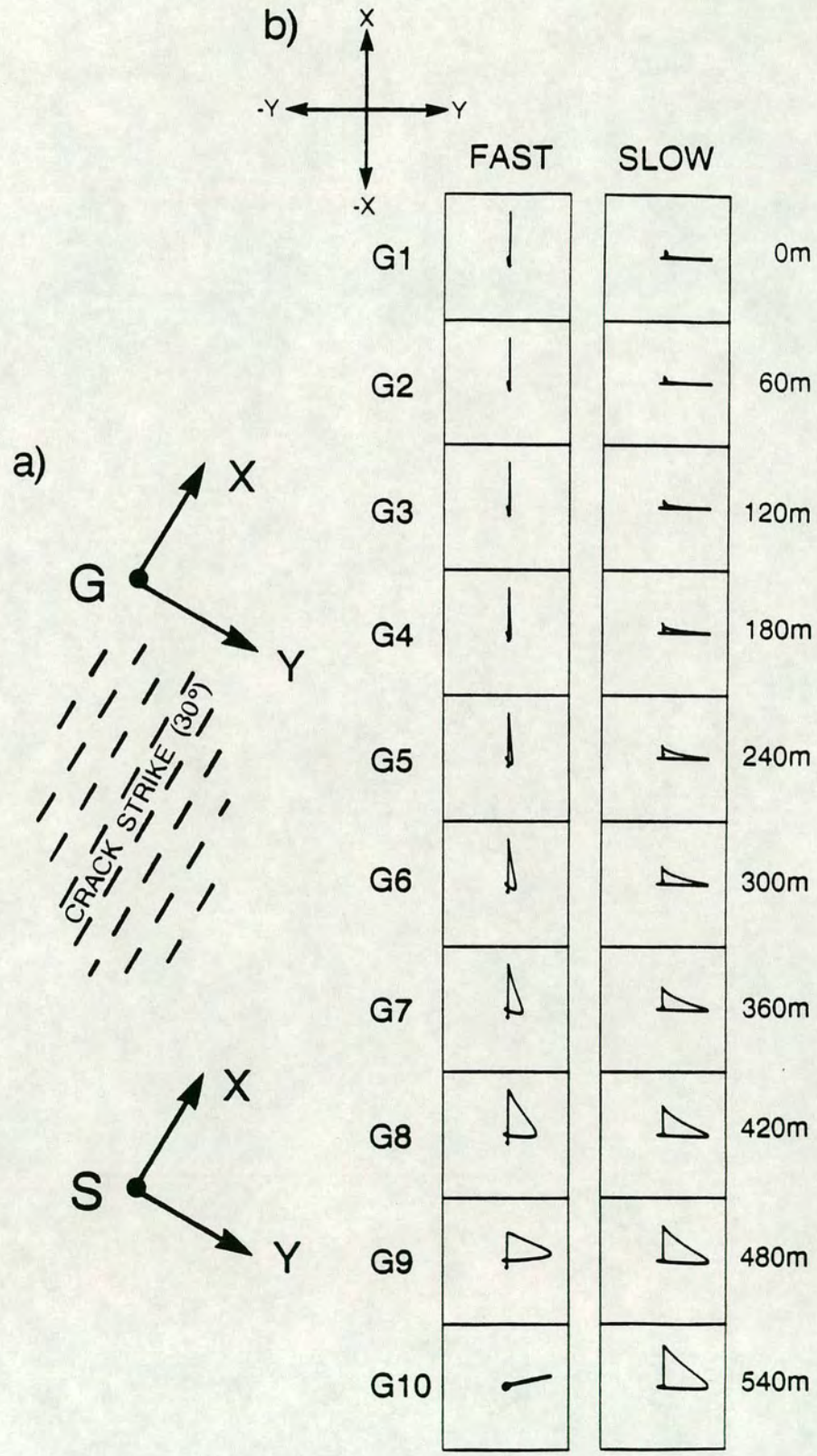

FIGURE A1.7: Seismograms from Figure A1.6b have been recalculated for the sources parallel to and perpendicular to the crack strike. The horizontal polarization diagrams show that the recorded shear-wave arrival is non-linear for offsets of greater than a few degrees. The *X*-direction is parallel to the strike of the cracks.

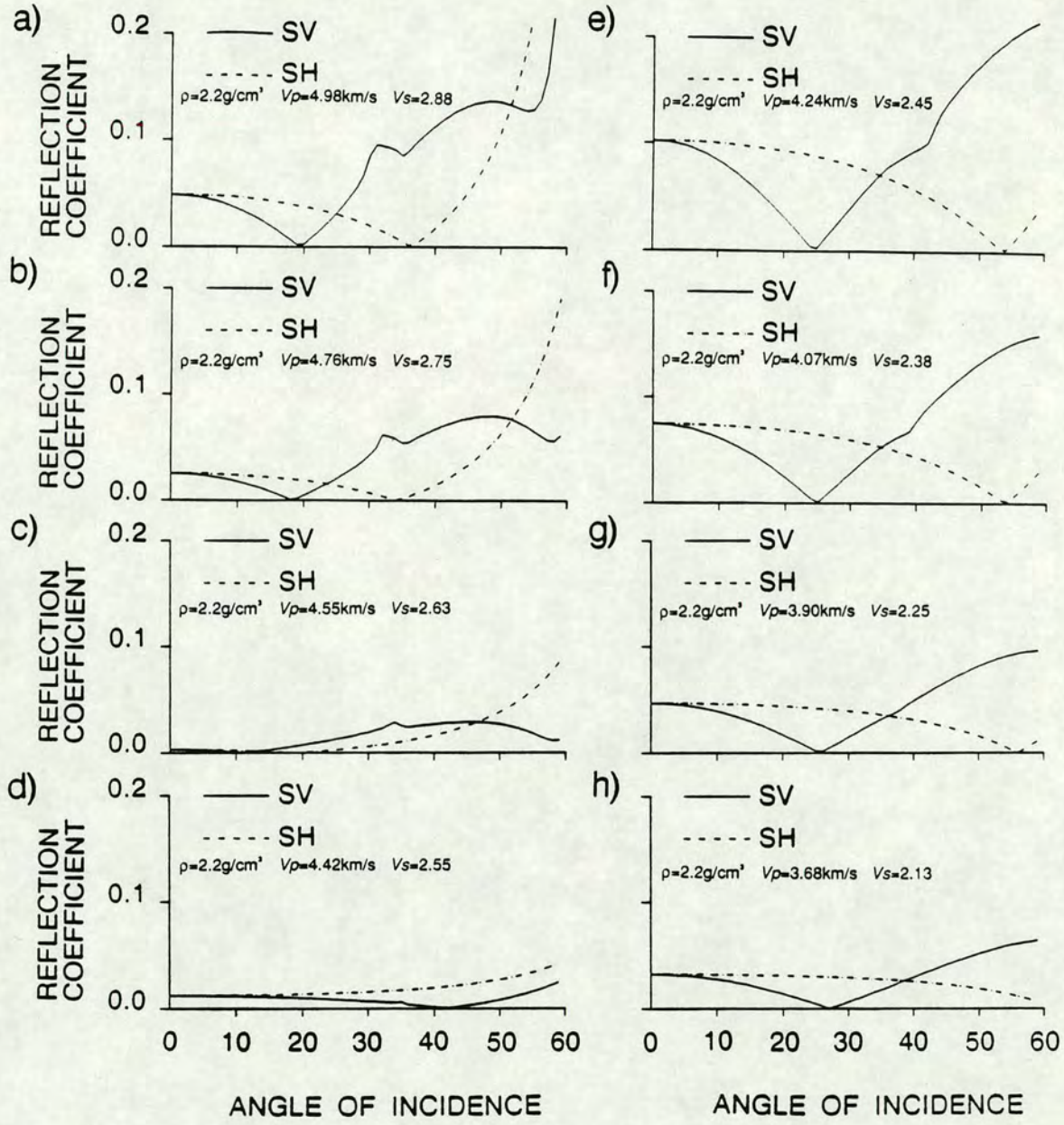

FIGURE A1.8: Reflection coefficients for *SV*- and *SH*-waves against angle of incidence for a range of velocity contrasts. The reflection coefficients for the *SV*- and *SH*-waves diverge for incidence angles of only a few degrees from the vertical. This leads to distortions in the reflected shear-wave if the incident wave was not strictly polarized *SV* or *SH*. In all cases the has a density of 2.3g/cm^3 and *Vp* and *Vs* of 4.33km/s and 2.50km/s respectively. The parameters of the reflecting layer are shown by each graph.

the incidence angles at which such anomalies occur for a range of interface parameters are shown. Figure A1.8 shows the variation of reflection coefficients with offset for *SV*- and *SH*-waves for an isotropic/isotropic interface for a range of velocity contrasts from low-to-high to high-to-low. An isotropic/isotropic interface is used for simplicity so that such distortions are not confused with the additional effects caused by the presence of anisotropy.

Figure A1.8 shows that in most cases the *SV* and *SH* reflection coefficients deviate from each other at incidence angles of more than a few degrees. Exceptions to this are in Figures A1.8c and A1.8d, where both reflection coefficients are small for near vertical incidence. In the models, the density of Layer 2 was held constant so that the observed effects are only due to changes in velocity contrast. To get a more physically plausible structure it would be possible to scale the densities with velocity as suggested by Gardner, Gardner & Gregory [1974]. Changes in density contrast also affects the amplitude of the reflected waves. In all cases, the *SV* and *SH* curves diverge for angles of incidence greater than about 12°, and in most cases for smaller angles of incidence. Figure A1.8f has the same isotropic parameters as used in the models in Figures A1.5, A1.6 and A1.7. It can be seen in Figure A1.7b that the difference in *SV* and *SH* reflection coefficients start at about 4°. This causes noticeable distortions at about geophone 4 (angle of incidence 10°). There are slight differences between Figures A1.7b and A1.8f as the graphs in Figure A1.8 have been calculated for plane waves an isotropic/isotropic interface for simplicity. ANISEIS, used curved wavefronts to calculate the seismograms in Figure A1.7.

Distortions at an isotropic/anisotropic interface

The AVO curves in Figures A1.3 and A1.4 were calculated for the case of crossline cracks and it was mentioned that interpretation would be more difficult, in the case of an isotropic/anisotropic reflector, if the acquisition plane was not along a symmetry plane. This is again due to the reflection coefficients at the interface. The model shown in Figure A1.5 has been recalculated with 5% anisotropy in the lower layer and an isotropic upper layer. Figure A1.9 shows how the reflected signal is distorted. Even for vertical incidence (geophone 1) it is seen that the polarization of

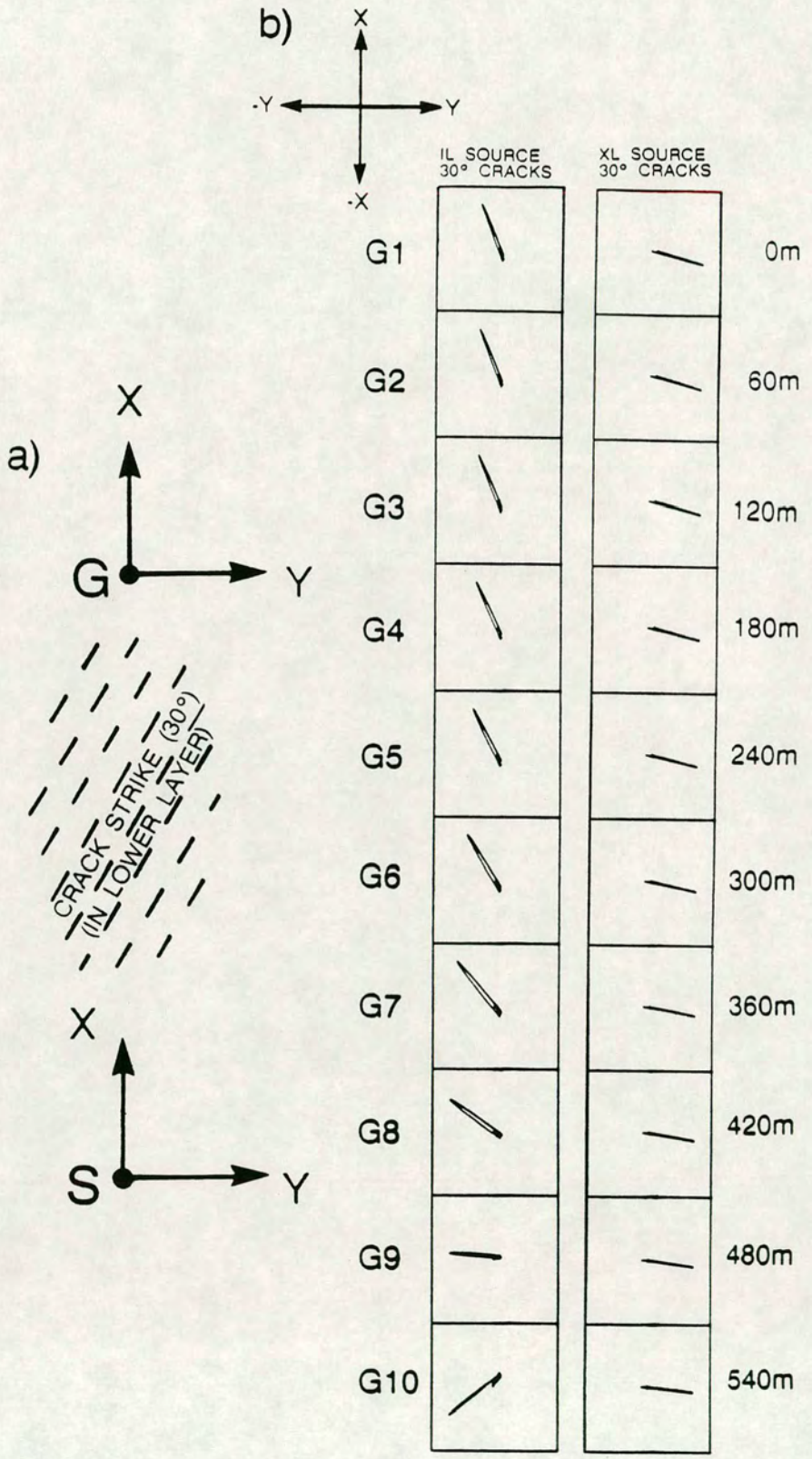

FIGURE A1.9: Seismograms from Figure A1.6b have again been recalculated but now the upper layer is isotropic and the lower layer has 5% anisotropy. Sources are in the inline and crossline directions. The shear-waves, which propagate only through the isotropic surface layer have been rotated upon reflection even for vertical propagation.

the reflected shear-wave has been rotated. The effect of these rotations at a reflecting incidence for vertical propagation on the analysis of shear-wave splitting in reflection surveys has been investigated by Li & Crampin [1990]. The distortion occurs because the reflecting layer has different reflection coefficients parallel and perpendicular to the crack strike. In this case, where the upper layer is isotropic both the *SV*- and *SH*-waves are rotated (but not split) upon reflection. At a low-to-high velocity interface the incident shear-waves are rotated away from the crack strike (and towards the crack strike for a high-to-low velocity interface), are nonorthogonal and do not have *SV* or *SH* polarizations after reflection. The situation is even more complex for the offset data where the polarization of the fast split shear-wave in the lower layer need not be parallel to the crack strike and also the effects described by Liu, Crampin & Yardley [1990] become significant.

The distortions mentioned here with offset reflection data are also likely to cause problems in CMP stacking (as discussed in Chapter Three). However, in many cases, the reflectors of interest are deep and all the reflected traces to be stacked have incidence angles within a few degrees of normal incidence. For such near normal incidence angles the distortions are small.

The conclusion of this section is that reflected shear-wave amplitudes are difficult to measure if the cracks are not parallel or perpendicular to the inline direction.

A1.4 CONCLUSIONS

The information content of shear-wave amplitude variations with offset have been investigated together with a study of the problems of their field measurement. Whilst shear-wave AVO curves are sensitive to crack parameters the presence of near-surface anisotropic layers means that it is impractical to measure them.

The shear-wave AVO curves are sensitive to percentage anisotropy in the reflecting layer. The greatest and most robust change is for near vertical incidence reflections. [I review current methods for using this property to determine fracture density in Chapter Seven.]

The shear-wave AVO curves also change with variations in crack content for thin cracks; however, such changes are only significant for wide offset data and the use of

shear-waves to examine crack content may be more suited to crosshole surveys.

Reflected shear-wave amplitudes for non-vertical incidence are difficult to measure if the acquisition plane is not parallel or perpendicular to the crack strike for isotropic/anisotropic interfaces due to the differences in reflection coefficients for *SV*- and *SH*-waves. Further distortions occur if the upper layers are also anisotropic.

Where layers are thick, analysis of transmitted shear-wave may yield the best method of quantifying the anisotropy as much information about the velocity structure and properties of the reflector need to be known to go from reflected amplitudes to rock parameters. Also, absolute amplitudes are hard to measure in field data. More work is required to see whether AVO analysis is viable for very thin layers, where the time delays for transmitted split shear-waves would be too small to resolve.

Reflected amplitudes are harder to interpret if the anisotropic symmetry is more complex (e.g. combinations of crack and thin layer anisotropy; changes in crack strike or dip with depth) or if the seismic interfaces dip. This is because the AVO curves are also affected by reflector dip and the presence of PTL-anisotropy.

REFERENCES

ACHENBACH, J.D. 1973. *Wave propagation in elastic solids.* North-Holland Publishing Company.

AHMED, H. 1989. Investigation of azimuthal anisotropy from offset VSP data - A case study. *51st EAEG meeting, Berlin, Abstract,* 133-134.

AKI, K. and RICHARDS, P.G., 1980. *Quantitative Seismology.* vol. 1, Freeman, San Francisco.

ALFORD, R.M. 1986. Shear data in the presence of azimuthal anisotropy, Dilley, Texas. *56th SEG meeting, Houston, Expanded Abstracts,* 476-479.

BANDY, O.L. and ARNAL, R.B. 1969. Middle Tertiary basin development, San Joaquin Valley, California. *GSA Bulletin* **80**, 783-820.

BARTHELEMY, P., TREMOLIERES, P. and ANDRIEUX, J. 1992. Fracture spacing related to bed thickness: geological or mechanical bed limits? *4th EAPG Conference, Paris, Abstract,* 156-157.

BARTON, D.C. 1948. Lost Hills, California - an anticlinal minimum. In: *Geophysical case histories.* L.L. Nettleton (ed.), SEG Publications, 515-522.

BARTOW, J.A. 1987. Cenozoic nonmarine sedimentation in the San Joaquin basin, central California. In: *Cenozoic basin development of coastal California.* R.V. Ingersol and W.G. Ernst (eds), Englewood Cliffs, New Jersey, Prentice-Hall, 146-171.

BECKER, D.F. and PERELBERG, A.I. 1986. Seismic detection of subsurface fractures. *56th SEG meeting, Houston, Expanded Abstracts,* 466-468.

BECKER, D.F., BISHOP, G.W., CLAYTON, K.N., PETERSON, D.N., RENDLEMAN, C.A. and SHAH, P.M. 1990. Shear-wave anisotropy at Marcelina Creek. *SEG Workshop: Vector Field Seismology Update, San Francisco, Abstract,* p.19.

BECKER, D.F., BISHOP, G.W., PETERSON, D.N., RENDLEMAN, C.A. and SHAH, P.M., 1989. Implications of seismic anisotropy within the Pembrook Unit, Midland, Texas. *SEG Workshop: Recording and Processing Vector Wavefield Data, Snowbird, Abstract,* p.60.

BECKHAM, W.E. 1990. Effect of anisotropic overburden on deep fracture analysis from surface multicomponent measurements: model and field example. *4th International Workshop on Seismic Anisotropy, Edinburgh, Abstract.*

BOOTH, D.C. and CRAMPIN, S. 1983. The anisotropic reflectivity technique: theory. *Geophysical Journal of the Royal Astronomical Society* **72**, 755-766.

BOOTH, D.C. and CRAMPIN, S. 1985. Shear-wave polarizations on a curved wavefront at an isotropic free surface. *Geophysical Journal of the Royal Astronomical Society* **83**, 31-45.

BRECKELS, I.M. and VAN EEKELEN, H.A.M. 1982. Relationship between horizontal stress and depth in sedimentary basins. *Journal of Petroleum Technology* **34**, 2191-2199.

BROWN, R.J., CRAMPIN, S. and GALLANT, E.V. 1992. Modelling shear-wave singularities in an orthorhombic medium. *5th International Workshop on Seismic Anisotropy, Banff, Abstract.*

BUSH, I. 1990. *Modelling shear-wave anisotropy in the Paris Basin.* Ph.D. thesis, University of Edinburgh.

BUSH, I. and CRAMPIN, S. 1991. Paris Basin VSPs: case history establishing combinations of fine-layer (or lithologic) anisotropy and crack anisotropy from modelling shear wavefields near point singularities. *Geophysical Journal International* **107**, 433-447.

CAMPDEN, D.A. 1990. *Analysis of multicomponent VSP data for shear-wave anisotropy.* Ph.D. thesis, University of Edinburgh.

CAMPDEN, D.A., CRAMPIN, S., MAJER, E.L. and McEVILLY, T.V. 1990. Modeling the Geysers VSP: a progress report. *The Leading Edge* **9**, (8), 36-39.

CHERRY, J.T. and WATERS, K.H. 1968. Shear wave recording using continuous recording methods: part 1. *Geophysics* **33**, 229-239.

CHOI, S. and GANGI, A.F. 1991. Effect of source imbalances on the determination of fracture orientations from VSP data. *61st SEG meeting, Houston, Expanded Abstracts,* 61-64.

CLIET, Ch., BRODOV, L., TIKHONOV, A., MARIN, D. and MICHON, D. 1991. Anisotropy survey for reservoir definition. *Geophysical Journal International* **107**, 417-427.

CORBETT, K., FRIEDMAN, F. and SPANG, J. 1987. Fracture development and mechanical stratigraphy of Austin Chalk, Texas. *American Association of Petroleum Geologists Bulletin* **71**, 17-28.

CRAMPIN, S. 1970. The dispersion of surface waves in multilayered anisotropic media. *Geophysical Journal of the Royal Astronomical Society* **21**, 387-402.

CRAMPIN, S. 1984a. An introduction to wave propagation in anisotropic media. *Geophysical Journal of the Royal Astronomical Society* **76**, 17-28.

CRAMPIN, S. 1984b. Effective elastic-constants for wave propagation through cracked solids. *Geophysical Journal of the Royal Astronomical Society* **76**, 135-145.

CRAMPIN, S. 1985a. Evaluation of anisotropy by shear-wave splitting. *Geophysics* **50**, 142-152.

CRAMPIN, S. 1985b. Evidence for aligned cracks in the Earth's crust. *First Break* **3**, (3), 12-15.

CRAMPIN, S. 1987a. Geological and industrial implications of extensive-dilatancy anisotropy. *Nature* **328**, 491-496.

CRAMPIN, S. 1987b. Crack porosity and alignment from shear-wave VSPs. In: *Shear-wave Exploration: Geophysical Developments*. S.H. Danbom and S.N. Domenico (eds), SEG Special Publications, 227-251.

CRAMPIN, S. 1988. Nonparallel shear-wave polarizations in sedimentary basins. *58th SEG meeting, Anaheim, Expanded Abstracts*, 1130-1132.

CRAMPIN, S. 1989. Suggestions for a consistent terminology for seismic anisotropy. *Geophysical Prospecting* **37**, 753-770.

CRAMPIN, S. 1990. Alignment of the near-surface inclusions and appropriate crack geometries for geothermal hot-dry-rock experiments. *Geophysical Prospecting* **38**, 621-631.

CRAMPIN, S. 1992a. The effects of crack geometry on wave propagation through aligned cracks. *5th International Workshop on Seismic Anisotropy, Banff, Abstract.*

CRAMPIN, S. 1992b. Arguments for EDA. *5th International Workshop on Seismic Anisotropy, Banff, Abstract.*

CRAMPIN, S., BOOTH, D.C., KRASNOVA, M.A., CHESNOKOV, E.M., MAXIMOV, A.B. and TARASOV, N.T. 1986. Shear-wave polarizations in the Peter the First Range indicating crack-induced anisotropy in a thrust-fault regime. *Geophysical Journal of the Royal Astronomical Society* **84**, 401-412.

CRAMPIN, S., CHESNOKOV, E.M. and HIPKIN, R.G. 1984. Seismic anisotropy - the state of the art: II. *Geophysical Journal of the Royal Astronomical Society* **76**, 1-16.

CRAMPIN, S., EVANS, R. and ATKINSON, B.K. 1984. Earthquake prediction: a new physical basis. *Geophysical Journal of the Royal Astronomical Society* **76**, 147-156.

CRAMPIN, S. and LOVELL, J.H. 1991. A decade of shear-wave splitting in the Earth's crust: what does it mean? What use can we make of it? And what should we do next? *Geophysical Journal International* **107**, 387-407.

CRAMPIN, S., LYNN, H.B. and BOOTH, D.C. 1989. Shear-wave VSPs: a powerful new tool for fracture and reservoir description. *Journal of Petroleum Technology* **5**, 283-288.

DIBBLEE, T.W. 1973. Stratigraphy of the southern Coast Ranges near the San Andreas fault from Cholame to Maricopa. *USGS Professional Paper 764*, 45p.

DOUMA, J. and CRAMPIN, S. 1990. The effect of a changing aspect ratio of aligned cracks on shear-wave vertical seismic profiles: a theoretical study. *Journal of Geophysical Research* **95**, 11293-11300.

DRAVIS, J.J. 1979. *Sedimentology and diagenesis of the upper Cretaceous Austin Chalk formation, South Texas and Northern Mexico.* Ph.D. Thesis, Rice University, Houston.

EDELMANN, H.A.K. and SCHMOLL, H. 1983. Seismic measurement with horizontally polarized shear-waves (German text). *Erdol-Erdgas* **99**, 23-32.

ELKINS, L.F. and SKOV, A.M. 1960. Determination of fracture orientation from pressure interference. *Petroleum Transactions, American Institute of Mining Engineers* **219**, 301-304.

EVANS, J.R. 1984. Effects of the free surface on shear wavetrains. *Geophysical Journal of the Royal Astronomical Society* **76**, 165-172.

FUCHS, K. 1968. The reflection of spherical waves from transition zones with arbitrary depth-dependent elastic moduli and density. *Journal of Physics of the Earth* **16**, 27-41.

FUCHS, K. and MULLER, G. 1971. Computation of synthetic seismograms with the reflectivity method and comparison with observations. *Geophysical Journal of the Royal Astronomical Society* **23**, 417-433.

GAISER, J.E. and CORRIGAN, D. 1990. Observation of azimuthal anisotropy in the near-surface. *4th International Workshop on Seismic Anisotropy, Edinburgh, Abstract.*

GARDNER, G.H.F., GARDNER, L.W. and GREGORY, A.R. 1974. Formation velocity and density - the diagnostic basics for stratigraphic traps. *Geophysics* **39**, 770-780.

GAROTTA, R. 1989. Definition of azimuthal anisotropy attributes from converted waves. *SEG Workshop: Recording and Processing Vector Wavefield Data, Snowbird, Abstract,* 22-24.

GHOSE, R. and TAKAHASHI, T. 1991. Multiazimuthal seismic reception in a borehole: implications on field delineation of seismic anisotropy. *61st SEG meeting, Houston, Expanded Abstracts,* 34-37.

GILBERT, F. and BACKUS, G.E. 1966. Propagator matrices in elastic wave and vibration problems. *Geophysics* **31**, 326-332.

HUDSON, J.A. 1980. Overall properties of a cracked solid. *Mathematical Proceedings of the Cambridge Philosophical Society* **88**, 371-384.

HUDSON, J.A. 1981. Wave speeds and attenuation of elastic waves in material containing cracks. *Geophysical Journal of the Royal Astronomical Society* **64**, 133-150.

IGEL, H. and CRAMPIN, S. 1990. Extracting shear wave polarizations from different source orientations: synthetic modelling. *Journal of Geophysical Research* **95**, 11283-11292.

JITUBOH, C.K., SAMS, M.S., KING, M.S. and WORTHINGTON, M.H. 1991. Field studies of the anisotropic properties of sedimentary rocks. *53rd EAEG meeting, Florence, Expanded Abstracts,* 284-285.

KAARSBERG, E.A. 1968. Elasticity of isotropic and anisotropic rock samples. *Transactions of the Society of Mining Engineers* **241**, 470-475.

KAYE, G.W.C. and LABY, T.H. 1986. *Tables of physical and chemical constants.* Longman, London.

KIM, C. 1989. Total wave field seismic data from the Lost Hills field, Kern County California. *SEG Workshop: Recording and Processing Vector Wavefield Data, Snowbird, Abstract,* 80-81.

KRAMER, D. 1991. Multicomponent multioffset VSP processing. *61st SEG meeting, Houston, Expanded Abstracts,* 38-42.

KUICH, N. 1989. Seismic fracture identification and horizontal drilling: keys to optimizing productivity in a fractured reservoir, Giddings Field, Texas. *Gulf Coast Association Geological Society Transactions* **39**, 153-158.

LAND, P.E. 1984. Lost Hills oil field. *California Division of Oil and Gas Publication TR32*, 2-16.

LATIL, M., BARDAN, C., BURGER, J. and SOURIEAU, P. 1980. *Enhanced oil recovery*, Gulf Publishing Company, Houston.

LAWTON, D.C. and BERTRAM, M.B. 1992. Field tests of three-component geophones. *5th International Workshop on Seismic Anisotropy, Banff, Abstract.*

LEFEUVRE, F. and QUEEN, J.H. 1992. Propagator matrix processing of single source 3-component VSPs. *5th International Workshop on Seismic Anisotropy, Banff, Abstract.*

LEFEUVRE, F., WINTERSTEIN, D. and MEADOWS, M. 1991. Propagator matrix and layer stripping methods: a comparison of shear-wave birefringence detection on two data sets from Railroad Gap and Lost Hills fields. *61st SEG meeting, Houston, Expanded Abstracts*, 55-60.

LEWIS, C., DAVIS, T.L. and VUILLERMOZ, C. 1991. Three-dimensional multicomponent imaging of reservoir heterogeneity, Silo Field, Wyoming. *Geophysics* **56**, 2048-2056.

LI, X-Y. 1992. *Shear-wave splitting in reflection surveys: theory, methods and case studies*. Ph.D. Thesis, University of Edinburgh.

LI, X-Y. and CRAMPIN, S. 1990. Dynamic and Kinematic features of shear-waves in a horizontally stratified earth. *4th International Workshop on Seismic Anisotropy, Edinburgh, Abstract.*

LI, X-Y. and CRAMPIN, S. 1991a. Complex component analysis of shear-wave splitting: theory. *Geophysical Journal International* **107**, 597-604.

LI, X-Y. and CRAMPIN, S. 1991b. Complex component analysis of shear-wave splitting: case studies. *Geophysical Journal International* **107**, 605-613.

LI, X-Y. and CRAMPIN, S. 1991c. Linear-transform techniques for analyzing shear-wave splitting in four-component seismic data. *61st SEG meeting, Houston, Expanded Abstracts*, 51-54.

LI, X-Y., CRAMPIN, S., and MUELLER, M.C. 1992. Shear-wave characteristics in the Austin Chalk from three reflection lines in South Texas. *54th EAEG meeting, Paris, Expanded Abstracts*, 616-617.

LI, X-Y., CRAMPIN, S., and MacBETH, C. 1993. Interpreting non-orthogonal shear-waves in multicomponent VSPs. *55th EAEG meeting, Stavanger, Expanded Abstracts*, paper C009.

LIU, E. and CRAMPIN, S. 1990. Effects of the internal shear-wave window: comparison with anisotropy induced splitting. *Journal of Geophysical Research* **95**, 11275-11281.

LIU, E., CRAMPIN, S. and YARDLEY, G.S. 1990. Polarizations of reflected shear-waves. *Geophysical Research Letters* **17**, 1137-1140.

LORENZ, J.C., TEUFEL, L.W. and WARPINSKI, N.R. 1991. Regional fractures I: a mechanism for the formation of regional fractures at depth in flat lying reservoirs. *American Association of Petroleum Geologists Bulletin* **75**, 1714-1737.

LUTHI, S.M. and SOUTHAITE, P. 1990. Fracture apertures from electrical borehole scans. *Geophysics* **55**, 821-833.

LYNN, H.B. and THOMSEN, L.A. 1986. Reflection shear-wave data along the principal axes of azimuthal anisotropy. *56th SEG meeting, Houston, Expanded Abstracts*, 473-476.

MacBETH, C. 1991a. Inverting shear-wave polarizations for anisotropy using three-component offset VSPs: synthetic seismograms. *Geophysical Journal International* **107**, 571-583.

MacBETH, C. 1991b. Inversion for subsurface anisotropy using estimates of shear-wave splitting. *Geophysical Journal International* **107**, 585-595.

MacBETH, C. and CRAMPIN, S. 1991. Processing of seismic data in the presence of anisotropy. *Geophysics* **56**, 1320-1330.

MacBETH, C., WILD, P., CRAMPIN, S. and BRODOV, L.Y. 1993. Optimal acquisition geometry for recording shear-wave anisotropy. *Canadian Journal of Exploration Geophysics*, in press.

MacBETH, C. and YARDLEY, G.S. 1992. Optimal estimation of crack strike. *Geophysical Prospecting* **40**, 849-872.

MacBETH, C., ZENG, X., YARDLEY, G.S. and CRAMPIN, S. 1993. Interpreting data matrix asymmetry in near-offset shear-wave VSP data. *Geophysics*, submitted.

MARTIN, M.A. and DAVIS, T.L. 1987. Shear-wave birefringence: a new tool for evaluating fractured reservoirs. *The Leading Edge* **6**, (1), 22-25.

MASON, T.D. 1988. Oil and gas developments in West Coast in 1987. *American Association of Petroleum Geologists Bulletin* **72**, 149-157.

McCAMY, K., MEYER, R.P. and SMITH. T.J. 1962. Generally applicable solutions of Zoeppritz's amplitude equations. *Bulletin of the Seismological Society of America* **52**, 923-955.

McGUIRE, M.D., BOWERSOX, J.R. and EARNEST, L.J. 1983. Diagenetically enhanced entrapment of hydrocarbons; southeastern Lost Hills fractured shale pool, Kern County California. In: *Petroleum generation and occurrence in the Miocene Monterey formation, California.* M. Isaacs (ed.) Pacific Section SEPM, 171-183.

MEADOWS, M.A. and WINTERSTEIN, D.F. 1992. Seismic detection of a hydraulic fracture from shear-wave VSP data at Lost Hills field, California. *5th International Workshop on Seismic Anisotropy, Banff, Abstract.*

MEDWEDEFF, D.A., 1989. Growth fault-bend folding at southeast Lost Hills, San Joaquin Valley, California. *American Association of Petroleum Geologists Bulletin* **73**, 54-67.

MILLER, G.F. and PURSEY, H. 1954. The field and radiation impedance of mechanical radiators on the free surface of a semi-infinite isotropic solid. *Proceedings of the Royal Society, Series A 223*, 521-541.

MILLER, D.E., COSTA, J. and SCHOENBERG, M. 1992. Inversion for the Devine anisotropic structure. *54th EAEG meeting, Paris, Expanded Abstracts*, 88-89.

MORRIS, J.H. and RARING, A.M. 1987. Oil and gas developments in South Texas in 1986. *American Association of Petroleum Geologists Bulletin* **71**, 134-139.

MUELLER, M.C. 1990. Prediction of lateral variability in fracture intensity using multicomponent shear-wave surface seismic as a precursor to horizontal drilling. *4th International Workshop on Seismic Anisotropy, Edinburgh, Abstract.*

MUELLER, M.C. 1991. Prediction of lateral variability in fracture intensity using multicomponent shear-wave surface seismic as a precursor to horizontal drilling. *Geophysical Journal International* **107**, 409-415.

MUELLER, M.C. 1992. Using shear waves to predict lateral variability in vertical fracture intensity. *The Leading Edge* **11**, (2), 29-35.

MURTHA, P.E. 1989. Preliminary analysis of the ARCO multicomponent seismic group experiment. *SEG Workshop: Recording and Processing Vector Wavefield Data, Snowbird, Abstract*, p.61.

NUR, A. 1989. Four-dimensional seismology and (true) direct detection of hydrocarbons: the petrophysical basis. *The Leading Edge* **8**, (9), 30-36.

ODELL, P.R. 1990. The exploitation of Western Europe's hydrocarbon resources: the politico-economic framework and prospects. *52nd EAEG meeting, Copenhagen, Abstract*, p.1.

OHANIAN, V. and BECKHAM, W.E. 1992. Depth variant fracture orientation from multicomponent VSP data, a field example. *5th International Workshop on Seismic Anisotropy, Banff, Abstract.*

OSTRANDER, W.J. 1984. Plane-wave reflection coefficients for gas sands at nonnormal angles of incidence. *Geophysics* **49**, 1637-1648.

POLLITZ, F.F. 1986. Pliocene change in Pacific plate motion. *Nature* **320**, 738-741.

POSTMA, G.W. 1955. Wave propagation in a stratified medium. *Geophysics* **20**, 780-806.

PRUETT, R.C. 1989. Polarity documentation for multicomponent seismic sources and receivers. *SEG Workshop: Recording and Processing Vector Wavefield Data, Snowbird, Abstract*, p.37.

PUJOL, J., BURRIDGE, R. and SMITHSON, S.B. 1985. Velocity determination from offset vertical seismic profiling data. *Journal of Geophysical Research* **90**, 1871-1880.

QUEEN, J.H., LEFEUVRE, F., SINTON, J.B., COX, V.D. and BULLER, P.L. 1992. Propagator matrix analysis of multicomponent data from the Conoco borehole test facility. *5th International Workshop on Seismic Anisotropy, Banff, Abstract.*

RAIKES, S.A. 1991. Shear-wave characterization of the BP Devine test site, Texas. *61st SEG meeting, Houston*, 65-68.

RATHORE, J.S. and FJÆR, E. 1992. Anisotropy as a function of crack size. *5th International Workshop on Seismic Anisotropy, Banff, Abstract.*

RATHORE, J.S., FJÆR, E., HOLT, R.M. and RENLIE, L. 1991. Acoustic anisotropy of synthetics with controlled crack geometries. *53rd EAEG meeting, Florence, Expanded Abstracts*, 538-539.

RATHORE, J.S., FJÆR, E., HOLT, R.M. and RENLIE, L. 1992. Experimental and theoretical acoustic anisotropy in controlled cracked synthetic rocks. *5th International Workshop on Seismic Anisotropy, Banff, Abstract.*

REASER, D.F. and COLLINS, E.W. 1988. Style of faults and associated fractures in Austin Chalk, northern extension of Balcones fault zone, Central Texas. *Transactions, Gulf Coast Association of Geological Societies* **38**, 267-276.

SALLAS, J.J. and WEBER, R.M. 1984. Comments on "The amplitude and phase of a vibrator" by Lerwill. *Geophysical Prospecting* **30**, 935-938.

SCOTT, R.J. 1977. The Austin Chalk-Buda trend of South Texas. *Transactions, Gulf Coast Association of Geological Societies* **27**, 164-168.

SLACK, R.D., EBROM, D.A., TATHAM, R.H. and McDONALD, J.A. 1992. The effects of multiple anisotropic layers on shear-wave analysis techniques. *5th International Workshop on Seismic Anisotropy, Banff, Abstract.*

SMIDT, J.M. 1989. VSP processing with full downgoing-wavefield deconvolution applied to the total wavefield. *First Break* **7**, (6), 247-257.

SPENCER, T.W. and CHI, H.C. 1990. Thin layer fracture density. *60th SEG meeting, San Francisco, Expanded Abstracts,* 1386-1387.

SPENCER, T.W. and CHI, H.C. 1991. Thin layer fracture density. *Geophysics* **56**, 833-843.

SQUIRES, S.G., KIM, C.D.Y. and KIM, D.Y. 1989. Interpretation of total wave-field data over Lost Hills field, Kern County, California. *Geophysics* **54**, 1420-1429.

STAPP, W.L. 1977. The geology of the fractured Austin and Buda formations in the subsurface of South Texas. *Transactions, Gulf Coast Association of Geological Societies* **27**, 208-229.

TATHAM, R.H. 1985. Shear-waves and lithology. In: *Seismic shear waves.* Dohr, G. (ed.), Geophysical Press, 87-133.

TATHAM, R.H. and McCORMACK, M.D. 1991. *Multicomponent seismology in petroleum exploration.* Society of Exploration Geophysicists.

TAYLOR, D.B. 1990. *ANISEIS Manual, version 4.5,* Applied Geophysical Software, Houston.

THOMSEN, L. 1988. Reflection seismology over azimuthally anisotropic media. *Geophysics* **53**, 304-313.

THOMSEN, L. 1991. Elastic anisotropy due to aligned cracks in porous rocks. *53rd EAEG meeting, Florence, Expanded Abstracts,* 224-245.

THURSTON, S.P., MASON, T.D. and JAMES, E.D. 1987. Oil and gas developments in West Coast in 1986. *American Association of Petroleum Geologists* **71**, 145-156.

TINKLE, A.R., WATTS, D.E., BEITEL, J.E. and COOK, G.R. 1989. Analysis of P and S wave signatures from the Bolt OMNIPULSE. *SEG Workshop: Recording and Processing Vector Wavefield Data, Snowbird, Abstract,* p.48.

WANG, Z. and NUR, A. 1988. Effect of temperature on wave velocities in sands and sandstones with heavy hydrocarbons. *SPE Reservoir Engineering* **3**, 158-164.

WANG, Z. and NUR, A. 1990. Wave velocities in hydrocarbon saturated rocks: experimental results. *Geophysics* **55**, 723-733.

WARPINSKI, N.R. and TEUFEL, L.W. 1991. *In situ* stress measurements at Rainer Mesa, Nevada Test Site - Influence of topography and lithology on the stress state in Tuff. *Journal of Rock Mechanics, Mineral Science and Geomechanics* **28**, 143-161.

WEEKS, A.W. 1945. Balcones, Luling, and Mexia fault zones in Texas. *American Association of Petroleum Geologists Bulletin* **29**, 1733-1737.

WILD, P. and CRAMPIN, S. 1991. The range of effects of azimuthal isotropy and EDA anisotropy in sedimentary basins. *Geophysical Journal International* **107**, 513-529.

WILD, P., MacBETH, C., CRAMPIN, S., LI, X-Y and YARDLEY, G.S. 1993. Processing and interpreting vector wavefield data. *Canadian Journal of Exploration Geophysics*, in press.

WINTERSTEIN, D.F. and MEADOWS, M.A. 1990a. Shear-wave polarizations and subsurface stress directions at Lost Hills field. *60th SEG meeting, San Francisco, Expanded Abstracts,* 1420-1423.

WINTERSTEIN, D.F. and MEADOWS, M.A. 1990b. Changes in shear-wave polarization azimuth with depth in Cymric and Railroad Gap oil fields. *60th SEG meeting, San Francisco, Expanded Abstracts,* 1424-1426.

WINTERSTEIN, D.F. and MEADOWS, M.A. 1991a. Shear-wave polarizations and subsurface stress directions at Lost Hills field. *Geophysics* **56**, 1331-1348.

WINTERSTEIN, D.F. and MEADOWS, M.A. 1991b. Changes in shear-wave polarization azimuth with depth in Cymric and Railroad Gap oil fields. *Geophysics* **56**, 1349-1364.

YARDLEY, G. and CRAMPIN, S. 1989. Extensive-dilatancy anisotropy: information content of reflection surveys and vertical seismic profiles. *SEG Workshop: Recording and Processing Vector Wavefield Data, Snowbird, Abstract,* p.14.

YARDLEY, G.S. and CRAMPIN, S. 1990. Automatic determination of anisotropic parameters from shear-wave splitting in the Lost Hills VSP. *60th SEG meeting, San Francisco, Expanded Abstracts*, 479-481.

YARDLEY, G.S. and CRAMPIN, S. 1991. Extensive-dilatancy anisotropy: relative information in VSPs and reflection surveys. *Geophysical Prospecting* **39**, 337-355.

YARDLEY, G.S. and CRAMPIN, S. 1993. Shear-wave anisotropy in the Austin Chalk, Texas, from multi-offset VSP data: case studies. *Canadian Journal of Exploration Geophysics*, in press.

YARDLEY, G.S., GRAHAM G. and CRAMPIN, S. 1991. Viability of shear-wave amplitude versus offset studies in anisotropic media. *Geophysical Journal International* **107**, 493-503.

ZENG, X. and MacBETH, C. 1993a. Accuracy of shear-wave splitting estimations from near-offset VSP data. *Canadian Journal of Geophysics*, in press.

ZENG, X. and MacBETH, C. 1993b. Algebraic processing techniques for estimating shear-wave splitting in zero-offset VSP data: theory. *Geophysical prospecting*, submitted.

ZIOLKOWSKI, A. 1991. Why don't we measure seismic signatures? *Geophysics* **56**, 190-201.

ZOBACK, M.L. 1992. First- and second-order patterns of stress in the lithosphere: the World Stress Map Project. *Journal of Geophysical Research* **97**, 11703-11,728.

ZOBACK, M.D., ZOBACK, M.L., MOUNT,V.S., SUPPE, J., EATON, J.P., HEALY, J.H., OPPENHEIMER, D., REASENBERG, P., JONES, L., RELEIGH, C.B., WONG, I.G., SCOTTI, O. and WENTWORTH, C. 1987. New evidence on the state of stress of the San Andreas Fault system. *Science* **238**, 1105-1111.

ZOBACK, M.D. and ZOBACK, M.L. 1991. Tectonic stress field of North America and relative plate motions. In: *Neotectonics of North America*. D.B. Slemmons, E.R. Engdahl, M.D. Zoback and D.D. Blackwell (eds), Geological Society of America.